

**DOCTORAL THESIS**

# Development of Silicon Oxynitride Nanocomposites with Single-Walled Carbon Nanotubes as Protective Coatings for Solar Cells

Elizaveta Shmagina

TALLINN UNIVERSITY OF TECHNOLOGY  
DOCTORAL THESIS  
20/2025

**Development of Silicon Oxynitride  
Nanocomposites with Single-Walled  
Carbon Nanotubes as Protective Coatings  
for Solar Cells**

ELIZAVETA SHMAGINA



TALLINN UNIVERSITY OF TECHNOLOGY  
School of Engineering  
Department of Materials and Environmental Technology

This dissertation was accepted for the defence of the degree 13/03/2025

**Supervisor:** Assoc. Prof. Sergei Bereznev  
School of Engineering  
Department of Materials and Environmental Technology  
Tallinn University of Technology  
Tallinn, Estonia

**Opponents:** Dr. Smagul Karazhanov, Senior Researcher  
Department for Solar Energy Materials and Technologies  
Institute for Energy Technology (IFE)  
Kjeller, Norway

Prof. Deniss Klauson  
Institute of Engineering and Circular Economy  
TTK University of Applied Sciences  
Tallinn, Estonia

**Defence of the thesis:** 22/04/2025, Tallinn

**Declaration:**

Hereby I declare that this doctoral thesis, my original investigation and achievement, submitted for the doctoral degree at Tallinn University of Technology has not been submitted for doctoral or equivalent academic degree.

Elizaveta Shmagina

-----  
signature



European Union  
European Regional  
Development Fund



Investing  
in your future

Copyright: Elizaveta Shmagina, 2025  
ISSN 2585-6898 (publication)  
ISBN 978-9916-80-277-9 (publication)  
ISSN 2585-6901 (PDF)  
ISBN 978-9916-80-278-6 (PDF)  
DOI <https://doi.org/10.23658/taltech.20/2025>

Shmagina, E. (2025). *Development of Silicon Oxynitride Nanocomposites with Single-Walled Carbon Nanotubes as Protective Coatings for Solar Cells* [TalTech Press]. <https://doi.org/10.23658/taltech.20/2025>

TALLINNA TEHNIKAÜLIKOOL  
DOKTORITÖÖ  
20/2025

**Üheseinaliste süsiniknanotorudega  
ränioksünitriidist nanokomposiitmaterjalide  
arendamine päikesepatareide kaitsekateteks**

ELIZAVETA SHMAGINA







# Contents

List of publications .....	7
Author's contribution to the publications .....	8
Introduction .....	9
Abbreviations and symbols .....	11
1 Literature review .....	13
1.1 Photovoltaics as one of the most promising alternative energy sources .....	13
1.1.1 Types and structure of solar cells .....	13
1.1.2 Factors affecting solar cell operation stability .....	15
1.1.3 Proper protection as a way to improve the stability of a solar cell .....	17
1.2 Polysilazanes as potential encapsulating materials .....	19
1.2.1 Perhydropolysilazane .....	21
1.3 Composites and nanocomposites .....	23
1.3.1 CNTs as a filler for creating a PSZ-based composite coating .....	24
1.3.2 Creating anisotropy of properties within a nanocomposite .....	25
1.4 Summary of the literature review and the aim of the study .....	26
2 Experimental .....	28
2.1 Preparation of $\text{SiO}_x\text{N}_y$ matrix films from PHPS .....	28
2.2 Preparation of $\text{SiO}_x\text{N}_y/\text{SWCNT}$ composite coatings .....	28
2.3 Elimination of the substrate influence on the FTIR and EDX measurements results .....	30
2.4 Characterization methods .....	31
2.5 Determination of optical constants .....	31
2.6 Measurement of mechanical and adhesive properties .....	32
3 Results and Discussion .....	34
3.1 Study of $\text{SiO}_x\text{N}_y$ matrix films .....	34
3.1.1 Comparative study of the influence of the curing method on the morphology and composition of single-layer matrix films .....	34
3.1.2 Influence of the curing method on morphology and composition of multi-layer matrix films .....	39
3.1.3 Long-term stability study of single- and multi-layer matrix films .....	41
3.1.4 Optical properties of single-layer matrix films .....	43
3.1.5 Mechanical and adhesive properties of as-cured and aged single-layer matrix films .....	47
3.2 Study of $\text{SiO}_x\text{N}_y/\text{SWCNT}$ composite coatings .....	50
3.2.1 Characterization of SWCNT films .....	50
3.2.2 Formation of $\text{SiO}_x\text{N}_y/\text{SWCNT}$ composite coatings in different configurations and study of their morphology .....	52
3.2.3 Comparative study of the influence of the SWCNTs embedding on the composition of $\text{SiO}_x\text{N}_y/\text{SWCNT}$ composite coatings .....	54
3.2.4 Optical properties of $\text{SiO}_x\text{N}_y/\text{SWCNT}$ composite coatings .....	57
3.2.5 Mechanical and adhesive properties of as-cured and aged $\text{SiO}_x\text{N}_y/\text{SWCNT}$ composite coatings .....	60
Conclusions .....	63
References .....	65
Acknowledgements .....	76

Abstract.....	77
Lühikokkuvõte.....	80
Appendix 1 .....	83
Appendix 2 .....	95
Appendix 3 .....	109
Curriculum vitae.....	134
Elulookirjeldus.....	136

## List of publications

The list of author's publications, on the basis of which the thesis has been prepared:

- I **E. Shmagina**, M. Danilson, V. Mikli, S. Bereznev, Comparative study of perhydropolysilazane protective films, *Surface Engineering* 38 (2022) 769–777, <https://doi.org/10.1080/02670844.2022>.
- II **E. Shmagina**, O. Volobujeva, A.G. Nasibulin, S. Bereznev, Fabrication of novel SiO<sub>x</sub>N<sub>y</sub>/SWCNT laminate-type composite protective coating using low-temperature approach, *Ceramics International* 50 (2024) 34312–34320, <https://doi.org/10.1016/j.ceramint.2024.06.250>
- III **E. Shmagina**, M. Antonov, A. Kasikov, O. Volobujeva, E.M. Khabushev, T. Kallio, S. Bereznev, Structural, Mechanical, and Optical Properties of Laminate-Type Thin Film SWCNT/SiO<sub>x</sub>N<sub>y</sub> Composites, *Nanomaterials* 14 (2024) 1806, <https://doi.org/10.3390/nano14221806>

## **Author's contribution to the publications**

Contribution to the papers in this thesis are:

- I Deposition of PHPS films, search for optimal curing parameters, measurement of UV-Vis and FTIR spectra, XPS data fitting, interpretation and visualization of the UV-Vis, FTIR, XPS, SEM, SEM EDX and line-scan results, author performed major part of writing in cooperation with co-authors.
- II Fabrication of  $\text{SiO}_x\text{N}_y/\text{SWCNT}$  composites, measurement of UV-Vis, FTIR and Raman spectra, interpretation and visualization of the UV-Vis, FTIR, Raman, SEM, SEM EDX results, author performed major part of writing in cooperation with co-authors.
- III Fabrication of  $\text{SiO}_x\text{N}_y/\text{SWCNT}$  composites, measurement of UV-Vis, FTIR and Raman spectra, performing the scratch tests, interpretation and visualization of the UV-Vis, FTIR, Raman, SEM, SEM EDX, SE results, author performed major part of writing in cooperation with co-authors.

## Introduction

A number of very serious challenges, ever increasing due to the impact of human activity on the environment and climate, have prompted discussions about the need to switch to alternative energy sources [1]. In addition to reducing environmental impacts, this transition is important in terms of growing population and economic growth, which drive an increased demand for energy, especially since fossil fuels are a finite source of energy [2]. It is projected that by 2050, 39% of global electricity production will come from renewable sources [3]. The current situation in Europe clearly illustrates the need for more serious actions aimed at developing new technologies and improving existing ones [4].

Photovoltaic (PV) energy, produced from an infinite and widely available source – solar radiation, is a promising alternative to energy from fossil fuels [5]. The strong increase in fossil fuel prices for energy production in recent years, the unfavorable global economic situation, and the increasing commercialization of solar cells (SC) have led to a significant reduction in the cost of PV technologies, which makes their use even more attractive. [6]. However, environmental factors are critically affecting the performance and lifetime of SCs [7]. In this regard the reliable and efficient technology of glass inflexible encapsulation for SCs has become widely used. But, the high weight (at least 2/3 of the total weight of the solar panel) and inflexibility significantly limit the use of standard glass protection for SCs, especially for modern flexible devices. In recent years, numerous attempts have been made to replace cover glass with other types of protection, mainly with polymer-based materials [8]. This task is challenging, as such coatings must meet all functional requirements i.e. excellent barrier protection against gases, humidity and ultraviolet (UV) irradiation, mechanical protection and often flexibility, chemical and thermal stability, etc., and, at the same time, the fabrication technology must be low-temperature, dependable, scalable, and inexpensive. Therefore, the selection of optimal protection is promising from both a technical and economic point of view, which is especially important nowadays.

Pre-ceramic polymer perhydropolysilazane (PHPS) is a promising candidate to be an encapsulant material due to its capabilities to transform/cure into vitreous  $\text{SiO}_x\text{N}_y$  films using relatively simple technologies avoiding the use of vacuum and high-energy waste processes. Diluted in organic solvents, this pre-ceramic material combines the process ability of liquid polymers and the high functional properties of resulting ceramics (glasses), and it also offers potential scalability of the technological process. Currently, PHPS-derived  $\text{SiO}_x\text{N}_y$  films are actively used as encapsulant coatings, such as for SCs and microelectronics, due to their high barrier (against oxygen, water and UV irradiation), dielectric, and anti-corrosion properties, as well as their non-toxicity and high thermal and chemical stability [9,10]. The high optical transmittance of PHPS-derived films makes them promising for optical applications [11].

However, there are some disadvantages. Despite the outstanding barrier properties reported in the literature, the long-term stability of PHPS-derived  $\text{SiO}_x\text{N}_y$  films raises questions, as it has not been well studied. Additionally, due to their inorganic nature, PHPS-derived films exhibit high mechanical hardness but relatively poor ductility. This effect became increasingly pronounced with an increase in the film thickness, starting from 250 nm and leading to brittle fracture of the material, which limits its use in the manufacture of flexible devices. [12]. One experimentally proven way to increase the flexibility of PHPS-derived layers is the strategy of alternating them with layers of more flexible (organic) materials. This results in a multilayer protective coating, but this leads

to problems with adhesion (peeling) of the layers during operation [9,12]. Therefore, composite technology looks promising as another alternative option that has not yet been widely explored, as the choice of different fillers allows for significant tuning of the properties of the resulting  $\text{SiO}_x\text{N}_y$ /filler composite films.

Possessing a high elastic modulus and extremely high strength, carbon nanotubes (CNTs) have established themselves as a promising reinforcing filler material in a number of different matrices such as polymers, ceramics, etc. They can also influence the matrix's thermal and structural properties [13,14]. Moreover, the alignment or orientation of CNTs within a matrix material gives possibility to prepare composite films with predictable anisotropy of coatings properties [15]. It should be noted that such composites based on PHPS-derived films with CNTs have not yet been studied.

Thus, the main focus of this doctoral thesis was to improve the state-of-the-art  $\text{SiO}_x\text{N}_y$  protective coatings derived from PHPS by combining them with CNTs. During this work, a simple and scalable process for the formation of protective nanocomposite coatings with oriented CNTs was developed. For the first time, the structural and functional properties of such composites were studied and described, and the effect of optical antireflection was found and investigated. In addition, several knowledge gaps regarding filler-free PHPS-derived films were addressed. Extensive work was conducted to compare the influence of two different low-temperature curing methods of PHPS on the structure and functional properties of the resulting  $\text{SiO}_x\text{N}_y$  coatings. For the first time, the optical constants of PHPS-derived films were measured and compared, and a study of the long-term stability of the composition and properties of prepared coatings was conducted. It was found that the PHPS-based coatings developed and investigated during the project could be promising for a wide range of other applications, not limited to the protection of flexible SCs.

The doctoral thesis is based on three publications and structurally consists of three chapters. The first chapter is a literature review that provides an overview of existing PV technologies, discussing their structure and the factors affecting their stability and operation. Special attention is given to device encapsulation approaches and the materials used for this purpose, leading to the consideration of PHPS as an alternative protective material for thin-film encapsulation. This chapter also describes the structure and properties of PHPS, the methods of its transformation/curing into  $\text{SiO}_x\text{N}_y$ , and an overview of successful strategies for the application of PHPS-derived  $\text{SiO}_x\text{N}_y$  films in PV and other fields. In addition, the chapter discusses objective disadvantages, which may be possible to overcome by creating a nanocomposite  $\text{SiO}_x\text{N}_y$ /filler coating with embedded and oriented CNTs as a filler.

Chapter 2 provides detailed information about the materials and methods used to prepare the samples and to characterize the properties of the  $\text{SiO}_x\text{N}_y$ /CNT composite coatings and  $\text{SiO}_x\text{N}_y$  matrix films that are the subject of this thesis. Chapter 3, which contains the main results and their discussion, is divided into two sections. The first section focuses on the study and comparison of the structure and properties of filler-free PHPS-derived matrix films cured by two different low-temperature methods. The second section is entirely devoted to the formation and characterization of  $\text{SiO}_x\text{N}_y$ /CNT composite films. Each of these sections is divided into subsections based on the subject of discussion.

The results obtained during the work on this thesis were presented as poster and oral presentations at several Estonian and international conferences from 2021 to 2024. They were also published as three peer-reviewed articles on which this thesis is based.

## Abbreviations and symbols

$\Delta$	Phase difference of reflected light
$\Delta n$	Difference between refractive indices
A, B, C, and D	Material coefficients in the Cauchy dispersion formulas
AFM	Atomic force microscopy
a-Si	Amorphous silicon
CdTe	Cadmium telluride
CNTs	Carbon nanotubes
COF	Coefficient of friction
CS	Cross-section
CVD	Chemical vapor deposition
$d$	Thickness
EDX	Energy dispersive X-ray spectroscopy
EU	European Union
EVA	Ethylene vinyl acetate
FTIR	Fourier transform infrared spectroscopy
$k$	Absorption index
$L_c$	Critical load
MWCNTs	Multi-walled carbon nanotubes
$n$	Refractive index
PCE	Power conversion efficiency
PET	Polyethylene terephthalate
PHPS	Perhydropolysilazane
PSZ	Polysilazane
PV	Photovoltaic
PVF	Polyvinyl fluoride
$R^2$	Correlation parameter between measured and calculated SE data
RBM	Radial breathing mode
$r_p$	Fresnel reflection coefficient for p-polarization state
$r_s$	Fresnel reflection coefficient for s-polarization state
RT	Room temperature
SCs	Solar cells
SE	Spectroscopic ellipsometry
SEM	Scanning electron microscopy
SLG	Soda lime glass
SWCNTs	Single-walled carbon nanotubes
$\tan \psi$	Ratio of the reflection coefficients for different light polarizations



TCO	Transparent conducting oxide
TO	Transverse optical
UV	Ultraviolet
UV-Vis-NIR	Ultraviolet-visible-near infrared
XPS	X-ray photoelectron spectroscopy
$\delta_p$	Phase component of the reflected light in p-polarization state
$\delta_s$	Phase component of the reflected light in s-polarization state
$\lambda$	Wavelength

# 1 Literature review

## 1.1 Photovoltaics as one of the most promising alternative energy sources

The importance of switching from traditional to alternative energy sources has been discussed for a long time. This discussion was motivated by the need to address the complex problem of the sustainable development of humanity [16]. This problem is associated with the increasingly harmful impact of human activities on the environment, which subsequently threatens the entire ecosystem of the planet. Transitioning to environmentally sustainable development is one of the major goals of the recent agenda of European Union (EU) policymakers. The European Commission has developed its environmental policy under the European Green Deal, which aims to achieve climate neutrality of the EU by 2050 [17,18].

To achieve these goals, comprehensive work is being conducted to change established processes in the economic, industrial, agricultural, transportation, energy, and other related fields. All measures taken in various sectors aim to build a circular economy. This economy optimizes the consumption of resources, organizes their recycling and reuse, while simultaneously reducing emissions of harmful gases into the atmosphere and minimizing the disposal of waste into landfills [19,20]. An aspect that is inextricably linked to all of the above is energy use. The use of fossil fuels to generate electricity is a catalyst for the rapid increase in greenhouse gas emissions into the atmosphere [21]. Besides influencing climate factors, it also affects the environment. Statistics show that about 75% of EU greenhouse gas emissions come from energy use and production. This is why the change of energy sources is one of the most important steps towards a climate-neutral EU [17].

A reduction in emissions can be achieved by switching to renewable or green energy sources [7,22]. The variety of events in recent years and their impact on the EU energy sector clearly illustrated the need for more serious actions aimed at developing new technologies and improving existing ones [4,6].

Photovoltaics (PV) is developing rapidly and now is the third largest renewable energy source after hydroelectric power and wind power, and it has the greatest potential due to its universal geographical availability [23–26]. The source of electricity for PV is electromagnetic radiation, which most often comes from the sun but is not limited to it, thus becoming an abandoned and an inexhaustible source. The tool for this conversion is special semiconductor devices called solar cells (SCs).

Given these factors, the intensive development of solar power generators is becoming increasingly important in many areas of the economy, including energy, construction, agriculture, transportation, and aviation. In recent years, the production of SCs has become increasingly cost-effective, leading to their increasingly widespread use.

### 1.1.1 Types and structure of solar cells

Solar cells consist of multiple layers of different materials that perform specific functions to ensure the successful conversion of photons into electrical energy over the long term.

The entire volume of developed solar cells is usually divided into three generations according to the architecture and type of material used for photon absorption.

First-generation SCs include devices based on mono- and polycrystalline silicon wafers, which have the highest certified power conversion efficiency among currently

existing commercial SC modules (PCE = 26.7%). However, the high cost of these devices, arising from the need to use very high purity silicon (gives around 40% of the total cost), as well as the high consumption of materials, high energy usage, the complexity of the production process of the entire device, significant CO<sub>2</sub> emissions accompanying this production process, and incompatibility with flexible applications has led to the search for alternative options [27].

Second-generation is often called thin-film SCs and includes a range of different materials used, such as amorphous silicon, cadmium telluride (Figure 1.1a and b, respectively), gallium arsenide, copper indium gallium selenide, etc. with PCE in range from 5 to 20 % [1]. Their main competitive advantage compared to the first-generation is a reduction in the volume of materials used to form the functional layers of the SC, which significantly reduces the cost of production [28]. The main disadvantage of this generation is the use of toxic materials such as cadmium.

Third-generation includes organic SCs, quantum dot SCs, perovskite SCs, dye-sensitized SCs, and other new technologies that demonstrate promising conversion efficiency values (up to 26% for perovskite and 19% for organic SCs) comparable to the previous two generations. Moreover, the cost of the perovskite itself is just 3.1% of the entire device cost. However, these efficiencies of SCs decrease with increasing device area [7,27,29].

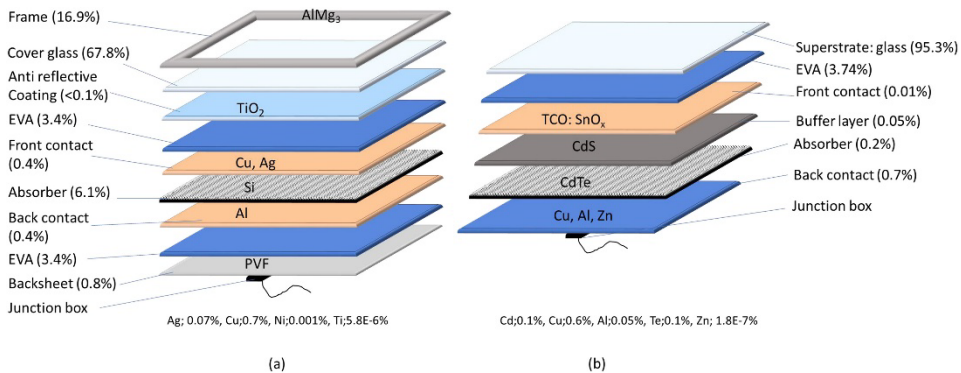


Figure 1.1. Typical structures of the second-generation SC with absorbers made of (a) amorphous silicon (a-Si) and (b) cadmium telluride. The figure also shows the mass fractions of the components relative to the weight of the entire SC. EVA: Ethylene vinyl acetate, TCO: Transparent conducting oxide, PVF: Polyvinyl fluoride [30].

The first two generations of SCs demonstrate a lifespan exceeding 20 years and are actively used in the market, with the first-generation SCs being predominant due to its high photoconversion efficiency, stability, and availability. Meanwhile, the third-generation SCs are in the laboratory study stage mainly due to problems with the actual efficiency and stability of the devices. For example, the lifespan for organic SCs with initial PCE of 10.2% not exceeding 6 years [7,21,27,31].

Usually, individual solar cells are connected to form a photovoltaic module, shown in Figure 1.2. The SCs are covered with an encapsulant, and the opaque back sheet protects the entire module from environmental factors and mechanical impacts. A fairly thick glass (about 3–4 mm thick) is used as the front protective cover. The frame is made of aluminum alloy and serves to create additional mechanical strength, but some types of

devices can be manufactured without it, as shown in Figure 1.1b [8,30]. In the case of flexible SCs, flexible transparent polymer substrates such as polyethylene terephthalate (PET), metal foil, etc., are used instead of glass [5,32].

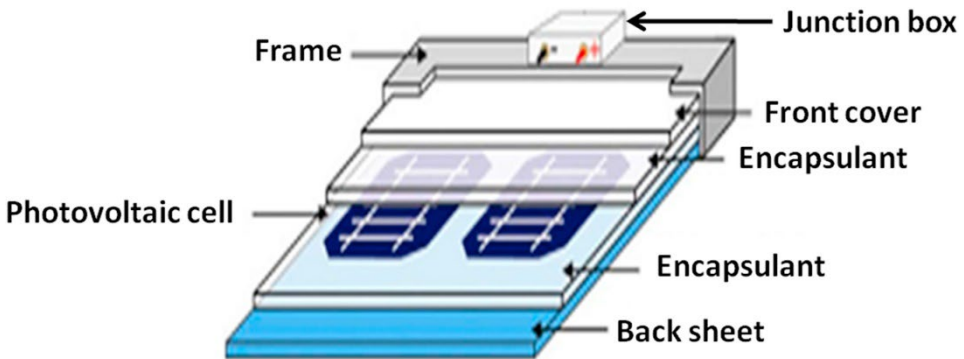


Figure 1.2. Schematic diagram of PV module components [8].

Without protection/encapsulation, solar cells of any generation, even the most stable ones, will degrade and lose their efficiency under the influence of external factors. Each generation of SCs has its own vulnerabilities that determine the rate of device degradation. Based on these vulnerabilities, it is necessary to select the most optimal encapsulation options. The following section provides an overview of the factors causing and accelerating the degradation of the SCs.

### 1.1.2 Factors affecting solar cell operation stability

Factors affecting the operation and lifespan of any SC can be divided into external and internal, which include normal operational wear and degradation of materials caused by light irradiation and environmental impact. The quality of the materials used inside the module and the quality of its installation and maintenance also affect stability and wear [30,33].

Developments to improve the stability of SCs are being conducted in several directions. The most popular is additive engineering, which involves the search for special additives that can increase the stability of the functional layers responsible for photoconversion. As can be seen from the SC structures presented in Figure 1.1, the SC consists of many layers, and the interfaces between them make a significant contribution to the efficiency of the device [34].

Next direction of the SC parameters improvement is interface engineering. This is important to prevent delamination or the appearance of defects that introduce recombination losses or other effects that affect the stability and efficiency of the device. These two directions relate to the management of internal factors that affect stability [34].

Another important direction is encapsulation engineering, which aims to combat external factors [34]. As shown in Figure 1.3, the main external factors affecting the performance and stability of any solar cell are radiation (mainly from the ultraviolet (UV) part of the spectrum), heating and large temperature changes (standard cyclic test of SCs is carried out with temperature changes from  $-40$  to  $85$  °C), such environmental influences

as oxygen and water, and mechanical impact, e.g. from hail [7,24,25]. The criticality of these factors on the operation of the SC depends on the sensitivity and stability of the materials used inside the device. One of the most important aspects for PV solar power is ensuring reliable protection of SCs from external damage, as the environment can be very aggressive.

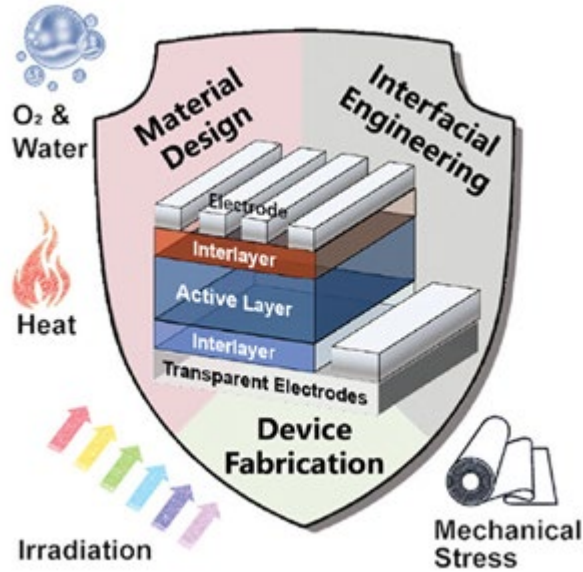


Figure 1.3. Factors affecting the operation and lifespan of solar cells [7].

Poor stability and rapid degradation of materials involved in photoconversion are problems that prevent the achievement of higher efficiency values, longer lifespans, and the commercialization of third-generation SCs. Most studies are related to the elimination of internal factors affecting stability, with the influence of external factors being in the shadow of the first ones. Generally, it can be said that the predominant amount of research and development in the field of photovoltaics aims to find new materials or optimize existing materials used inside the device [1,35]. However, achieving a synergistic effect must be considered, as third-generation absorbers often degrade under the influence of moisture and oxygen. The penetration of these agents can be significantly reduced by selecting the correct barrier protection for the device [7,24,27]. For example, perovskite technology is significantly cheaper than silicon (more than three times), but it can be made even cheaper. About 34% of the cost of an SC comes from glass and other packaging materials. Replacing them with cheaper and lighter options can further reduce costs while enabling the creation of flexible devices [27].

An additional factor complicating the situation is the high sensitivity of some materials used in third-generation SCs to high temperatures (e.g. for perovskites temperatures above 150 °C) and energies. This means that many traditional methods of fabricating SC layers are not compatible with these materials. This circumstance also stimulates research and development into alternative materials and methods for producing the functional layers of SCs [27,32].

From the above, it becomes clear that developing new options for flexible and reliable encapsulation is critically important for third-generation SCs. However, the use of new materials and approaches for encapsulating devices of other generations to reduce their weight and, if necessary, ensure their flexibility is equally relevant based on the concepts of sustainable development and the circular economy.

### **1.1.3 Proper protection as a way to improve the stability of a solar cell**

As noted in Section 1.1.1, the conventional approach of the SC protection formation uses an encapsulant, glass, and a back cover, which are most often connected to the SC by vacuum hot pressing. The process takes place at temperatures of 150–200 °C and requires special vacuum equipment [8,33].

A good encapsulating material must meet a number of criteria, such as excellent barrier properties against moisture and oxygen, high optical transmittance in the operating wavelength range of the SC, UV irradiation resistance, chemical inertness, high adhesion, thermal stability, and mechanical strength [7,32]. Meeting these criteria is important for all types of SCs but is especially critical for the third-generation devices due to stability issues with the materials used in them.

Due to the long list of requirements, selecting a material for encapsulation is not a trivial task. A number of encapsulation methods that use high-temperature processes, like vacuum hot pressing and some materials like polyvinyl butyral, successfully applied to silicon SCs, are also not applicable to the sensitive third-generation [34,36]. The most commonly used materials for encapsulating perovskite SCs are currently hollow glass, UV-curable resins, and polymeric sealants such as ethylene vinyl acetate (EVA) [27,33].

However, EVA having optimal protective properties and optical transmittance of 91%, which is used in about 80% of all existing PV modules, degrades very quickly under environmental influences, suffering from aging stability issues and thus reduces the PCE of the device. Tests showed severe degradation of EVA after 125 days of exposure to damp heat [33]. Therefore, it cannot be used as a material for encapsulation of sensitive flexible devices. As a result, many studies are now focused on improving the characteristics of EVA and finding alternative encapsulates [8,33].

The conventional crystalline silicon solar panel has a weight-to-area ratio of 13.7 kg/m<sup>2</sup> and, as shown in Figure 1.1, the glass contributes a minimum of 68% of the total SC weight [30]. However, the high weight, brittleness, low radiative cooling, and inflexibility significantly limit the application of this standard glass protection. Numerous attempts have been made to replace the cover glass with other types of protection, mostly with polymer-based materials [34,36]. However, this task is challenging as such encapsulation materials must combine high protective properties with low-temperature, reliable, scalable, and inexpensive production technology [24]. Reducing the weight of PV modules is also important not only from economic and technological points of view, but for reducing the amount of waste in the limited amount of established recycling technologies.

Figure 1.4 shows three approaches to encapsulating third-generation SCs [7,36]. Glass encapsulation continues to be used in applications where flexibility and low weight are not required. By analogy with the glass-glass option, double-sided lamination of SCs was developed. Both of these approaches use the same production algorithm, which consists of placing the SC between two glasses or two pieces of laminating material (PET and other transparent polymer foils), with the edges being filled with sealant (EVA, etc.). This technology is scalable to roll-to-roll processes but still is far from optimal since the connection of all components is achieved by hot pressing. Thin-film encapsulation is

becoming increasingly promising due to its advantages, such as direct formation of a coating on the SC, scalability, cost-effectiveness of the approach, minimal weight, smaller thickness and the production of high-quality material. This encapsulation option appears to be the most promising for the protection of flexible SCs [7,24].

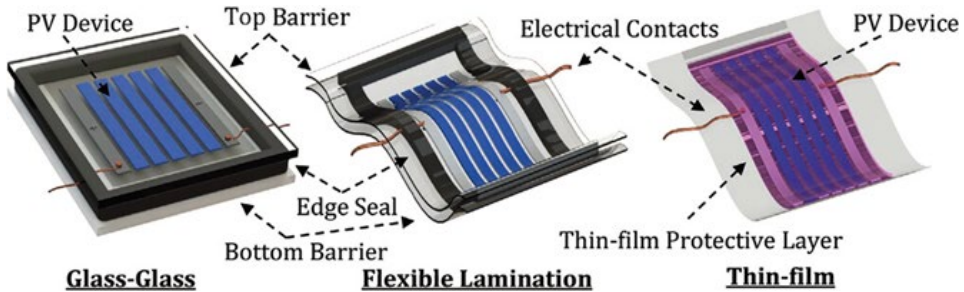


Figure 1.4. Encapsulation options for the third-generation of the SC [7].

Inorganic materials used for encapsulation mainly are alumina oxide ( $\text{Al}_2\text{O}_3$ ) and silicon-containing materials (like  $\text{SiO}_x$ ) [24,33], which provide excellent protection against moisture and oxygen, high optical transmittance but sometimes have defects in the form of pores and suffer from mechanical fragility. They are applied mainly using atomic layer or physical vapor deposition and chemical vapor deposition techniques, which are expensive methods that may create harsh conditions during the deposition process, which will be detrimental to sensitive materials used inside SC. In addition, these methods have limited productivity for large-scale production.

Organic materials such as EVA, polyvinyl butyral, epoxy resin and different siloxane polymer derivatives are more flexible but often provide worse protection from moisture and oxygen and can be more expensive [7,24,33]. Encapsulation with siloxane derivatives, which are organic silicon-based polymers (polydimethylsiloxane, etc.), however, gives good results for perovskite flexible SCs, showing good protective properties of the thin-film coating [34,37]. Polydimethylsiloxane was successfully used as an encapsulant in PV before the dominance of EVA. However, due to its higher cost, it was abandoned in favor of EVA, but in the case of the third generation of SCs, it is again gaining popularity as an encapsulant [36].

Disadvantages of above-mentioned inorganic and organic encapsulation materials can be reduced if they are used as layers in a multilayer protective coating. For example, the addition of protective silicon dioxide films to organic encapsulants during optimization of the encapsulation stack of perovskite SCs has significantly improved their stability without reducing the performance of SCs [38].

It should be noted that organic and inorganic silicon-based materials are promising for use in encapsulation of optoelectronic devices due to the similarity of functional properties to glass while having several advantages over traditionally used rigid glass, like flexibility, etc. [39].

Expanding the functionality of encapsulation coatings is an important aspect of optimization and developing of the SCs design [33]. Many materials used in the preparation of SCs degrade rapidly under the influence of UV radiation. An additional protective layer blocking radiation at wavelengths less than 400 nm allows the maintenance of high device efficiency compared to a 30% loss of efficiency in an encapsulated device not covered by

this layer over the same period of time [40]. Controlling the optical properties of solar cells by adding antireflective coatings or patterns increases the penetration of solar radiation into the device [36,41].

As can be seen from the above, when trying to move away from the traditional inflexible glass technology of solar cell protection, significant difficulties arise in finding alternative and flexible materials. Silicon-based materials appear to be the most promising option currently being explored for encapsulating flexible and sensitive SCs of the third-generation. Among silicon-based materials, polysilazanes can be singled out separately. These precursors allow the production of carbon-free (inorganic) glass-like flexible coatings and appear to be a promising candidate for the role of an alternative to classical encapsulation glass.

## **1.2 Polysilazanes as potential encapsulating materials**

Polysilazane (PSZ) is a close relative of siloxanes and is also being tested as an encapsulant for SCs. PSZ belongs to the group of special preceramic silicon-based polymers (Figure 1.5) with a Si–N–Si backbone, including various reactive or inert side groups at the Si and N atom sites [42,43]. PSZs are called preceramic because the result of transformation of the polymer precursor under certain conditions is ceramics. PSZs most commonly used in liquid form as solution in organic solvents.

These polymers have received much attention from science and industry in recent decades due to their wide range of attractive functional properties and corresponding applications. Due to their chemical structure and reactivity, PSZs are beneficial for chemical functionalization, allowing for the tuning of material properties [44,45]. Additionally, to achieve the goal of adjusting properties if this is the task, PSZs are often used as components for the formation of hybrid or composite materials [46].

PSZs can be used to form ceramic fibers, which can then be used as reinforcing materials in various composites [47]. However, the dominant application area for PSZs is in formation of coatings and thin films.



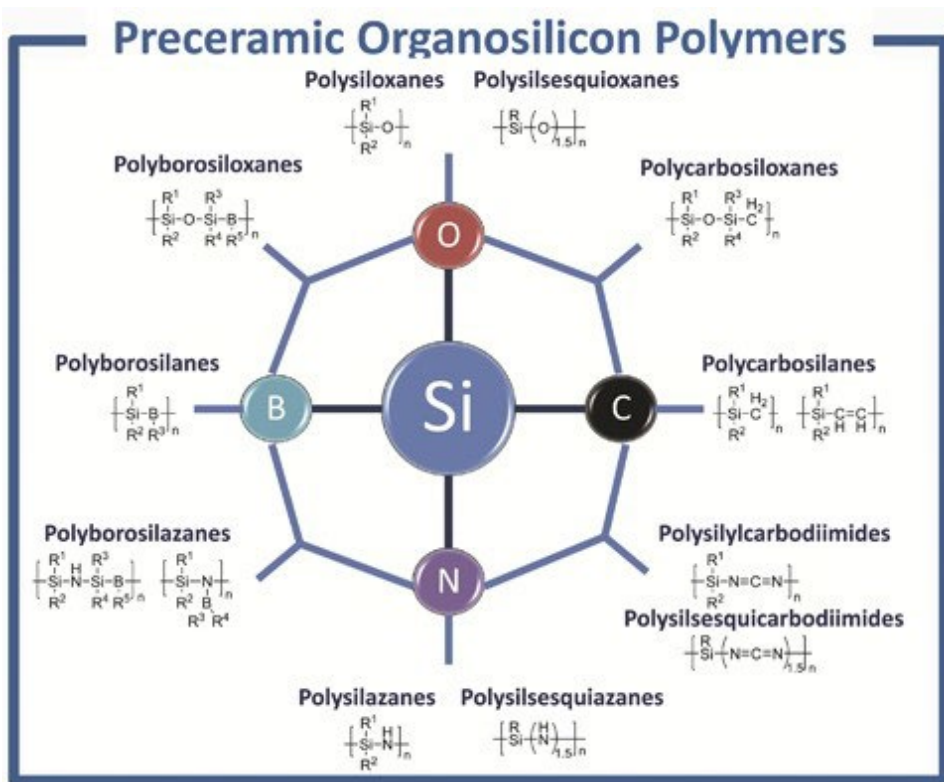


Figure 1.5. Family of preceramic Si-based polymers [42].

The coatings fabricated from PSZ solution have been identified as promising materials to meet extreme requirements for protection PV in space [48]. Films obtained from PSZs have a transmission of more than 95% in the visible range of the spectrum, excellent adhesion to various materials due to the formation of hydrogen bridges [49], excellent thermal and chemical stability, and recyclability [50]. Due to their liquid compatible nature, most of the economic, simple, and scalable coating methods are applicable to PSZ systems, such as spray coating, dip coating, spin coating, etc. [51].

PSZ use as anti-graffiti coatings looks very promising [52], as well as their use as anti-corrosion coatings for metals [44,46]. PSZ-based flexible transparent coatings are also known to improve the emissivity of solar cells, which can help to control system power fluctuations [28].

PSZs are divided into two subgroups: (i) inorganic; and (ii) organic, depending on the side groups. In the first case, only hydrogen atoms act as substituents. In the second case, hydrogen can be partially or completely replaced by other functional groups. There is a wide range of different PSZs on the commercial market, which, in addition to substituents, differ in solvents and the presence or absence of a catalyst. Inorganic PSZs are of greater interest as protective coatings due to their greater hardness and better barrier properties compared to organic PSZs [49].

### 1.2.1 Perhydropolysilazane

Inorganic PSZ is also called perhydropolysilazane (PHPS). This preceramic polymer is synthesized by an ammonolysis reaction from chlorosilanes, during which ammonium chloride is also formed and removed by filtration. After distillation, which removes ammonia and solvent, a white powder of PHPS is obtained [53]. This powder is soluble in organic solvents such as dibutyl ether and xylene. There are many solutions of different PHPS concentrations manufactured by Merck, IOTA, etc. on the market. One of the advantages of PHPS is that, depending on the conditions, the polymer can be transformed into ceramic or vitreous films ranging from silicon dioxide ( $\text{SiO}_2$ ) to silicon nitride ( $\text{Si}_3\text{N}_4$ ) PHPS-derived films [53,54].

In the case of preceramic polymers, cross-linking/transformation of precursor to ceramic material is commonly referred to as curing. Due to the presence of many Si-H and Si-N groups, PHPS is very reactive with hydroxyl groups and oxygen [55,56]. Consequently, the curing of PHPS occurs by hydrolysis and condensation reactions (Figure 1.6) in different environments, such as oxygen, moisture, aqueous ammonium solution, and hydrogen peroxide solution [57–59]. At low temperatures (close to room temperature (RT)), this transformation with aqueous ammonium or hydrogen peroxide solution proceeds slowly, requiring up to 24 hours. The reactions can be accelerated by introducing additional energy (usually with heating) into the system or by adding a catalyst [60].

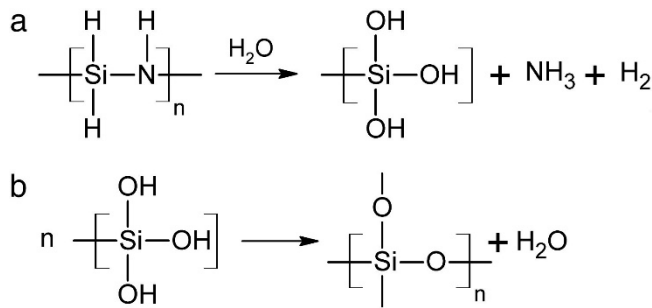


Figure 1.6. Curing of PHPS through (a) a hydrolysis reaction in humid atmosphere followed by (b) a condensation reaction [60].

The traditional method of curing PHPS, as recommended by its commercial manufacturers, is thermal annealing in an air atmosphere at moderate temperatures between 180 °C to 250 °C. The selected temperature affects the annealing time, which can range from 1 hour to 5 minutes respectively. At RT under ambient conditions, the transformation takes about two weeks. Using diethylethanolamine as a catalyst can reduce this time to 7 days under the same conditions, based on experimental results [49].

Annealing (curing) at high temperatures, known as pyrolysis, transforms PHPS into amorphous or crystalline ceramics [60–64]. This process is conducted at temperatures ranging from 400 °C to 1000 °C and can be performed in different atmospheres. The choice of atmosphere influences the transformation mechanisms of the PHPS and affects the final properties and composition of the resulting material. Pyrolysis of PHPS in a nitrogen atmosphere results in nitride ceramics, while an air atmosphere produces oxide ceramics [53,65]. The ceramic transition of PHPS begins at about 200 °C and ends at about 700 °C in the case of pyrolysis in air. During pyrolysis in nitrogen, the ceramic

transition temperatures are slightly higher. The inorganic nature of PHPS allows for higher ceramic yields and lower shrinkage values, distinguishing it from its organic relatives [65]. Shrinkage causes a number of technical problems like loss of dimensional accuracy, creation of porosity and reduction of mechanical strength, etc.

However, high-temperature exposure is not compatible with the application of PHPS-derived films to heat-sensitive materials, which are now actively used in photovoltaics and other technologies. For example, PET substrate, often used for lamination of SCs, cannot be heated above 70 °C, as it will lose its functional properties (barrier, optical, etc.) [60]. The use of high-humidity atmospheres or immersion of the PHPS film in solution for its conversion is also incompatible with sensitive PV materials.

An alternative low-temperature dry method is photoinduced curing of PHPS films in the presence of oxygen under the influence of ultraviolet radiation [9,66,67]. It was found that with this curing method, it is important to use UV radiation with wavelengths not exceeding 220 nm. This value is determined by the photon energy required to break the bonds in Si–H and Si–N groups to initiate the oxidation process of the PHPS to an amorphous vitreous film [54]. This process also avoids shrinkage due to the introduction of oxygen into the film [12].

In recent years, many applications of this curing method have been demonstrated using different UV radiation sources and times, ranging from a few seconds to hours [10,68–70]. By analogy with pyrolysis in different atmospheres, the possibility of obtaining silicon nitride through photoinduced transformation of PHPS was also investigated [71].

It was reported that PHPS films can be completely converted to SiO<sub>2</sub> using thermal curing. In contrast, UV curing will produce an under-converted silicon oxynitride (SiO<sub>x</sub>N<sub>y</sub>) film with a very high residual content of nitrogen, inexorably affecting the final properties of the coating. Some studies report non-uniform cross-sectional transformation of PHPS from UV curing. This is manifested by the formation of a near-surface layer of silicon dioxide on top of the main volume of the film, which consists of SiO<sub>x</sub>N<sub>y</sub> [9,67]. The higher the overall coating thickness, the more pronounced this effect.

However, these conclusions about the effectiveness of transformation depending on curing method used are based on a comparison of pyrolyzed films with UV-cured films [67]. Despite the abundance of literature on the different methods of curing and using PHPS-derived films, there is still no detailed comparison of their composition and, most importantly, the morphological and functional properties of films when using UV-induced and low-temperature thermal curing.

It is important to note that the long-term stability of the composition and properties of PHPS-derived films has not been extensively studied, although this information is crucial for using the material as a protective barrier coating.

It was illustrated by several research groups that PHPS-derived films have high optical transmittance (> 85% with PET substrate) [68,70]. However, there are significant gaps in the information regarding other optical properties, such as refractive indices ( $n$ ) of PHPS-derived films. The refractive index of uncured PHPS film was determined as  $n = 1.56$  [70]. Pyrolysis at 1000 °C leads to the complete transformation of PHPS into silicon dioxide, which is confirmed by the value of  $n = 1.463$ , close to the tabular value for SiO<sub>2</sub> ( $n = 1.46$ ) [61]. Curing of PHPS over ammonia vapor leads to the formation of a film with  $n = 1.48$ , subsequent pyrolysis at 900 °C causes a drop in  $n$  value to 1.45. This drop occurs due to the decrease in the residual nitrogen content in the PHPS-derived film during pyrolysis [57]. As mentioned above, UV curing may result in non-uniform film transformation across its cross-section (i.e. change in nitrogen content across the

cross-section), which should affect its optical properties. However, no data on measurements of such inhomogeneous PHPS-derived films have been found, so it is necessary to compare the optical properties of films cured by low-temperature UV-induced and thermally induced methods.

Some mechanical and adhesive properties of PHPS-derived films have been studied. The literature provides information on the measured hardness and Young's modulus (elasticity) of coatings using nanoindentation [61,72]. Adhesion data can be found from the cross-cut test or a tape peel test [49,66,73]. However, the values given in the articles may differ from each other by an order of magnitude. This difference in values is caused by the influence of numerous external and internal factors on the measurement result. A comparison of the adhesion and mechanical behavior of PHPS-derived films cured by low-temperature methods under dynamic mechanical influence has not been carried out for either as-cured or aged coatings.

Due to their inorganic nature, PHPS-derived films demonstrate better barrier properties compared to organic PSZs and are, therefore, most used for these purposes [66–73]. 250 nm thick PHPS-derived films show excellent oxygen and moisture barrier properties on PET substrates [67]. Thinner PHPS-derived films deposited on PET substrates also show optimal barrier properties [72]. However, as film thickness increases, it begins to lose its barrier properties on flexible substrates due to increasing mechanical fragility with thickness [67].

The use of PHPS makes it possible to form a protective film directly on the device, i.e. it allows for thin-film encapsulation (Figure 1.4) [12]. PHPS-derived films were successfully tested as one of the functional layers in multilayer protective encapsulants for perovskite and organic SCs [9,12]. With this encapsulation approach, the perovskite SC lost less than 10% of its PCE over 250 hours of a dump heat test, while a similar PET-encapsulated SC degraded completely in less than 50 hours [12].

Mechanical fragility and lack of elasticity negatively affect the possibility of using PHPS-derived films as flexible encapsulants. Currently, their most successful application for barrier protection is reported only as a component in a multilayer structure [9,12,66]. Unfortunately, this approach introduces additional interfaces between layers and associated adhesion and degradation problems.

One prospective way to improve the insufficient mechanical and flexible properties of PHPS-derived films could be the creation of composites based on them.

### **1.3 Composites and nanocomposites**

Composites are mixtures of two or more different materials that have clearly defined interfaces. The creation of composites and nanocomposites is a proven strategy for influencing material properties. The motivation for their use is to improve the insufficient properties of one material by adding another or to combine the best properties of all components in one composite material. Thus, composites have properties that differ from their components, making composite materials unique and very attractive for a wide range of applications [74].

This strategy can be implemented in bulk materials, thin films, and even fibers [22,75,76]. If at least one of the components is in the nanometer range, the term nanocomposite is applicable. The use of nanostructures allows for the creation of composites with unique properties due to the quantum-size effects of nanomaterials. The attractiveness of using nanomaterials also lies in their high surface area-to-volume ratio, resulting in significant changes in the properties of the composite with the

embedding of a small amount of nanofiller [77]. Nowadays, based on the goals of sustainable development, great attention is paid to the development of cost-effective and highly functional composites [78].

In general, a composite consists of a matrix material and filler materials that can be introduced into the matrix in various ways. Glass, ceramics, and metals are most often used as matrices, but polymers have become truly widespread [76,79,80]. The filler is usually either fibers, which are more in the micrometer range, or various forms of nanostructures [76].

In most cases, composites are created to improve the mechanical properties of the matrix, but the areas of application are not limited to this [81]. With the active development of nanomaterials, the possibilities of using composites extend to electronics, optics, sensors, and PVs [15,82–84]. For example, one strategy for improving the encapsulation of SCs using EVA is the introduction of various fillers into the polymer matrix, which positively affects the protective properties and long-term stability of the composite material [8].

Composites with nanocarbon materials as fillers are especially popular due to the wide range of unique properties of carbon allotropic forms [79,80]. Among the nanocarbon allotropes, there are different dimensional forms: diamond (3D), graphite (2D), graphene (1D), and fullerene (0D) [85]. In addition to the dimensions, they differ in hybridization of carbon atoms and their volume distribution, which determines the properties of the material. Graphene is one atomic layer of graphite. Carbon nanotubes (CNTs) are also one of these forms. They are classified as single-walled carbon nanotubes (SWCNTs) or multi-walled carbon nanotubes (MWCNTs), which are one or many seamlessly rolled sheets of graphene, respectively [86].

The use of CNTs to enhance the mechanical stability or thermal management of polymers has been intensively explored and confirmed [87–89]. In this regard, CNTs are a promising candidate for the role of filler to improve the mechanical and flexible properties of PHPS-derived films.

### **1.3.1 CNTs as a filler for creating a PSZ-based composite coating**

Active research into carbon nanotubes began in the 1990s and continues to the present day. Like any nanoparticle, CNTs can be synthesized using top-down and bottom-top methods. Arc discharge, chemical vapor deposition (CVD), and laser ablation methods are traditionally used for synthesis. Depending on the chosen method, different sources of carbon and energy are required for the synthesis of CNTs [77,90,91].

As mentioned above, nanotubes can be obtained by rolling a graphene sheet into a cylinder along the lattice vector of the graphene plane. The number of rolled graphene sheets determines the number of nanotube walls. The choice of vector determines the diameter and chirality of the tubes. The diameter of the tubes is in the nanometer range, while their length can reach hundreds of micrometers. The vector also affects whether the nanotubes display metallic or semiconductor properties [86,92,93].

It should be noted that the  $\text{SiO}_x\text{N}_y$  coatings are insulators, which can contribute to the accumulation of electrostatic charge, potentially leading to damage of the PV module as a result of discharge. In this regard, embedding a conductive filler such as CNTs can help mitigate this issue.

CNTs have outstanding optical and mechanical properties, as well as high thermal conductivity [90,94]. All these properties are directly related to the chemical bonds in the network of carbon atoms, that is, the backbone of the CNTs. These properties are

affected by the diameter-to-length ratio of the tubes, chirality, defects, and functionalization of the tube surface. Due to their physical, chemical, and biological properties, as well as the ability to form a wide variety of structures – from bundles and fibers to films – while having a very low weight, these tubes have found an extremely wide range of applications in completely different fields such as semiconducting inks, sensors, electrodes, etc. [90,95–97]. CNTs are produced on a large industrial scale, making their price lower compared to many other nanomaterials, which is an additional advantage.

Possessing a high elastic modulus, extremely high strength, and irreversible deformation occurring only under very extreme conditions, CNTs have established themselves as a promising reinforcing material in some polymer and metal matrices. Among other things, they can influence the matrix's thermal and structural properties [13,14,98,99]. However, for CNTs and nanomaterials of other forms, agglomeration caused by van der Waals interactions is a problem when introducing them into a matrix [81]. Additionally, the improvements mentioned above depend on the initial characteristics of the tubes themselves, their interfacial interaction with the matrix, and their alignment [100].

The successful formation of various CNT composites based on siloxanes and organic PSZs has been reported [101–103]. On the other hand, studies of the formation and properties of CNT composites with PHPS has not been reported yet. This opens the door for research towards the formation of CNT/PHPS-derived thin film composites.

### **1.3.2 Creating anisotropy of properties within a nanocomposite**

In addition to the materials used, the properties of the composite are also influenced by its architecture, meaning the spatial organization of the filler within the matrix. The architecture determines how the composite material will respond to external stimuli. Creating a uniform distribution of filler is a difficult task when producing effective composites due to the problem of nanomaterial agglomeration. Poor control of the dispersion of CNTs inside the polymer matrix often leads to less effective results in achieving the unique properties [100]. In contrast, the alignment of CNTs within a matrix material leads to anisotropy of properties, which cannot be obtained in disordered composites [15]. Controlling the orientation of the filler within the matrix is one of the key challenges in obtaining highly efficient nanocomposite materials [104].

Several types of architectures are used in the formation of composites: homogeneous, laminate, alignment, and network (Figure 1.7). All of them have their advantages and disadvantages and are selected based on the final objectives of using the composite material.

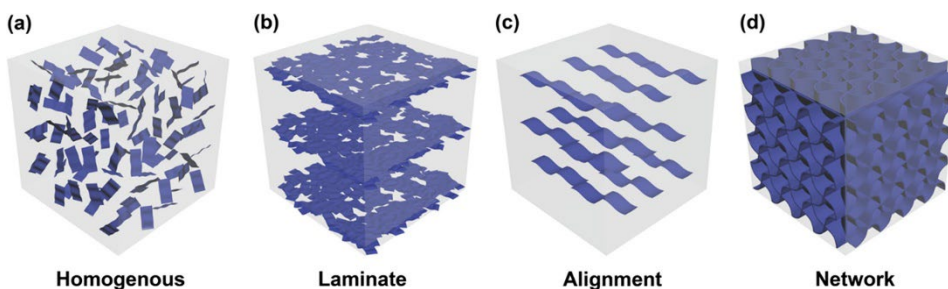


Figure 1.7. The schematic illustration of four types of nanocomposite architectures: (a) homogenous, (b) laminate, (c) alignment, and (d) network [75].

In the case of CNTs, it is difficult to achieve a uniform distribution of the filler in the matrix because it implies the absence of contact between the fillers, but the nanotubes are very long. As a result, even when loading a small amount of filler, the CNTs will encounter each other and form a network architecture of different densities.

An ensemble of CNTs aligned in one direction enhances the properties of each individual nanotube. In this case, the direction of alignment plays a key role in the anisotropic properties of the obtained composite. Several possible methods for aligning CNTs in the polymer matrix include using magnetic or electric fields, acoustic waves, mechanical force, shear force field, etc. [96,105,106].

The successful creation of a composite with mechanically stretch-aligned MWCNTs in a pyrolyzed organic PSZ matrix has been reported, making it possible to achieve anisotropy of electrical conductivity in the alignment direction for a large volume fraction of the embedded filler (60 vol%) [103]. There is a lack of studies connected with the preparation and investigation of oriented nanocomposite coatings with an ordered distribution of CNTs in the PSZ matrix, cured with low-temperature methods, to induce unique anisotropic properties (thermal, electrical, optical, etc.) in the obtained films.

From the above mentioned, it can be concluded that new research is needed in this promising direction of creating composite films with unique properties based on PHPS-derived films with oriented CNTs as a filler to obtain a promising material for flexible solar cell encapsulation.

#### 1.4 Summary of the literature review and the aim of the study

To achieve energy security and sustainable development goals, it is important to develop alternative energy sources [16,22]. Particular attention is given to photovoltaics due to its significant development potential [23,25]. Research and development in this field primarily focuses on studying and optimizing materials directly involved in photoconversion, such as absorbers, buffer materials, etc. [1,35]. However, in recent years, the importance of research and development in the protection/encapsulation of PV devices and increasing the functional range of materials used for this purpose has been emphasized [24,39,41].

Thin films obtained by curing the preceramic polymer PHPS have great potential for use as an encapsulant coating [11,67]. Several studies have shown promise in this direction, primarily due to high similarity of PHPS-derived films to the functional properties of glass, a traditional protective material for SCs. At the same time, PHPS-derived films have several additional advantages over rigid glass, such as potential

compatibility with flexible technologies, lower thickness and weight, compatibility with liquid and low-temperature production processes, the possibility of direct coating deposition on the surface of devices, and scalability to roll-to-roll processes [54,66,72]. These qualities make the technology potentially economically viable and better aligned with the sustainable approach.

Despite the diversity of research and development in relation to PHPS-derived coatings, the following gaps in knowledge have been noted:

- There is no detailed comparison of the structure and properties of PHPS-derived films obtained by the two most popular low-temperature curing methods of PHPS, namely (i) low-temperature annealing; and (ii) UV radiation induced curing.
- The long-term stability of PHPS-derived films is not well-studied yet, although it is a critical aspect for commercialization of the technology.
- The optical constants of PHPS-derived films have not been studied in much detail, although this knowledge is extremely important for the engineering design of optoelectronic devices.
- There is a large dispersion of data related to the mechanical properties of PHPS-derived films and a lack of comparison of these data measured under the same conditions for layers cured by different low-temperature methods.

The main disadvantages of PHPS-derived films are their mechanical fragility and limited flexibility caused by the inorganic nature of the precursor, which prevents the use of these films as stand-alone flexible coatings. Currently, PHPS-derived films are most successfully used as part of multilayer coatings, alternating with organic layers [9,12]. A promising way to overcome this drawback is the creation of matrix/filler composites. CNTs appear to be the most promising filler due to their outstanding mechanical properties and the possibility of their orientation/alignment within the matrix to obtain anisotropy of reinforcing properties [90,103]. Such composites based on PHPS-derived matrices have not yet been studied.

In this regard, the novelty and the aim of this study is to develop current state-of-the-art  $\text{SiO}_x\text{N}_y$  protective coatings derived from PHPS, combining them with CNTs in aligned nanocomposite structures. The application area of these coatings is focused on flexible optoelectronics but is not limited to it.

Based on the information above, the objectives of the work can be formulated as follows:

- Comparison of the influence of different low-temperature curing methods (thermally induced and UV irradiation induced) of PHPS on the compositional and morphological properties of the resulting  $\text{SiO}_x\text{N}_y$  matrix films.
- Development of technological route for the formation of oriented composite  $\text{SiO}_x\text{N}_y$ /CNT coatings various laminate-type configurations.
- Study of the compositional, morphological, optical, and mechanical properties of  $\text{SiO}_x\text{N}_y$  matrix films and  $\text{SiO}_x\text{N}_y$ /CNT composite coatings.
- Study of long-term stability of  $\text{SiO}_x\text{N}_y$  matrix films and  $\text{SiO}_x\text{N}_y$ /CNT composite coatings.



## 2 Experimental

In this chapter, the formation routes of thin  $\text{SiO}_x\text{N}_y$  matrix films and  $\text{SiO}_x\text{N}_y/\text{SWCNT}$  composite coatings, as well as the analytical methods used for their characterization, are summarized. More details are described in Articles I–III.

### 2.1 Preparation of $\text{SiO}_x\text{N}_y$ matrix films from PHPS

A commercially available 20% solution of perhydropolysilazane (PHPS) in dibutyl ether, purchased from Merck KGaA (NN-120-20, durXtreme GmbH, Germany), was used as a precursor for the formation of matrix films.

Two types of solid substrates were used in the work: (i) soda lime glass (SLG); and (ii) SLG coated with a molybdenum layer (SLG/Mo) of 1  $\mu\text{m}$  thickness. The choice of substrate for sample formation was determined by the requirements of the characterization method. Before deposition of the films, the substrates were ultrasonically cleaned with analytical grade isopropanol and a 20% aqueous solution of Decon 90 (Decon Laboratories Ltd, England) for 5 min in sequence. The substrates were then washed in Millipore water (Simplicity, Millipore Corp., France) and dried with 99.995% pure dry nitrogen.

The PHPS films were formed on the surface of cleaned substrates using the spin coating method at 2000 rpm for 1 min. For that purpose, in Article I was used spin-coater KW-4A (Chemat Technology, USA) and in Articles II and III Polos SPIN 150i programmable spin-coater (S.P.S. Ltd., Netherlands). Afterwards, the samples were dried on a hot plate at 40 °C for 2 min to remove residual dibutyl ether from the films. The samples were then converted into  $\text{SiO}_x\text{N}_y$  vitreous films using two low-temperature methods, which were compared throughout the work. In the first case, curing was conducted using thermal annealing in a Brother HD-14S muffle furnace (Zhengzhou Brother Furnace CO Ltd., China) at a temperature of 180 °C for 60 min, in accordance with the recommendations of the PHPS manufacturer. In the second case, the transformation occurred under the influence of UV radiation at wavelengths of 185 and 254 nm in air using Novascan digital UV ozone system (Novascan Technologies Inc., USA). The irradiation time was determined experimentally and was 40 min. Multi-layer PHPS-derived films were formed by sequentially repeating deposition/drying/curing cycles. More detailed information regarding PHPS matrix film formation and curing can be found in Article I.

### 2.2 Preparation of $\text{SiO}_x\text{N}_y/\text{SWCNT}$ composite coatings

Thin films of horizontally oriented single-walled carbon nanotubes (SWCNTs) synthesized using aerosol (floating catalyst) chemical vapor deposition (CVD) from two different batches were used as a filler for the formation of composite layers.

For the synthesis of SWCNTs used in Article II, ferrocene vapor was used as a catalyst precursor for iron nanoparticle formation, and CO was used as a carrier gas and carbon source for SWCNT growth. The nanotubes were grown in the gas phase by decomposing carbon monoxide on formed iron nanoparticles in a high-temperature (800 °C) reactor. SWCNTs were collected downstream onto filter paper in the form of thin films randomly oriented in the horizontal plane (Figure 2.1a). The thickness of the films was regulated by the time of SWCNT collection and could vary within  $\pm 10\%$ .

The SWCNTs used for the preparation of the composite coatings described in Article III were synthesized by the same CVD method in a high-temperature reactor using

hydrocarbon feedstock (ethylene and toluene), ferrocene vapor as a catalyst precursor, and hydrogen as a carrier gas. SWCNTs have a mean bundle length of approximately 30  $\mu\text{m}$ , a diameter in the range of 1.4–2.3 nm, and a density of approximately 0.12  $\text{g}/\text{cm}^3$ . A major advantage of using the SWCNTs prepared by this technique is the convenience and ease of their transfer from filter paper to the target surface by dry transfer. Additionally, the advantage of the technology is the ability to cut filter paper with SWCNTs lying on it into pieces of any shape and size.

The first batch of SWCNTs were provided by Prof. Albert Nasibulin from Skolkovo Institute of Science and Technology. The second batch were provided by Prof. Tanja Kallio from Aalto University. More information on the synthesis, characterization, and application of these SWCNTs can be found here [107–110].

$\text{SiO}_x\text{N}_y$ /SWCNT composite coatings were formed in two architectures/configurations corresponding to the order of SWCNT transfer: TOP and BOTTOM. A schematic representation of the technological route for the formation of composites is shown in Figure 2.1b. In the TOP case, the SWCNT filler film were transferred from paper to a spin coated and dried PHPS matrix film. In the BOTTOM configuration, the SWCNT film were dry transferred to the cleaned substrate (SLG or SLG/Mo), followed by the deposition and drying of the PHPS layer. Both composite architectures were then cured using two different curing methods, as described in Section 2.1 above. Additional treatment of the Mo surface with vapors from a 40% aqueous solution of HF acid for 10 minutes facilitated the dry transfer of the SWCNT film onto the Mo surface. More detailed information on the formation and curing of the  $\text{SiO}_x\text{N}_y$ /SWCNT composite coatings is available in Articles II and III.

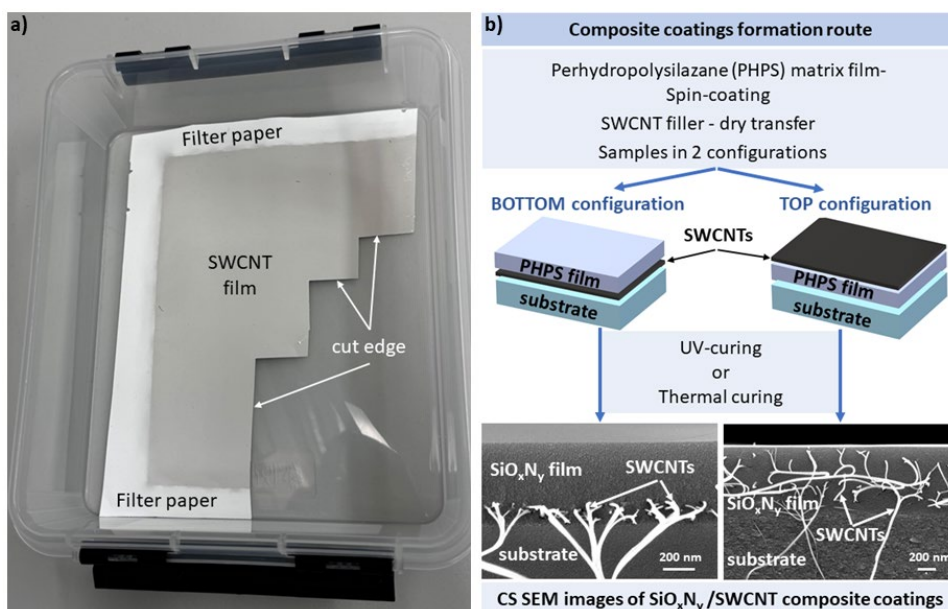


Figure 2.1. (a) Photograph of SWCNT film on top of the filter paper, (b) illustration of  $\text{SiO}_x\text{N}_y$ /SWCNT composite coatings formation route.

### 2.3 Elimination of the substrate influence on the FTIR and EDX measurements results

The PHPS-derived films studied in this work were quite close in chemical composition to SLG substrates. In some cases, this may affect the interpretation of the analytical data obtained from measurements. For example, this was clearly evidenced in the case of FTIR spectroscopy. In Figure 2.2, the red curve corresponds to the spectrum of the SLG substrate, where the absorption bands were mainly located in the fingerprint region (the region with wavenumber values between  $1500\text{ cm}^{-1}$  and  $400\text{ cm}^{-1}$ ) and showed high intensity. The positions of these bands almost completely overlap with the peaks of some vibrations of chemical bonds characteristic of PHPS-derived films, inevitably leading to distortion of the measured data (red dotted curve). The black curve illustrates the spectrum of the SLG/Mo substrate, in which only very weak peaks of molybdenum oxide are evident. Thus, the use of an SLG/Mo substrate makes it possible to avoid the overlap between the FTIR spectra of the SLG and the prepared PHPS-based structures (black dotted curve).

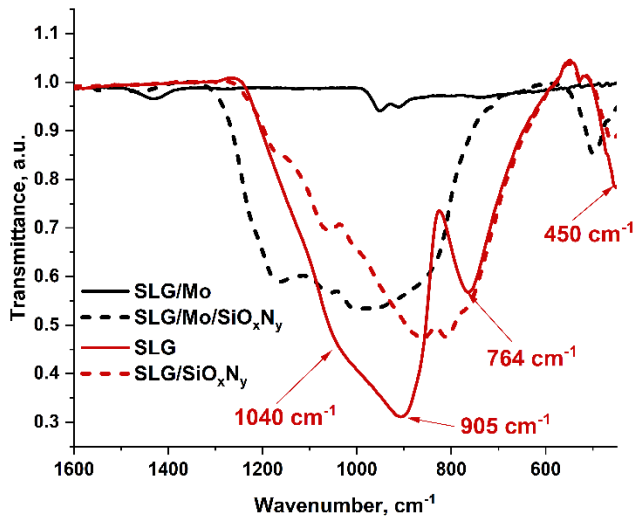


Figure 2.2. FTIR spectra of the SLG and SLG/Mo substrates used in the work and PHPS-derived films deposited onto these substrates.

Similarly, SLG/Mo substrates were used for EDX measurements of the chemical composition of prepared PHPS-based samples. When measuring from the surface of the sample, the accelerating voltage was selected in order to obtain a weak signal from molybdenum, which was then excluded from the final data received from measurement.

Detailed information on the substrate type used for different sample characterization methods is presented in the next section of this chapter.

## 2.4 Characterization methods

The characterization methods used in this study are represented in Table 2.1. More detailed information regarding the equipment and conditions for conducting measurements is available in Articles I–III.

Table 2.1. Characterization methods used in the work.

Properties	Characterization method	Characterization tool	Article	Substrate
Morphology, thickness	Scanning electron microscopy (SEM)	Zeiss Ultra 55, Germany Zeiss Merlin, Germany	I II, III	SLG and SLG/Mo
Functional groups determination	Fourier transform infrared (FTIR) spectroscopy	Platinum-ATR Alpha, Bruker Optic GmbH, Germany	I–III	SLG/Mo
Transmittance Absorbance Reflectance	UV-Vis-NIR spectrophotometry	UV-1800, Shimadzu Corp., Japan	I–III II, III II, III	SLG
Surface elemental composition	X-ray photoelectron spectroscopy (XPS)	Kratos Axis UltraDLD XPS System, England	I	SLG/Mo
Elemental composition	Energy dispersive X-ray (EDX) spectroscopy	Zeiss Ultra 55, Bruker Esprit 1.82 Zeiss Merlin, Bruker EDX-XFlash6/30 detector	I II, III	SLG/Mo
SWCNT structure	Raman spectroscopy	Horiba LabRam HR800	II, III	SLG
Optical constants, thickness	Spectroscopic ellipsometry (SE)	GES-5E, Semilab Co., Hungary	III	SLG
Mechanical and adhesive properties	Universal materials tribo-test device	CETR UMT-2, Bruker, USA	III	SLG/Mo

## 2.5 Determination of optical constants

Among the objectives of this work was the determination of the optical constants, namely refractive index ( $n$ ) and absorption index ( $k$ ) of the  $\text{SiO}_x\text{N}_y$  films and  $\text{SiO}_x\text{N}_y$ /SWCNT composite coatings. One of the methods that can be used for this purpose is spectroscopic ellipsometry (SE), which provides information about not only  $n$  and  $k$  but also the film thickness ( $d$ ). This is an indirect method of obtaining information about the material and, therefore, requires additional explanation (see also Article III).

During SE measurements, the values of the reflection coefficient ratio for different light polarizations ( $\tan \Psi$ ) and the phase difference ( $\Delta$ ) of light reflected from the sample were recorded and defined for each wavelength of the range used as:

$$\tan \Psi = \frac{|r_p|}{|r_s|} \text{ and } \Delta = \delta_p - \delta_s \quad (1)$$

where  $r_p$  and  $r_s$  are Fresnel reflection coefficients for p- and s-polarization states of the light, and  $\delta_p$  and  $\delta_s$  are phase components in p- and s-polarization states of the reflected light, respectively.

The measured data were modeled and analyzed using SEA software in the energy range of 1.3 – 5.5 eV. In most media, the refractive index is not constant but depends on the wavelength of the radiation passing through it, thereby demonstrating dispersion. The dispersion function was modeled using the Cauchy dispersion formulas:

$$n = n_0 + \frac{A}{\lambda^2} + \frac{B}{\lambda^4} \text{ and } k = C + \frac{D}{\lambda^2} \quad (2)$$

where  $n$  is the refractive index,  $k$  is the extinction coefficient (absorption index), and  $\lambda$  is the wavelength.  $A$ ,  $B$ ,  $C$ , and  $D$  are material coefficients. For modeling the SLG substrates, the refractive index was taken as:

$$n = 1.535 + \frac{0.0081}{\lambda^2} + \frac{0.00012}{\lambda^4} \quad (3)$$

based on former SE measurements.

## 2.6 Measurement of mechanical and adhesive properties

To study the mechanical and adhesive properties of the samples, a scratch test with progressive load was performed using a universal materials tribo-test device (Figure 2.3c). This test helps to identify and study many different types of failures, such as coating peeling, plastic deformation, and film or substrate cracking [111].

Figure 2.3a show the basic diagram of the scratch test with a fixed position of the stylus and a moving sample [112]. During our tests, the Rockwell (HRC) spherical-shaped diamond indenter with a diameter of 200  $\mu\text{m}$  and a cone angle of 120° was used as the stylus. The indenter moved along the surface of the fixed samples with a linearly increasing load of 200 g/mm (1.96 N/mm), starting from 50 g (0.49 N) and ending at 2050 g (20.10 N) in a single pass. The length of each scratch was 10 mm. This approach allowed us to determine the point of failure of the coating, called the critical load ( $L_c$ ) point.  $L_c$  values were determined using SEM by measuring the distance from the beginning of the scratch to the first visible damage to the coating. The type of damage received by the samples after scratching, as well as the adhesion of the films to the substrate, were also studied visually using SEM.

During the tests, the change in the coefficient of friction (COF) of the films was also measured as the load increased. The coefficient of friction became unstable and began to increase sharply when the adhesion of the coating to the substrate changed (failure is initiated). Thus, the critical load can also be confirmed by measuring the change in the COF during the test [112].

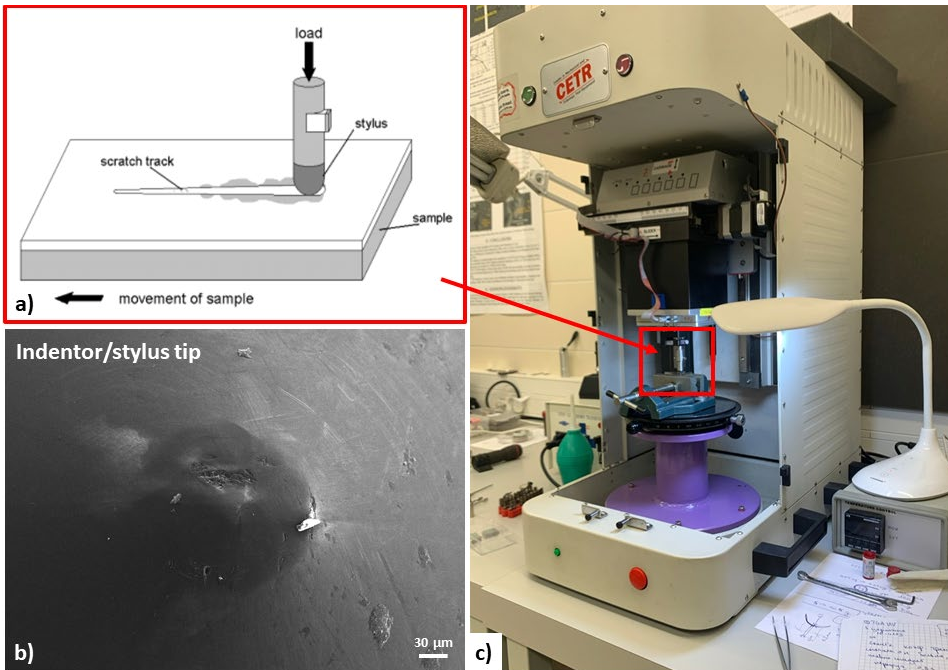


Figure 2.3. (a) A simple diagram of the scratch test [112], (b) SEM image of the Rockwell (HRC) spherical diamond indenter (stylus) with a diameter of 200 μm and a cone angle of 120°, and (c) photograph of the universal materials tribo-test apparatus with scratch test module.

### 3 Results and Discussion

This chapter of the thesis discusses the main results obtained during the work on the project and published in Articles I–III. Section 3.1 focuses on the comparative study of two low-temperature curing methods of the preceramic polymer PHPS and the resulting films. In the next stage of work, these PHPS-derived films were used as matrices for the formation of composites. Section 3.2 provides an overview of the morphological and functional properties of laminate-type composite coatings obtained by embedding SWCNTs as a filler into PHPS-derived matrix films.

#### 3.1 Study of $\text{SiO}_x\text{N}_y$ matrix films

This section combines the data published in Articles I and III concerning the study of PHPS-derived matrix films. To address the knowledge gaps illustrated in Chapter 1 of this thesis, the compositions of single-layer PHPS-derived films cured by low-temperature annealing and UV light irradiation were studied. The study investigated the influence of the PHPS curing method on the resulting  $\text{SiO}_x\text{N}_y$  films' morphological, optical, and mechanical properties, as well as their long-term stability. Additionally, the possibility of forming multi-layer  $\text{SiO}_x\text{N}_y$  films and their morphological features were studied.

##### 3.1.1 Comparative study of the influence of the curing method on the morphology and composition of single-layer matrix films

Deposited and cured PHPS films showed a dense and uniform morphology both on the surface and in cross-sectional (CS) views, ensuring excellent adhesion to the substrate. The choice of thermally or UV induced curing method did not visually affect the CS morphology of single-layer films on the SLG/Mo substrate, as seen in the SEM images in Figure 3.1. This observation also applied to the surfaces of the samples (images could be found in Article III). The choice of substrate affected the thickness of the resulting coating. On SLG/Mo substrates, the film thickness ranged from 350–460 nm. Films formed and cured on SLG substrates appeared equally uniform and adhesive but were slightly thicker, ranging from 550–580 nm. This difference was caused by the different wettability of the substrate surfaces by the preceramic polymer solution, which was higher in the case of the molybdenum.

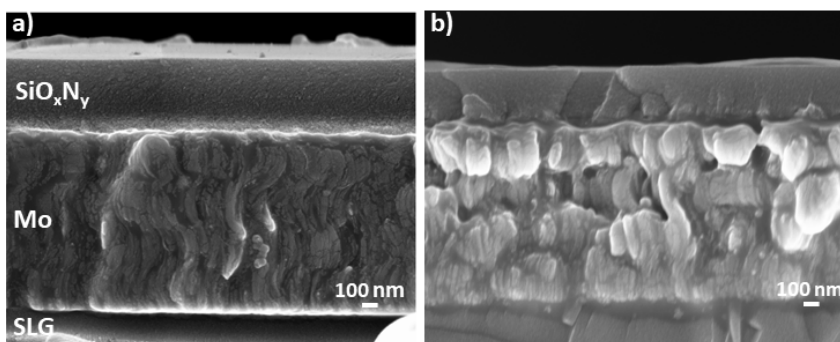


Figure 3.1. Cross-sectional SEM images of SLG/Mo/ $\text{SiO}_x\text{N}_y$  samples: (a) cured thermally, and (b) under UV light irradiation.

As described in the literature review, comparisons of the degree of UV-cured films' conversion were made only with pyrolyzed PHPS films. This comparison was not entirely correct because the result of pyrolysis is a ceramic film, while low-temperature (from RT to 250 °C) curing methods, in some cases, did not even allow the ceramic transition (which starts at temperatures above 200 °C) of the material to begin. Therefore, in our work, UV-cured films were compared with samples cured by low-temperature thermal annealing at a temperature corresponding to the minimum recommended by the precursor manufacturer (180 °C) and compatible with certain heat-sensitive materials (Article I).

In the case of PHPS-derived films, FTIR spectroscopy is a common and reliable method for assessing the degree of material transformation during the curing procedure, as it shows the presence of different functional groups [72]. For complete transformation of the PHPS to silicon dioxide, only absorption bands caused by different vibrational modes of Si–O bonds remained on the FTIR spectrum [67].

Figure 3.2 shows a comparison of the FTIR spectra of the samples, where the green curve corresponds to the spectrum of the thermally cured sample, and the purple curve corresponds to the spectrum of the UV-cured sample. Both curves have approximately the same set of characteristic bands, which differ significantly in intensity, thus changing the shape of the spectrum.

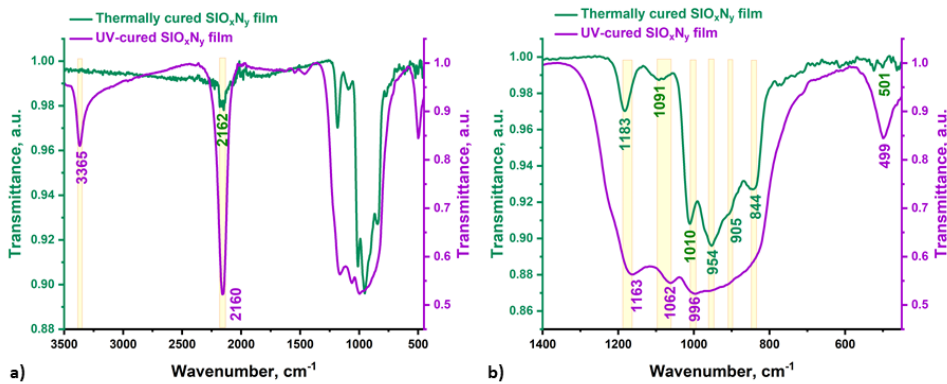


Figure 3.2. (a) FTIR spectra of the thermally and UV-cured SLG/Mo/SiO<sub>x</sub>N<sub>y</sub> samples, (b) enlarged area of the 'fingerprint region'.

The medium-intensity absorption band at 3365 cm<sup>-1</sup> in the spectrum of the UV-cured sample (purple) was caused by stretching vibrations of Si–N bonds [12,113], while the broad shoulder starting at 3365 cm<sup>-1</sup> and extending toward lower wavenumbers up to 2500 cm<sup>-1</sup> was caused by vibrations of –OH groups [11,12]. Bands in the spectra of the samples around 2160 cm<sup>-1</sup> were caused by stretching vibrations of Si–H [45,52].

In the fingerprint region (1500–400 cm<sup>-1</sup>), enlarged in Figure 3.2b, there are many vibrational modes of different functional groups. The close relative position and different intensities of their absorption bands make it difficult to interpret the obtained spectra [114]. A slight shift towards lower wavenumbers of several bands in the spectrum of the UV-cured sample relative to the spectrum of the thermally annealed sample is clearly visible, as demonstrated in Table 3.1. Similar behavior had already been observed for the transverse optical (TO) mode of the antisymmetric stretching vibrations of Si–O bonds.



If a quartz-like silicon structure with bond angles of  $144^\circ$  was formed during curing, the vibrational peak will be located around  $1065\text{ cm}^{-1}$  [66]. Thus, the position of the peak in the spectrum of our UV-cured film corresponds to this case of the organization of bonds between silicon and oxygen.

The formation of a cage-like structure of silicon with bond angles of up to  $150^\circ$  in the thermally cured film was indicated by the shift in the position of the absorption band of these vibrations towards larger wavenumbers, which could reach up to  $1140\text{ cm}^{-1}$  [66,72,115]. This suggests that the curing method influences the structure of the spatial organization of atoms within the films, which, in turn, affects the properties of the resulting coatings.

It was possible to clearly determine the presence in both spectra of a peak located around  $1170\text{ cm}^{-1}$ , associated with bending vibrations in Si–N [71]. Additionally, bands caused by stretching vibrations of this bond should be located around  $950$  and  $840\text{ cm}^{-1}$  [67,116,117]. The peak related to Si–H bonds, also located around  $840\text{ cm}^{-1}$ , complicates the analysis of this region of the spectrum [118]. Peaks for stretching, bending, and rocking vibrations in Si–O are located around  $1005$ ,  $830$ , and  $500\text{ cm}^{-1}$ , respectively [65,67,119,120].

*Table 3.1. Displacements of the vibrational band positions in the FTIR spectra for single-layer  $\text{SiO}_x\text{N}_y$  matrix films.*

Sample	Bonds and their spectral positions, $\text{cm}^{-1}$				
	Si–N	N–H	Si–O	Si–O	Si–O
Thermal curing	2162	1183	1091	1010	501
UV curing	2160	1163	1062	996	499

In the spectra of films cured by both methods, absorption bands of functional groups containing nitrogen and hydrogen atoms were observed, which indicates incomplete conversion of PHPS into silicon dioxide. The relative intensity of Si–O peaks compared to other bands in each of the spectra provides information about the different oxygen contents in these films.

To evaluate the elemental composition of the studied PHPS-derived films, EDX analysis was used. Measurements were taken from the surface of the samples to obtain the elemental composition averaged over the thickness of the films (Table 3.2). Atomic mass affects the sensitivity of EDX analysis, so atoms lighter than beryllium were beyond detection, making it impossible to estimate the content of hydrogen atoms in our samples. The measurement error decreased with increasing atomic mass. The results showed that UV curing promotes the transformation of PHPS into silicon oxynitride with a lower concentration of nitrogen atoms compared to thermally cured films. Thus, during UV curing, more oxygen atoms penetrate into the film, indicating a more successful curing process of the preceramic polymer towards silicon dioxide.

*Table 3.2. Thickness-averaged elemental atomic concentrations of thermally annealed and UV-cured  $\text{SiO}_x\text{N}_y$  single-layer matrix films on SLG/Mo substrates measured by SEM-EDX.*

	Thermally cured	UV-cured
Silicon, at%	14.3	17.3
Oxygen, at%	26.4	64.3
Nitrogen, at%	59.3	18.4

To study the surface chemical composition of the samples at a depth of 2–4 nm, XPS analysis was used (Figure 3.3). In the spectra of films cured by both methods, peaks of silicon, nitrogen, oxygen, and carbon were observed. Hydrogen was not detectable using this analytical method. Oxygen and silicon peaks were dominant in the spectra of both samples. Nitrogen was present on the surfaces of both films, but in the case of UV curing, its concentration was three times lower compared to the thermally annealed film. In Figure 3.3a, the inset shows an enlarged Si 2p peak, its deconvolution into three components, and its correlation with the chemical bonds that cause these components. Thus, in the case of thermal curing, the surface of the film represents an incompletely transformed PHPS due to the presence of Si–N (101.55 eV) and Si–Si (100.01 eV) components [121,122]. The Si 2p peak of the UV-cured sample consisted of one component located at about 103.1 eV, responsible for the Si–O bonds (Figure 3.3b) [123]. The position of this component was shifted towards higher binding energies compared to the equivalent component for thermal curing, indicating greater oxygen saturation in the case of UV curing [121]. The presence of a carbon peak in both spectra was due to adventitious C from the air, as well as possible minimal traces of dibutyl ether.

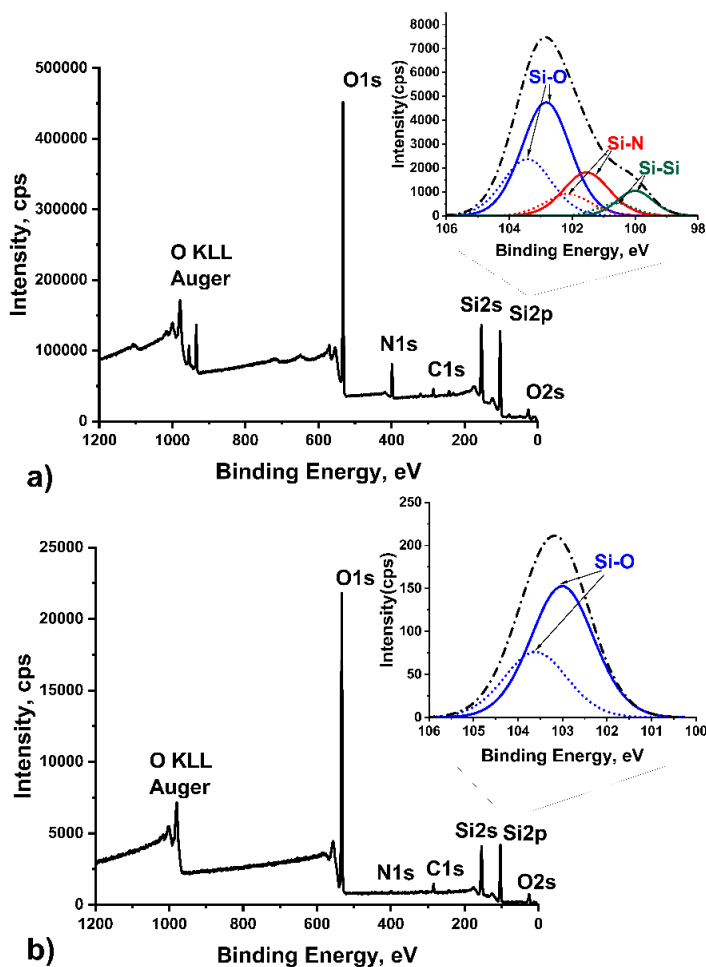


Figure 3.3. XPS spectra of near-surface layers with enlarged Si 2p peaks of SLG/Mo/SiO<sub>x</sub>N<sub>y</sub> samples cured (a) thermally, (b) under UV light irradiation.

Additionally, XPS studies enabled limited depth profiles of the elemental composition to be measured. However, the dielectric nature of PHPS-derived films led to an accumulation of positive charge during long-term measurements, distorting the obtained data. Therefore, the qualitative results of this analysis are presented below. The samples were etched in argon plasma to allow measurements at depths of approximately 12 nm and 22 nm from the surface. In the case of the thermally cured film, the concentrations of oxygen, silicon, and nitrogen remained stable over the whole depth profile measured. For the UV-cured film, a decrease in oxygen content with an increase in nitrogen and silicon content was recorded at a depth of about 22 nm. The results of XPS studies of matrix films are schematically presented in Figure 3.4, indicates that in the case of UV curing, a film with a non-uniform composition in the CS is formed with an upper layer saturated with oxygen. Low-temperature curing produced a film with a lack of oxygen in the CS.

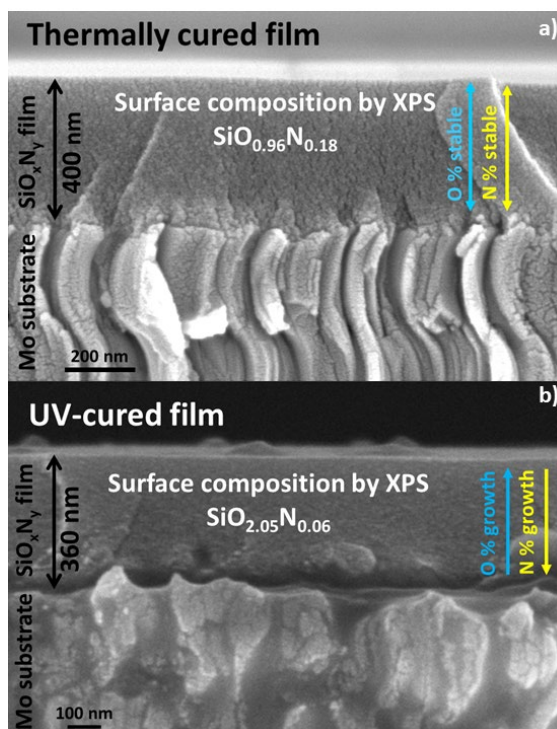


Figure 3.4. Cross-sectional SEM images of the SLG/Mo/SiO<sub>x</sub>N<sub>y</sub> samples cured (a) thermally and (b) under UV light irradiation with XPS measurements data and with trend of the oxygen and nitrogen content based on limited depth profile XPS data.

Based on all the above-mentioned, thermal curing for 60 min at 180 °C produced a partially transformed film, while UV curing led to a more complete transformation of the PHS into SiO<sub>2</sub>. This comparative study is detailed in Article I.

### 3.1.2 Influence of the curing method on morphology and composition of multi-layer matrix films.

The single-layer SiO<sub>x</sub>N<sub>y</sub> films may be too thin for some potential applications. With an average layer thickness of about 500 nm, the four-layer film thickness should be about 2 μm, making it more suitable for use as a protective coating. An improvement in the protective properties of the films obtained by sequential deposition of several PHS layers was also reported [12].

As can be seen from the SEM image (Figure 3.5a), upon sequential thermal curing, the four-layer film became homogeneous in CS with a maximum thickness of about 4.5 μm. In the case of UV curing (Figure 3.5b), the four-layer film maintained a uniform thickness of about 2.5 μm. But four layers of PHS deposition were visually distinguishable in CS, and the third and fourth layers merged into one. Each layer was about 600 nm thick. This clearly illustrates the heterogeneous transformation of the film during UV curing (Article I). The difference in the thickness of the four-layer structures indicated that the surface of the thermally cured SiO<sub>x</sub>N<sub>y</sub> film was less wettable by the PHS solution in comparison to the surface of UV-cured SiO<sub>x</sub>N<sub>y</sub> film.

The analysis of the FTIR spectra of multi-layer films is presented in Section 3.1.3 and can also be found in Article I.

The thickness of the multi-layer films was sufficient for line-scan EDX analysis of the CS of the films in order to obtain a depth profile of the elemental composition (Figure 3.5c and d). In the thermally cured sample (Figure 3.5c), the Si content fluctuated around the average value, which was much higher relative to the O, while the oxygen content increased closer to the film surface. For the UV-cured sample (Figure 3.5d), the Si content also fluctuated around the average value. However, the curve illustrating the O content in the sample showed three clearly distinguishable stand-alone peaks that could be associated with the film sub-layers, visually identified in the CS SEM image of the UV-cured film. The O content in the first two sub-layers was relatively low, but in the top layer, it grew significantly compared to the Si content. This confirmed the XPS data related to the conversion of the near-surface layers of the UV-cured PHPS film to  $\text{SiO}_2$ .

An increase in the O content as it approached the film-air interface for the thermally annealed film indicated the penetration of oxygen into the sample after the curing process. This will be discussed in more detail in Section 3.1.3, which covers the long-term stability of matrix films.

The study of the morphology and structure of multi-layer  $\text{SiO}_x\text{N}_y$  films can be found in Article I.

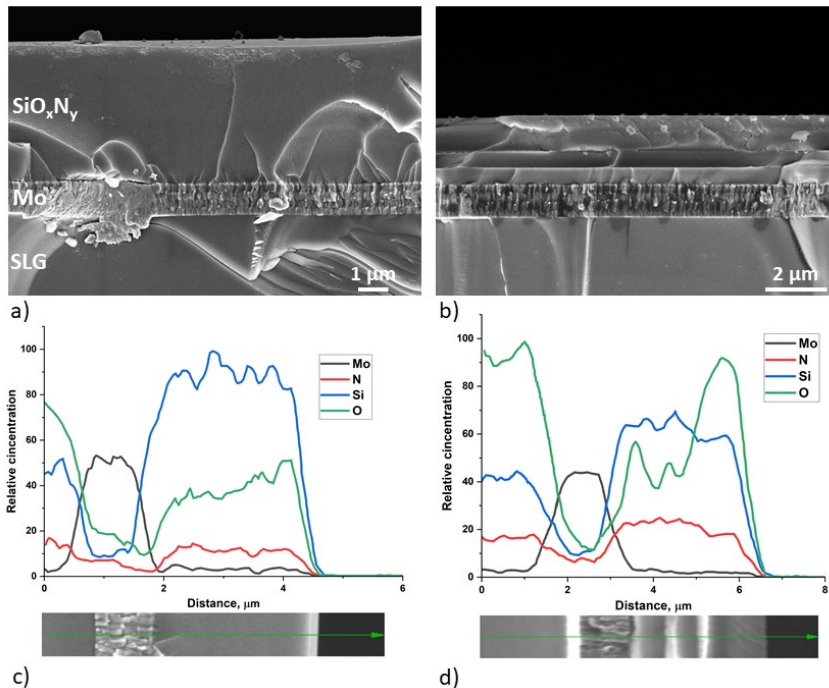


Figure 3.5. Cross-sectional SEM images of  $\text{SiO}_x\text{N}_y$  films on SLG/Mo substrate obtained from 4 deposition/drying/curing cycles for (a) thermal curing or for (b) UV-curing; (c) and (d) line-scan SEM-EDX elemental profiles of the films, respectively.

### 3.1.3 Long-term stability study of single- and multi-layer matrix films

As mentioned in the literature review, no detailed study of the long-term stability of the composition, structure, and properties of PHPS-derived films has been carried out for either thermal or UV curing methods so far. Therefore, we first studied the stability of the composition of single-layer and multi-layer films using FTIR spectroscopy (Article I).

Prepared samples were studied both immediately after the curing procedure and after aging in a desiccator at room temperature (RT) for two months. Figure 3.6 shows the measured spectra in the fingerprint region, as this is the area where the main changes in the shape of the spectra occur. The correlation of all the main vibrational bands with the functional groups that cause them is shown in the Figure 3.6. More noticeable changes in the shape of the spectra occurred in the case of single-layer samples (Figure 3.6a and c). After two months of aging, there was a significant increase in the intensity of the peaks caused by vibrations of Si-O bonds compared to the other peaks in both spectra, indicating oxygen penetration into the films during aging. Figure 3.6b and d show the FTIR spectra of the four-layer PHPS-derived films. The shape of the spectra of these samples demonstrated relatively smaller changes as a result of aging. This was caused by the significantly greater thickness of the films compared to single-layer samples, which complicated the process of oxygen penetration deep into thick films.

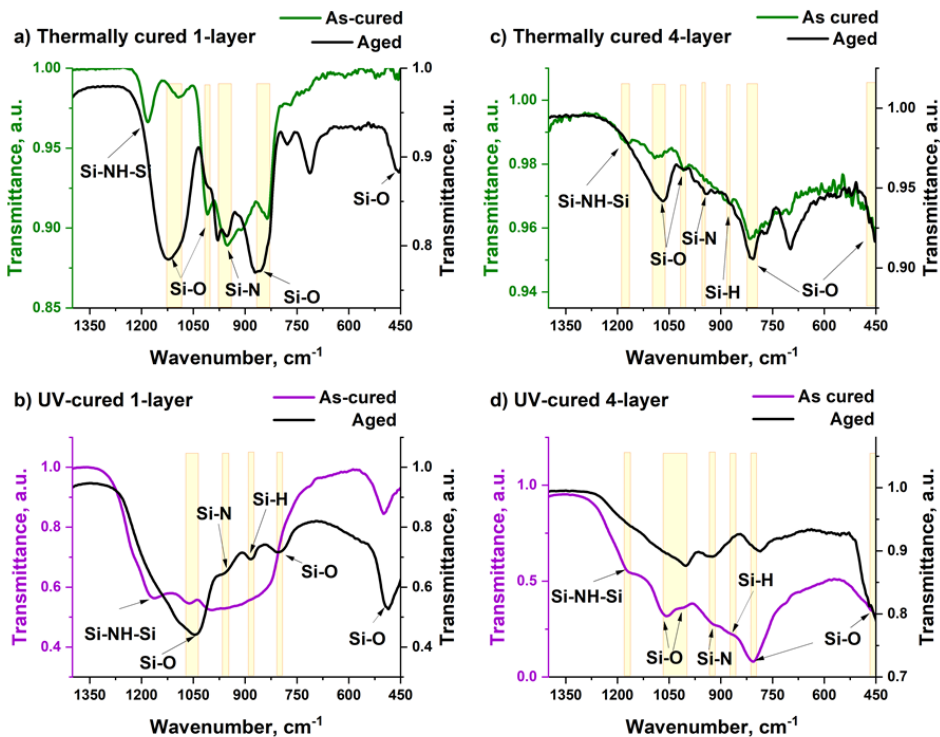


Figure 3.6. FTIR spectra of the (a), (c) thermally cured or (b), (d) UV-cured samples; colored lines are for as-cured samples, and black lines are for aged samples.

A detailed study of the dynamics of the aging of matrix films using FTIR spectroscopy was conducted and the results were published in Article III. The single-layer films were aged in plastic boxes in a desiccator at RT, without any additional influences. FTIR spectra for each sample were recorded in three marked areas and then averaged. To optimally track the dynamics of aging, the spectra were recorded immediately after curing, after 24 hours, and after one week, 3 weeks, and 6 months.

For both curing methods, as the films age, the shape of the spectra underwent changes (the main changes in peak intensity are marked by red arrows in Figure 3.7). In the spectrum of a thermally as-cured sample, a low-intensity peak of TO mode of asymmetric stretching vibrations of the Si–O–Si bond was detected at about  $1089\text{ cm}^{-1}$ , whose intensity gradually increased with aging, although its position remained unchanged. More details related to this peak are described in Section 3.1.1. One week after UV curing, the peak representing this bond began to appear in the spectrum around  $1068\text{ cm}^{-1}$ . In the spectrum of the as-cured sample, this band overlapped with neighboring bands, but as the sample aged, the relative intensity of this band increased, and its position shifted toward lower wavenumbers. After 6 months, this peak was located at  $1050\text{ cm}^{-1}$ , indicating a quartz-like structure within the film [54].

In the spectrum of a 6-month-aged UV-cured film, a band around  $1123\text{ cm}^{-1}$  appeared, which could also be attributed to vibrational modes of the Si–O–Si bonds. The position of these peaks indicated that clusters with a cage-like structure and quartz-like structure were both formed inside the film during the aging process.

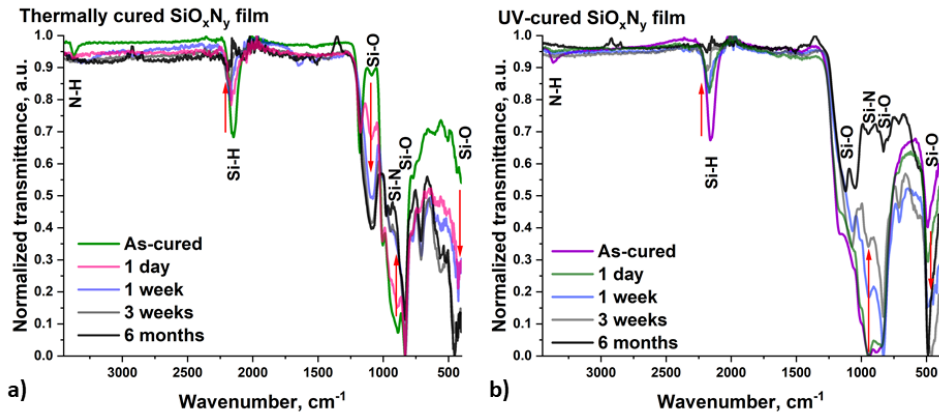


Figure 3.7. FTIR spectra of  $\text{SiO}_x\text{N}_y$  films measured during aging/ripening process of (a) thermally cured sample, (b) UV-cured sample.

In the case of a thermally cured sample, the most noticeable changes in the shape of the spectrum occurred during the first week after curing, then slowed down significantly. In contrast, for UV-cured samples, this process took longer. For multi-layer films, this process took even longer due to their greater thickness. As the films aged, significant changes occurred in their composition and structure. This process can be called ripening, where the oxygen content increased significantly, but the nitrogen and hydrogen content decreased. As a result, the peaks attributable to bonds between silicon and oxygen dominated in intensity, indicating that the composition of the films became close to silicon dioxide.

After six months of ripening, the spectra of films cured by two different methods exhibited different shapes, reflecting differences in their structure, and therefore, their functional properties. Notably, immediately after UV curing, the films contained less residual nitrogen and were closer in composition to silicon dioxide than thermally cured films. This is visible from the FTIR spectra and is confirmed by the XPS and SEM-EDX data shown for single-layer films in Section 3.1.1. Therefore, if the goal is to prepare films close in composition to silicon dioxide, UV curing could be considered as the preferable method.

### **3.1.4 Optical properties of single-layer matrix films**

In Article I and Article II, the high optical transmittance of prepared  $\text{SiO}_x\text{N}_y$  matrix films (near 90% without subtracting the contribution of the SLG substrate and > 98% with subtracting) was demonstrated. However, there were significant gaps in the information regarding other optical properties, such as refractive indices ( $n$ ) of PHPS-derived films cured by different methods, as well as the long-term stability of the optical properties of these films. Therefore, in Article III, we conducted a study aimed at filling these gaps.

There are various ways to determine the optical constants of films deposited on optically transparent substrates. In our work, we used spectroscopic ellipsometry (SE). Since this was an indirect method of obtaining data, the convergence of theoretical data to experimental data was assessed using the  $R^2$  correlation parameter. The closer  $R^2$  was to 1, the closer the calculated data were to the experimental data.

Generally, the N and O content within the film strongly influences its optical properties [124]. Additionally, FTIR results showed that during aging/ripening, the  $\text{SiO}_x\text{N}_y$  matrix films changed their composition and structure. These changes were expected to affect the optical properties of the films. Therefore, measurements were carried out the day after curing the films, as well as at different time intervals after curing, in order to track the dynamics of changes in the optical parameters of the samples. The measurement results are presented in Table 3.3.



Table 3.3. Optical parameters of PHPS-derived films calculated based on SE measurements.

Sample	Aging time	$d_1$ , mm	$n_{355}$	$n_{633}$	$k_{355}$	$d_2$ , mm	$n_{355}$	$n_{633}$	$k_{355}$	$R^2$
Uncured PHPS	1 day	673	1.61	1.56	0.08					0.99
Thermally cured $\text{SiO}_x\text{N}_y$	1 day	625	1.60	1.56	0.09					0.99
	1.5 month	508	1.54	1.49	0	44.2	1.51	1.47	0	0.98
	3.5 months	598	1.51	1.49	0.06					0.99
	13 months	507	1.50	1.46	0					0.99
UV-cured $\text{SiO}_x\text{N}_y$	1 day	571	1.58	1.55	0.17	200	1.49	1.46	0.15	0.96
	1.5 month	752	1.49	1.47	0					0.99
	3.5 months	613	1.50	1.46	0.02					1
	13 months	598	1.49	1.47	0					0.98

Figure 3.8 shows the dependences of the refractive index at the wavelengths of 355 and 633 nm on the aging/ripening time of the matrix films, based on the data in Table 3.3. To obtain the highest possible  $n$  value as a limiting case, an uncured PHPS film was prepared and measured, with the results shown in the figures as red triangles. This film contained the highest amount of nitrogen and the lowest amount of oxygen, which led to fairly high  $n$  values of about 1.6. These data allowed better evaluation of the efficiency of the transformation of PHPS into  $\text{SiO}_x\text{N}_y$  using thermal and UV curing.

A thermally cured, 1-day-aged  $\text{SiO}_x\text{N}_y$  matrix film also exhibited  $n$  values very close to 1.6. In contrast, the  $n$  values for the 1-day-aged UV-cured film were on average 0.02 lower. In the UV-cured sample, the nitrogen content was lower in comparison to the thermally annealed PHPS film, which led to a decrease in the refractive index value. This is consistent with results indicated in Section 3.1.3, which illustrate the influence of the curing method on the structure and properties of the resulting  $\text{SiO}_x\text{N}_y$  films.

In the UV-cured, 1-day-aged  $\text{SiO}_x\text{N}_y$  film, a fairly thick sub-layer in a two-layer model with  $d_2$  of 200 nm and an  $n$  value very close to the values for silicon dioxide, was formed on top of the  $d_1$  sub-layer, which has a higher refractive index (see Table 3.3 and Figure 3.9b). The typical refractive index value for amorphous stoichiometric silicon dioxide is 1.465 at a wavelength of 633 nm [125].

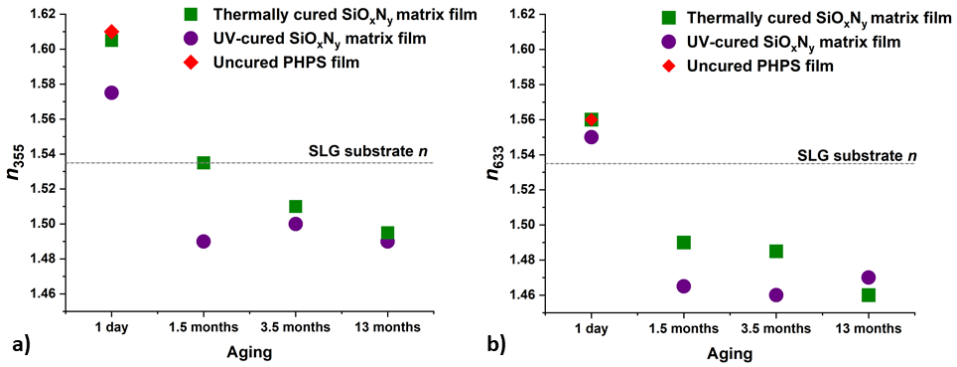


Figure 3.8. Dependence of the refractive index values on the sample aging time for  $n$  at wavelengths (a) 355 nm and (b) 633 nm.

The analysis of the transmittance spectra of samples improved the accuracy in calculating optical constants during modeling of SE data. To achieve this, the transmittance spectra of  $\text{SiO}_x\text{N}_y$  matrix films cured by both methods and aged for 1.5 months (Figure 3.9a) were measured. All spectra were measured during a single working session of the spectrophotometer, with the uncoated SLG substrate placed in the reference channel. The dried uncured PHPS sample was used for comparison, and its transmittance spectrum was measured 2 days after the film was prepared. This sample exhibited the lowest transmittance of all samples measured, indicating the highest refractive index.

Both cured samples had refractive indices lower than those of the substrate, placing their transmittance curves almost completely above the 99.7% level (our spectrophotometer channels were unbalanced by approximately 0.3%), as indicated by the gray line (Figure 3.9a). If the samples were optically homogeneous, the interference minima would be located at the level of the gray line. The interference minima in the spectra of the cured samples were located below this level. This shift indicated a negative inhomogeneity of the films, i.e., a gradient in the refractive index across the CS of the samples [126]. The beating of interference fringe amplitudes observed in the spectrum of a UV-cured sample also pointed to possible optical inhomogeneity in the material [127]. Specifically, the  $n$  values at the substrate-film interface were higher than those at the film-air interface. The gradient was more pronounced in the annealed film, as its minima were located lower relative to the gray line. Meanwhile, the UV-cured film had the lowest absolute value of  $n$  of all measured samples, since its spectrum was located above the others. All the observations described above are also reflected in the SE data (Table 3.3).

From Figure 3.8a and b, it can be seen that the refractive index value showed a tendency to decrease as the films aged. After 1.5 months of aging, the  $n$  values of the films approached the refractive index ( $n = 1.535$ ) of the SLG substrate (gray dotted line in Figure 3.8a and b), or dropped below it, with further aging tending toward the  $n$  values characteristic for silicon dioxide ( $n_{633} = 1.485$ ). This decrease related to a gradual reduction in nitrogen content and an increase in oxygen content in films cured by both methods, showing their gradual ripening towards silicon dioxide. These findings were in good agreement with the FTIR results presented in Section 3.1.3.

As the samples ripened, the structure of sub-layers and the magnitude of the  $n$  gradient also changed. According to the SE data, a 1-day-aged UV-cured film had a rather thick upper sub-layer ( $\frac{1}{4}$  of the total thickness) with a smaller  $n$  value and a fairly large ( $\Delta n = 0.09$ ) gradient value (Figure 3.9b). Previous reports have noted the formation of this top sub-layer, which was more converted to silicon dioxide than the buried sub-layer formed during UV curing [67]. We also detected this effect using the XPS and EDX line-scan techniques for single- and multi-layer  $\text{SiO}_x\text{N}_y$  films.

It should be noted that when a PHPS film was illuminated from the surface with UV light, the PHPS located closer to the film-air interface transformed more rapidly into a silicon dioxide sub-layer. This sub-layer then began to partially block the diffusion of oxygen deep into the film. As a result, the process of PHPS transformation to  $\text{SiO}_x\text{N}_y$  in the underlying volume slowed down. This created a gradient of cross-sectional chemical composition in the UV-cured  $\text{SiO}_x\text{N}_y$  film. Therefore, we did not see a step-like change in the composition and in the refractive index value, but rather a smooth transition, which is shown by the dash-dotted and solid lines in Figure 3.9b, respectively.

During aging, the magnitude of the gradient decreased so much that it was no longer noticeable in SE calculations (Table 3.3) and was only detected in the 1.5-month-aged sample using the transmittance spectrum (Figure 3.9a). In the case of thermal curing, the as-cured film was uniformly converted into silicon oxynitride, with a higher residual nitrogen content compared to the UV-cured PHPS film. However, after aging, the composition became similar to the UV-cured samples. An upper sub-layer with a lower  $n$  value compared to the rest of the material was detected (Figure 3.9c), which then ceased to be determined due to a decrease in the magnitude of the  $n$  gradient in the CS of the samples as they continued to ripen (Table 3.3).

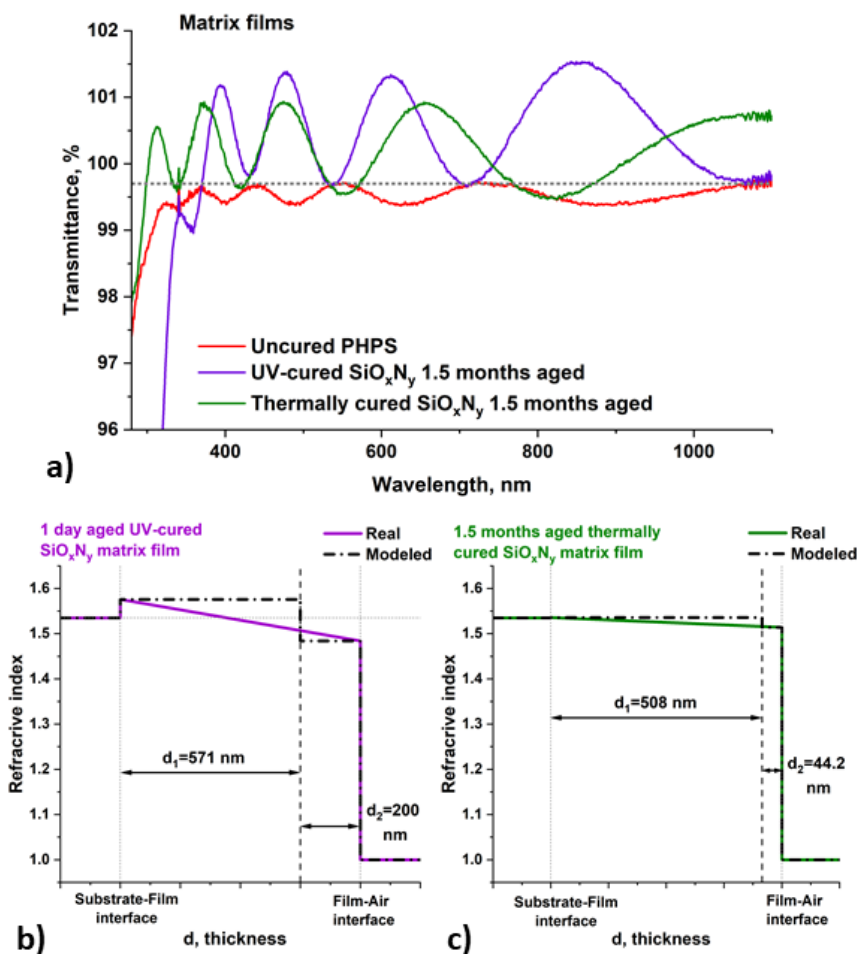


Figure 3.9. (a) Transmittance spectra of uncured PPHS film and 1.5-months aged UV and thermally cured SiO<sub>x</sub>N<sub>y</sub> films. (b) The refractive index profiles along the thickness of the SiO<sub>x</sub>N<sub>y</sub> films for 1-day UV-cured and (c) 1.5-months thermally cured matrix films.

This study illustrated the dependence of the optical properties of PPHS-derived films on the curing method used, specifically on the degree of conversion of the preceramic polymer to SiO<sub>2</sub>. The results suggest that SiO<sub>x</sub>N<sub>y</sub> matrix films could function as antireflective coatings for materials with refractive indices higher than theirs. As the SiO<sub>x</sub>N<sub>y</sub> film ripens, the magnitude of the antireflection effect will increase due to an increase in  $\Delta n$  between the film and the underlying material.

### 3.1.5 Mechanical and adhesive properties of as-cured and aged single-layer matrix films

As discussed in the literature review, no comparison of adhesion and mechanical behavior of low-temperature-cured PPHS-derived films under dynamic mechanical stress under the same measurement conditions had been performed. In this regard, in Article III a study and comparison of these properties for our samples was conducted.

$\text{SiO}_x\text{N}_y$  matrix films on SLG/Mo substrates were scratched using a universal materials tribo-test device, 1-day, and 1- and 3-weeks after curing, to evaluate their initial adhesion and mechanical behavior as well as the long-term stability of those properties.

For thermally annealed films, after contact with the surface of the sample (at the lowest load of 50 g), the indenter began to damage the coating (Figure 3.10a and d), with the scratch visually identified along its entire length (Figure 3.10e). The freshly cured film had very high ductility, and it was subject to a thinning effect, which resulted in a 250 g critical load ( $L_c$ ) value at the point of failure of the coating. However, one week after curing, the behavior of the annealed films changed, with adhesion to the substrate becoming strong, and hardness increasing noticeably, together with a  $L_c$  value up to 970 g (Figure 3.10f).

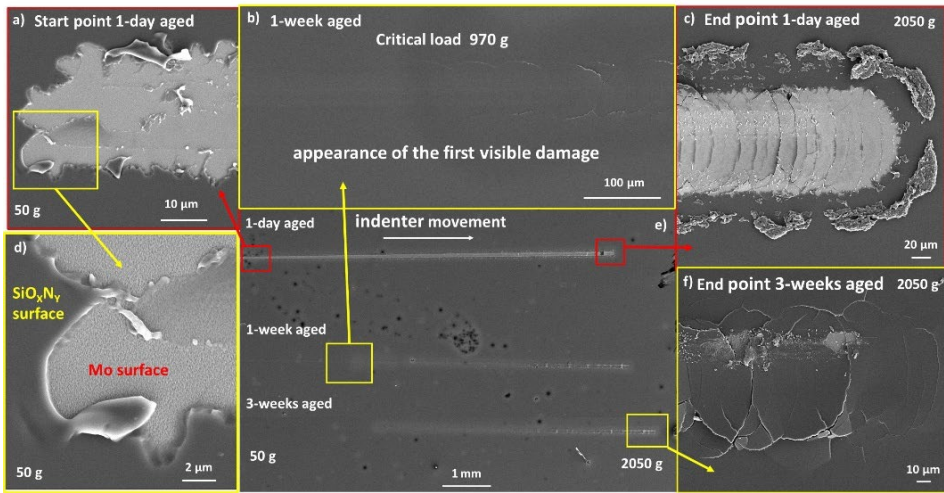


Figure 3.10. SEM images of scratches obtained from the progressive load tests taken after 1-day, 1- and 3-weeks of aging of a thermally cured SLG/Mo/ $\text{SiO}_x\text{N}_y$  sample: (a) the contact point of the indenter with the surface, (b) the appearance of the first visible damage to the film used to determine  $L_c$ , (c) the end of a scratch, (d) magnified image of the contact point, (e) general appearance of all scratches, and (f) scratch end point. Aging time and load are indicated in the images.

1-day-aged UV-cured  $\text{SiO}_x\text{N}_y$  films exhibited high hardness and excellent adhesion to the SLG/Mo substrate vs. 1-day-aged thermally cured films, maintaining this behavior and  $L_c$  values during the aging process. After reaching the  $L_c$ , semicircular cracks began to appear on the surface of the sample. As the load increased, semicircular cracks turned into ring-shaped cracks (Figure 3.11a). At high magnification, it became clear that this type of damage occurred because brittle SLG was located under the Mo layer, while the  $\text{SiO}_x\text{N}_y$  film remained tightly attached to the Mo surface, thus illustrating very good adhesion to the molybdenum layer (Figure 3.11b). The compressive stress from the indenter passed deep through the film and molybdenum and led to a brittle fracturing of the glass [111,128]. Notably, the film did not peel off from the substrate beyond the scratch, although with very heavy loads, damage could spread beyond the scratch area.

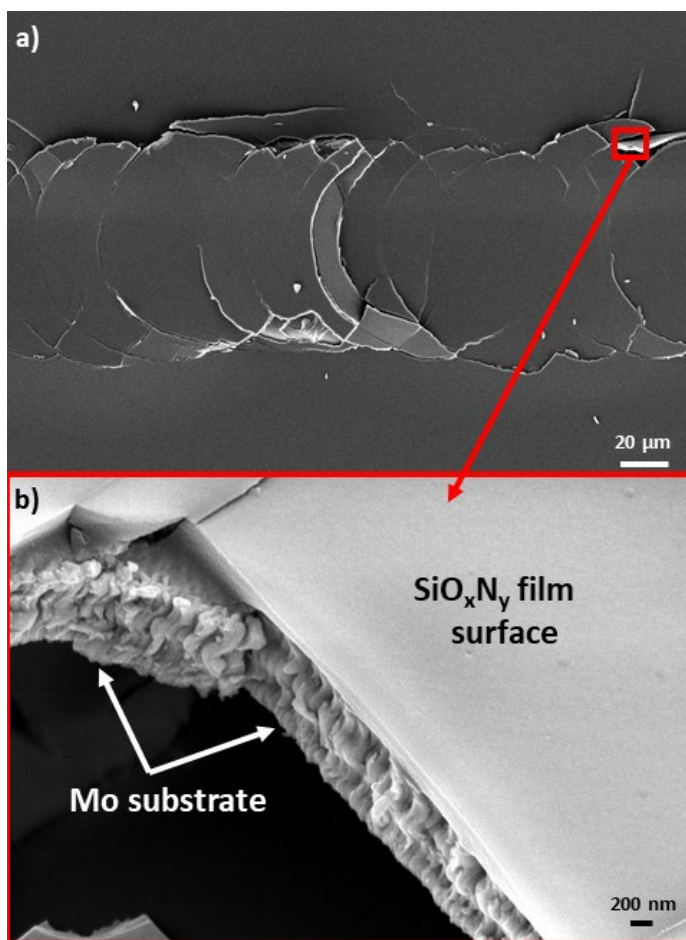


Figure 3.11. SEM images of UV-cured sample: (a) a fracture of a scratch on an  $\text{SiO}_x\text{N}_y$  matrix film under high load (near the end of the scratch), and (b) a magnified image of one of the fragments.

This difference in the behavior of 1-day-aged films was also associated with their CS structure after curing. The plasticity and lack of hardness of fresh thermally cured films were associated with the absence of a top layer of silicon dioxide and the presence of a very high nitrogen content throughout the film thickness. As a result of aging and ripening, the nitrogen content in the film decreased, and a layer similar in composition to silicon dioxide appeared on the surface. These changes made the aged film more comparable to the UV-cured samples.

For all samples, the coefficient of friction (COF) values did not exceed an average of 0.05. Such low COF values indicated the high smoothness of the film surface. The high smoothness of the film surfaces was also confirmed by the atomic force microscopy (AFM) results. The average surface roughness of the UV-cured and thermally annealed  $\text{SiO}_x\text{N}_y$  films was around 0.6 nm. Figure 3.12 shows COF curves for some samples. For all samples, the same behavior was observed for the COF value, depending on the scratching time.

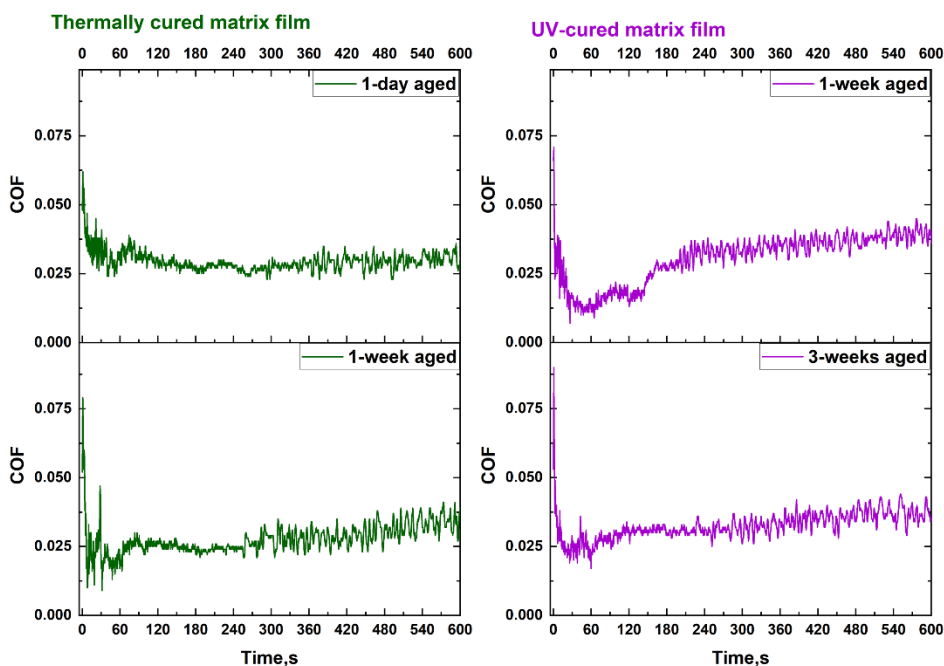


Figure 3.12. Friction coefficient curves recorded during progressive load scratch tests of  $\text{SiO}_x\text{N}_y$  matrix films. Curing method and aging time are indicated in the pictures.

Thus, the scratch test with progressive load showed that the adhesive properties and mechanical behavior of the coatings are greatly influenced by the composition of the films. Thermal curing proved to be a less fortunate method for the formation of protective coatings from PHPS, while UV curing produced harder, more stable films with excellent adhesion to the SLG/Mo substrate. The low COF values made PHPS-derived matrix films promising coatings for improved lubricious and scratch-resistant properties, which is an especially important factor in many industrial processes. More detailed information regarding progressive load scratch testing of the matrix films can be found in Article III.

### 3.2 Study of $\text{SiO}_x\text{N}_y$ /SWCNT composite coatings

This section involves a discussion about the results obtained for composite samples that were published in Articles II and III. First, information about the SWCNT films used in the work was presented. Then, the principles of the formation of composites in different configurations were described, after which the results obtained during the study of the functional properties of  $\text{SiO}_x\text{N}_y$ /SWCNT composite protective coatings were discussed.

#### 3.2.1 Characterization of SWCNT films

As mentioned in Chapter 2, the SWCNTs used were collected on filter paper after synthesis, thereby forming thin films. For the formation of the composites described in Articles II and III, SWCNTs from two different batches were used. The batches differed in the precursors for synthesis, which was described in detail in Chapter 2, as well as in the thickness of the films. In both cases, the morphology of synthesized SWCNT films was



studied using SEM. The micrographs from Article II showed that the dry transferred to the SLG substrate SWCNTs composed a uniform, thin, and close-packed film (Figure 3.13a and b). The SEM images of SWCNTs on the SLG substrate and carbon adhesive tape published in Article III looked similar.

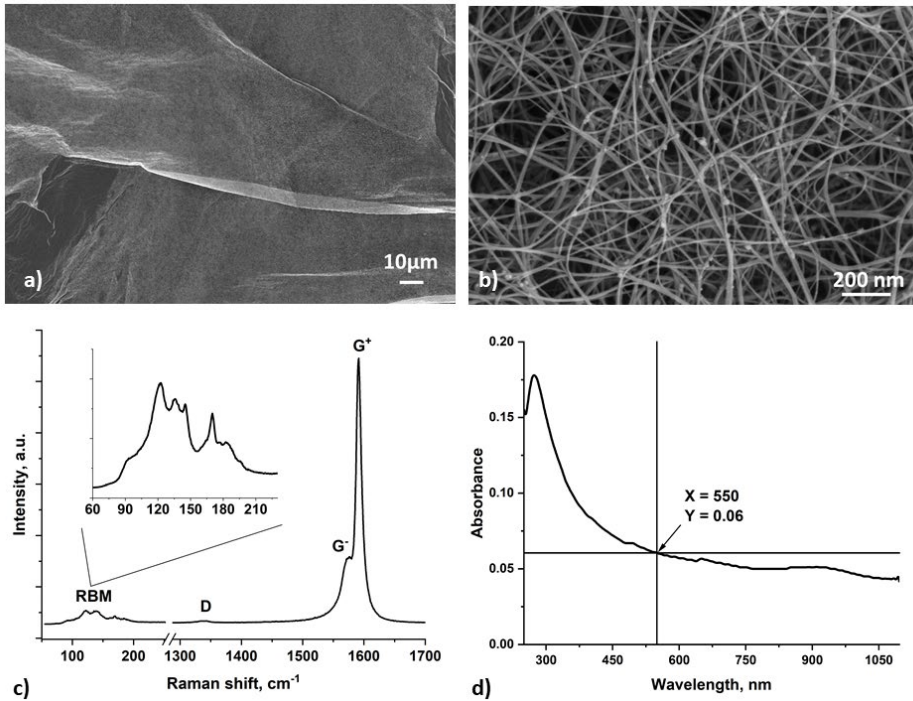


Figure 3.13. SEM images of SWCNT film on SLG substrate with different scales (a) 10 μm and (b) 200 nm, (c) Raman spectrum of a SWCNT film with an enlarged region of radial breathing modes, (d) optical absorption spectrum of a SWCNT film on a glass substrate with an absorbance of 0.06.

The SWCNT layers were studied by Raman spectroscopy (Figure 3.13c and in Article III). The enlarged area of the spectrum in the region of small wavenumbers illustrated the so-called radial breathing mode (RBM) region, which was observed in the spectra of both batches of nanotubes. These peaks were caused by synchronous radial vibrations of carbon atoms perpendicular to the axis of the nanotube. These peaks clearly indicated the presence of SWCNTs [129].

The D peak (approximately 1350 cm<sup>-1</sup>) indicated the presence of defects in the tube structure: the lower the intensity of this peak, the fewer defects (vacancies, undesirable doping etc.) in the tubes. To estimate the level of defects, the ratio of the intensities of the G peak to the D peak was used. In the case of the first batch (Article II), this value was 16, indicating the high quality of the SWCNTs, based on the values given in the literature, where it was indicated that 28 is an indicator of a small number of defects, and 2 is a large number [130,131]. For the second batch of SWCNTs (Article III), this value was 24.



The G peak, located at  $1591\text{ cm}^{-1}$ , corresponded to the tangential stretching of carbon-carbon bonds in the plane. It is observed in the spectra of any carbon structures with  $sp^2$  hybridization [132]. In the spectra of SWCNTs, this peak is split into two closely spaced subpeaks of different intensities due to the twisting of the graphene sheet. Nanotube defects also affect the splitting and broadening of the G peak. With a large number of defects, it becomes wider and split into more than two subpeaks [129]. In our case, the shape of this peak confirmed the high quality of the SWCNTs synthesized in both batches used.

High transmittance in the visible spectral region is a key requirement for optical coatings. Additionally, some materials require protection from UV radiation because it is often harmful to them due to its high energy. Therefore, absorption in this region of the spectrum is an advantage for a protective coating. The absorbance spectra of SWCNTs (Figure 3.13d) showed fairly high transmittance in the visible wavelength range, with a characteristic absorption peak in the nearest UV region, caused by  $\pi$  plasmon absorption [97].

It was possible to determine the thickness of the SWCNT film using its optical absorption spectrum. To calculate the thickness, the absorption value at a wavelength of 550 nm, which was 0.06, had to be multiplied by the correlation coefficient value of 239 [133,134]. Thus, the SWCNT film from batch 1 (Article II) had a thickness of approximately 14 nm. For SWCNTs from batch 2 (Article III), the absorption value at the wavelength of 550 nm was 0.054, corresponding to a film thickness of 13 nm.

Thus, in the course of a small preliminary study described in this section, we were able to verify the high quality of the used SWCNTs, as well as the small thickness of the films they form.

### **3.2.2 Formation of $\text{SiO}_x\text{N}_y/\text{SWCNT}$ composite coatings in different configurations and study of their morphology**

To prepare  $\text{SiO}_x\text{N}_y/\text{SWCNT}$  composite films, SWCNTs could be transferred either on top of the uncured PHPS layer or directly onto the substrate (SLG or SLG/Mo), followed by spin coating of the PHPS layer onto the SWCNT layer. A comparison of the adhesion and morphology of the nanocomposite coatings on the different surfaces was recommended, since SWCNT films demonstrated different adhesion to the surfaces of different materials [135]. When transferring a SWCNT film onto cleaned Mo, the adherence was poor in contrast with adhesion of the SWCNT layer to SLG substrate. To overcome this problem, we used a dry process of fluorination of the Mo surfaces, described in Chapter 2. This made it possible to alter the surface properties of the Mo substrate. After this treatment, the SWCNT film was easily transferred onto the Mo surface, followed by coverage with a layer of PHPS by the spin-coating technique.

The composite coatings were formed in two configurations: (i) BOTTOM, where the SWCNT film was transferred to the substrate surface before spin coating the PHPS solution; and (ii) TOP, where SWCNTs were transferred to the surface of a formed but uncured PHPS film. The investigation of these different configurations was important for evaluating the result of SWCNTs transfer to a hard (SLG and SLG/Mo) and soft (uncured PHPS) substrate. It helped in controlling the distribution of SWCNTs within the matrix film and determining the possible influence of the configuration on the functional properties of the composite coating.

The samples of both configurations were cured using both thermal and UV-assisted methods to thoroughly assess the possible change in their final morphological and functional properties. We examined the surface and CS morphology of the thermally

cured samples using SEM (Figure 3.14). For both TOP and BOTTOM architecture, the surface of the cured samples was mainly uniform, without any noticeable pores. Only under very high magnification was it possible to see some inhomogeneity points, with its minor presence on the film surface. The CS micrographs showed that in the case of the TOP architecture, the composite film thickness was around 400 nm and the SWCNT layer was predominantly located in the upper part of the  $\text{SiO}_x\text{N}_y$  matrix, not penetrating into its depth. For the BOTTOM configuration, the film thickness was 480 nm, with the SWCNT film layer predominantly located in the bottom part of the  $\text{SiO}_x\text{N}_y$  matrix. It should be noted that in both cases, the SWCNT film continued to be densely packed in cross-section after entering into the coating matrix. When the sample was fractured to create a cross-section, the SWCNTs were stretched and torn. These fragments could be seen emerging from the film in the images, illustrating the additional bonding effect of SWCNT fillers inside the composite film.

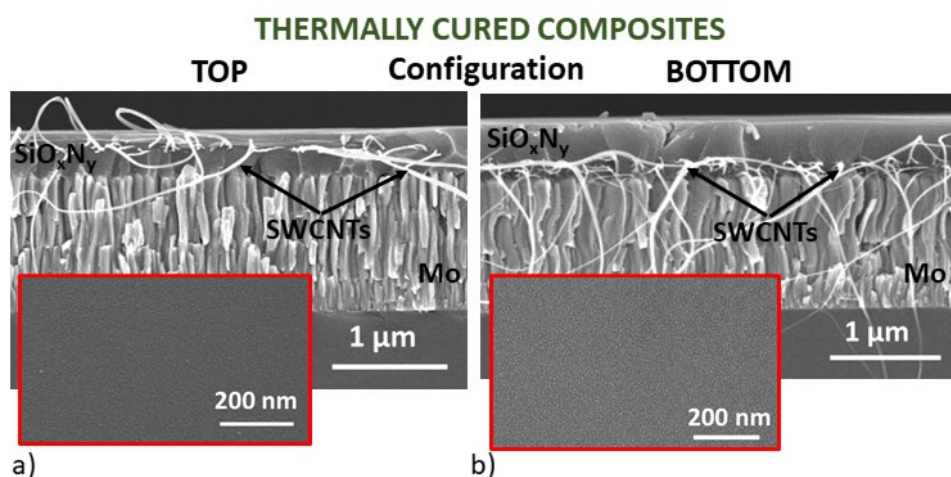


Figure 3.14. SEM cross-sectional and surface (in the red frame) images of  $\text{SiO}_x\text{N}_y$ /SWCNT composite films on SLG/Mo substrates with architecture (a) TOP and (b) BOTTOM.

The surface of UV-cured  $\text{SiO}_x\text{N}_y$ /SWCNT composite films on SLG/MO substrate (Figure 3.15a and d) appeared the same as that of the thermally cured ones. In the CS (Figure 3.15b, c, e), the SWCNT distribution within the matrix showed the trends observed for thermally cured composite samples. However, in the case of the TOP configuration, SWCNTs were predominantly located in the upper layers of the  $\text{SiO}_x\text{N}_y$  matrix film but might shift and spread deeper, moving from the laminated structure of the composite to a network (Figure 3.15b and Article III). This behavior could be due to the diffusion of stressed SWCNTs in viscous matrix material. During UV-induced curing, the film was gradually cured starting from the surface downward, allowing the SWCNTs to remain longer in the viscous, uncured matrix film, which could lead to their spreading throughout the volume of the matrix film.

## UV-CURED COMPOSITES

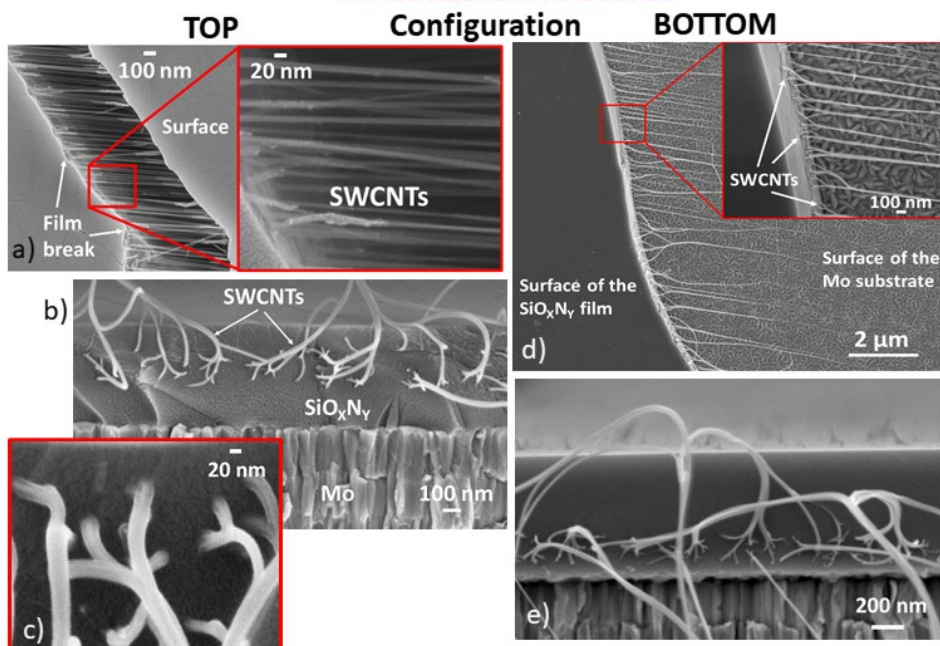


Figure 3.15. SEM images of  $\text{SiO}_x\text{N}_y/\text{SWCNT}$  composite films: with TOP architecture, where (a) cracked surface under high magnification, and (b, c) CS with film thickness 520 nm; with BOTTOM architecture, where (d) surface with partially removed film, and (e) CS with film thickness 650 nm.

Figure 3.14 and Figure 3.15 showed SEM images of composites on SLG/Mo substrates. However, the observed morphological properties were similar for composites on SLG substrates, the images of which are presented in Articles II and III.

During this part of study composites with the different laminate architectures were successfully obtained using the developed methods. It was found that the filler in the form of a horizontally oriented SWCNT film is successfully transferred by dry transfer technique to both hard and soft substrate surfaces. The filler showed excellent compatibility with the  $\text{SiO}_x\text{N}_y$  matrix. The developed technological path of composite coatings formation avoided the problem of SWCNTs agglomeration inside the matrix in all investigated conditions.

### 3.2.3 Comparative study of the influence of the SWCNTs embedding on the composition of $\text{SiO}_x\text{N}_y/\text{SWCNT}$ composite coatings

Based on the absorption spectrum of SWCNTs (Figure 3.13d), it was assumed that they could affect the curing process when embedded in the PHPS matrix because their absorption peak is in the UV region of the spectrum. In order to study the possible influence of the SWCNT filler film on the conversion of the PHPS matrix material for both curing methods in Article II, only half of the total area of the PHPS layer was filled with the SWCNT film (for both TOP and BOTTOM configurations). Thus, each sample consisted of a region representing only pure  $\text{SiO}_x\text{N}_y$  and an area with filler embedded in the  $\text{SiO}_x\text{N}_y$  matrix.

The FTIR spectra were measured at several points in both regions and then averaged into one curve per region. A detailed description of the correlation of the peaks appearing in the spectra of PHPS-derived films, with the functional groups that caused them, is given in the section on the study of the long-term stability of matrix films (Section 3.1.3). A detailed interpretation of the spectra shown in Figure 3.16 is available in Article II.

As seen from the comparisons of the spectra in Figure 3.16a and b, in the case of thermal curing, the presence of the SWCNT film (black curves) did not have any effect on the shape of the spectra for both sample architectures studied. Small differences in the film thickness caused minor differences in the peak intensity. Also, differences in sample architecture did not affect the spectra. In all four spectra, the peak distribution typical for thermal curing stood out.

Generally, the peaks of Si–O functional groups were the most intense in all the spectra of thermally cured samples, indicating a high degree of PHPS conversion (peaks near 1085, 1010, 830 and 450  $\text{cm}^{-1}$  [65-67,119,120]). However, the signals of nitrogen and hydrogen were also present in all measured spectra, indicating the formation of an  $\text{SiO}_x\text{N}_y$  film.

In the case of UV-cured samples we also did not see a significant difference between the spectra measured in the area of pure  $\text{SiO}_x\text{N}_y$  (purple curves in Figure 3.16c and d) and the spectra measured in the area of the composite film (black curves). The difference in the relative intensities of some peaks was caused by small changes in film thickness in different areas of the sample. All spectra of UV-cured samples showed a characteristic shift in the positions of the Si–O vibration bands compared to annealed films.

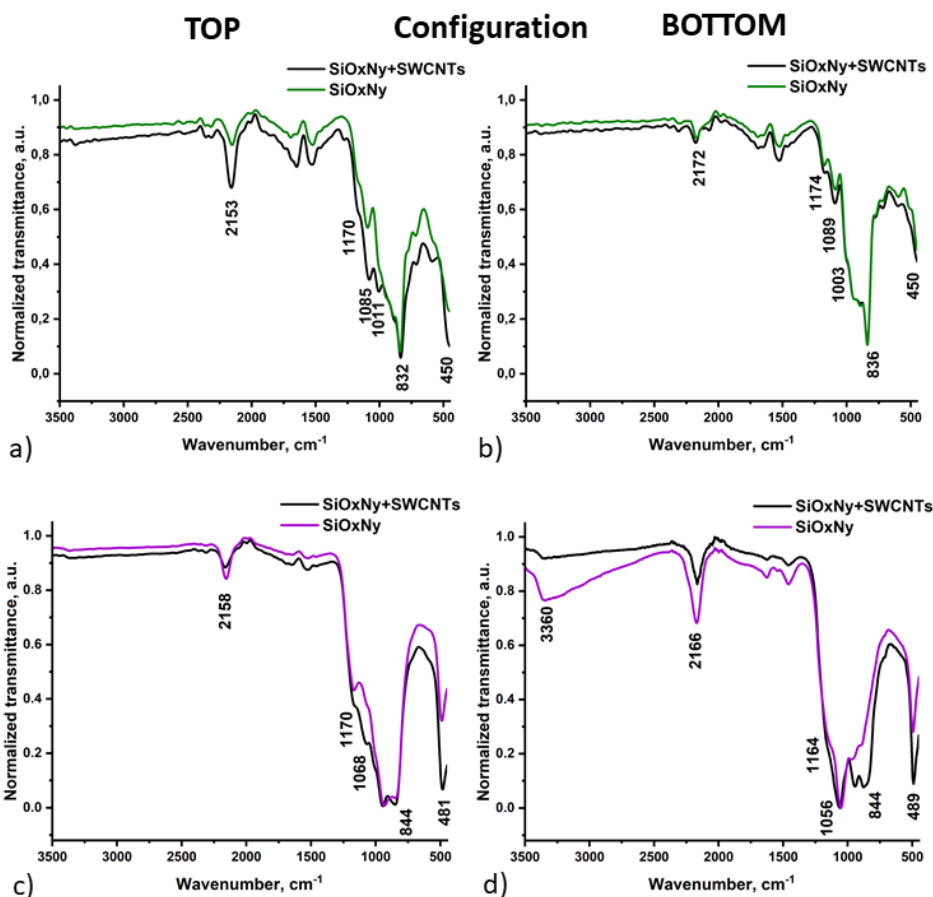


Figure 3.16. FTIR spectra of the thermally cured samples measured in the area with SWCNTs (black curve) and in the area without SWCNTs (green curve) for (a) TOP and (b) BOTTOM configurations. FTIR spectra of the UV-cured samples measured in the area with SWCNTs (black curve) and in the area without SWCNTs (purple curve) for (c) TOP and (d) BOTTOM configurations.

Table 3.4 and Table 3.5 show the results of the EDX elemental analysis of the  $\text{SiO}_x\text{N}_y/\text{SWCNT}$  composite films on SLG/Mo substrate from the film surface. However, this data must be considered mainly as qualitative since the limiting factor of this measurement technique was its sensitivity to the atomic weight of the elements (relatively low accuracy for determination of light elements), as already mentioned. However, it was possible to make some remarks regarding the presence of the carbon filler within the matrix material. From Table 3.4 and Table 3.5, it can be seen that the contribution of SWCNTs to overall carbon content was non-detectable by EDX, i.e., very low. Indicated traces of carbon belong to solvent residues, which were also detected in the FTIR spectra. It should be noted that the decrease in carbon content in UV-cured  $\text{SiO}_x\text{N}_y/\text{SWCNT}$  films of both configurations was related to the strong UV irradiation of prepared layers with a wavelength of 185 nm in the presence of oxygen, accompanied by the formation of ozone and the oxidation of the organic residues in the cured films [54].

Table 3.4. The thickness-averaged elemental atomic percentage of  $\text{SiO}_x\text{N}_y$ -based TOP configuration films on SLG/Mo substrate measured by EDX.

	Thermally cured film		UV-cured film	
	Without SWCNTs	With SWCNTs	Without SWCNTs	With SWCNTs
Silicon, at%	33	32	30	29
Oxygen, at%	54	54	68	68
Nitrogen, at%	7	7	0	1
Carbon, at%	6	7	2	2

Table 3.5. The thickness-averaged elemental atomic percentage of  $\text{SiO}_x\text{N}_y$ -based BOTTOM configuration films on SLG/Mo substrate measured by EDX.

	Thermally cured film		UV-cured film	
	Without SWCNTs	With SWCNTs	Without SWCNTs	With SWCNTs
Silicon, at%	39	39	31	31
Oxygen, at%	52	52	68	68
Nitrogen, at%	5	6	0	0
Carbon, at%	4	3	1	1

Based on the above, it can be concluded that the embedding of SWCNTs into  $\text{SiO}_x\text{N}_y$  matrix and the architecture chosen do not affect the degree of conversion of PHPS to silicon dioxide during curing. Similarly to the matrix films, the final nitrogen content in composite films is affected by the choice of curing method. The concentration of the SWCNT filler inside the  $\text{SiO}_x\text{N}_y$  matrix remained low and not detectable with EDX.

### 3.2.4 Optical properties of $\text{SiO}_x\text{N}_y$ /SWCNT composite coatings

In Section 3.1.4 we discussed the values of optical constants for matrix films obtained using the SE technique. It should be noted that the observed patterns of refractive index behavior and values were the same for the composite samples.

The main area of application of the coatings being developed in this thesis imposed restrictions in the form of needing high transmittance. The transmittance of the  $\text{SiO}_x\text{N}_y$ /SWCNT composite films on the SLG substrate was studied in Article II. The  $\text{SiO}_x\text{N}_y$  matrix film (blue curve in Figure 3.17) had very high transparency (near 100%) over a wide range of wavelengths and had an absorption peak in the near UV region of the spectrum. The behavior of the spectrum of the pure SWCNT film (black curve) was similar to the spectrum of the matrix film, except with lower transmittance values over the entire measurement range (from 82% to 89% for visible light range). The transmittance spectrum of the UV-cured  $\text{SiO}_x\text{N}_y$ /SWCNT composite film (purple curve) was located between the spectra of SWCNTs and  $\text{SiO}_x\text{N}_y$ . At the same time, the transmittance of the composite was at least 2% higher than the SWCNT film over the entire range of the visible and IR regions of the spectrum. We investigated this antireflection effect in more detail in Article III.

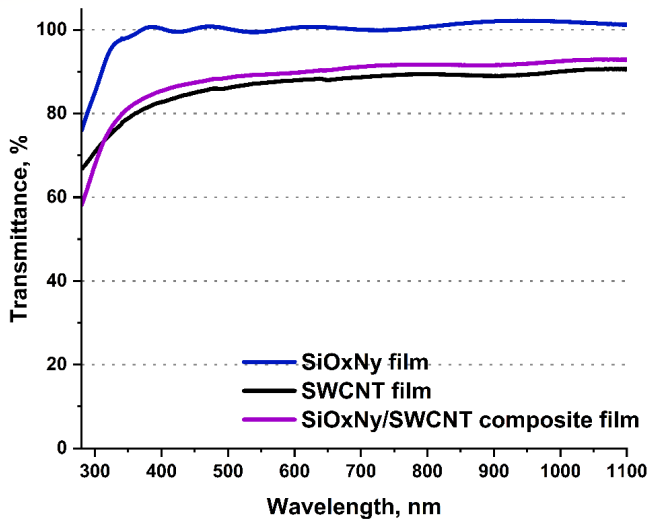


Figure 3.17. The transmittance spectra of a UV-cured  $\text{SiO}_x\text{N}_y$  matrix film (blue curve), a SWCNT film (black curve), and a UV-cured  $\text{SiO}_x\text{N}_y$ /SWCNT composite film (purple curve). The uncoated SLG substrate was placed in the reference channel of the spectrophotometer during measurements.

In Article III, we extended our measurements to similar composites and the remaining samples studied to better evaluate the observed effect.

In order to estimate the value of antireflection, the transmittance spectra of the SWCNT films transferred to the SLG substrate were measured first (Figure 3.18a). Then, in accordance with the BOTTOM configuration, PPHS/SWCNT composite films were prepared and cured by both thermal and UV-assisted methods. As shown in Figure 3.18a, the transmittance of different areas of the SWCNT film varied slightly, making it difficult to adequately assess the magnitude of the effect in TOP configuration composites. This was due to the inability to measure the transmittance of the specific piece of SWCNT film used in the formation of the TOP composite.

After curing, the transmittance spectra of the BOTTOM  $\text{SiO}_x\text{N}_y$ /SWCNT samples were measured again within the same operating session of the device, which decreased the influence of additional errors associated with the operation of the spectrophotometer. For all spectra in Figure 3.18, measurements were taken against the uncoated SLG substrate in the reference channel. It can be seen that for both curing methods, the transmittance of the composite samples increased in comparison with the transmittance of a pure SWCNT film on the SLG substrate. In the case of UV curing, the increase in transmittance was higher (approximately 2.5%) compared to the thermally cured composite (approximately 1.4%).

For better evaluation of the observed effect, we studied the change in transmittance depending on the stage of formation of the UV-cured composite film (Figure 3.18b). First, the spectrum of the SWCNT film transferred to the SLG substrate was measured (black curve). A PPHS film was then spin coated on top of the SWCNTs, and the spectrum of this uncured composite sample showed a 1.6% increase in transmittance in the mid-visible range (blue curve). After curing, the transmittance increased by another 1.4% (purple

solid curve). All spectra were recorded within a single spectrophotometer run with the same baseline and without bare SLG substrate in the reference channel.

Thus, in the case of UV curing, we found two factors that influenced the magnitude of the antireflection effect. The first was associated with the formation of the composite sublayer in the PHS matrix (see Figure 3.14a and Figure 3.15e) by the introduction of SWCNTs into the PHS. The second factor, which increased the magnitude of the effect, was related to the curing of the PHS-derived matrix film accompanied by a decrease in the refractive index in the formed  $\text{SiO}_x\text{N}_y$ .

The SE results show that immediately after UV curing, the film had a fairly thick top  $d_2$  layer with a low  $n$  value, which led to the appearance of an antireflection effect (Table 3.3). The broadband nature of the antireflection effect was caused by the presence of a gradient in  $n$  across the film, which was identified in Section 3.1.4. Broadband antireflection is in great demand in many areas of photonics, as it replaces the construction of a traditional package of thin antireflection films with one coating, thereby simplifying and accelerating the manufacturing process [136,137]. This makes PHS-derived matrix films very promising as antireflective coatings.

One week after curing, a new transmittance spectrum of the composite film was measured (Figure 3.18b, dash-dotted curve). The transmittance value remained virtually unchanged after one week of aging, indicating that despite noticeable changes in the FTIR spectra, related changes in composition were not sufficient to significantly affect the antireflective properties of the UV-cured coating.

An increase of 1.6% in transmittance for the UV-cured sample and a 1.4% increase for the thermally annealed sample were associated with the formation of the PHS/SWCNT composite coating. The increase effect occurred when a SWCNT film was embedded into a matrix whose refractive index was higher than that of the SLG substrate. This phenomenon may be related to the creation of a nanostructured interface from the walls of SWCNTs within the PHS matrix, which affected the propagation of light through the composite. It should be noted that nanostructuring is one of the promising strategies for creating antireflection coatings [137].

Previous reports have highlighted a significant increase in transmittance (about 4.5%) and a decrease in reflection in nanostructured composite polymer electrodes with SWCNTs, especially when nanotubes were arranged as vertical arrays [138]. Additionally, the antireflection effect was observed for SWCNT films randomly oriented in the horizontal plane deposited on the surface of a silicon wafer. With a small thickness (about 32 nm), the SWCNT films were semi-transparent while acting as an antireflection coating for the substrate [136].

From the reflectance spectra (Figure 3.18c and d), it was clear that both matrix films had less reflection compared to the SLG substrate. However, when SWCNTs were embedded into the matrix, the reflection of the composite film decreased further, confirming the presence of a synergistic antireflection effect.



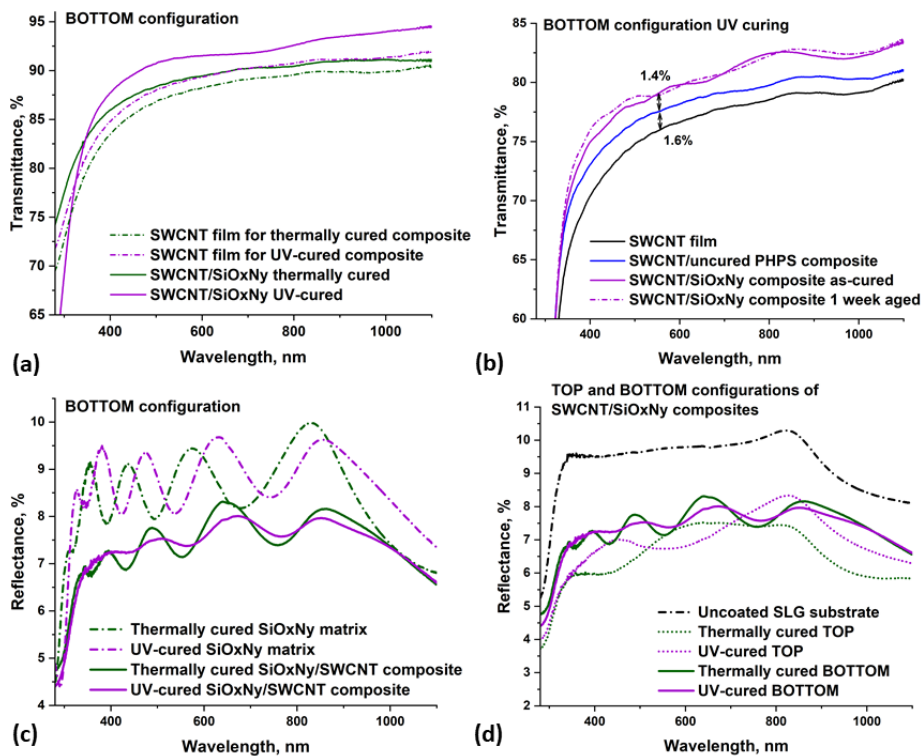


Figure 3.18. (a) and (b) transmittance spectra showing the antireflection effect in the SiO<sub>x</sub>N<sub>y</sub>/SWCNT composite samples; (c) and (d) reflection spectra confirming the presence of an antireflection effect in the SiO<sub>x</sub>N<sub>y</sub>/SWCNT composite samples

It should be noted that the matrix films showed an increase of around 1.4% in transmittance immediately after UV curing, which is a relatively small value compared to other specially designed antireflective coatings [139]. On the basis of the results of SE, an increase in the transmittance value should occur as the value of  $n$  decreases with ripening for films cured by both methods. It was reported that by creating a microporous structure inside a silica film deposited on a glass slide substrate, it was possible to increase transmittance by just over 3%. This increased transmittance was caused by a decrease in the refractive index of the film due to the possible creation of a large number of pores [140]. Thus, one of the possible ways to increase the antireflection effect in PHPS-derived films could be controlled creation of inhomogeneous porosity in the deposited layer to decrease the  $n$  value closer to the film-air interface.

### 3.2.5 Mechanical and adhesive properties of as-cured and aged SiO<sub>x</sub>N<sub>y</sub>/SWCNT composite coatings

By analogy with the SiO<sub>x</sub>N<sub>y</sub> matrix films, SiO<sub>x</sub>N<sub>y</sub>/SWCNT composite coatings were scratched 1-day, and 1- and 3-weeks after curing using the universal tribo-test device under identical conditions.

UV-cured SiO<sub>x</sub>N<sub>y</sub>/SWCNT composites exhibited high hardness and excellent adhesion to the SLG/Mo substrate, maintaining these properties during the aging process

(Figure 3.19b), like UV-cured matrix films, which were described in Section 3.1.5. The critical load value did not change noticeably with film aging/ripening. At low loads, no traces of the indenter remained on the samples (Figure 3.19a). The point of indenter contact with the film surface could sometimes be determined only by the presence of a subtle contrast in SEM images or by measuring the length from the end of the scratch. After reaching the  $L_c$ , semicircular cracks (discussed in Section 3.1.5) began to appear on the surface of the sample. As the load increased, they turned into ring-shaped cracks.

The embedding of SWCNTs into the matrix caused a visible reinforcing effect against the rupture of the composite coating (Figure 3.19f). However, the presence of one filler layer was not enough to influence the values of the critical load withstood by the coating.

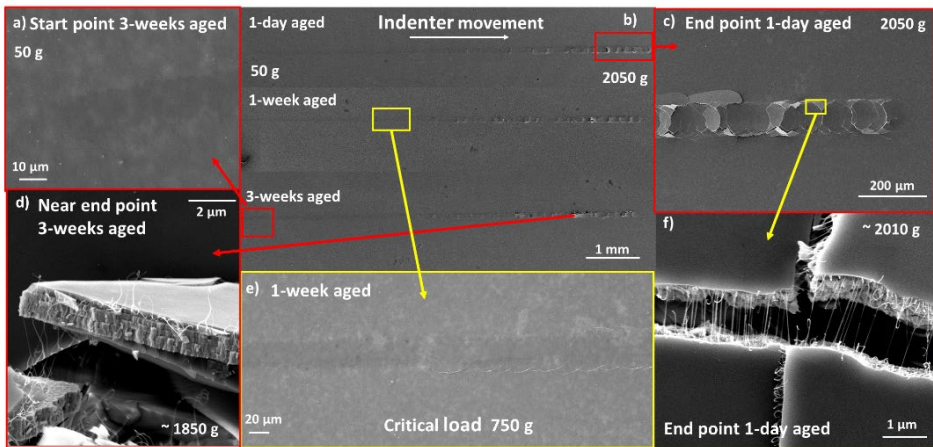


Figure 3.19. SEM images of scratches from progressive load tests taken after 1-day and 1- and 3-weeks of aging of a UV-cured  $\text{SiO}_x\text{N}_y/\text{SWCNT}$  composite film on a SLG/Mo substrate: (a) start point where the indenter contact with the film, 50 g; (b) general appearance of all scratches; (c) the end of a scratch, 2050 g; (d) a fragment of the SLG/Mo substrate with a composite film on top of it; (e) the appearance of the first visible damage to the film, making it possible to determine  $L_c$ ; (f) fragments of the substrate with a composite film on top of them, held together by stretched SWCNTs.

The results for the thermally cured  $\text{SiO}_x\text{N}_y/\text{SWCNT}$  composite film were similar to  $\text{SiO}_x\text{N}_y$  matrix films. High ductility and low adhesion for as-cured films (Figure 3.20), which, during ripening, turned into high hardness and adhesion. It is important to note that despite the strong thinning effect on the as-cured annealed composite, the SWCNTs remain inside the matrix residues, as can be seen in Figure 3.20c and d.

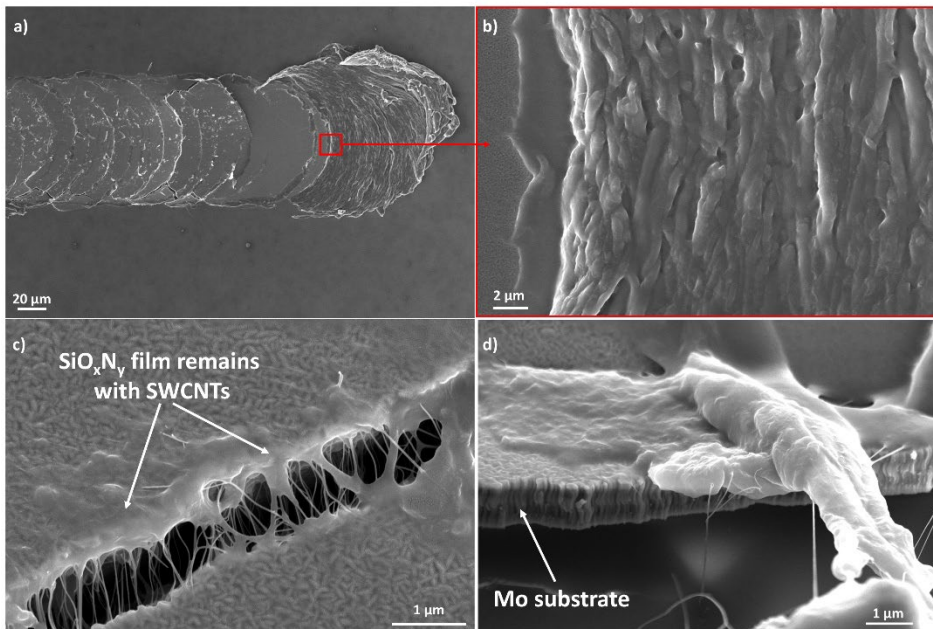


Figure 3.20. HR-SEM images of as-annealed  $\text{SiO}_x\text{N}_y/\text{SWCNT}$  composite sample: (a) destruction of the end of a scratch at 2050 g load and (b) magnified image of the plastically deformed and extruded film beyond the end point of the scratch; (c) and (d) fragments of the substrate with the remains of the composite film inside the scratch track.

We did not present COF graphs in this section, since they were similar to those presented in Section 3.1.5. The COF values for composite films also did not exceed 0.05. The ATM results for composite samples confirmed the high smoothness of the surface, with an average roughness not exceeding 0.7 nm.

Thus, the embedding of SWCNTs into the  $\text{SiO}_x\text{N}_y$  matrix did not affect the adhesive and surface properties of the resulting composites. However, there was a visible reinforcing effect by the SWCNT network against the tearing of the  $\text{SiO}_x\text{N}_y/\text{SWCNT}$  coatings.

## Conclusions

The aim of this doctoral work was to develop state-of-the-art protective coatings based on  $\text{SiO}_x\text{N}_y$  matrix films derived from the preceramic polymer PHPS with embedded SWCNTs as a filler in oriented nanocomposite structures ( $\text{SiO}_x\text{N}_y/\text{SWCNTs}$ ). To achieve this aim, a detailed comparison of the structures and properties of  $\text{SiO}_x\text{N}_y$  films obtained by two low-temperature curing methods of PHPS was conducted.

The conclusions drawn from the study of  $\text{SiO}_x\text{N}_y$  matrix films are as follows:

1. The method used for curing greatly affected the degree of conversion of the PHPS to  $\text{SiO}_x\text{N}_y$  and the functional properties of as-cured films:
  - Thermal curing yielded an  $\text{SiO}_x\text{N}_y$  film with a high nitrogen content uniformly distributed in the cross-section of the film, as measured by SEM-EDX (59.3 at%) and XPS. The film had a high  $n_{355} = 1.6$ , according to the SE results, as well as high plasticity and poor adhesion to the SLG/Mo substrate, according to the results of the progressive load scratch test.
  - UV curing gave an  $\text{SiO}_x\text{N}_y$  film with a much lower nitrogen content (18.4 at% by SEM-EDX) with a gradient of nitrogen distribution in the cross-section, leading to the  $n$  gradient with values  $n_{355} = 1.49$  near the surface and 1.58 closer to the film-substrate interface. The top sub-layer of almost completely transformed PHPS ( $\text{SiO}_{2.05}\text{N}_{0.06}$  by XPS) did not exceed 20 nm. The films showed higher adhesion and hardness.

Generally, UV curing led to a more complete transformation of PHPS towards  $\text{SiO}_2$  compared to thermal curing.

2. The composition and functional properties of PHPS-derived films changed during the aging process. Specifically, the films continued to ripen, i.e., gradually converting more to  $\text{SiO}_2$  composition with different dynamics:
  - For thermal curing, FTIR spectroscopy showed that the most active ripening occurred during the first week. After that, films started to demonstrate behavior similar to the UV-as-cured films in scratch tests. After 1.5 months, films began to show a weakly expressed gradient structure, where the  $n_{355}$  value at the film-air interface was 1.51, and at the film-substrate interface, 1.54. After 13 months, the  $\Delta n$  ceased to be determinable, and the film had an  $n_{355} = 1.50$ .
  - For UV-cured films, noticeable changes occurred in relation to optical constants during aging. As films aged, they lost their distinct gradient structure, and their  $k$  and  $n$  values decreased. After 1.5 months of ripening, the films showed an  $n_{355}$  value at the level of 1.49–1.50.

The conclusions drawn from the study on the formation of  $\text{SiO}_x\text{N}_y/\text{SWCNT}$  composite coatings are as follows:

1. A simple and effective approach was developed to produce oriented composites with different architectures of SWCNTs. Excellent compatibility of SWCNTs with the PHPS-derived matrix was revealed. The choice of architecture did not affect the degree of PHPS transformation for both curing methods, as shown by FTIR and SEM-EDX results.
2. The morphological and functional properties of the prepared composites were studied.  $\text{SiO}_x\text{N}_y$  /SWCNT composite coatings exhibited properties similar to  $\text{SiO}_x\text{N}_y$  matrix films. However, the incorporation of SWCNTs to  $\text{SiO}_x\text{N}_y$  matrix

films resulted in an increase in the resistance against tearing of the coatings, thus illustrating the potential for improving mechanical properties.

3. The antireflective effect in composite coatings was identified and confirmed, manifesting itself in varying degrees of intensity depending on the curing method used. This antireflective effect was caused by two factors: (i) the embedding of SWCNTs into the matrix film; and (ii) the initial values of optical constants of the as-cured matrix films and their change with the time.

Thus, there is a strong connection between the functional properties of the  $\text{SiO}_x\text{N}_y$  matrix films and  $\text{SiO}_x\text{N}_y/\text{SWCNT}$  composite coatings depending on the chosen curing method, i.e., on the degree of transformation of PPHS into  $\text{SiO}_2$ . Since all cured coatings exhibited low coefficients of friction, their potential application can be expanded to industries where scratch protection and enhanced lubrication or sliding properties are of crucial importance.

Also, our study was the first to compare the optical constants of  $\text{SiO}_x\text{N}_y$  films cured by low-temperature thermal annealing and UV irradiation. The findings show that all cured films have potential to be applied as antireflective broadband coatings in photonics.

Although, the thesis covers the initial stage of the studying and engineering of oriented  $\text{SiO}_x\text{N}_y/\text{SWCNT}$  thin film nanocomposites and demonstrates their potential for further research in the direction of the development of the functional composite coatings. For instance, vertical orientation of CNTs within the matrix can potentially improve the thermal management of the coating. Additionally, the desired properties and functionality of the coatings could likely be fine-tuned through the rational selection of other fillers, expanding thus the range of their potential applications.

## References

1. Pastuszak, J.; Węgierek, P. Photovoltaic Cell Generations and Current Research Directions for Their Development. *Materials* **2022**, *15*, 5542, doi:10.3390/MA15165542.
2. Sorrell, S. Reducing Energy Demand: A Review of Issues, Challenges and Approaches. *Renewable and Sustainable Energy Reviews* **2015**, *47*, 74–82, doi:10.1016/J.RSER.2015.03.002.
3. Bhattacharya, M.; Paramati, S.R.; Ozturk, I.; Bhattacharya, S. The Effect of Renewable Energy Consumption on Economic Growth: Evidence from Top 38 Countries. *Applied Energy* **2016**, *162*, 733–741, doi:10.1016/J.APENERGY.2015.10.104.
4. Adedoyin, F.F.; Erum, N.; Taşkin, D.; Chebab, D. Energy Policy Simulation in Times of Crisis: Revisiting the Impact of Renewable and Non-Renewable Energy Production on Environmental Quality in Germany. *Energy Reports* **2023**, *9*, 4749–4762, doi:10.1016/J.EGYR.2023.03.120.
5. Li, X.; Li, P.; Wu, Z.; Luo, D.; Yu, H.-Y.; Lu, Z.-H. Review and Perspective of Materials for Flexible Solar Cells. *Materials Reports: Energy* **2021**, *1*, 100001, doi:10.1016/J.MATRE.2020.09.001.
6. Gajdzik, B.; Wolniak, R.; Nagaj, R.; Žuromskaitė-Nagaj, B.; Grebski, W.W. The Influence of the Global Energy Crisis on Energy Efficiency: A Comprehensive Analysis. *Energies* **2024**, *17*, 947, doi:10.3390/EN17040947.
7. Wu, M.; Ma, B.; Li, S.; Han, J.; Zhao, W. Powering the Future: A Critical Review of Research Progress in Enhancing Stability of High-Efficiency Organic Solar Cells. *Advanced Functional Materials* **2023**, *33*, 2305445, doi:10.1002/ADFM.202305445.
8. Gaddam, S.K.; Pothu, R.; Boddula, R. Advanced Polymer Encapsulates for Photovoltaic Devices – A Review. *Journal of Materiomics* **2021**, *7*, 920–928, doi:10.1016/J.JMAT.2021.04.004.
9. Kim, D.; Jeon, G.G.; Kim, J.H.; Kim, J.; Park, N. Design of a Flexible Thin-Film Encapsulant with Sandwich Structures of Perhydropolysilazane Layers. *ACS Applied Materials & Interfaces* **2022**, *14*, 34678–34685, doi:10.1021/acsami.2c06699.
10. Back, H.S.; Kim, M.J.; Baek, J.J.; Kim, D.H.; Shin, G.; Choi, K.H.; Cho, J.H. Intense-Pulsed-UV-Converted Perhydropolysilazane Gate Dielectrics for Organic Field-Effect Transistors and Logic Gates. *RSC Advances* **2019**, *9*, 3169–3175, doi:10.1039/C8RA09831J.
11. Baek, J.J.; Park, S.M.; Kim, Y.R.; Chang, K.C.; Heo, Y.-J.; Bae, G.Y.; Choi, K.H.; Shin, G. Intense Pulsed UV Light Treatment to Design Functional Optical Films from Perhydropolysilazane: An Alternative to Conventional Heat Treatment Processes. *Journal of Materials Science* **2022**, *57*, 254–273, doi:10.1007/S10853-021-06598-3.
12. Channa, I.A.; Distler, A.; Zaiser, M.; Brabec, C.J.; Egelhaaf, H.-J. Thin Film Encapsulation of Organic Solar Cells by Direct Deposition of Polysilazanes from Solution. *Advanced Energy Materials* **2019**, *9*, 1900598, doi:10.1002/AENM.201900598.
13. Arash, B.; Wang, Q.; Varadan, V.K. Mechanical Properties of Carbon Nanotube/Polymer Composites. *Scientific Reports* **2014**, *4*, 6479, doi:10.1038/srep06479.

14. Ding, C.; Lu, Z.; Li, S.; Wang, Z.; Yu, P.; Ye, S. Microstructures, Thermal and Mechanical Properties of Al–Si–CNT Composites for Thermal Management Applications. *Materials Chemistry and Physics* **2023**, *297*, 127368, doi:10.1016/J.MATCHEMPHYS.2023.127368.
15. Bhattacharya, M. Polymer Nanocomposites – A Comparison between Carbon Nanotubes, Graphene, and Clay as Nanofillers. *Materials* **2016**, *9*, 262, doi:10.3390/MA9040262.
16. Ruggerio, C.A. Sustainability and Sustainable Development: A Review of Principles and Definitions. *Science of The Total Environment* **2021**, *786*, 147481, doi:10.1016/J.SCITOTENV.2021.147481.
17. European Green Deal – European Council Available online: <https://www.consilium.europa.eu/en/policies/green-deal/> (accessed on 23 October 2024).
18. Energy, Climate Change, Environment – European Commission Available online: [https://commission.europa.eu/energy-climate-change-environment\\_en](https://commission.europa.eu/energy-climate-change-environment_en) (accessed on 23 October 2024).
19. Velenturf, A.P.M.; Purnell, P. Principles for a Sustainable Circular Economy. *Sustainable Production and Consumption* **2021**, *27*, 1437–1457, doi:10.1016/J.SPC.2021.02.018.
20. Suárez-Eiroa, B.; Fernández, E.; Méndez-Martínez, G.; Soto-Oñate, D. Operational Principles of Circular Economy for Sustainable Development: Linking Theory and Practice. *Journal of Cleaner Production* **2019**, *214*, 952–961, doi:10.1016/J.JCLEPRO.2018.12.271.
21. Kabeyi, M.J.B.; Olanrewaju, O.A. Sustainable Energy Transition for Renewable and Low Carbon Grid Electricity Generation and Supply. *Frontiers in Energy Research* **2021**, *9*, 743114, doi:10.3389/FENRG.2021.743114.
22. Devasahayam, S.; Hussain, C.M. Thin-Film Nanocomposite Devices for Renewable Energy Current Status and Challenges. *Sustainable Materials and Technologies* **2020**, *26*, e00233, doi:10.1016/J.SUSMAT.2020.E00233.
23. Mitrašinić, A.M.; Radosavljević, M. Photovoltaic Materials and Their Path toward Cleaner Energy. *Global Challenges* **2023**, *7*, 2200146, doi:10.1002/GCH2.202200146.
24. Sutherland, L.J.; Weerasinghe, H.C.; Simon, G.P. A Review on Emerging Barrier Materials and Encapsulation Strategies for Flexible Perovskite and Organic Photovoltaics. *Advanced Energy Materials* **2021**, *11*, 2101383, doi:10.1002/AENM.202101383.
25. Fouad, M.M.; Shihata, L.A.; Morgan, E.S.I. An Integrated Review of Factors Influencing the Performance of Photovoltaic Panels. *Renewable and Sustainable Energy Reviews* **2017**, *80*, 1499–1511, doi:10.1016/J.RSER.2017.05.141.
26. Creutzig, F.; Agoston, P.; Goldschmidt, J.C.; Luderer, G.; Nemet, G.; Pietzcker, R.C. The Underestimated Potential of Solar Energy to Mitigate Climate Change. *Nature Energy* **2017**, *2*, 17140, doi:10.1038/NENERGY.2017.140.
27. Chen, H.; Chu, L.; Yan, W. Stability Challenges in Industrialization of Perovskite Photovoltaics: From Atomic-Scale View to Module Encapsulation. *Advanced Functional Materials* **2024**, *35*, 2412389, doi:10.1002/ADFM.202412389.

28. Pscherer, M.; Günthner, M.; Kaufmann, C.A.; Rahm, A.; Motz, G. Thin-Film Silazane/Alumina High Emissivity Double Layer Coatings for Flexible Cu(In,Ga)Se<sub>2</sub> Solar Cells. *Solar Energy Materials and Solar Cells* **2015**, *132*, 296–302, doi:10.1016/J.SOLMAT.2014.09.015.
29. Prajapat, K.; Mahajan, U.; Kumar, A.; Dhonde, M.; Sahu, K.; Vyas, S.; Riyad, Y.M.; El-Bahy, Z.M. Next-Generation Counter Electrodes for Dye-Sensitized Solar Cells: A Comprehensive Overview. *Sustainable Materials and Technologies* **2024**, *42*, e01178, doi:10.1016/J.SUSMAT.2024.E01178.
30. Maani, T.; Celik, I.; Heben, M.J.; Ellingson, R.J.; Apul, D. Environmental Impacts of Recycling Crystalline Silicon (c-Si) and Cadmium Telluride (CDTE) Solar Panels. *Science of The Total Environment* **2020**, *735*, 138827, doi:10.1016/J.SCITOTENV.2020.138827.
31. Tao, J.; Yu, S. Review on Feasible Recycling Pathways and Technologies of Solar Photovoltaic Modules. *Solar Energy Materials and Solar Cells* **2015**, *141*, 108–124, doi:10.1016/J.SOLMAT.2015.05.005.
32. Chen, X.; Xu, G.; Zeng, G.; Gu, H.; Chen, H.; Xu, H.; Yao, H.; Li, Y.; Hou, J.; Li, Y. Realizing Ultrahigh Mechanical Flexibility and >15% Efficiency of Flexible Organic Solar Cells via a “Welding” Flexible Transparent Electrode. *Advanced Materials* **2020**, *32*, 1908478, doi:10.1002/ADMA.201908478.
33. Ma, S.; Yuan, G.; Zhang, Y.; Yang, N.; Li, Y.; Chen, Q. Development of Encapsulation Strategies towards the Commercialization of Perovskite Solar Cells. *Energy & Environmental Science* **2022**, *15*, 13–55, doi:10.1039/D1EE02882K.
34. Wang, T.; Yang, J.; Cao, Q.; Pu, X.; Li, Y.; Chen, H.; Zhao, J.; Zhang, Y.; Chen, X.; Li, X. Room Temperature Nondestructive Encapsulation via Self-Crosslinked Fluorosilicone Polymer Enables Damp Heat-Stable Sustainable Perovskite Solar Cells. *Nature Communications* **2023**, *14*, 1342, doi:10.1038/s41467-023-36918-x.
35. Kauk-Kuusik, M.; Li, X.; Pilvet, M.; Timmo, K.; Grossberg, M.; Raadik, T.; Danilson, M.; Mikli, V.; Altosaar, M.; Krustok, J.; Raudoja, J. Study of Cu<sub>2</sub>CdGeSe<sub>4</sub> Monograin Powders Synthesized by Molten Salt Method for Photovoltaic Applications. *Thin Solid Films* **2018**, *666*, 15–19, doi:10.1016/J.TSF.2018.09.025.
36. Aitola, K.; Sonai, G.G.; Markkanen, M.; Kaschuk, J.J.; Hou, X.; Miettunen, K.; Lund, P.D. Encapsulation of Commercial and Emerging Solar Cells with Focus on Perovskite Solar Cells. *Solar Energy* **2022**, *237*, 264–283, doi:10.1016/J.SOLENER.2022.03.060.
37. Rolston, N.; Printz, A.D.; Hilt, F.; Hovish, M.Q.; Brüning, K.; Tassone, C.J.; Dauskardt, R.H. Improved Stability and Efficiency of Perovskite Solar Cells with Submicron Flexible Barrier Films Deposited in Air. *Journal of Materials Chemistry A* **2017**, *5*, 22975–22983, doi:10.1039/C7TA09178H.
38. Dong, Q.; Liu, F.; Wong, M.K.; Tam, H.W.; Djurišić, A.B.; Ng, A.; Surya, C.; Chan, W.K.; Ng, A.M.C. Encapsulation of Perovskite Solar Cells for High Humidity Conditions. *ChemSusChem* **2016**, *9*, 2597–2603, doi:10.1002/SSC.201600868.
39. Ma, S.; Yuan, G.; Zhang, Y.; Yang, N.; Li, Y.; Chen, Q. Development of Encapsulation Strategies towards the Commercialization of Perovskite Solar Cells. *Energy & Environmental Science* **2022**, *15*, 13–55, doi:10.1039/D1EE02882K.
40. Li, Y.; Huang, X.; Ding, K.; Sheriff, H.K.M., Jr.; Ye, L.; Liu, H.; Li, C.-Z.; Ade, H.; Forrest, S.R. Non-Fullerene Acceptor Organic Photovoltaics with Intrinsic Operational Lifetimes over 30 Years. *Nature Communications* **2021**, *12*, 5419, doi:10.1038/s41467-021-25718-w.



41. Mercier, T.M.; Rahman, T.; Krishnan, C.; Khorani, E.; Shaw, P.J.; Pollard, M.E.; Boden, S.A.; Lagoudakis, P.G.; Charlton, M.D.B. High Symmetry Nano-Photonic Quasi-Crystals Providing Novel Light Management in Silicon Solar Cells. *Nano Energy* **2021**, *84*, 105874, doi:10.1016/J.NANOEN.2021.105874.
42. Colombo, P.; Mera, G.; Riedel, R.; Sorarù, G.D. Polymer-Derived Ceramics: 40 Years of Research and Innovation in Advanced Ceramics. *Journal of the American Ceramic Society* **2010**, *93*, 1805–1837, doi:10.1111/J.1551-2916.2010.03876.X.
43. Francis, A. Progress in Polymer-Derived Functional Silicon-Based Ceramic Composites for Biomedical and Engineering Applications. *Materials Research Express* **2018**, *5*, 062003, doi:10.1088/2053-1591/AACD28.
44. Furtat, P.; Lenz-Leite, M.; Ionescu, E.; Machado, R.A.F.; Motz, G. Synthesis of Fluorine-Modified Polysilazanes *via* Si–H Bond Activation and Their Application as Protective Hydrophobic Coatings. *Journal of Materials Chemistry A* **2017**, *5*, 25509–25521, doi:10.1039/C7TA07687H.
45. Zhu, J.; Shen, G.; Jiang, W.; Shen, X. The Preparation and Properties Study of Novel Hydrophobic/Superhydrophobic Coatings Based on Fluorine Modified Perhydropolysilazane. *Journal of Dispersion Science and Technology* **2021**, *44*, 779–786, doi:10.1080/01932691.2021.1974871.
46. Parchovianský, M.; Parchovianská, I.; Švančárek, P.; Medved', D.; Lenz-Leite, M.; Motz, G.; Galusek, D. High-Temperature Oxidation Resistance of PDC Coatings in Synthetic Air and Water Vapor Atmospheres. *Molecules* **2021**, *26*, 2388, doi:10.3390/MOLECULES26082388.
47. Flores, O.; Bordia, R.K.; Nestler, D.; Krenkel, W.; Motz, G. Ceramic Fibers Based on SiC and SiCN Systems: Current Research, Development, and Commercial Status. *Advanced Engineering Materials* **2014**, *16*, 621–636, doi:10.1002/ADEM.201400069.
48. Wang, D.; Ma, J.; Li, P.; Fan, L.; Wu, Y.; Zhang, Z.; Xu, C.; Jiang, L. Flexible Hard Coatings with Self-Evolution Behavior in a Low Earth Orbit Environment. *ACS Applied Materials & Interfaces* **2021**, *13*, 46003–46014, doi:10.1021/acsami.1c13807.
49. Zhan, Y.; Grottenmüller, R.; Li, W.; Javid, F.; Riedel, R. Evaluation of Mechanical Properties and Hydrophobicity of Room-Temperature, Moisture-Curable Polysilazane Coatings. *Journal of Applied Polymer Science* **2021**, *138*, 50469, doi:10.1002/APP.50469.
50. Günthner, M.; Kraus, T.; Dierdorf, A.; Decker, D.; Krenkel, W.; Motz, G. Advanced Coatings on the Basis of Si(C)N Precursors for Protection of Steel against Oxidation. *Journal of the European Ceramic Society* **2009**, *29*, 2061–2068, doi:10.1016/J.JEURCERAMSOC.2008.11.013.
51. Barroso, G.; Li, Q.; Bordia, R.K.; Motz, G. Polymeric and Ceramic Silicon-Based Coatings – A Review. *Journal of Materials Chemistry A* **2019**, *7*, 1936–1963, doi:10.1039/C8TA09054H.
52. Rossi, S.; Deflorian, F.; Fedel, M. Polysilazane-Based Coatings: Corrosion Protection and Anti-Graffiti Properties. *Surface Engineering* **2019**, *35*, 343–350, doi:10.1080/02670844.2018.1465748.
53. Funayama, O.; Tashiro, Y.; Kamo, A.; Okumura, M.; Isoda, T. Conversion Mechanism of Perhydropolysilazane into Silicon Nitride-Based Ceramics. *Journal of Materials Science* **1994**, *29*, 4883–4888, doi:10.1007/BF00356538.

54. Prager, L.; Dierdorf, A.; Liebe, H.; Naumov, S.; Stojanović, S.; Heller, R.; Wennrich, L.; Buchmeiser, M.R. Conversion of Perhydropolysilazane into a SiO<sub>x</sub> Network Triggered by Vacuum Ultraviolet Irradiation: Access to Flexible, Transparent Barrier Coatings. *Chemistry – A European Journal* **2007**, *13*, 8522–8529, doi:10.1002/CHEM.200700351.
55. Bauer, F.; Decker, U.; Dierdorf, A.; Ernst, H.; Heller, R.; Liebe, H.; Mehnert, R. Preparation of Moisture Curable Polysilazane Coatings: Part I. Elucidation of Low Temperature Curing Kinetics by FT-IR Spectroscopy. *Progress in Organic Coatings* **2005**, *53*, 183–190, doi:10.1016/j.porgcoat.2005.02.006.
56. Dargère, N.; Bounor-Legaré, V.; Boisson, F.; Cassagnau, P.; Martin, G.; Sonntag, P.; Garois, N. Hydridosilazanes Hydrolysis-Condensation Reactions Studied by <sup>1</sup>H and <sup>29</sup>Si Liquid NMR Spectroscopy. *Journal of Sol-Gel Science and Technology* **2012**, *62*, 389–396, doi:10.1007/S10971-012-2738-2.
57. Kubo, T.; Kozuka, H. Conversion of Perhydropolysilazane-to-Silica Thin Films by Exposure to Vapor from Aqueous Ammonia at Room Temperature. *Journal of the Ceramic Society of Japan* **2006**, *114*, 517–523, doi:10.2109/jcersj.114.517.
58. Lee, J.-S.; Oh, J.-H.; Moon, S.-W.; Sul, W.-S.; Kim, S.-D. A Technique for Converting Perhydropolysilazane to SiO<sub>x</sub> at Low Temperature. *Electrochemical and Solid-State Letters* **2010**, *13*, H23–H25, doi:10.1149/1.3264092.
59. Kozuka, H.; Nakajima, K.; Uchiyama, H. Superior Properties of Silica Thin Films Prepared from Perhydropolysilazane Solutions at Room Temperature in Comparison with Conventional Alkoxide-Derived Silica Gel Films. *ACS Applied Materials & Interfaces* **2013**, *5*, 8329–8336, doi:10.1021/am400845y.
60. Morlier, A.; Cros, S.; Garandet, J.-P.; Alberola, N. Thin Gas-Barrier Silica Layers from Perhydropolysilazane Obtained through Low Temperature Curings: A Comparative Study. *Thin Solid Films* **2012**, *524*, 62–66, doi:10.1016/J.TSF.2012.09.065.
61. Kim, S.-D.; Ko, P.-S.; Park, K.-S. Perhydropolysilazane Spin-on Dielectrics for Inter-Layer-Dielectric Applications of Sub-30 nm Silicon Technology. *Semiconductor Science and Technology* **2013**, *28*, 035008, doi:10.1088/0268-1242/28/3/035008.
62. Riffard, F.; Joannet, E.; Buscail, H.; Rolland, R.; Perrier, S. Beneficial Effect of a Pre-Ceramic Polymer Coating on the Protection at 900 °C of a Commercial AISI 304 Stainless Steel. *Oxidation of Metals* **2017**, *88*, 211–220, doi:10.1007/S11085-016-9705-1.
63. Wang, K.; Günthner, M.; Motz, G.; Flinn, B.D.; Bordia, R.K. Control of Surface Energy of Silicon Oxynitride Films. *Langmuir* **2013**, *29*, 2889–2896, doi:10.1021/LA304307Y.
64. Yang, N.; Wang, W.; Cai, W.; Lu, K. Corrosion and Tribocorrosion Mitigation of Perhydropolysilazane-Derived Coatings on Low Carbon Steel. *Corrosion Science* **2020**, *177*, 108946, doi:10.1016/J.CORSCI.2020.108946.
65. Günthner, M.; Wang, K.; Bordia, R.K.; Motz, G. Conversion Behaviour and Resulting Mechanical Properties of Polysilazane-Based Coatings. *Journal of the European Ceramic Society* **2012**, *32*, 1883–1892, doi:10.1016/J.JEURCERAMSOC.2011.09.005.
66. Prager, L.; Helmstedt, U.; Herrnberger, H.; Kahle, O.; Kita, F.; Münch, M.; Pender, A.; Prager, A.; Gerlach, J.W.; Stasiak, M. Photochemical Approach to High-Barrier Films for the Encapsulation of Flexible Laminary Electronic Devices. *Thin Solid Films* **2014**, *570*, 87–95, doi:10.1016/J.TSF.2014.09.014.

67. Morlier, A.; Cros, S.; Garandet, J.-P.; Alberola, N. Structural Properties of Ultraviolet Cured Polysilazane Gas Barrier Layers on Polymer Substrates. *Thin Solid Films* **2014**, *550*, 85–89, doi:10.1016/J.TSF.2013.10.140.
68. Ohishi, T.; Yamazaki, Y. Formation and Gas Barrier Characteristics of Polysilazane-Derived Silica Coatings Formed by Excimer Light Irradiation on PET Films with Vacuum Evaporated Silica Coatings. *Materials Sciences and Applications* **2017**, *8*, 1–14, doi:10.4236/MSA.2017.81001.
69. Kobayashi, Y.; Yokota, H.; Fuchita, Y.; Takahashi, A.; Sugahara, Y. Characterization of Gas Barrier Silica Coatings Prepared from Perhydropolysilazane Films by Vacuum Ultraviolet Irradiation. *Journal of the Ceramic Society of Japan* **2013**, *121*, 215–218, doi:10.2109/JCERSJ.121.215.
70. Blankenburg, L.; Schrödner, M. Perhydropolysilazane Derived Silica for Flexible Transparent Barrier Foils Using a Reel-to-Reel Wet Coating Technique: Single- and Multilayer Structures. *Surface and Coating Technology* **2015**, *275*, 193–206, doi:10.1016/J.SURFCOAT.2015.05.019.
71. Sasaki, T.; Sun, L.; Kurosawa, Y.; Takahashi, T.; Suzuri, Y. Nanometer-Thick SiN Films as Gas Barrier Coatings Densified by Vacuum UV Irradiation. *ACS Applied Nano Materials* **2021**, *4*, 10344–10353, doi:10.1021/ACSANM.1C01862.
72. Naganuma, Y.; Horiuchi, T.; Kato, C.; Tanaka, S. Low-Temperature Synthesis of Silica Coating on a Poly(Ethylene Terephthalate) Film from Perhydropolysilazane Using Vacuum Ultraviolet Light Irradiation. *Surface and Coatings Technology* **2013**, *225*, 40–46, doi:10.1016/J.SURFCOAT.2013.03.014.
73. Ohishi, T.; Ichikawa, K. Formation and Gas Barrier Properties of Silica Thin Films Formed on Heat Resistant PET (Polyethylene Terephthalate) Substrate by Excimer Light Irradiation to Polysilazane Coatings. *Materials Letters* **2019**, *247*, 143–146, doi:10.1016/J.MATLET.2019.03.115.
74. Hull, D.; Clyne, T.W. An Introduction to Composite Materials, 2<sup>nd</sup> Edition (Cambridge Solid State Science Series). **1996**, 344.
75. Zhang, X.; Zhao, N.; He, C. The Superior Mechanical and Physical Properties of Nanocarbon Reinforced Bulk Composites Achieved by Architecture Design – A Review. *Progress in Materials Science* **2020**, *113*, 100672, doi:10.1016/J.PMATSCI.2020.100672.
76. Lee, J.K.Y.; Chen, N.; Peng, S.; Li, L.; Tian, L.; Thakor, N.; Ramakrishna, S. Polymer-Based Composites by Electrospinning: Preparation & Functionalization with Nanocarbons. *Progress in Polymer Science* **2018**, *86*, 40–84, doi:10.1016/J.PROGPOLYMSCI.2018.07.002.
77. Baig, N.; Kammakam, I.; Falath, W. Nanomaterials: A Review of Synthesis Methods, Properties, Recent Progress, and Challenges. *Materials Advances* **2021**, *2*, 1821–1871, doi:10.1039/D0MA00807A.
78. Das, G.S.; Tripathi, V.K.; Dwivedi, J.; Jangir, L.K.; Tripathi, K.M. Nanocarbon-Based Sensors for the Structural Health Monitoring of Smart Biocomposites. *Nanoscale* **2024**, *16*, 1490–1525, doi:10.1039/D3NR05522A.
79. Zhao, M.-Q.; Zhang, Q.; Huang, J.-Q.; Wei, F. Hierarchical Nanocomposites Derived from Nanocarbons and Layered Double Hydroxides – Properties, Synthesis, and Applications. *Advanced Functional Materials* **2012**, *22*, 675–694, doi:10.1002/ADFM.201102222.

80. Ye, W.; Shi, Y.; Zhou, Q.; Xie, M.; Wang, H.; Bou-Saïd, B.; Liu, W. Recent Advances in Self-Lubricating Metal Matrix Nanocomposites Reinforced by Carbonous Materials: A Review. *Nano Materials Science* **2024**, *6*, 701–713, doi:10.1016/J.NANOMS.2024.02.007.
81. Han, B.; Sun, S.; Ding, S.; Zhang, L.; Yu, X.; Ou, J. Review of Nanocarbon-Engineered Multifunctional Cementitious Composites. *Composites Part A: Applied Science and Manufacturing* **2015**, *70*, 69–81, doi:10.1016/J.COMPOSITESA.2014.12.002.
82. Reduwan Billah, S.M. Composites and Nanocomposites. In: Jafar Mazumder, M., Sheardown, H., Al-Ahmed, A. (eds) *Functional Polymers. (Polymers and Polymeric Composites: A Reference Series)*. **2019**, 1–67, doi:10.1007/978-3-319-92067-2\_15-1.
83. Seo, Y.; Cho, S.; Kim, S.; Choi, S.; Kim, H. Synthesis of Refractive Index Tunable Silazane Networks for Transparent Glass Fiber Reinforced Composite. *Ceramics International* **2017**, *43*, 7895–7900, doi:10.1016/J.CERAMINT.2017.03.112.
84. Peng, J.; Ye, P.; Xu, F.; Bu, X.; Wang, R.; Lin, D.; Yuan, S.; Zhu, Y.; Wang, H. Highly Transparent, Self-Cleaning, and UV-Shielding Composite Coating: When Eco-Friendly Waterborne Omniphobic Surface Cooperates with Quantum Dots. *Composites Part B: Engineering* **2024**, *284*, 111731, doi:10.1016/J.COMPOSITESB.2024.111731.
85. Li, Y.-T.; Sun, K.; Luo, D.; Wang, Y.-M.; Han, L.; Liu, H.; Guo, X.-L.; Yu, D.-L.; Ren, T.-L. A Review on Low-Dimensional Novel Optoelectronic Devices Based on Carbon Nanotubes. *AIP Advances* **2021**, *11*, 110701, doi:10.1063/5.0063774/989505.
86. Sajid, M.I.; Jamshaid, U.; Jamshaid, T.; Zafar, N.; Fessi, H.; Elaissari, A. Carbon Nanotubes from Synthesis to *In Vivo* Biomedical Applications. *International Journal of Pharmaceutics* **2016**, *501*, 278–299, doi:10.1016/J.IJPHARM.2016.01.064.
87. Moniruzzaman, M.; Winey, K.I. Polymer Nanocomposites Containing Carbon Nanotubes. *Macromolecules* **2006**, *39*, 5194–5205, doi:10.1021/MA060733P.
88. Coleman, J.N.; Khan, U.; Gun'ko, Y.K. Mechanical Reinforcement of Polymers Using Carbon Nanotubes. *Advanced Materials* **2006**, *18*, 689–706, doi:10.1002/ADMA.200501851.
89. Han, Z.; Fina, A. Thermal Conductivity of Carbon Nanotubes and Their Polymer Nanocomposites: A Review. *Progress in Polymer Science* **2011**, *36*, 914–944, doi:10.1016/J.PROGPOLYMSCI.2010.11.004.
90. Dresselhaus, M.S.; Dresselhaus, G.; Charlier, J.C.; Hernández, E. Electronic, Thermal and Mechanical Properties of Carbon Nanotubes. *Philosophical Transactions of the Royal Society A: Mathematical, Physical and Engineering Sciences* **2004**, *362*, 2065–2098, doi:10.1098/RSTA.2004.1430.
91. Baughman, R.H.; Zakhidov, A.A.; De Heer, W.A. Carbon Nanotubes – The Route toward Applications. *Science* **2002**, *297*, 787–792, doi:10.1126/SCIENCE.1060928.
92. Merkoçi, A. Carbon Nanotubes in Analytical Sciences. *Microchim Acta* **2006**, *152*, 157–174, doi:10.1007/s00604-005-0439-z.
93. Tiwari, P.; Janas, D. Emergent Pseudocapacitive Behavior of Single-Walled Carbon Nanotube Hybrids: A Materials Chemistry Perspective. *Materials Chemistry Frontiers* **2022**, *6*, 2386–2412, doi:10.1039/D2QM00146B.

94. Foygel, M.; Morris, R.D.; Anez, D.; French, S.; Sobolev, V.L. Theoretical and Computational Studies of Carbon Nanotube Composites and Suspensions: Electrical and Thermal Conductivity. *Physical Review B: Condensed Matter and Materials Physics* **2005**, *71*, 104201, doi:10.1103/PHYSREVB.71.104201.
95. Nasibulin, A.G.; Kaskela, A.; Mustonen, K.; Anisimov, A.S.; Ruiz, V.; Kivistö, S.; Rackauskas, S.; Timmermans, M.Y.; Pudas, M.; Aitchison, B.; Kauppinen, M.; Brown, D.P.; Okhotnikov, O.G.; Kauppinen, E.I. Multifunctional Free-Standing Single-Walled Carbon Nanotube Films. *ACS Nano* **2011**, *5*, 3214–3221, doi:10.1021/NN200338R.
96. Rouhi, N.; Jain, D.; Burke, P.J. High-Performance Semiconducting Nanotube Inks: Progress and Prospects. *ACS Nano* **2011**, *5*, 8471–8487, doi:10.1021/NN201828Y.
97. Cheung, W.; Patel, M.; Ma, Y.; Chen, Y.; Xie, Q.; Lockard, J. V.; Gao, Y.; He, H.  $\pi$ -Plasmon Absorption of Carbon Nanotubes for the Selective and Sensitive Detection of  $\text{Fe}^{3+}$  Ions. *Chemical Sciences* **2016**, *7*, 5192–5199, doi:10.1039/C6SC00006A.
98. Bozey, A.; Makableh, Y.F.; Abu-Zurayk, R.; Khalaf, A.; Al Bawab, A. Thermal and Structural Properties of High Density Polyethylene/Carbon Nanotube Nanocomposites: A Comparison Study. *Chemosensors* **2021**, *9*, 136, doi:10.3390/CHEMOSENSORS9060136.
99. Cao, Q.; Rogers, J.A. Ultrathin Films of Single-Walled Carbon Nanotubes for Electronics and Sensors: A Review of Fundamental and Applied Aspects. *Advanced Materials* **2009**, *21*, 29–53, doi:10.1002/ADMA.200801995.
100. De Volder, M.F.L.; Tawfick, S.H.; Baughman, R.H.; Hart, A.J. Carbon Nanotubes: Present and Future Commercial Applications. *Science* **2013**, *339*, 535–539, doi:10.1126/SCIENCE.1222453.
101. David, L.; Asok, D.; Singh, G. Synthesis and Extreme Rate Capability of Si-Al-C-N Functionalized Carbon Nanotube Spray-on Coatings as Li-Ion Battery Electrode. *ACS Applied Materials & Interfaces* **2014**, *6*, 16056–16064, doi:10.1021/AM5052729.
102. Francis, A.; Riedel, R. Unusual Magnetic Behavior of SiCN/Multiwalled Carbon Nanotubes Nanocomposites. *Journal of Applied Physics* **2009**, *105*, 07A318 doi:10.1063/1.3062958.
103. Yang, J.; Downes, R.; Schrand, A.; Park, J.G.; Liang, R.; Xu, C. High Electrical Conductivity and Anisotropy of Aligned Carbon Nanotube Nanocomposites Reinforced by Silicon Carbonitride. *Scripta Materialia* **2016**, *124*, 21–25, doi:10.1016/J.SCRIPTAMAT.2016.06.023.
104. Han, Z.; Fina, A. Thermal Conductivity of Carbon Nanotubes and Their Polymer Nanocomposites: A Review. *Progress in Polymer Science* **2011**, *36*, 914–944, doi:10.1016/J.PROGPOLYMSCI.2010.11.004.
105. Jenkins, K.R.; Chan, J.; Jacobberger, R.M.; Berson, A.; Arnold, M.S. Substrate-Wide Confined Shear Alignment of Carbon Nanotubes for Thin Film Transistors. *Advanced Electronic Materials* **2019**, *5*, 1800593, doi:10.1002/AELM.201800593.
106. Ghavidel, A.K.; Zadshakoyan, M.; Arjmand, M. Mechanical Analysis of Aligned Carbon Nanotube Bundles under Electric Field. *International Journal of Mechanical Sciences* **2021**, *196*, 106289, doi:10.1016/J.IJMECSCI.2021.106289.

107. Moiala, A.; Nasibulin, A.G.; Brown, D.P.; Jiang, H.; Khriachtchev, L.; Kauppinen, E.I. Single-Walled Carbon Nanotube Synthesis Using Ferrocene and Iron Pentacarbonyl in a Laminar Flow Reactor. *Chemical Engineering Science* **2006**, *61*, 4393–4402, doi:10.1016/J.CES.2006.02.020.
108. Rajanna, P.M.; Meddeb, H.; Sergeev, O.; Tsapenko, A.P.; Bereznev, S.; Vehse, M.; Volobujeva, O.; Danilson, M.; Lund, P.D.; Nasibulin, A.G. Rational Design of Highly Efficient Flexible and Transparent p-Type Composite Electrode Based on Single-Walled Carbon Nanotubes. *Nano Energy* **2020**, *67*, 104183, doi:10.1016/J.NANOEN.2019.104183.
109. Khabushev, E.M.; Krasnikov, D.V.; Goldt, A.E.; Fedorovskaya, E.O.; Tsapenko, A.P.; Zhang, Q.; Kauppinen, E.I.; Kallio, T.; Nasibulin, A.G. Joint Effect of Ethylene and Toluene on Carbon Nanotube Growth. *Carbon* **2022**, *189*, 474–483, doi:10.1016/J.CARBON.2021.12.052.
110. Drozdov, G.; Ostanin, I.; Xu, H.; Wang, Y.; Dumitrică, T.; Grebenko, A.; Tsapenko, A.P.; Gladush, Y.; Ermolaev, G.; Volkov, V.S.; Eibl, S.; Rude, U.; Nasibulin, A.G. Densification of Single-Walled Carbon Nanotube Films: Mesoscopic Distinct Element Method Simulations and Experimental Validation. *Journal of Applied Physics* **2020**, *128*, 184701, doi:10.1063/5.0025505.
111. Othman, M.F.; Bushroa, A.R.; Abdullah, W.N.R. Evaluation Techniques and Improvements of Adhesion Strength for TiN Coating in Tool Applications: A Review. *Journal of Adhesion Science and Technology* **2015**, *29*, 569–591, doi:10.1080/01694243.2014.997379.
112. Jennett, N.M.; Owen-Jones, S. The Scratch Test: Calibration, Verification and the Use of a Certified Reference Material, Measurement Good Practice Guide No 54. (National Physics Laboratory) **2002**, <https://eprintspublications.npl.co.uk/2716/1/mggp54.pdf>.
113. Song, C.; Song, J.; Wang, X. Interface and Size Effects of Amorphous Si/Amorphous Silicon Oxynitride Multilayer Structures on the Photoluminescence Spectrum. *Coatings* **2024**, *14*, 977, doi:10.3390/COATINGS14080977.
114. Chen, N.; Reesa-Jayan, B.; Liu, A.; Lau, J.; Dunn, B.; Gleason, K.K. iCVD Cyclic Polysiloxane and Polysilazane as Nanoscale Thin-Film Electrolyte: Synthesis and Properties. *Macromolecular Rapid Communications* **2016**, *37*, 446–452, doi:10.1002/MARC.201500649.
115. Canar, H.H.; Bektaş, G.; Turan, R. On the Passivation Performance of SiN<sub>x</sub>, SiO<sub>x</sub>N<sub>y</sub> and Their Stack on c-Si Wafers for Solar Cell Applications: Correlation with Optical, Chemical and Interface Properties. *Solar Energy Materials and Solar Cells* **2023**, *256*, 112356, doi:10.1016/J.SOLMAT.2023.112356.
116. Zhang, Z.; Shao, Z.; Luo, Y.; An, P.; Zhang, M.; Xu, C. Hydrophobic, Transparent and Hard Silicon Oxynitride Coating from Perhydropolysilazane. *Polymer International* **2015**, *64*, 971–978, doi:10.1002/PI.4871.
117. Ermakova, E.; Shayapov, V.; Saraev, A.; Maximovsky, E.; Kirienko, V.; Khomyakov, M.; Sulyaeva, V.; Kolodin, A.; Gerasimov, E.; Kosinova, M. Effect of Plasma Power on Growth Process, Chemical Structure, and Properties of PECVD Films Produced from Hexamethyldisilane and Ammonia. *Surface and Coating Technology* **2024**, *490*, 131131, doi:10.1016/J.SURFCOAT.2024.131131.

118. Jin, X.; Guo, X.; Zhai, L.; Vogelbacher, F.; Xia, Y.; Li, M.; Xu, C.; Zhang, Z. Robust and Flexible Free-Standing Polyimide/SiO<sub>x</sub> Nanocomposite One-Dimensional Photonic Crystals with High Reflectance. *Journal of Materials Science* **2023**, *58*, 1656–1669, doi:10.1007/S10853-022-08136-1/FIGURES/7.
119. Derrick, M.R.; Stulik, D.; Landry, J.M. *Infrared Spectroscopy in Conservation Science*; The Getty Conservation Institute: Los Angeles, **1999**, 248.
120. Nakajima, K.; Uchiyama, H.; Kitano, T.; Kozuka, H. Conversion of Solution-Derived Perhydropolysilazane Thin Films into Silica in Basic Humid Atmosphere at Room Temperature. *Journal of the American Ceramic Society* **2013**, *96*, 2806–2816, doi:10.1111/JACE.12513.
121. Akkaya, A.; Boyarbay, B.; Çetin, H.; Yıldızlı, K.; Ayyıldız, E. A Study on the Electronic Properties of SiO<sub>x</sub>N<sub>y</sub>/p-Si Interface. *Silicon* **2018**, *10*, 2717–2725, doi:10.1007/s12633-018-9811-6.
122. Moulder, J.F.; Stickle, W.F.; Sobol, P.E.; Bomben, K.D. *Handbook of X-Ray Photoelectron Spectroscopy*; Chastain, J., Ed.; Perkin-Elmer Corporation, Physical Electronics Division: Eden Prairie, USA, **1992**, 260.
123. NIST X-Ray Photoelectron Spectroscopy Database, Version 3.5 Available online: <https://srdata.nist.gov/xps/> (accessed on 19 September 2022).
124. Shi, Y.; He, L.; Guang, F.; Li, L.; Xin, Z.; Liu, R. A Review: Preparation, Performance, and Applications of Silicon Oxynitride Film. *Micromachines* **2019**, *10*, 552, doi:10.3390/mi10080552.
125. Kalnitsky, A.; Tay, S.P.; Ellul, J.P.; Chongsawangvirod, S.; Andrews, J.W.; Irene, E.A. Measurements and Modeling of Thin Silicon Dioxide Films on Silicon. *Journal of the Electrochemical Society* **1990**, *137*, 234–238, doi:10.1149/1.2086373.
126. Montecchi, M.; Montecchi, R.M.; Nichelatti, E. Reflectance and Transmittance of a Slightly Inhomogeneous Thin Film Bounded by Rough, Unparallel Interfaces. *Thin Solid Films* **2001**, *396*, 264–275, doi:10.1016/S0040-6090(01)01253-6.
127. Akaoglu, B.; Atilgan, İ.; Katircioğlu, B. Correlation between Optical Path Modulations and Transmittance Spectra of a-Si:H Thin Films. *Applied Optics* **2000**, *39*, 1611–1616, doi:10.1364/AO.39.001611.
128. Barletta, M.; Tagliaferri, V.; Gisario, A.; Venettacci, S. Progressive and Constant Load Scratch Testing of Single- and Multi-Layered Composite Coatings. *Tribology International* **2013**, *64*, 39–52, doi:10.1016/J.TRIBOINT.2013.03.002.
129. Jorio, A.; Saito, R. Raman Spectroscopy for Carbon Nanotube Applications. *Journal of Applied Physics* **2021**, *129*, 021102, doi:10.1063/5.0030809.
130. Komarova, N.S.; Krivenko, A.G.; Ryabenko, A.G.; Naumkin, A. V. Active Forms of Oxygen as Agents for Electrochemical Functionalization of SWCNTs. *Carbon* **2013**, *53*, 188–196, doi:10.1016/J.CARBON.2012.10.047.
131. Alekseeva, A.A.; Krasnikov, D.V.; Livshits, G.B.; Romanov, S.A.; Popov, Z.I.; Varlamova, L.A.; Sukhanova, E.V.; Klimovich, A.S.; Sorokin, P.B.; Savilov, S.V.; Nasibulin, A.G. Films Enriched with Semiconducting Single-Walled Carbon Nanotubes by Aerosol N<sub>2</sub>O Etching. *Carbon* **2023**, *212*, 118094, doi:10.1016/J.CARBON.2023.118094.
132. Minati, L.; Speranza, G.; Bernagozzi, I.; Torrenzo, S.; Toniutti, L.; Rossi, B.; Ferrari, M.; Chiasera, A. Investigation on the Electronic and Optical Properties of Short Oxidized Multiwalled Carbon Nanotubes. *The Journal of Physical Chemistry C* **2010**, *114*, 11068–11073, doi:10.1021/JP101868S.

133. Panasenko, I.V.; Bulavskiy, M.O.; Iurchenkova, A.A.; Aguilar-Martinez, Y.; Fedorov, F.S.; Fedorovskaya, E.O.; Mikladal, B.; Kallio, T.; Nasibulin, A.G. Flexible Supercapacitors Based on Free-Standing Polyaniline/Single-Walled Carbon Nanotube Films. *Journal of Power Sources* **2022**, *541*, 231691, doi:10.1016/J.JPOWSOUR.2022.231691.
134. Ermolaev, G.A.; Tsapenko, A.P.; Volkov, V.S.; Anisimov, A.S.; Gladush, Y.G.; Nasibulin, A.G. Express Determination of Thickness and Dielectric Function of Single-Walled Carbon Nanotube Films. *Applied Physics Letters* **2020**, *116*, 48, doi:10.1063/5.0012933.
135. Rajanna, P.M.; Luchkin, S.; Larionov, K.V.; Grebenko, A.; Popov, Z.I.; Sorokin, P.B.; Danilson, M.; Bereznev, S.; Lund, P.D.; Nasibulin, A.G. Adhesion of Single-Walled Carbon Nanotube Thin Films with Different Materials. *The Journal of Physical Chemistry Letters* **2020**, *11*, 504–509, doi:10.1021/ACS.JPCLETT.9B03552.
136. De Nicola, F.; Hines, P.; De Crescenzi, M.; Motta, N. Moth-Eye Effect in Hierarchical Carbon Nanotube Anti-Reflective Coatings. *Carbon* **2016**, *108*, 262–267, doi:10.1016/J.CARBON.2016.07.011.
137. Chiang, K.-T.; Lin, S.-H.; Ye, Y.-Z.; Zeng, B.-H.; Cheng, Y.-L.; Lee, R.-H.; Lin, K.-Y.A.; Yang, H. Leafhopper-Inspired Reversibly Switchable Antireflection Coating with Sugar Apple-like Structure Arrays. *Journal of Colloid and Interface Science* **2023**, *650*, 81–93, doi:10.1016/j.jcis.2023.06.179.
138. Boulanger, N.; Barbero, D.R. Nanostructured Networks of Single Wall Carbon Nanotubes for Highly Transparent, Conductive, and Anti-Reflective Flexible Electrodes. *Applied Physics Letters* **2013**, *103*, 021116, doi:10.1063/1.4813498.
139. Jin, Z.; Deng, Z.; Jia, H.; Yang, C.; Wang, Y.; Wu, H.; Zhu, S.; Yang, X. Preparation and Characterization of Superhydrophilic TiO<sub>2</sub>-SiO<sub>2</sub> Films for Double-Layer Broadband Antireflective Coating. *Journal of Porous Materials* **2024**, *31*, 1955–1964, doi:10.1007/S10934-024-01648-Y.
140. Lu, M.; Liu, Q.; Wang, Z.; Zhang, X.; Luo, G.; Lu, J.; Zeng, D.; Zhao, X.; Tian, S. Facile Preparation of Porous SiO<sub>2</sub> Antireflection Film with High Transmittance and Hardness via Self-Templating Method for Perovskite Solar Cells. *Materials Today Chemistry* **2023**, *29*, 101473, doi:10.1016/J.MTCHEM.2023.101473.



## Acknowledgements

I would like to express my sincere and boundless gratitude to my supervisor, Assoc. Prof. Sergei Bereznev, for seeing my potential to conduct this research and choosing me. I am grateful to him for his mentorship, wisdom, patience, empathy, and all-round help and support throughout this long and eventful journey.

I would like to express my sincere gratitude to the Head of the Department, Prof. Maarja Grossberg-Kuusik, for giving me the opportunity to carry out the research component of my PhD in the Department of Materials and Environmental Technology, as well as for her help, support, and empathy towards me during this difficult time, which coincided with my studies. I want to sincerely thank the Head of the Laboratory of Photovoltaic Materials, Prof. Marit Kauk-Kuusik, and all my other colleagues in the lab for their endless support, help, and faith in me throughout my studies. I am immensely grateful to fate for leading me to this lab and finding such wonderful colleagues. I am grateful to all my co-authors, but especially to Dr. Aarne Kasikov, Dr. Maksim Antonov, Dr. Mati Danilson, Dr. Olga Volobujeva, and Dr. Valdek Mikli for their contribution to this work and my development as a scientist. I would also like to thank Dr. Kaia Tõnsuaadu for her assistance with the FTIR measurements. I am grateful to our partners, Prof. Albert Nasibulin from Skolkovo Institute of Science and Technology and Prof. Tanja Kallio from Aalto University, for providing the SWCNTs that I used in this research.

I am grateful to the former Head of the Doctoral Educational Programme, Prof. Ilona Oja Acik, and its current Head, Dr. Mai Uibu, for their help and support in matters concerning the educational component of my doctoral studies. I am also thankful to Prof. Malle Krunks for her guidance at the doctoral seminars; this experience helped me to present orally at conferences. Additionally, I want to thank other PhD students, some of whom have become my friends, for the opportunity to share our common PhD sorrows and joys in a cozy atmosphere over a cup of tea, thereby supporting each other.

Finally, I would like to express my boundless gratitude to my dear friends. Without their support and understanding, despite the distance that separated me from most of them, I would not have been able to reach the end of this journey. I am grateful to fate for giving me each of you. I would like to express my special and most important gratitude to my husband, who steadfastly endured all the sorrows and joys of this path together with me. I am infinitely grateful to him that he always supported me in my endeavors and believed in me. I dedicate this dissertation to my parents who passed away prematurely. Without their inspiring example, I would not have become who I am today.

This research was supported by the Estonian Research Council under grants PRG1023 and TT13, by the Estonian Ministry of Education and Research GREENTECH project with grant number TK210, and by the project “Increasing the knowledge intensity of Ida-Viru entrepreneurship,” co-funded by the European Union. Additionally, the research was supported by the European Union through the European Regional Development Fund (ERDF) project ‘Center of Excellence’ under grant number TK141, and by the ERDF project Center of Technologies and Investigations of Nanomaterials NAMUR+ under grant number 2014-2020.4.01.16-0123. The mechanical measurement part of the work was supported within the frames of the MNHA22040 M-ERA.NET DuplexCER project. This work has been partially supported by ASTRA ‘TUT Institutional Development Programme for 2016-2022 “Graduate School of Functional Materials and Technologies” under grant number 2014-2020.4.01.16-0032’. The DoRa+ 1.1 travel scholarship, financed by the Archimedes Foundation, supported my participation at the international conference.

## Abstract

# Development of Silicon Oxynitride Nanocomposites with Single-Walled Carbon Nanotubes as Protective Coatings for Solar Cells

The importance of switching to alternative energy sources has been discussed for many years, but the current situation in Europe clearly illustrates the need for more serious actions aimed at developing new technologies and improving existing ones. Photovoltaic solar energy is one of the promising alternatives. However, environmental factors critically affect the operation and lifespan of solar cells (SCs). Additionally, the use of standard rigid glass protection is limited due to its substantial weight and inflexibility. In recent years, mainly polymer-based coatings have been considered as a possible alternative to glass. But this change is not simple, as such encapsulation coatings must meet all functional and protective requirements, and their manufacturing technology must be reliable, inexpensive, compatible with low temperatures, and scalable.

Liquid preceramic polymer perhydropolysilazane (PHPS) has great potential as a protective material due to its ability to transform into vitreous  $\text{SiO}_x\text{N}_y$  films using relatively simple and scalable technologies. Current state-of-the-art research and development recommends the use of PHPS-derived  $\text{SiO}_x\text{N}_y$  films as encapsulants for SCs and microelectronics due to their dielectric and high barrier properties against moisture, gases, and UV radiation, along with non-toxicity, very high thermal and chemical stability, and high optical transmittance. However, due to their inorganic nature, PHPS-derived films exhibit high mechanical hardness but lack elasticity, which negatively affects their application in some flexible technologies. Therefore, composite film technology appears promising as the selection of different fillers provides opportunities to improve the properties of the resulting  $\text{SiO}_x\text{N}_y$ /filler composite layers. Due to their outstanding mechanical properties, carbon nanotubes (CNTs) have established themselves as a promising reinforcing filler material in a number of different matrixes, including polymers. Moreover, the alignment or orientation of CNTs within a matrix material leads to anisotropy of coatings properties. Such composites based, on PHPS-derived films with CNTs, have not yet been prepared and studied.

The aim of this work was to develop current, state-of-the-art  $\text{SiO}_x\text{N}_y$  protective coatings derived from PHPS, combining them with single-walled (SW) CNTs in oriented nanocomposite structures. This work includes: (i) comparison of the influence of different low-temperature curing methods of PHPS on the compositional and morphological properties of single-layer and multi-layer  $\text{SiO}_x\text{N}_y$  matrix films; (ii) elaboration of the technology for the formation of horizontally oriented composite  $\text{SiO}_x\text{N}_y$ /SWCNT coatings in various configurations; and (iii) study of the compositional, morphological, optical, and mechanical properties, as well as the long-term stability of  $\text{SiO}_x\text{N}_y$  matrix films and  $\text{SiO}_x\text{N}_y$ /SWCNT nanocomposite coatings based on them.

In this work, thin PHPS-derived films were deposited on soda lime glass (SLG) or SLG/Molybdenum substrates using the spin-coating method. Curing was performed using two different low-temperature methods: (i) thermally induced curing at 180 °C for 60 min; and (ii) UV-assisted curing under irradiation from UV lamps (wavelengths 185 and 254 nm) for 40 min. The appropriate time for UV curing was determined experimentally. Multi-layer structures were obtained by cyclically repeating the routine deposition/curing stages. SWCNTs were synthesized by the aerosol chemical vapor

deposition method and were collected in the form of randomly oriented thin films with an approximate film thickness of 13–14 nm on filter paper.  $\text{SiO}_x\text{N}_y/\text{SWCNT}$  composite coatings were prepared in two configurations/architectures: (i) TOP, where the SWCNT film was dry transferred from filter paper to a spin-coated PHPS film; and (ii) BOTTOM, where the SWCNT film was dry transferred to the SLG and SLG/Mo substrates, followed by deposition of the PHPS layer. Then, laminate-type composites of both configurations were cured. Characterization of all studied samples was carried out using scanning electron microscopy (SEM) equipped with energy dispersive X-ray (EDX) spectroscopy, UV-Vis-NIR spectroscopy, X-ray photoelectron spectroscopy (XPS), Fourier transform infrared spectroscopy (FTIR), and spectroscopic ellipsometry (SE). A scratch test with progressive load on an universal materials tribo-test device was used to examine the behavior of prepared coatings under mechanical influence, with special attention to adhesive properties.

It was found that the method of PHPS curing dramatically affects the morphology and chemical composition of the resulting film. Thermal curing produced a uniform  $\text{SiO}_x\text{N}_y$  film with high residual nitrogen content. In contrast, UV-assisted curing led to the formation of a coating with a gradient of nitrogen distribution throughout the film cross-section (CS). Specifically, the thin top sub-layer (approximately 20 nm) of the UV-cured film was converted to  $\text{SiO}_2$ , with minimal traces of nitrogen, while in the buried layers of the film, the oxygen content decreased and the nitrogen content increased accordingly. These trends were also consistent for multi-layer films. According to SEM-EDX, XPS, and FTIR analyses, neither method resulted in the complete transformation of PHPS, but UV curing resulted in a more complete transformation toward  $\text{SiO}_2$  compared to thermal curing.

Based on the aim of the study, a simple and effective approach has been developed to produce oriented laminate-type  $\text{SiO}_x\text{N}_y/\text{SWCNT}$  composite coatings with different architectures. It was found that the filler does not affect the PHPS conversion process in either thermal curing or UV-assisted curing. The SWCNT film was compatible with the matrix film and did not lead to the formation of pores, cavities, or channels inside the  $\text{SiO}_x\text{N}_y$ , as visualized in SEM micrographs. Additionally, it did not affect the surface morphology of the composite coating, which remains very smooth. UV-Vis-NIR spectroscopy showed that the composite films cured by both methods had better transmittance than pure SWCNT films, indicating their potential as optical antireflection coatings, in addition to other promising applications in optoelectronics, microelectronics, etc. The observed antireflective effect is caused by two factors: (i) the introduction of SWCNTs into the  $\text{SiO}_x\text{N}_y$  matrix film; and (ii) the optical constants of the  $\text{SiO}_x\text{N}_y$  matrix film.

The major knowledge gap related to PHPS-derived films was their long-term stability. We studied the aging of prepared  $\text{SiO}_x\text{N}_y$  matrix films and  $\text{SiO}_x\text{N}_y/\text{SWCNT}$  composites at different time intervals after curing. It was found that all investigated samples tend to ripen from a  $\text{SiO}_x\text{N}_y$  composition to  $\text{SiO}_2$ , with varying dynamics depending on the curing method applied. With ripening, samples not only changed their chemical composition and morphology but also their optical and mechanical properties.

In order to study the optical properties of the  $\text{SiO}_x\text{N}_y$  matrix films and  $\text{SiO}_x\text{N}_y/\text{SWCNT}$  composite layers, the SE method was applied. Thermally as-cured  $\text{SiO}_x\text{N}_y$  films showed a high refractive index value of  $n_{355} = 1.6$ , reflecting relatively high nitrogen content. For the UV as-cured film, the nitrogen gradient in the CS resulted in a refractive index gradient, with values of  $n_{355} = 1.49$  near the surface and 1.58 closer to the film-substrate

interface. During the ripening process,  $\text{SiO}_x\text{N}_y$  layers cured by both methods showed a decrease in  $n$  values favoring the values attributable to  $\text{SiO}_2$ , and the evident  $n$  gradient in the CS of UV-cured samples disappeared. Thus, all studied films can be potentially applied as broadband antireflective coatings for a number of optical materials with  $n$  values above 1.5.

It was found that the adhesive properties of the deposited coatings and their behavior under mechanical influence are critically dependent on the curing method. Indeed, UV-cured matrix films and  $\text{SiO}_x\text{N}_y$ /SWCNT composites exhibited high hardness and excellent adhesion to the SLG/Mo substrate, maintaining these properties during the aging process. All thermally cured samples showed relatively lower adhesion of the  $\text{SiO}_x\text{N}_y$  film to the SLG/Mo substrate, as well as lower hardness and high plasticity. However, a week after curing, the behavior of the films became similar to that of UV-cured samples, increasing the critical load withstand value by three times. The introduction of SWCNTs into the  $\text{SiO}_x\text{N}_y$  matrix caused a visible reinforcing effect against the rupture of the composite coating.

In this work, composite thin films with horizontally oriented SWCNT filler inside a vitreous  $\text{SiO}_x\text{N}_y$  matrix derived from PHPS were obtained and studied for the first time. A strong relationship between the PHPS curing method and the composition, morphology, and optical and mechanical properties of the resultant films was found and illustrated. Thermal curing has been determined to be a less favorable method for converting PHPS to a highly reliable protective coating compared to UV-assisted curing. The data obtained regarding the optical properties indicate that  $\text{SiO}_x\text{N}_y$  matrix films and  $\text{SiO}_x\text{N}_y$ /SWCNT composites can function as broadband antireflective coatings. All cured films studied in this work demonstrated low coefficients of friction, which could be useful in applications where scratch protection and increased lubrication/sliding are of critical importance. All of the above-mentioned results show promising potential for further research and application of composite coatings based on PHPS matrix films with nanofillers.

## Lühikokkuvõte

# Üheseinaliste süsiniknanotorudega ränioksünitriidist nanokomposiitmaterjalide arendamine päikeseplatade kaitsekattedeks

Alternatiivsetele energiaallikatele ülemineku tähtsusest on räägitud pikka aega, kuid praegune olukord Euroopas näitab selget vajadust tõsisemate meetmete järele, mis on suunatud uute tehnoloogiate väljatöötamisele ja olemasolevate täiustamisele. Fotogalvaaniline päikeseenergia on üks võimalikest alternatiivenergiaallikatest. Keskkonnategurid mõjutavad aga kriitiliselt päikeseplatade tööd ja eluiga. Samal ajal on standardse jäiga klaasikaitse kasutamine piiratud selle suure kaalu ja paindumatusse tõttu. Viimastel aastatel on klaasile võimalikuks alternatiiviks peetud peamiselt polümeeripõhiseid katteid. Kuid see muudatus ei ole lihtne, kuna sellised kapseldatud katted peavad vastama kõigile funktsionaalsetele ja kaitseõuetele ning nende tootmistehnoloogia peab olema skaleeritav, töökindel, odav ja sobima madalate temperatuuridega.

Vedel eelkeraamiline polümeer perhüdropolüsilasaan (PHPS) omab suurt potentsiaali kaitsematerjali kandidaadina tänu oma võimele muutuda suhteliselt lihtsate ja skaleeritavate tehnoloogiate abil klaasjateks  $\text{SiO}_x\text{N}_y$  kiledeks. Praegune tipptasemel teadus- ja arendustegevus soovib PHPS-st saadud  $\text{SiO}_x\text{N}_y$  kilesid kasutada kapseldajatena päikeseplatade ja mikroelektronika jaoks. Need on sobilikud tänu oma dielektrilistele omadustele ning kaitsevõimekusele niiskuse, gaaside ja UV-kiirguse vastu, samuti tänu oma mittetoksilisusele, väga kõrgele termilisele ja keemilisele stabiilsusele ning kõrgele optilisele läbilaskvusele. Kuigi anorgaanilise olemuse tõttu on PHPS-st saadud kiledel kõrge mehaaniline kõvadus, puudub neil elastsus, mis mõjutab negatiivselt nende kasutamist painduvates tehnoloogiates. Selle probleemi võimalik lahendus on komposiitkilede tehnoloogia arendus, kuna erinevate täiteainete lisamine võimaldab parandada  $\text{SiO}_x\text{N}_y$ /täiteaine komposiitkihtide omadusi. Tänu oma silmapaistvatele mehaanilistele omadustele on süsinik-nanotorud (CNT) tõestanud end tugevdava täitematerjalina mitmesugustes maatriksites, sealhulgas polümeerides. Lisaks põhjustab CNT-de joondamine või orientatsioon maatriksmaterjalis katte omaduste anisotroopiat. Selliseid CNT-dega PHPS-st tuletatud kilede komposiite ei ole senini veel valmistatud ega uuritud.

Selle töö eesmärk oli välja töötada PHPS-ist tuletatud  $\text{SiO}_x\text{N}_y$  kaitsekatted, kombineerides neid orienteeritud nanokomposiitstruktuurides üheseinaliste (SW) CNT-dega. See töö hõlmab: (i) PHPS-i erinevate madaltemperatuursete kõvendamismeetodite mõju võrdlust ühe- ja mitmekihiliste  $\text{SiO}_x\text{N}_y$  maatrikskilede koostisele ja morfoloogilistele omadustele; (ii) erinevates konfiguratsioonides horisontaalselt orienteeritud komposiitkatete  $\text{SiO}_x\text{N}_y$ /SWCNT moodustamise tehnoloogia väljatöötamist; ja (iii)  $\text{SiO}_x\text{N}_y$  maatrikskilede ja nendel põhinevate  $\text{SiO}_x\text{N}_y$ /SWCNT nanokomposiitkatete koostise, morfoloogiliste, optiliste ja mehaaniliste omaduste ning pikaajalise stabiilsuse uuringuid.

Õhukesed PHPS-st tuletatud kiled kanti naatriumklaasile (SLG) või SLG/Mo alusele kasutades vurrkatmise ehk *spin coating* meetodit. Kõvendamiseks kasutati kahte erinevat madaltemperatuurset meetodit: (i) termiliselt indutseeritud kõvendamine 180 °C juures 60 minutit; ja (ii) UV-lampide kiirgusega kõvendamine (lainepikkusel 185 ja 254 nm) 40 minutit. Sobiv kõvendamisaeg UV-kiirguse jaoks määrati katseliselt.

Mitmekihilised struktuurid saadi korrates tsükliliselt sadestamise/kõvendamise etappe. SWCNT-d sünteesiti aerosoolide keemilisel sadestamisel aurufaasist meetodiga ja koguti filterpaberile juhuslikult orienteeritud õhukeste kiledena, mille paksus oli ligikaudu 13–14 nm.  $\text{SiO}_x\text{N}_y$ /SWCNT valmistati kahes konfiguratsioonis/arhitektuuris: (i) PEALMINE, kus SWCNT kile kanti kuivalt filterpaberilt PHPS-kilele; ja (ii) ALUMINE, kus SWCNT kile kanti kuivalt SLG ja SLG/Mo alustele, millele järgnes PHPS kihi sadestamine. Seejärel kõvendati mõlema konfiguratsiooni laminaat-tüüpi komposiidid. Kõikide uuritud proovide iseloomustamiseks kasutati skaneerivat elektronmikroskoopiat (SEM), mis oli varustatud energiadiispersiivse röntgen-mikroanalüsaatoriga (EDX), UV-Vis-NIR spektroskoopiat, röntgenfotoelektron-spektroskoopiat (XPS), Fourier' teisenduse infrapunaspektroskoopiat (FTIR) ja spektraalellipsomeetriat (SE). Kriimustuskatse, mille käigus rakendati progresseeruvat koormust kasutades universaalset tribomeetrit, viidi läbi valmistatud katte käitumise uurimiseks mehaanilise mõju all, pöörates erilist tähelepanu adhesiivsetele omadustele.

Leiti, et PHPS-i kõvendamise meetod mõjutab oluliselt saadud kile morfoloogiat ja keemilist koostist. Termiline kõvendamine andis tulemuseks ühtlase  $\text{SiO}_x\text{N}_y$  kile, millel oli kõrge jääklämmastiku sisaldus. Seevastu UV-kiirguse abil kõvendamise tulemusel moodustus kile, millel oli lämmastiku jaotuse gradient läbi kile ristlõike (CS). UV-kõvendatud kile õhuke ülemine kiht (ligikaudu 20 nm) koosnes  $\text{SiO}_2$ -st sisaldades minimaalselt lämmastiku jälgi, samas kui kile sisemistes kihtides vähenes hapniku sisaldus ja lämmastiku sisaldus suurenes vastavalt. Samad tulemused saadi ka mitmekihiliste kiledel puhul. EDX, XPS ja FTIR analüüside tulemuste näitasid, et kumbki meetod ei taganud PHPS-i täielikku muundumist. Siiski saavutati UV-kõvendamise tulemusel võrreldes termilise kõvendamisega oluliselt täielikum üleminek  $\text{SiO}_2$ -ks.

Uuringu eesmärgist lähtuvalt töötati välja lihtne ja tõhus meetod erineva arhitektuuriga orienteeritud laminaat-tüüpi  $\text{SiO}_x\text{N}_y$ /SWCNT komposiitkihtide valmistamiseks. Leiti, et täiteaine ei mõjuta PHPS-i konversiooniprotsessi ei termilisel ega ka UV-kõvendamisel. SEM analüüsi tulemused näitasid, et SWCNT-kile ühildub maatrikskilega ega põhjusta nähtavate pooride, õõnsuste ega kanalite moodustumist  $\text{SiO}_x\text{N}_y$  sees. Samuti ei mõjuta see komposiitkihi pinna morfoloogiat, mis jääb väga sile. UV-Vis-NIR spektroskoopiaga leiti, et mõlemal meetodil kõvendatud komposiitkiledel on parem läbilaskvus kui puhastel SWCNT kiledel. See näitab nende potentsiaali optiliste peegeldusvastaste kattekihtidena, lisaks teistele paljulubavatele rakendustele optoelektronikas, mikroelektronikas jne. Leiti, et täheldatud peegeldusvastast toimet põhjustavad kaks tegurit: (i) SWCNT-de lisamine  $\text{SiO}_x\text{N}_y$  maatrikskiledesse; ja (ii)  $\text{SiO}_x\text{N}_y$  maatrikskile optilised konstandid.

Peamine teadmiste puudujääk PHPS-ist tuletatud kiledel oli seotud nende pikaajalise stabiilsusega. Seega käesolevas töös uuriti valmistatud  $\text{SiO}_x\text{N}_y$  maatrikskiledel ja  $\text{SiO}_x\text{N}_y$ /SWCNT komposiitide vananemist erinevatel ajavahemikel pärast kõvenemist. Leiti, et kõik uuritud proovid muutuvad küpsemisprotsessi käigus  $\text{SiO}_x\text{N}_y$  koostisest  $\text{SiO}_2$ -ks. See protsess toimub erineva dünaamikaga sõltuvalt kasutatud kõvendusmeetodist. Küpsemise käigus muutusid proovidel nii nende keemiline koostis ja morfoloogia, kui ka optilised ja mehaanilised omadused.

$\text{SiO}_x\text{N}_y$  maatrikskiledel ja  $\text{SiO}_x\text{N}_y$ /SWCNT komposiitkihtide optiliste omaduste uurimiseks kasutati SE meetodit. Termiliselt kõvendatud  $\text{SiO}_x\text{N}_y$  kiled näitasid kõrget murdumisnäitaja väärtust  $n_{355} = 1,6$ , mis viitab suhteliselt kõrgele lämmastikusisaldusele. UV-kiirgusega kõvendatud kile puhul põhjustas lämmastikugradient kattekihi ristlõikes murdumisnäitaja gradiendi, mille väärtused olid  $n_{355} = 1,49$  pinna ja 1,58 kile-aluspinna

siirdeala lähedal. Küpsemisprotsessi käigus näitasid mõlemal meetodil kõvendatud  $\text{SiO}_x\text{N}_y$  kihid murdumisnäitaja langust  $\text{SiO}_2$ -le omistatavate väärtuste suunas ning UV-kõvendatud proovide ristlõikes esinenud murdumisnäitaja gradient kadus. Seega saab kõiki uuritud kilesid potentsiaalselt kasutada lairiba peegeldusvastaste kattekihtidena mitmesuguste optiliste materjalide jaoks, mille murdumisnäitaja väärtus on üle 1,5.

Leiti, et sadestatud katete adhesiivsed omadused ja nende käitumine mehaanilise mõju all sõltuvad kriitiliselt ka kõvendusmeetodist. UV-kõvendatud maatrikskiled ja  $\text{SiO}_x\text{N}_y$ /SWCNT komposiidid näitasid kõrget kõvadust ja suurepärast adhesiooni SLG/Mo aluspinnaga, säilitades need omadused ka vananemisprotsessi käigus. Termiliselt kõvendatud  $\text{SiO}_x\text{N}_y$  kiled näitasid nõrka adhesiooni SLG/Mo aluspinnaga, madalamat kõvadust ja kõrget plastilisust. Kuid nädal pärast kõvendamist muutus kilede käitumine sarnaseks UV-kõvendatud proovidega, suurendades kriitilise koormuse taluvusväärtust 3 korda. SWCNT-de lisamine  $\text{SiO}_x\text{N}_y$  maatriksisse tugevdas materjali struktuuri ning parandas komposiitkatte vastupidavust purunemisele.

Käesolevas töös valmistati ja uuriti esmakordselt PHPS-st tuletatud horisontaalselt orienteeritud SWCNT täiteainega klaasjaid  $\text{SiO}_x\text{N}_y$  komposiitkatteid. Tõestati tugev seos PHPS-i kõvendusmeetodi ja saadud kilede koostise, morfoloogia, optiliste ja mehaaniliste omaduste vahel. Leiti, et PHPS-i muutmisel ülikindlaks kaitsekatteks on UV-kiirgusega kõvendamise meetod võrreldes termilise kõvendamisega efektiivsem ja sobivam. Optiliste omaduste kohta saadud andmed näitavad, et  $\text{SiO}_x\text{N}_y$  maatrikskiled ja  $\text{SiO}_x\text{N}_y$ /SWCNT komposiidid võivad toimida lairiba peegeldusvastaste katetena. Kõikidel kõvendatud kiledel oli madal hõõrdeteguri väärtus, mis võib olla kasulik rakendustes, kus kriimustuskaitse ja määrimine/libisemine on kriitilise tähtsusega. Saadud tulemused näitavad, et nanotäiteainetega PHPS-maatrikskiledel põhinevad komposiitkatted omavad suurt potentsiaali edasiste teaduslike uuringute ja praktiliste rakenduste jaoks.

# Appendix 1

## Publication I

E. Shmagina, M. Danilson, V. Mikli, S. Bereznev, Comparative study of perhydropolysilazane protective films, *Surf. Eng.* 38 (2022) 769–777, <https://doi.org/10.1080/02670844.2022.2155445>.







## Comparative study of perhydropolysilazane protective films

Elizaveta Shmagina , Mati Danilson , Valdek Mikli and Sergei Bereznev

Department of Materials and Environmental Technology, School of Engineering, Tallinn University of Technology Tallinn, Estonia

### ABSTRACT

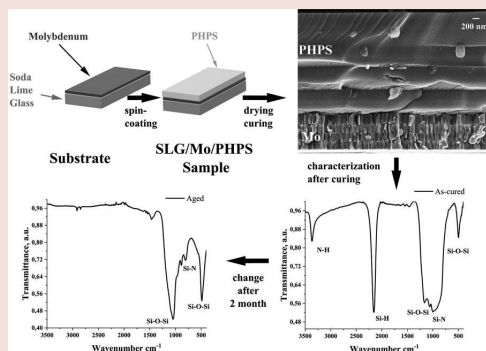
Silicon dioxide thin films are a promising alternative to protective glass in solar cells. In this work, one-layer and four-layer thin films of a perhydropolysilazane (PHPS) were spin-coated from solution in dibutyl ether and cured by exposure to moderate temperatures or ultraviolet (UV) light to obtain glassy SiO<sub>x</sub> layers. Optical and morphological properties as well as their long-term stability were studied using XPS, FTIR, UV-Vis spectroscopy, and SEM microscopy with EDX analysis. The results showed that the process of converting PHPS layers to SiO<sub>x</sub> continues after the completion of the curing procedure for both methods. However, the composition of the thermally cured films is similar to silicon oxide, while the UV-cured samples demonstrate a composition similar to silicon dioxide due to differences in the reactions occurring during the curing process. The prolonged transformation process opens up possibilities for creating self-improving protective coatings based on PHPS.

### ARTICLE HISTORY

Received 20 September 2022  
Revised 18 November 2022  
Accepted 1 December 2022

### KEYWORDS

PHPS; polysilazane; pre-ceramic; polymer; thermal; UV; curing; barrier; protective; coating



## Introduction

One of the most important bottlenecks for the photovoltaic (PV) technology is to ensure reliable protection of solar cells (SCs) from external factors because the environment can be very aggressive. Nowadays, glass is the main protective material used in PV technology. Nevertheless, the high weight, brittleness, and inflexibility limit the application of this protection significantly, especially for organic and aerospace PVs. For now, the most successful attempts to substitute cover glass have been with polymer-based coatings [1–4]. However, this task is not trivial; on the one hand, such coatings must combine low thickness, low water, and gas permeability rates, while on the other hand, the technology must be low-temperature, reliable, scalable, and inexpensive.

Coatings fabricated from an inorganic pre-ceramic polymer perhydropolysilazane have a composition similar to glass and can be considered a promising

alternative. The PHPS layers can be deposited by spin-coating, and after curing, it forms films with excellent optical and protective properties as well as strong adhesion to different substrates [5–7]. A precursor consisting of repeating monomer units – (SiH<sub>2</sub>–NH)– can be converted to SiO<sub>x</sub> in various ways, e.g. by hydrolysis in an aqueous solution of ammonia [8] or in a solution of hydrogen peroxide [9]. It should be noted, that the process is not fast; it takes up to 24 h and often leads to incomplete poly condensation of the PHPS precursor [10]. Pyrolysis both at sufficiently high temperatures around 600°C [2,10–14] and at moderate temperatures around 250°C is also used for curing [15]. Unfortunately, heating above 100°C is not always compatible with the production of devices based on thermosensitive materials. An alternative method is the photo-assisted conversion of PHPS in the presence of oxygen, where ultraviolet radiation with wavelengths shorter than

220 nm is used to break Si–N and Si–H bonds, followed by oxidation of the material to amorphous SiO<sub>x</sub> [1–3,6,11]. This value is defined by photon energies sufficient to break the covalent bonds between silicon and nitrogen in PHPS. An important advantage is the revealed absence of material shrinkage during curing due to oxygen saturation [16]. Just a slight heating of the samples up to 40°C was observed during the irradiation of the samples with UV lamps. Thus, this approach provides rapid, inexpensive, and low-temperature deposition of SiO<sub>x</sub> films in an industrial scale, which is extremely important for a wide range of applications. However, despite active study and optimization of that approach over the past 15 years, there is no unified algorithm to describe the UV conversion of PHPS.

This promising UV-assisted method has been successfully applied to encapsulate flexible perovskite SCs. A hybrid protective coating based on PHPS with CdSe/ZnS quantum dots has been fabricated to increase the photo conversion efficiency of the device due to the photoluminescence of the quantum dots and its lifespan in ambient conditions due to the use of PHPS as a final encapsulating coating [17].

In our studies, we focused our attention on the deposition of cross-sectionally uniform PHPS layers to create new protective coatings for solar cells using the promising UV-assisted technology. Still, according to the literature, the complete conversion of PHPS to SiO<sub>2</sub> can only be achieved by thermal curing [1]; therefore, as a reference, we used samples thermally cured according to the PHPS manufacturer recommendations. Thus, it is necessary to compare in detail the properties of the films obtained by thermal and UV curing methods and analyse their long-term stability; such a study has not been previously reported. In our work, we compared the morphology and composition of thin films obtained by the two main curing technologies of PHPS and studied the long-term stability of the produced films, which was not studied before.

## Materials and methods

### Preparation of the coatings

A commercially available 20% solution of PHPS in dibutyl ether (NN-120-20, durXtreme GmbH, Germany) was used for the thin film deposition. The films were prepared by spin-coating either onto the surface of a soda lime glass (SLG) or onto a SLG coated with molybdenum (SLG/Mo) substrate. Before the deposition, the substrates were washed in an ultrasonic bath for 5 min in isopropanol and then in a 20% Decon 90 solution (Decon Laboratories Ltd, England). Next, the substrates were washed in Millipore water followed by drying under a flow of dry nitrogen

of 99.995% purity. The PHPS solution was deposited on the surface of the cleaned substrates by spin-coating at 2000 rpm for 1 min (Chemat Technology spin-coater KW-4A). Then, the solvent residuals were evaporated on a hot plate at 40°C for 2 min. After that, the prepared SLG/PHPS and SLG/Mo/PHPS structures were subjected to a curing process, which was carried out in two different ways. In the first case, the samples were cured in a muffle furnace (XD-14S, Zhengzhou Brother Furnace CO LTD, China) at 180°C for 60 min. In the second case, the samples were irradiated with UV light with wavelengths of 185 and 254 nm simultaneously in air (Novascan UV/Ozone cleaning system). The distance between the samples and the UV lamps was 15 mm. The curing time was chosen to be 40 min based on experimental and literature data [1]. Using the curing techniques described above, both single-layer and four-layer films were prepared. Multi-layer structures were obtained by cyclic repeating of the deposition/drying/curing stages.

### Characterization

To confirm the optical properties of the obtained films, transmittance spectra were measured by a UV-Vis-NIR spectrophotometer (UV-1800, Shimadzu Corp., Japan) in the 200–1100 nm wavelength range for samples onto SLG substrates.

To determine the degree of transformation of the PHPS films into SiO<sub>2</sub> after curing and control of the presence of the intermediate compounds and functional groups, the samples were studied using Fourier transform infrared spectroscopy (FTIR). The spectrometer that was used makes measurements by the attenuated total reflection (ATR) technique in the range of 400–4000 cm<sup>-1</sup> with a resolution of 4 cm<sup>-1</sup> (Platinum-ATR Alpha FT-IR spectrometer, Bruker Optic GmbH, Germany).

X-ray photoelectron spectroscopy (XPS) (Kratos Axis Ultra<sup>DLD</sup> XPS System, England) was used to study the chemical composition of the surface and near-surface layers of the prepared films. The films were studied using a monochromatic Al KαX-ray source (1486.6 eV) with a resolution of about 0.68 eV and with a switched-on system for compensating the accumulated charge on the sample. The energy scales of the spectra were charge-corrected according to the position of the O1s peak at 532.6 eV in the scale of the binding energy (BE).

The surface and cross-sectional morphology of the obtained samples and the thickness of the cured films were studied using high resolution-scanning electron microscopy (HR-SEM) (ZEISS Ultra 55, Germany) with an accelerating voltage from 5 kV. To eliminate the low-conductivity effect, the films were covered with an Au 80%-Pd 20% thin layer that was

approximately 1 nm thick by using the radio frequency sputtering technique. To study the composition of the films, a Bruker Esprit 1.82 energy dispersive X-ray (EDX) spectroscopy system was used at a 15 kV accelerating voltage and for X-ray Line-scan 5 kV was used.

## Results and discussion

### Single-layer films

HR-SEM was applied to study the morphology of the single-layer films obtained by both curing methods of PHPS on the SLG/Mo substrates (Figure 1(a,b)). Deposited and cured films showed a dense and uniform morphology both on the surface and in the cross-section views. Usually, for a 20% PHPS solution and a substrate rotation speed of 2000 rpm during spin-coating, the expected film thickness is about 600 nm according to studies using polyethylene terephthalate (PET), polycarbonate, and silicon wafers as the substrates [5,11]. In our studies, the thermally and UV-cured films were determined to be 460 and 350 nm thick, respectively. It is noteworthy that

similar measurements of PHPS/SLG samples demonstrated the film thickness for both curing methods to be in the range of 550–580 nm, which is in good agreement with the literature data. The decrease in thickness of films on the Mo/SLG substrate can be caused by the higher wettability of the molybdenum surface by the PHPS solution in dibutyl ether vs. the surface of the above-mentioned substrates.

It should be noted that the window coatings of the SCs must be transparent in the operating wavelength range of the device. Our films showed high transmittance (near 90%) in the visible wavelength range, which is in good agreement with the data published in the literature [6,17,18].

The positions and intensities of the characteristic bands in the IR spectra of the samples were compared and analysed. The transformation of the PHPS can be considered complete if the bands corresponding to the Si–N, Si–H, and N–H bonds completely disappear in the spectrum and only the peaks related to the Si–O bonds remain [11].

Figure 1(c,d) shows a comparison of the ATR-FTIR spectra of the UV cured vs. the thermally cured samples. Both spectra show, in general, a similar set

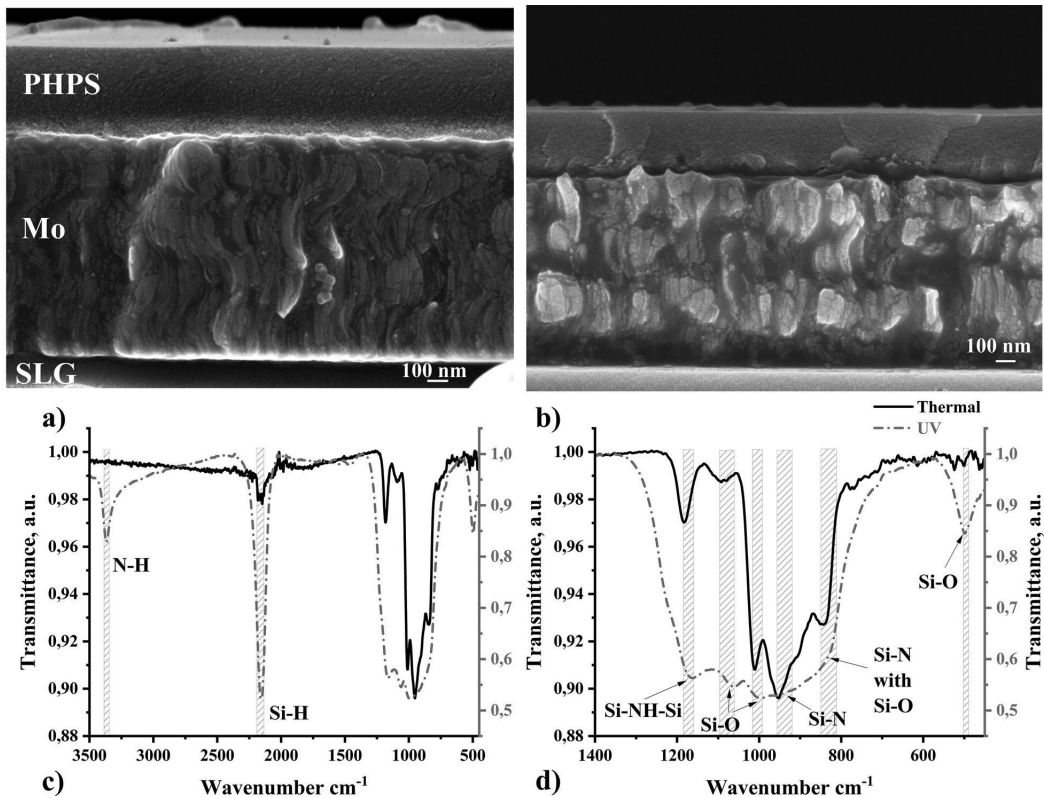


**Figure 1.** Cross-sectional HR-SEM images of PHPS/Mo/SLG samples cured thermally (a) and under UV light irradiation (b); ATR-FTIR spectra of samples (c) where the black curve is for the thermally cured film and the grey curve is for the UV cured film, (d) enlarged area of the ‘fingerprints’.

of characteristic bands, which differ greatly in the peak intensities. In the thermally cured film spectrum in the area of the ‘fingerprints’, a slight shift was observed in the positions of the peaks towards higher wavenumbers relative to the spectrum of the UV cured film (Table 1). A similar behaviour in the position of the band responsible for the transverse optical (TO) mode of the antisymmetric stretching vibrations of Si–O has already been described previously [2]. For a quartz-like structure of silicon with a bond angle of  $144^\circ$ , the vibrational band is located at about  $1065\text{ cm}^{-1}$ . A shift in the position to higher wavenumbers up to  $1140\text{ cm}^{-1}$  indicates the formation of a cage-like structure with larger bond angles up to  $150^\circ$ . The reactions responsible for the conversion of PHPS to  $\text{SiO}_2$  under UV light irradiation and temperature exposure are different [1], which leads to the formation of films with relatively different structures.

Absorption bands around  $3370$  and  $1170\text{ cm}^{-1}$  could be assigned to N-H stretching and bending vibrations, and a sharp peak near  $2160\text{ cm}^{-1}$  belongs to Si-H stretching vibrations [19,20]. The spectral region from  $830$  to  $1100\text{ cm}^{-1}$  has many closely spaced characteristic bands; the overlap of these bands complicates the bond assignments of these peaks [21]. Peaks located near  $950$  and  $840\text{ cm}^{-1}$  are related to the Si–N stretching vibrations [11]. The peaks related to the Si–O located near  $1005$ ,  $830$ , and  $500\text{ cm}^{-1}$  could be assigned to stretching, bending, and rocking vibrations, respectively [22,23]. The spectra show strong peaks related to the bonds with N and H, indicating incomplete conversion for both curing methods used. Thus, the films have the composition  $\text{SiO}_x\text{N}_y$  rather than  $\text{SiO}_2$ . However, this can be regarded as an advantage because the presence of nitrogen should increase protective properties and transparency of the films [24].

The XPS technique was used to more precisely study the near-surface (2–4 nm) composition of the films (Figure 2). For both samples, the O 1s, Si 2s, and 2p peaks are dominant in the spectra. The presence of residual N in the films for both curing methods was confirmed. However, for the thermally cured film, its concentration is noticeably higher. The Si 2p peak of the thermally cured film deconvolutes into three components, which indicates the morphological diversity of the film [25]. The peak around  $100.01\text{ eV}$  belongs to elemental silicon [26]. Two remaining peaks at  $101.55$  and  $102.83\text{ eV}$  refer to Si–

N bonds in  $\text{SiO}_x\text{N}_y$  and Si–O bonds in  $\text{SiO}_x$ , respectively [27,28]. The positions of these peaks shift depending on the content of N and O in the film, and the composition of the films, in general, can vary in the range from  $\text{Si}_3\text{N}_4$  to  $\text{SiO}_2$ . A stronger shift in the position of the last peak towards higher binding energies indicates that the film is more O-rich [26]. The decomposition of the Si 2p peak for the UV-cured film is simpler and consists of a single Si–O peak at the  $103.01\text{ eV}$  position, which indicates a higher O concentration in the film and better conversion compared to the first sample. The presence of a carbon peak in the spectra is associated with the contact of the film surface with air and the presence of carbon-containing impurities from the solvent of PHPS [15].

Based on the elemental analysis data, the relative O to Si ratios in the cured films were calculated excluding N. Near-surface layers of the sample cured by UV light were completely converted to silicon dioxide ( $\text{SiO}_{2.05}$ ), while upper layers of the thermally cured sample showed a composition close to that of silicon oxide ( $\text{SiO}_{0.96}$ ).

Also, the depth profile of the samples can be determined using XPS. However, due to the dielectric nature of the prepared films, a constant positive charging occurs in the sample during the long-term measurements, which cannot be compensated. Therefore, the results obtained by measuring the depth profile should be perceived qualitatively, not quantitatively. We measured both samples after 720 and 1320 s of etching in argon plasma, which resulted in an etching depth of no more than 12 and 22 nm, respectively. The measurements showed a stable O, Si, and N content across the depth for the thermally cured film, while after 1320 s, the UV-cured film showed a significant decrease in the O content with a simultaneous increase in the Si and N content. These measurements confirm the formation of a compositionally heterogeneous PHPS film after UV curing, which is in good agreement with other publications [1,6,11].

In addition, the cured films were studied using EDX analysis to determine the overall composition (Table 2). In the measurements, the elemental composition is averaged over the entire thickness of the films, which is confirmed by the presence of Mo in the results (Mo excluded from Table 2). The O content vs. Si is around two times higher for the UV-cured sample vs. the thermally cured sample. This indicates a more complete conversion of the film cured under UV light irradiation to  $\text{SiO}_2$ . This result is supported by the more significant difference in the intensities of the bands related to Si–O bonds in the ATR-FTIR spectra of the UV-cured sample compared with the intensity of the comparable peaks in the spectra of the thermally cured one.

**Table 1.** Displacements of the band positions in the ATR-FTIR spectra for one-layer thermally and UV cured samples.

Sample	Bonds and their spectral positions, $\text{cm}^{-1}$				
	Si–N	N–H	Si–O	Si–O	Si–O
Thermalcuring	2162	1183	1091	1010	501
UV curing	2160	1163	1062	996	499



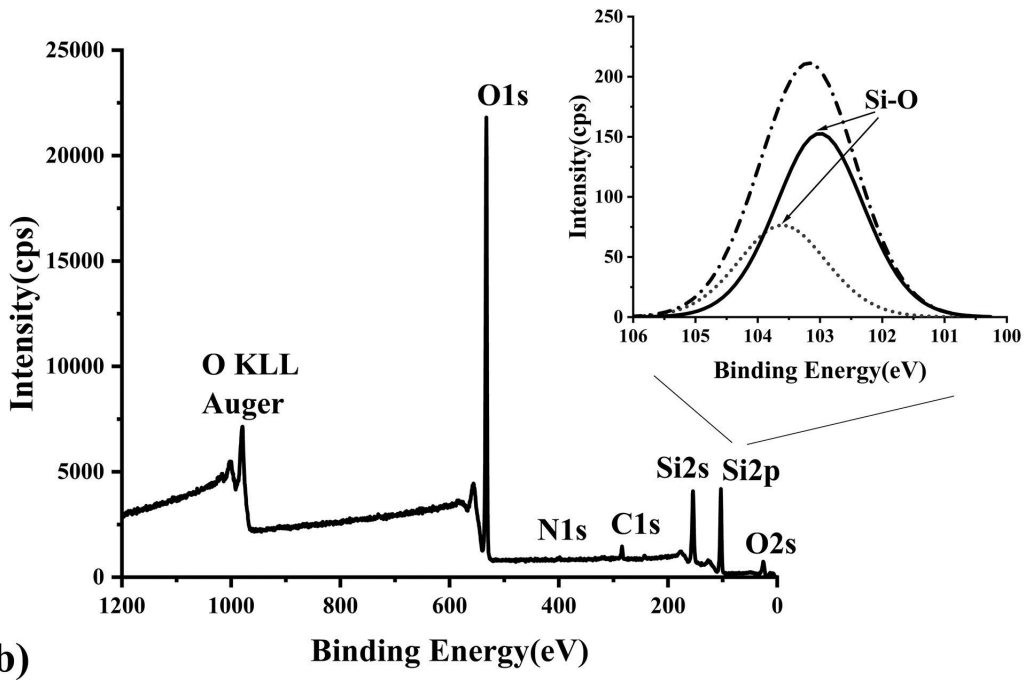
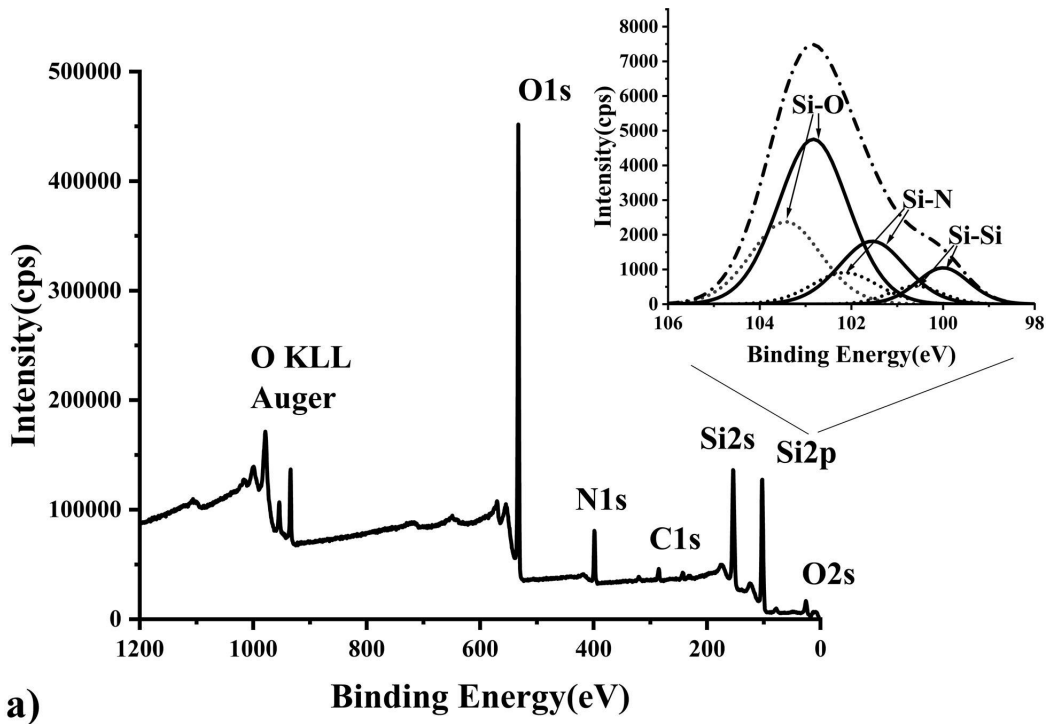


**Figure 2.** XPS spectra of near-surface layers with enlarged Si 2p peaks of the PHPS/Mo/SLG samples cured (a) thermally (b) under UV light irradiation.

**Table 2.** Thickness-averaged elemental atomic concentrations of thermally cured and UV cured PPHPs/Mo/SLG films measured by EDX.

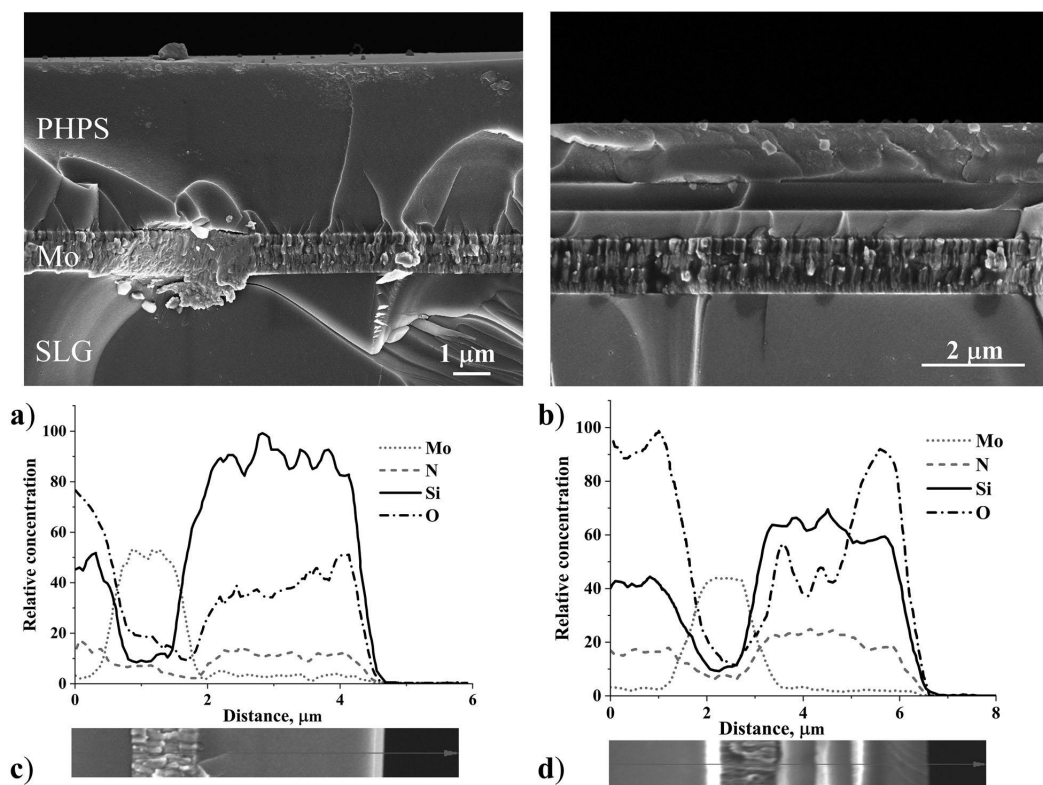
	Thermally cured, at.-%	UV cured, at.-%
Silicon	14.3	17.3
Oxygen	26.4	64.3
Nitrogen	59.3	18.4

### Multi-layer films

The single-layer films obtained above may be rather thin for some potential applications, and improvement of the protective properties of the films obtained by sequential deposition of several PPHPs layers was also reported [2,16]. The cross-section morphology of the deposited four-layer films was studied using HR-SEM (Figure 3(a,b)). As seen from the micrographs, the thermally cured film is the thickest (around 4.5  $\mu\text{m}$ ), while the UV-cured film has a thickness around 2.5  $\mu\text{m}$ . It is noteworthy that in the micrograph of the UV cured film (Figure 3(b)), 4 layers of PPHPs deposition are visually distinguishable and the third- and fourth-layers merged into one. Each layer is about 600 nm thick. This clearly illustrates the heterogeneous transformation of the film during UV curing.

The films with 4 layers were also studied using ATR-FTIR spectroscopy. In that case, the shape of the spectra of the thermally and UV-cured samples is better matched, which is in contrast to the single-layer samples. A slight shift in the positions of some peaks in the area of the fingerprints discussed for the single-layer films is also observed. In the spectrum of a thermally cured sample in the higher wavenumber region, the peak of N-H vibrations is completely absent.

The thickness of the multi-layer samples was sufficient for the line-scan EDX analysis of the cross-section of the films (Figure 3(c,d)). In the thermally cured sample (Figure 3(c)), the Si content fluctuates around the average value, which is much higher relative to the O, while the oxygen content increases closer to the film surface. For the UV-cured sample (Figure 3(d)), the Si content also fluctuates around the average value. But, instead of smoothly growing, the curve illustrating the O content in the sample shows three clearly distinguishable stand-alone peaks that can be associated with the film sub-layers, visually identified in the cross-sectional SEM image of the sample. The O content in the first two sub-layers is relatively low; however, in

**Figure 3.** Cross-sectional HR-SEM micrographs of PPHPs/Mo/SLG films obtained from four deposition/drying/curing cycles for (a) thermal curing or for (b) UV curing; (c) and (d) Line-scan HR-SEM EDX measurements of the films, respectively.

the top layer, it grows strongly vs. the Si content. This confirms the XPS data related to the complete conversion of the near-surface layers of the film to  $\text{SiO}_2$ . An increase in the O content as it approaches the edge of the film in both samples may indicate the penetration of O into the samples after the end of the curing process. Thus, it can be assumed that both curing methods are insufficient in completing the transformation process of PHPS into  $\text{SiO}_2$ , and the films seem to 'ripen' after its completion (see § 3.3).

### Change in the film composition over time

To study the hypothesis formulated in the previous section, single-layer and four-layer samples were studied using ATR-FTIR spectroscopy immediately after curing as well as after ageing in a desiccator at room temperature (RT) for two months.

Figure 4(a,c) shows the spectra of the single-layer samples. For both curing methods, there is a strong difference between the spectra of the as-cured and aged films. The change in the positions of the peaks makes it difficult to relate the spectra to each other. In the spectrum of the aged thermally cured sample (Figure 4(a)), there is a significant increase in the

intensity of the bands attributable to Si-O compared to the rest of the peaks. But, the Si-N peak has the highest intensity. A broad intense band located from  $800$  to  $1200\text{ cm}^{-1}$  in the spectrum of the as-cured UV film (Figure 4(c)) changed its shape and intensity after ageing. The spectrum of the aged film is dominated by an intense Si-O peak at about  $1048\text{ cm}^{-1}$ , and the Si-O band at about  $485\text{ cm}^{-1}$  also increased its intensity relative to the entire spectrum. It is noteworthy that the N-H and Si-H peaks in the higher wavenumber region completely disappeared after ageing of the film, which indicates an almost complete transformation of the aged coating into  $\text{SiO}_2$ .

Figure 4(b,d) shows the ATR-FTIR spectra of the four-layer PHPS films. The shape of the spectra demonstrates relatively smaller changes as a result of ageing. In the spectrum of the thermally cured sample (Figure 4(b)), the relative intensity of the Si-O peaks increased; however, the Si-N peak remained the most intense, which indicates the formation of a film with a high residual N content. More noticeable changes occurred in the spectrum of the UV-cured sample (Figure 4(d)); analogous to the single-layer sample in the higher

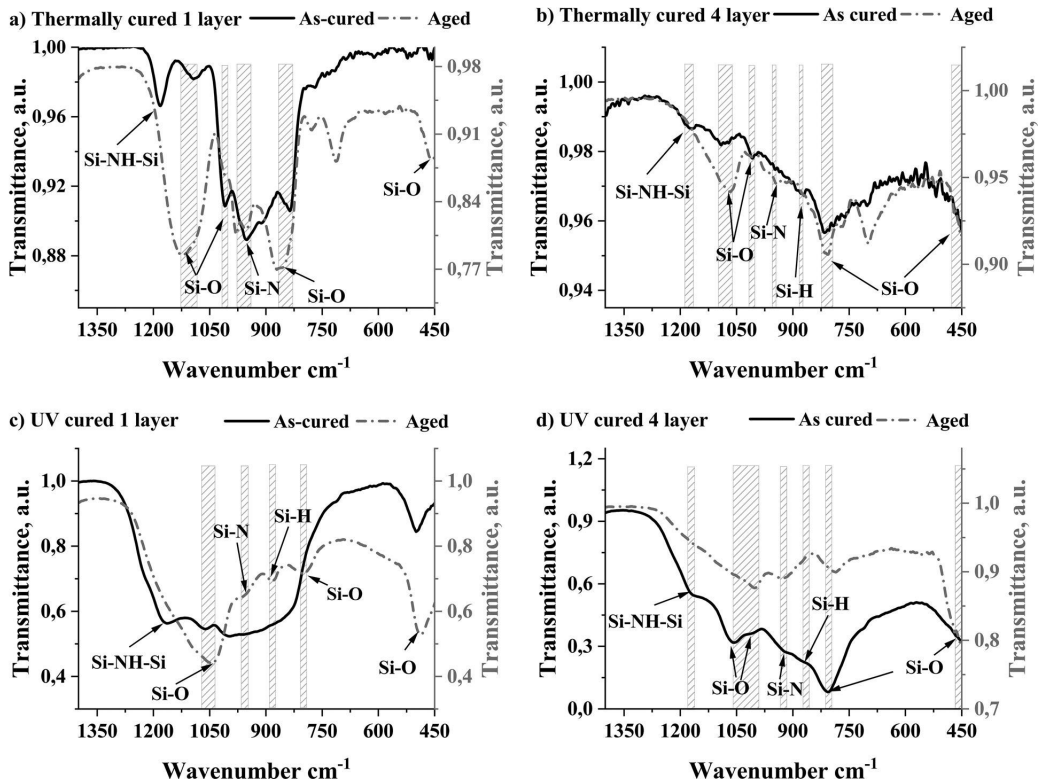


**Figure 4.** ATR-FTIR spectra of the (a), (b) thermal cured or (c), (d) UV cured samples; black lines are for as cured samples, and grey lines are for aged samples.



wavenumber region, the N–H and Si–H bands disappeared, and the relative intensity of the Si–O peaks in the smaller wavenumber region became higher, thereby making them as dominant in the spectrum of the aged sample.

Thus, the results of the ATR-FTIR spectra analysis of aged samples confirm our assumption that the films obtained by both curing methods are not completely transformed and continue to ‘ripen’ after the end of the conventional curing procedure. Evaluation of the dynamics of this process requires a more detailed study of the films after the completion of the conventional curing accompanied with elaboration of the more effective curing process, e.g. combination of the thermal and UV-curing for the single and multi-layer PHPS.

## Conclusions

One-layer and four-layer thermally and UV-cured thin films based on PHPS were prepared and comparatively studied with special attention to the morphology and compositional analysis of the obtained structures.

The thickness of the one-layer films did not exceed 600 nm, while the maximum thickness of the four-layer films was around 4.5  $\mu\text{m}$ . ATR-FTIR spectroscopy showed a shift in the Si–O peak positions in the layers cured by different methods, which indicates the formation of films with different structures. The presence of bonded N and H peaks in the spectra of the as-cured samples showed the formation of silicon oxynitride films with different concentrations of elements. Results showed the formation of the O-poor film for the thermal curing method and the O-rich film after UV curing. However, the UV cured film is not uniform over the cross-section, i.e. the process of complete conversion of the obtained PHPS layers to  $\text{SiO}_2$  is not finished. On the other hand, it was found that ‘ageing’ of the prepared films in a desiccator at RT significantly improves the compositional uniformity to  $\text{SiO}_2$ . This opens up possibilities for creating self-improving protective coatings based on PHPS. The presence of residual bonded N in the films can have a positive effect on the protective and optical properties of the films. However, for the industrial use, precise control of the concentration of N is necessary for the reproducibility of the coating properties. Thus, this opens up opportunities for a more detailed study of the ‘ripening’ dynamics of films and further optimization of the curing methods.

## Acknowledgements

The authors thanks Kaia Tõnsuaadu for her help with the ATR-FTIR measurements.

## Disclosure statement

No potential conflict of interest was reported by the author(s).

## Funding

This research was supported by the European Union through the European Regional Development Fund (ERDF) project “Center of Excellence” under [grant number TK141]; by ERDF project Centre of Technologies and Investigations of Nanomaterials NAMUR+ under [grant number 2014-2020.4.01.16-0123]; NAMUR+ core facility funded by the Estonian Research Council under [grant number TT13] and by the Estonian Research Council under [grant number PRG1023]. This work has been partially supported by ASTRA ‘TUT Institutional Development Programme for 2016-2022 ‘Graduate School of Functional Materials and Technologies’ under [grant number 2014-2020.4.01.16-0032]’.

## ORCID

Elizaveta Shmagina  <http://orcid.org/0000-0001-5525-5324>

Mati Danilson  <http://orcid.org/0000-0001-8105-6812>

Valdek Mikli  <http://orcid.org/0000-0002-2406-3562>

Sergei Bereznev  <http://orcid.org/0000-0001-6156-7738>

## References

- [1] Prager L, Dierdorf A, Liebe H, et al. Conversion of perhydropolysilazane into a  $\text{SiO}_x$  network triggered by vacuum ultraviolet irradiation: access to flexible, transparent barrier coatings. *Chem – Eur J*. 2007;13(30):8522–8529. doi:10.1002/CHEM.200700351.
- [2] Prager L, Helmstedt U, Herrnberger H, et al. Photochemical approach to high-barrier films for the encapsulation of flexible laminary electronic devices. *Thin Solid Films*. 2014;570:87–95. doi:10.1016/J.TSF.2014.09.014.
- [3] Kim D, Jeon GG, Kim JH, et al. Design of a flexible thin-film encapsulant with sandwich structures of perhydropolysilazane layers. *ACS Appl Mater Interf*. 2022;14(30):34678–34685. doi:10.1021/acsami.2c06699.
- [4] Wang Y, Ding G, Mao JY, et al. Recent advances in synthesis and application of perovskite quantum dot based composites for photonics, electronics and sensors. *Sci Technol Adv Mater*. 2020;21(1):278–302. doi:10.1080/14686996.2020.1752115.
- [5] Zhan Y, Grottenmüller R, Li W, et al. Evaluation of mechanical properties and hydrophobicity of room-temperature, moisture-curable polysilazane coatings. *J Appl Polym Sci*. 2021;138(21):50469. doi:10.1002/APP.50469.
- [6] Ohishi T, Yamazaki Y. Formation and gas barrier characteristics of polysilazane-derived silica coatings formed by excimer light irradiation on PET films with vacuum evaporated silica coatings. *Mater Sci Appl*. 2016;8(1):1–14. doi:10.4236/MSA.2017.81001.
- [7] Niizeki T, Nagayama S, Hasegawa Y, et al. Structural study of silica coating thin layers prepared from perhydropolysilazane: substrate dependence and water penetration structure. *Coatings*. 2016;6(4):64. doi:10.3390/COATINGS6040064.
- [8] Kubo T, Kozuka H. Conversion of perhydropolysilazane-to-silica thin films by exposure to vapor from

- aqueous ammonia at room temperature. *J Ceram Soc Jpn.* 2006;114(1330):517–523. doi:10.2109/jcersj.114.517.
- [9] Lee JS, Oh JH, Moon SW, et al. A technique for converting perhydropolysilazane to SiO<sub>x</sub> at low temperature. *Electrochem Solid State Lett.* 2010;13(1):II23–II25. doi:10.1149/1.3264092.
- [10] Morlier A, Cros S, Garandet JP, et al. Thin gas-barrier silica layers from perhydropolysilazane obtained through low temperature curings: a comparative study. *Thin Solid Films.* 2012;524:62–66. doi:10.1016/j.tsf.2012.09.065.
- [11] Morlier A, Cros S, Garandet JP, et al. Structural properties of ultraviolet cured polysilazane gas barrier layers on polymer substrates. *Thin Solid Films.* 2014;550:85–89. doi:10.1016/j.tsf.2013.10.140.
- [12] Funayama O, Tashiro Y, Kamo A, et al. Conversion mechanism of perhydropolysilazane into silicon nitride-based ceramics. *J Mater Sci.* 1994;29(18):4883–4888. doi:10.1007/BF00356538.
- [13] Kozuka H, Nakajima K, Uchiyama H. Superior properties of silica thin films prepared from perhydropolysilazane solutions at room temperature in comparison with conventional alkoxide-derived silica gel films. *ACS Appl Mater Interf.* 2013;5(17):8329–8336. doi:10.1021/am400845y.
- [14] Kim S-D, Ko P-S, Park K-S. Perhydropolysilazane spin-on dielectrics for inter-layer-dielectric applications of sub-30 Nm silicon technology. *Semicond Sci Technol.* 2013;28(3):035008, doi:10.1088/0268-1242/28/3/035008.
- [15] Günthner M, Pscherer M, Kaufmann C, et al. High emissivity coatings based on polysilazanes for flexible Cu(In,Ga)Se<sub>2</sub> thin-film solar cells. *Sol Energy Mater Sol Cells.* 2014;123:97–103. doi:10.1016/j.solmat.2014.01.027.
- [16] Channa IA, Distler A, Zaiser M, et al. Thin film encapsulation of organic solar cells by direct deposition of polysilazanes from solution. *Adv Energy Mater.* 2019;9(26):1900598. doi:10.1002/aenm.201900598.
- [17] Kim J, Jang JH, Kim J-H, et al. Inorganic encapsulation method using solution-processible polysilazane for flexible solar cells. *ACS Appl Energy Mater.* 2020;3(9):9257–9263. doi:10.1021/ACSAEM.0C01593.
- [18] Wang D, Ma J, Li P, et al. Flexible hard coatings with self-evolution behavior in a low earth orbit environment. *ACS Appl Mater Interfaces.* 2021;13(38):46003–46014. doi:10.1021/acsaami.1c13807.
- [19] Rossi S, Deflorian F, Fedel M. Polysilazane-based coatings: corrosion protection and anti-graffiti properties. *Surf Eng.* 2018;35(4):343–350. doi:10.1080/02670844.2018.1465748.
- [20] Zhu J, Shen G, Jiang W, et al. The preparation and properties study of novel hydrophobic/superhydrophobic coatings based on fluorine modified perhydropolysilazane. *J Dispers Sci Technol.* 2021. doi:10.1080/01932691.2021.1974871.
- [21] Chen N, Reaja-Jayan B, Liu A, et al. ICVD cyclic polysiloxane and polysilazane as nanoscale thin-film electrolyte: synthesis and properties. *Macromol Rapid Commun.* 2016;37(5):446–452. doi:10.1002/MARC.201500649.
- [22] Shokri B, Firouzjah MA, Hosseini SI. FTIR analysis of silicon dioxide thin film deposited by metal organic-based PECVD. In *Proceedings of 19th international symposium on plasma chemistry society*; Bochum, Germany; 2009. p. 26–31.
- [23] Derrick MR, Stulik D, Landry JM. *Infrared spectroscopy in conservation science.* Los Angeles (CA): The Getty Conservation Institute; 1999.
- [24] Shi Y, He L, Guang F, et al. A review: preparation, performance, and applications of silicon oxynitride film. *Micromachines (Basel).* 2019;10(8):552, doi:10.3390/mi10080552.
- [25] Major GH, Fairley N, Sherwood PMA, et al. Practical guide for curve fitting in X-ray photoelectron spectroscopy. *J VacSci Technol A: Vac, Surf Films.* 2020;38(6):061203, doi:10.1116/6.0000377.
- [26] Akkaya A, Boyarbay B, Etin HC, et al. A study on the electronic properties of SiO<sub>x</sub> N<sub>y</sub> /p-Si interface. *Silicon.* 2018;10:2717–2725. doi:10.1007/s12633-018-9811-6.
- [27] Moulder JF, Stickle WF, Sobol PE, et al. *Handbook of X-Ray photoelectron spectroscopy.* In: Chastain J, editor. Perkin-Elmer corporation. Eden Prairie: Physical Electronics Division; 1992.
- [28] NIST X-ray Photoelectron Spectroscopy (XPS) Database, Version 3.5. [cited 2022 Sep 19]. Available from: <https://srdata.nist.gov/xps/Default.aspx>.



## Appendix 2

### Publication II

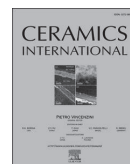
E. Shmagina, O. Volobujeva, A.G. Nasibulin, S. Bereznev, Fabrication of novel SiOxNy/SWCNT laminate-type composite protective coating using low-temperature approach, *Ceram. Int.* 50 (2024) 34312–34320, <https://doi.org/10.1016/j.ceramint.2024.06.250>





Contents lists available at ScienceDirect

Ceramics International

journal homepage: [www.elsevier.com/locate/ceramint](http://www.elsevier.com/locate/ceramint)

# Fabrication of novel SiO<sub>x</sub>N<sub>y</sub>/SWCNT laminate-type composite protective coating using low-temperature approach

Elizaveta Shmagina<sup>a,\*</sup>, Olga Volobujeva<sup>a</sup>, Albert G. Nasibulin<sup>b</sup>, Sergei Bereznev<sup>a</sup>

<sup>a</sup> Department of Materials and Environmental Technology, School of Engineering, Tallinn University of Technology, Ehitajate tee 5, 19086, Tallinn, Estonia

<sup>b</sup> Skolkovo Institute of Science and Technology, Nobel Str., 3, 121205, Moscow, Russian Federation

## ARTICLE INFO

Handling Editor: P. Vincenzini

### Keywords:

Carbon nanotube network  
Perhydropolysilazane  
Transparent thin films  
Nanocomposite coating

## ABSTRACT

Multifunctional thin films are becoming extremely popular in many technological fields. An increase in their functionality can be achieved by the creation of nanocomposite structures. This study represents novel thin composite coatings with a horizontally oriented single-walled carbon nanotube (SWCNT) filler inside a silicon oxynitride (SiO<sub>x</sub>N<sub>y</sub>) matrix obtained by (i) low-temperature thermal curing or by (ii) UV radiation-induced curing. The SiO<sub>x</sub>N<sub>y</sub>/SWCNT composite structures were prepared by simple dry transfer of a SWCNT film into a perhydropolysilazane (PHPS) polymer matrix film deposited by the spin-coating technique followed by curing. The structural, morphological, and optical properties of the SiO<sub>x</sub>N<sub>y</sub>/SWCNT composite films were studied using HR-SEM/EDX, ATR-FTIR, and UV–Vis spectroscopy. It was found that SWCNT films were uniformly transferred into the PHPS matrix, maintaining their horizontally oriented close-packed structure, and avoiding the problem of agglomeration, thereby forming a laminate-type composite. SWCNTs had no effect on the curing process of the PHPS matrix. The SWCNT concentration remained relatively low, resulting in highly transparent composite films. An antireflection effect in the composite film relative to the transmission of the SWCNT film was observed. The results indicate that SiO<sub>x</sub>N<sub>y</sub>/SWCNT composites are attractive for applications as protective, antireflective optical coatings.

## 1. Introduction

Modern photonic and electronic technologies are moving towards miniaturization, increasing efficiency, and overcoming factors limiting their wider use. The limitations are frequently related to providing adequate, often multifunctional, protection from a number of factors. Key requests are flexibility, gas barrier, corrosion, heat and mechanical protection, depending on the needs of the devices being implemented. Reality imposes restrictions on maintaining production scalability, economic profitability, and environmental friendliness. In this regard, polymer-derived ceramic (PDC) technology has become increasingly popular among scientists due to its high potential for industrial applications [1,2].

Perhydropolysilazane (PHPS) is a member of a large family of silicon-containing liquid pre-ceramic polymers. Its molecular skeleton consists only of a chain of Si and N atoms, with H atoms as substituents. PHPS has gained great popularity among researchers in recent years [3–6]. The increased interest is caused by the ability of this polymer to

transform, depending on conditions, into vitreous inorganic SiO<sub>x</sub> or SiO<sub>x</sub>N<sub>y</sub> films (and after pyrolysis to ceramics) that demonstrate a wide range of attractive properties [7–9]. The key ones are non-toxicity, variability in film thickness (from decades of nanometers to microns), relatively simple methods of thin film deposition and curing, and the scalability of the entire coating formation process from laboratory to industrial-scale production. Transformation of PHPS to SiO<sub>x</sub> or SiO<sub>x</sub>N<sub>y</sub> thin films or so-called curing occurs by hydrolysis in an oxygen and/or moisture atmosphere and can be induced in various ways [10]. Low-temperature curing technologies are very promising because of their compatibility with heat-sensitive materials that are now widely used. Therefore, the most promising and studied methods of PHPS transformation are thermal curing (at temperatures below 200°C) and curing under vacuum UV irradiation ( $\lambda < 200$  nm) [11,12]. It should be noted that broad comparative study of the both curing methods was reported in our previous study for the first time [13]. Table 1 shows the main data of the properties of PHPS-derived films cured by two above mentioned methods, which we obtained in our previous research [13].

\* Corresponding author.

E-mail addresses: [elshma@taltech.ee](mailto:elshma@taltech.ee), [lizakoritsa@gmail.com](mailto:lizakoritsa@gmail.com) (E. Shmagina), [olga.volobujeva@taltech.ee](mailto:olga.volobujeva@taltech.ee) (O. Volobujeva), [A.Nasibulin@skol.tech](mailto:A.Nasibulin@skol.tech) (A.G. Nasibulin), [sergei.bereznev@taltech.ee](mailto:sergei.bereznev@taltech.ee), [sergei.bereznev@gmail.com](mailto:sergei.bereznev@gmail.com) (S. Bereznev).

<https://doi.org/10.1016/j.ceramint.2024.06.250>

Received 26 February 2024; Received in revised form 13 June 2024; Accepted 18 June 2024

Available online 18 June 2024

0272-8842/© 2024 Elsevier Ltd and Techna Group S.r.l. All rights are reserved, including those for text and data mining, AI training, and similar technologies.

**Table 1**  
Main properties of PHPS-derived films after curing by two different methods.

Properties	Thermal curing	UV curing
Thickness, nm	~460	~350
Surface composition by XPS (atomic ratio)	SiO <sub>0.96</sub> N <sub>0.18</sub>	SiO <sub>2.05</sub> N <sub>0.06</sub>
Changes of surface composition after Ar plasma etching (approximately 20 nm) in XPS chamber	No changes	Trend to decrease in O Trend to increase in Si and N
FTIR main Si–O peak position, cm <sup>-1</sup>	1091 (bond angles 150°)	1062 (bond angles 144°)
Compositional uniformity through the thickness	Uniform	Non-uniform
Transmittance in visible range, %	≥95	≥95

Summarizing the findings, we can say that the method of curing the PHPS dramatically affects the morphology and chemical composition of the resulting film. Thermal curing results in the formation of a uniform, oxygen-depleted film. On the other hand, UV-assisted curing leads to the formation of a coating with a gradient of chemical composition through the film cross-section. Indeed, the thin surface layer of the UV-cured film is converted to silicon dioxide with minimal traces of nitrogen, but in buried layers of the film, the relative concentration of oxygen decreases, and the concentration of nitrogen increases accordingly. All this should affect the optical and mechanical properties of the cured films. Thus, it can be assumed that changing the curing parameters makes it possible to change the properties of the coatings based on PHPS [13].

High optical transmittance makes PHPS-derived films promising for use in optics. Due to their mechanical properties, the coatings are compatible with flexible technologies [14]. PHPS based SiO<sub>x</sub>N<sub>y</sub> films are actively used as encapsulants (e.g., for solar cells) because of their very high barrier properties against moisture and gases [15]. Their dielectric properties can be effectively used in different electronic devices such as transistors, etc. [16]. In addition, SiO<sub>x</sub>N<sub>y</sub> films have very high thermal and chemical stability, as well as anti-corrosion properties, which makes them promising for the protection of steel and other metals [4,17]. Also, PHPS-derived films demonstrate excellent adhesion to various materials, such as plastic, glass, and even cellulose-based films [18,19]. However, some disadvantages occur. Due to their inorganic nature, PHPS-derived films have high mechanical hardness but limited elasticity, which negatively affects the possibility of application in some flexible technologies [9,20].

One of the common ways to improve the properties of a number of materials is to combine them with another material and obtain a composite that joins the best properties of both components [21–24]. Composites with nanocarbon materials as fillers are especially popular due to the wide range of unique properties of carbon allotropic forms [25–28]. Carbon nanotubes (CNTs), which can be presented as one (single-walled, SWCNT) or multiple (multi-walled, MWCNT) seamlessly rolled sheets of graphene, are one of these forms. CNTs have outstanding optical and mechanical properties, as well as high thermal conductivity. These properties are determined by the diameter-to-length ratio of the tubes, chirality, which determines the type of CNT (metallic or semi-conducting), defects, and functionalization of the tube surface. Due to their physical, chemical, and biological properties, as well as the ability to form a wide variety of structures from bundles and fibers to films while having a very low weight, these tubes have found an extremely wide range of applications in completely different fields [29–31].

Possessing a high elastic modulus and extremely high strength, CNTs have established themselves as a promising reinforcing material in some polymer and metal matrices. Among other things, they can influence the matrix's thermal and structural properties [32–35]. However, for CNTs and nanomaterials of other forms, agglomeration is a problem when introducing them into a matrix. In addition, the improvements mentioned above depend on the initial characteristics of the tubes themselves, their interfacial interaction with the matrix, and their

alignment [36]. Random dispersion of CNTs into a polymer matrix often leads to less effective results [36]. In contrast, the alignment of CNTs within a matrix material leads to anisotropy of properties. Anisotropy can also be achieved by creating a laminate type of composite in which the filler layer alternates with layers of matrix material [37].

The idea of influencing the mechanical properties of PDC by creating a composite with CNTs is not new [2]. Moreover, although CNTs have high thermal stability, the preparation of composites with ceramics is still difficult due to the high pyrolysis temperatures of the matrix, which can exceed 1000 °C. Such high temperatures lead to degradation of the properties of CNTs. The disadvantages of this technological approach also include the long time required for cross-linking and pyrolysis of ceramics (about 7 h), which adversely affects the industrial potential of the method [1,38]. However, new methods for producing coatings based on polysilazanes and their relatively low-temperature curing technology may open up new opportunities for creating a variety of composites with CNT fillers without losing their unique properties.

In this work, for the first time, we propose a simple low-temperature technique to obtain thin, highly transparent, protective films based on PHPS with embedded, well packed and horizontally oriented, SWCNT filler. Such anisotropic composites could improve the durability of the coating compared to SiO<sub>x</sub>N<sub>y</sub> films and extend their potential for use in solar cells and other optoelectronic devices. Thin SWCNT films were introduced into the PHPS matrix film by a simple dry transfer method, avoiding liquid chemistry purification and the tube agglomeration problems. The composites were cured by low-temperature annealing or irradiation under UV light. The structural, morphological, and optical properties of the composite coatings prepared in different laminate configurations were studied using Fourier transform infrared spectroscopy (FTIR), high-resolution scanning electron microscopy with energy dispersive X-ray spectroscopy system (HR-SEM/EDX), and ultraviolet–visible (UV–Vis) spectroscopy techniques.

## 2. Materials and methods

A commercially available 20 % solution of PHPS in dibutyl ether (NN-120-20, durXtreme GmbH, Germany) was used as the matrix material for thin film formation. Layers were deposited by using a Polos SPIN 150i programmable spin-coater at a rotational speed 2000 rpm for 60 s. Soda-lime glass (SLG) and SLG coated with a 1 μm thick molybdenum layer (SLG/Mo) were used as substrates depending on the requirements of the characterization method. Curing of thin films was performed by low-temperature methods: thermally induced at 180 °C for 60 min or under the irradiation of UV lamps (185 and 254 nm) for 40 min. The experimental details of the spin-coating and curing of PHPS thin films were described in more detail in our previous study [13].

SWCNTs were obtained by the aerosol (floating catalyst) chemical vapor deposition (CVD) method using ferrocene vapor as a catalyst precursor for iron nanoparticles formation and CO as a carrier gas and carbon source for nanotubes growth. SWCNTs with an average diameter of 2 nm and a low fraction of metallic impurities grown in the gas phase of a high temperature reactor (more than 800 °C) by CO decomposition on formed iron catalyst nanoparticles were collected downstream in the form of randomly oriented thin films on a filter paper [39]. Detailed information related to the material characterization can be found elsewhere [40].

SiO<sub>x</sub>N<sub>y</sub>/SWCNT composite coatings were formed in two configurations: “top” and “bottom”. In the “top” case, the SWCNT film was transferred from paper to a spin-coated and dried PHPS film using dry transfer. In the “bottom” configuration, the SWCNT film was transferred to the substrate (SLG or SLG/Mo), followed by deposition of the PHPS layer. Then, composites of both configurations were cured thermally (180 °C, 1 h) in a Brother HD-14S oven or under UV irradiation (40 min) in a Novascan digital UV ozone system in exactly the same way as reported for pure PHPS films in our previous work [13]. Appropriate adhesion of the SWCNT film to the cleaned Mo was achieved after



treating the Mo surface with acid vapor from 40 % aqueous HF solution for 10 min.

High transparency is a key requirement for optical coatings. For the SLG-based samples, UV–Vis transmittance, absorbance and reflectance spectra were measured by a spectrophotometer (UV-1800, Shimadzu Corp., Japan) in the 280–1100 nm wavelength range with subtraction of the substrate contribution from the transmittance and absorbance measurement results.

Fourier transform infrared spectroscopy (FTIR) is the main method used to study the degree of PHPS film transformation after the curing procedure. A Platinum-ATR Alpha (Bruker Optic GmbH, Germany) spectrometer equipped with an attenuated total reflection (ATR) module was used for that purpose. To avoid the contribution of the SLG signal to the spectra, the Mo-coated glass substrates were used. The measurements were carried out in the range of 400–4000  $\text{cm}^{-1}$  with a resolution of 4  $\text{cm}^{-1}$ . For each sample, a minimum of 4 measurements were taken at different points to control the uniformity of layers and avoid possible “random” fluctuations. The practically identical spectra were then averaged into one.

The thickness, surface, and cross-sectional morphology of the obtained layers on both substrates were studied using high-resolution scanning electron microscopy (HR-SEM, Zeiss Merlin, Germany) with an accelerating voltage of 4 kV. To eliminate the low-conductivity effect, the samples were covered with a 1 nm Au 80%-Pd 20 % layer using the radio frequency sputtering technique. To study the composition of the films, an energy dispersive X-ray (EDX) spectroscopy system was used at a 10–15 kV accelerating voltage (Bruker EDX-XFlash6/30 detector). Samples only on Mo/glass substrates were used for EDX measurements to study the composition throughout the thickness of the films and avoid the influence of SLG.

A Horiba LabRam HR800 spectrometer equipped with a multi-channel CCD detection system in the backscattering configuration was used for the Raman studies of SWCNTs. The second harmonic (532 nm) of a solid-state Nd:YAG laser with a spot size of 5  $\mu\text{m}$  was applied for excitation of the scattering. To achieve more accurate results, the spectra were recorded at a minimum of 4 different areas of the sample surface

and then averaged. Measurements were carried out in the range from 55 to 1700  $\text{cm}^{-1}$ .

### 3. Results and discussion

#### 3.1. SWCNT films

Initially, films were formed on the surface of a filter paper and then cut to obtain pieces of any size and shape. The morphology of deposited SWCNT films was studied using HR-SEM. The micrographs show that the nanotubes compose a uniform, thin, close-packed film (Fig. 1a and b).

Also, the SWCNT layers were studied by Raman spectroscopy (Fig. 1c). The enlarged area of the spectrum in the region of small wavenumbers illustrates the so-called radial breathing mode (RBM) region. These peaks are caused by synchronous radial vibrations of carbon atoms perpendicular to the axis of the nanotube. These peaks are a sign that clearly indicates SWCNTs [41].

The D peak ( $\sim 1350 \text{ cm}^{-1}$ ) indicates the presence of defects in the tube structure: the lower the intensity of this peak, the fewer defects in the tubes. To estimate the level of defects, it is possible to use the ratio of the intensities of the G peak to the D peak. In our case, this value is 16, which indicates the high quality of the SWCNTs [42,43].

The G-peak located at  $1591 \text{ cm}^{-1}$  corresponds to the tangential stretching of carbon-carbon bonds in the plane. It is observed in the spectra of any carbon structures with  $\text{sp}^2$  hybridization [44]. In the spectra of SWCNTs, this peak is split into two closely spaced subpeaks of different intensities due to the twisting of the graphene sheet. Nanotube defects also affect the splitting and broadening of the G-peak. In the case of a large number of defects, it becomes wider and splits into more than two subpeaks [41]. In our case, the shape of this peak confirms the high quality of the SWCNTs.

High transmittance in the visible spectral region is a key requirement for optical coatings. Also, some materials require protection from UV radiation because it is often harmful to them due to its high energy. Therefore, absorption in this region of the spectrum is an advantage for a protective coating. The absorbance spectra of SWCNTs (Fig. 1d) show

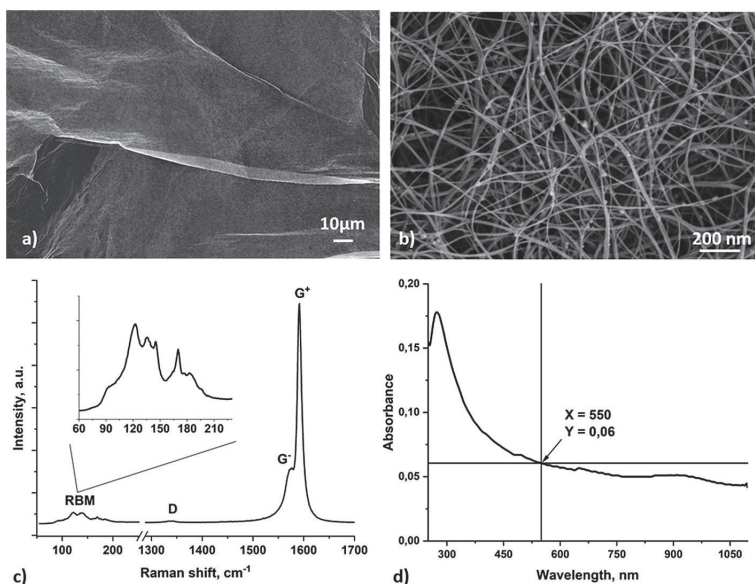


Fig. 1. (a) and (b) HR-SEM images of SWCNT film with different magnifications, (c) Raman spectrum of a SWCNT film with an enlarged region of radial breathing modes, (d) optical absorption spectrum of a SWCNT film on a glass substrate with an absorbance of 0,06 at a wavelength of 550 nm (at the middle of visible wavelength range).



fairly high transmittance in the visible wavelength range, with a characteristic absorption peak in the nearest UV region, which is caused by the  $\pi$  plasmons absorption [31]. Peaks corresponding to the second electronic excitation in semiconductor ( $S_{22}$ ) and metal ( $M_{11}$ ) tubes are not visible in the spectrum, which is caused by doping of SWCNT film by environmental species [45]. The optical transmission of SWCNT films depends on their thickness. Based on the measured absorbance value of 0.06 at a wavelength of 550 nm (Fig. 1d) multiplied by a correlation coefficient of 239, the thickness of the SWCNT film can be calculated to be approximately 14 nm [46,47].

### 3.2. $\text{SiO}_x\text{N}_y/\text{SWCNT}$ composite films

Our previous results showed that when using different PHPS curing methods, the resulting  $\text{SiO}_x\text{N}_y$  film has different contents of nitrogen and oxygen. It is known that it is possible to change the film's optical and electrical properties by changing the composition of the  $\text{SiO}_x\text{N}_y$  layer [48]. This leads to an expansion of the range of possible applications of these films and the possibility of adjusting their properties depending on the final requirements. Therefore, we continue to use both curing methods in our research.

To prepare  $\text{SiO}_x\text{N}_y/\text{SWCNT}$  composite films, SWCNTs can be transferred either on top of the spin-cast PHPS layer or directly onto the SLG substrate, followed by spin-coating of the PHPS layer onto the SWCNT layer. In some cases, we used glass coated with a 1  $\mu\text{m}$  thick layer of molybdenum as a substrate. This substrate is required for more accurate

ATR-FTIR and EDX measurements of deposited  $\text{SiO}_x\text{N}_y$  and  $\text{SiO}_x\text{N}_y/\text{SWCNT}$  films to eliminate parasitic signals from the glass. Moreover, a comparison of the adhesion and morphology of the nanocomposite coatings on the different surfaces is recommended. SWCNT films demonstrate different adhesion to the surfaces of different materials [49]. When transferring a SWCNT film onto cleaned Mo, the adherence of the SWCNT layer is poor. To overcome this, we used a dry process of fluorination of the Mo surface under hydrofluoric acid (HF) vapors for 300 s. This made it possible to change the surface properties of the Mo substrate. After this treatment, the SWCNT film was easily transferred onto the Mo surface, and then it could be covered with a layer of PHPS by the spin-coating technique. A shorter processing time of treatment with HF was not sufficient to change the surface properties of Mo and thus did not allow successful transfer.

A total of 4 types of single-layer samples were studied. There were two curing methods for composite films (UV radiation-induced or thermal), and the order of the layer formation (laminar architecture) for the final composite films differed. During the formation of the "bottom" architecture, the SWCNT film was transferred to the surface of the substrate (Mo or SLG) and then filled with a layer of PHPS. In the case of the "top" architecture, SWCNTs were transferred to a dried but not cured PHPS layer. The study of these two architectures was necessary to evaluate the result of SWCNTs transfer to a hard (SLG and SLG/Mo) and soft (PHPS) substrate. This made it possible to evaluate the interaction of the SWCNT film with the matrix as a result of transfer, including the orientation of the SWCNTs inside the matrix and the effect

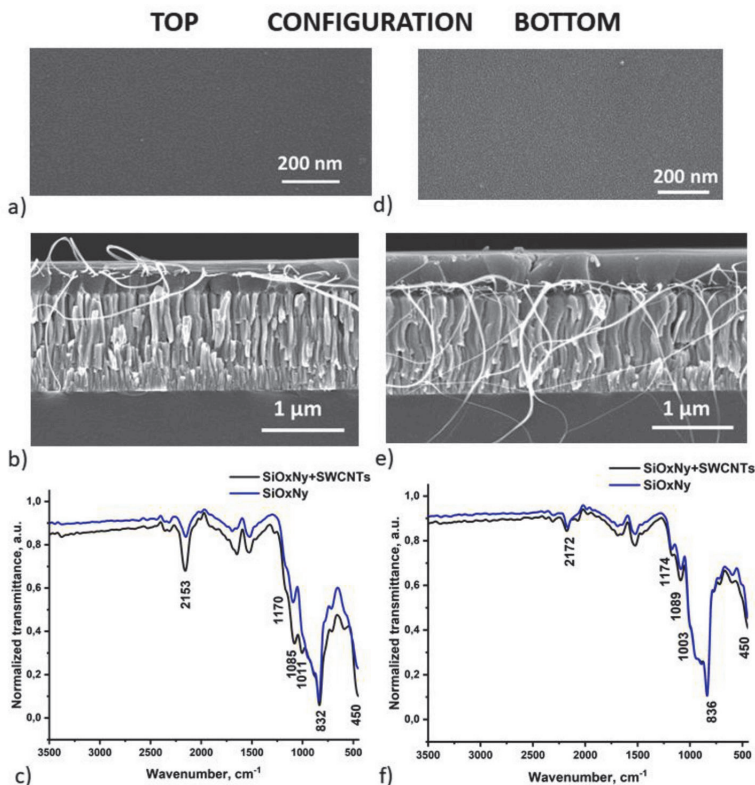


**Fig. 2.** HR-SEM images of  $\text{SiO}_x\text{N}_y/\text{SWCNT}$  composite film architecture "top": (a) surface, (b) cross-section. (c) ATR-FTIR spectra of the "top" sample were measured in the area with SWCNTs (black curve) and in the area without SWCNTs (blue curve). HR-SEM images of sample "bottom": (d) surface and (e) cross-section; (f) ATR-FTIR spectra of sample "bottom". All measurements performed for samples on Mo/glass substrates. (For interpretation of the references to colour in this figure legend, the reader is referred to the Web version of this article.)

of the filler on the surface smoothness of the  $\text{SiO}_x\text{N}_y$ .

### 3.2.1. Thermally cured $\text{SiO}_x\text{N}_y$ /SWCNT samples

As described above, PHPS/SWCNT structures of the “top” and “bottom” configurations were thermally cured at 180 °C for 1 h to prepare  $\text{SiO}_x\text{N}_y$ /SWCNT composite films.

We examined the surface morphology of the prepared samples as well as their cross-sections using HR-SEM (Fig. 2 a, b, d, e). For both “top” and “bottom” architectures, the surface of the cured samples is mainly uniform, without any noticeable pores. Only with very high magnification, it is possible to see some inhomogeneity points with its minor presence (Fig. 2a, d). The cross-sectional micrographs show that in the case of the “top” architecture, the thickness is around 400 nm and the SWCNT film is predominantly located in the upper part of the matrix and does not penetrate into its depth. For the “bottom” configuration, the thickness is 480 nm and the trend is the opposite. It should be noted that in both cases, the SWCNT film continues to be densely packed in cross-section after entering the coating matrix. The micrographs also show that the SWCNTs protrude beyond the edge of the matrix film (Fig. 2 b and e). This is caused by crashing the sample to obtain a cross-section and illustrates the high mechanical properties of the SWCNTs used.

FTIR spectroscopy is one of the key techniques for studying PHPS-derived films. It allows us to determine the degree of conversion of the polymer into a  $\text{SiO}_x\text{N}_y$  film and its structure.

In order to study the possible influence of the SWCNT filler film on the conversion of the PHPS matrix material, only half of the total area of the PHPS layer was filled with the SWCNT film (for both “top” and “bottom” configurations). Thus, each sample consisted of a region representing only pure  $\text{SiO}_x\text{N}_y$  and an area with filler embedded in the  $\text{SiO}_x\text{N}_y$  matrix. The FTIR spectra were measured at several points in both regions and then averaged into one curve per region. As can be seen from the comparisons of the spectra in Fig. 2 c and f, in the case of thermal curing, the SWCNT film (black curves) did not have any effect on the shape of the spectra for both sample architectures studied. Small differences in the film thickness cause minor differences in intensity. Also, differences in sample architecture did not affect the spectra. In all four spectra, peaks already typical for thermal curing stand out [13]. Peaks in the region of 1500–1700  $\text{cm}^{-1}$  may be caused by residual traces of dibutyl ether, the solvent for PHPS as well as by contamination of atmospheric carbon [50,51].

There is no peak in the spectra near 3380  $\text{cm}^{-1}$ , which is responsible for stretching vibrations of N–H bonds. That indicates densification of the film during the curing process [52]. This is a typical feature of thermally cured PHPS films. The medium-intensity peak caused by the bending vibrations of N–H bond is clearly visible near 1174  $\text{cm}^{-1}$  [19]. The peaks near 2160  $\text{cm}^{-1}$  are caused by stretching vibrations of the Si–H bond [53]. The region from 1000 to 800  $\text{cm}^{-1}$  is replete with closely spaced and, therefore, overlapping peaks of vibrations of different bonds of silicon with nitrogen, hydrogen, and oxygen [7]. Therefore, this area looks like one wide absorption band with a certain number of distinguishable peaks that do not greatly facilitate their analysis but allow us to conclude that these chemical elements are present in the film after the curing procedure. Si–N stretching vibrations bands located near 950 and 840  $\text{cm}^{-1}$  [54].

Peaks near 1087, 1007, 834, and 450  $\text{cm}^{-1}$  are caused by different vibration modes of the Si–O bond [14]. The peak near 830  $\text{cm}^{-1}$  overlaps the peaks of other bond vibrations, which does not allow its analysis. As in our previous work [13], the position of the first of the listed peaks is shifted towards the higher wavenumbers. This peak is caused by the transverse optical (TO) mode of asymmetric stretching vibrations of the bond, and its shift indicates the formation of a cage-like structure with a bond angle of 150° [55].

The peaks of silicon-oxygen bonds are the most intense in all the spectra. This indicates a high degree of PHPS conversion. However, the signals of nitrogen and hydrogen are also present in all measured

spectra, which indicates the formation of a silicon oxynitride film.

Table 2 and S1 show the results of the EDX elemental analysis of the  $\text{SiO}_x\text{N}_y$ /SWCNT composite films on Mo/glass substrate from surfaces. However, these data must be considered mainly qualitative since the limiting factor of this measurement technique is its sensitivity to the atomic weight of the elements (relatively low accuracy for the light elements determination). Hydrogen is below the sensitivity limits of EDX, so we cannot determine its concentration inside the film. However, we can make some remarks regarding the concentration of the carbon filler within the matrix material. From Table 2 and S1, it can be seen that the contribution of SWCNTs to overall carbon content is non-detectable by EDX, i.e., very low. These traces of carbon belong to solvent residues, which are also detected in the FTIR spectra. It should be noted the decrease of the carbon content in UV-cured  $\text{SiO}_x\text{N}_y$ /SWCNT films of both configurations. This effect is connected with strong UV irradiation of prepared layers with the wavelength of 185 nm in presence of oxygen accompanied with formation of ozone and oxidation of the organic residues in the cured films [53].

Based on the data obtained, we can conclude that novel composites of different laminate configurations were successfully obtained using our proposed methods. We found that the filler in the form of a horizontally oriented SWCNT film is successfully transferred by dry transfer to both hard and soft substrate surfaces. The filler does not have a significant effect on the composition of the  $\text{SiO}_x\text{N}_y$  matrix film. The SWCNT film retains its orientation after transfer to the matrix and does not agglomerate both in the case of transfer to a hard surface (SLG or Mo) or to a soft surface (uncured PHPS). It remains densely packed and does not affect the surface properties of the  $\text{SiO}_x\text{N}_y$  coating. The filler concentration is low throughout the entire volume of the matrix. The filler does not form new chemical bonds with PHPS.

### 3.2.2. Samples cured under UV radiation

An alternative to the thermally induced transformation process of PHPS is curing induced by exposure of the formed film to UV radiation. We used the optimal parameters (40 min under UV lamps with wavelengths of 185 and 254 nm at a distance of 15 mm) that we selected in our previous study [13].

The surface of these  $\text{SiO}_x\text{N}_y$ /SWCNT composite layers on Mo/SLG substrate (Fig. S1) and on SLG substrate (Fig. S2 a) looks the same as that of the thermally cured ones. In the cross-section (Fig. 3 b, c, f and Fig. S2 b), the SWCNT distribution within the matrix shows the trends observed for thermally cured composite samples.

Based on the absorption spectrum of SWCNTs (Fig. 1 d), it can be assumed that they can affect the curing process when embedded in the PHPS matrix because their absorption peak is in the UV region of the spectrum and the spectrum of the matrix film also contains an absorption peak in the near-UV region (Fig. 4). This can be clarified by studying the FTIR spectra of samples of both architectures (Fig. 3 d, g). For these purposes, just as in the case of thermally cured samples, only half of the total area of each sample was covered with a SWCNT film.

As in the case of thermally cured samples, we did not see a significant difference between the spectra measured in the area of pure  $\text{SiO}_x\text{N}_y$  (purple curves in Fig. 3 d, g) and the spectra measured in the area of the composite film (black curves in Fig. 3 d, g). The difference in the relative

**Table 2**  
The thickness-averaged elemental atomic percentage of  $\text{SiO}_x\text{N}_y$  based “top” configuration films on Mo/SLG substrate measured by EDX.

	Thermally cured film		UV cured film	
	Without CNTs, at %	With CNTs, at %	Without CNTs, at %	With CNTs, at %
Silicon	33	32	30	29
Oxygen	54	54	68	68
Nitrogen	7	7	0	1
Carbon	6	7	2	2

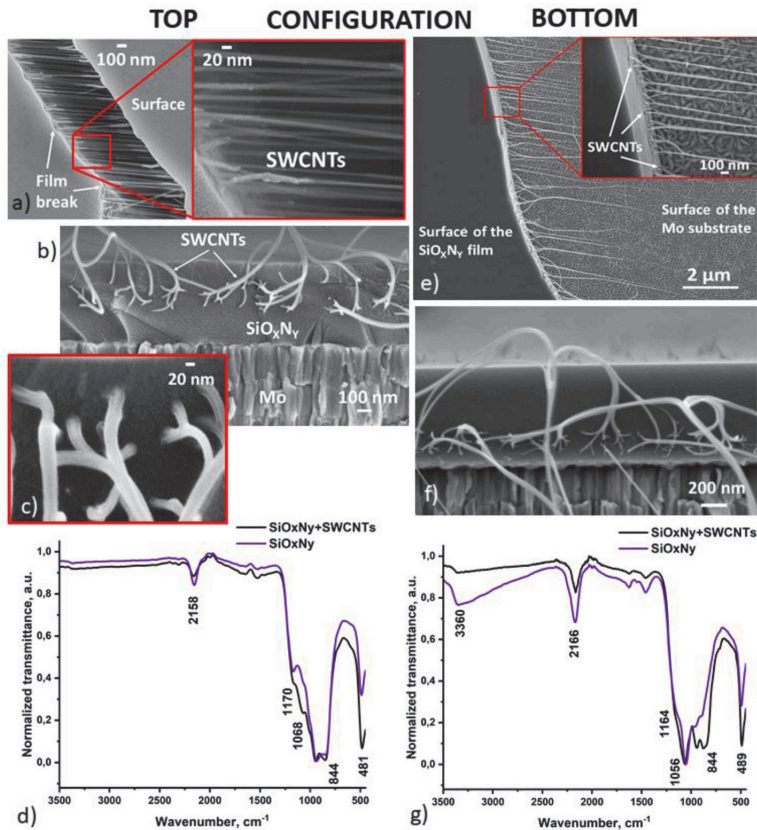


**Fig. 3.** HR-SEM images of composite film with “top” architecture: (a) surface under high magnification, and (b, c) cross-section with film thickness 520 nm. (d) ATR-FTIR spectra of the “top” sample were measured in the area with SWCNTs (black curve) and in the area without SWCNTs (purple curve). HR-SEM images of the (e) surface and (f) cross-section of the composite film with “bottom” architecture with thickness 650 nm, (g) ATR-FTIR spectra of the “bottom” sample. All measurements performed for samples on Mo/glass substrates. (For interpretation of the references to colour in this figure legend, the reader is referred to the Web version of this article.)

intensities of some peaks is caused by small changes in film thickness in different areas of the sample. The peak near  $3380\text{ cm}^{-1}$ , which is responsible for stretching vibrations of N–H bonds, occurs in all spectra [52]. It is more pronounced for “bottom” sample because wide band of OH vibrations occurred close to it [20]. The peak near  $2160\text{ cm}^{-1}$  is a sign of stretching vibrations of the Si–H bond [53]. Near  $1500\text{ cm}^{-1}$ , traces of the residual dibutyl ether, a solvent for PHPS, are observed in all spectra [50]. In the fingerprint region (the region with wavenumbers less than  $1500\text{ cm}^{-1}$ ), the mutual superposition of a large number of peaks from vibrations of silicon bonds with oxygen, nitrogen, and hydrogen is traditionally observed [56]. The peak caused by the bending vibrations of N–H bond is located near  $1168\text{ cm}^{-1}$  and creating a shoulder of wide multi bond peak in the fingerprint area [52]. The position of the peak of the transverse optical (TO) mode of asymmetric stretching vibrations of the Si–O–Si bond at about  $1064\text{ cm}^{-1}$  is an indicator of the quartz-like structure of silicon atoms inside the film, with bond angles of about  $144^\circ$  [55]. This confirms our previous conclusions about the different structures of PHPS films cured in different ways. Peaks near  $834$  and  $480\text{ cm}^{-1}$  are caused by Si–N bond and Si breathing or Si–O stretching vibrations [20,57,58]. Shifts in the positions of the Si–O bond peaks compared to the results of thermally cured samples indicate the formation of the films with different structure [55].

The optical transmittance spectra of SWCNT film, cured  $\text{SiO}_x\text{N}_y$  and

$\text{SiO}_x\text{N}_y/\text{SWCNT}$  composite layers on SLG substrates are represented in Fig. 4. To measure the spectra, the SWCNT film was transferred to the SLG surface, after which its transmittance was measured. Then, a PHPS film was spin-cast on top of the SWCNT film and cured according to the “bottom” architecture. After curing, the transmittance of the  $\text{SiO}_x\text{N}_y/\text{SWCNT}$  composite was measured within the same spectrophotometer operating session. Thus, both spectra measurements were carried out with the same baseline and for the same SWCNTs. To measure the transmittance of the pure  $\text{SiO}_x\text{N}_y$  film, another sample deposited on the cleaned SLG substrate was used. For all measurements, the SLG substrate signal was subtracted from the results.

As was written above, the main area of application of the coatings being developed imposes restrictions in the form needing high transmittance. The  $\text{SiO}_x\text{N}_y$  matrix film (blue curve in Fig. 4) has very high transparency over a wide range of wavelengths and has an absorption peak in the near UV region of the spectrum. The behavior of the spectrum of the pure SWCNT film (black curve) is similar to the spectrum of the matrix, only with lower transmittance values over the entire measurement range. The transmittance spectrum of the  $\text{SiO}_x\text{N}_y/\text{SWCNT}$  composite film (red curve) is located between the spectra of SWCNTs and  $\text{SiO}_x\text{N}_y$ . At the same time, the transmittance of the composite is at least 2% higher than the SWCNT film over the entire range of the visible and IR parts of the spectrum. This can be explained within the



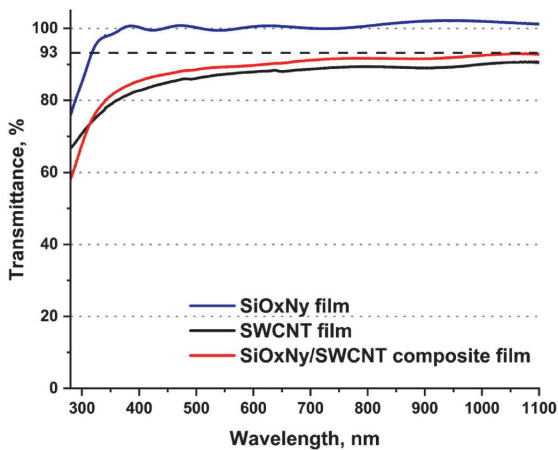


Fig. 4. Transmittance spectra of a UV-cured  $\text{SiO}_x\text{N}_y$  film (blue curve), a SWCNT film (black curve), and a UV-cured  $\text{SiO}_x\text{N}_y/\text{SWCNT}$  composite film (red curve). The contribution of the SLG substrate is subtracted from the spectra. (For interpretation of the references to colour in this figure legend, the reader is referred to the Web version of this article.)

framework of the theory of antireflection of optics. By introducing SWCNTs inside the matrix, we add additional interfaces in the form of SWCNT walls. Here, we need to remember the composition gradient of the matrix film across its thickness, which in turn causes a gradient of the refractive index across the thickness. All this leads to the creation of a package of thin films inside the composite, which affects the propagation of radiation through the composite and creates the antireflection effect that we observe in the optical spectrum of the composite [59]. The antireflection effect in the composite is confirmed by the reflectance spectra presented in the Supplementary Information (Fig. S3).

This observation requires us to study the properties of the composite coating in more detail in the continuation of our research. Also, this opens up new opportunities for using the coatings we are developing in optical technologies.

#### 4. Conclusions

In summary, novel composite thin films with horizontally oriented SWCNTs inside a  $\text{SiO}_x\text{N}_y$  matrix derived from PHPS were obtained and studied for the first time. Different configurations of  $\text{SiO}_x\text{N}_y/\text{SWCNT}$  composite films were prepared and studied depending on the location of the SWCNT filler layers within the matrix and depending on the matrix curing method. The behavior of the SWCNT film after transfer to hard and soft surfaces was also studied. In addition, we proposed a simple and effective way to activate the molybdenum surface to enhance the adhesion of SWCNTs to it during dry transfer.

According to the results of HR-SEM, EDX, and FTIR data, the filler in the form of a thin film of SWCNTs does not affect the PHPS conversion process either during the thermal curing method or the UV-assisted one. The proposed novel technological path of composite formation avoids the problem of SWCNTs agglomeration inside the matrix in all studied conditions. The SWCNT film remains tightly packed and does not lead to the formation of pores, cavities, or channels inside the  $\text{SiO}_x\text{N}_y$  matrix. Also, it does not affect the surface morphology of the composite coating, which remains very smooth and homogenous. All studied composite configurations illustrate the excellent compatibility of SWCNTs and the  $\text{SiO}_x\text{N}_y$  matrix film. The concentration of the SWCNT filler inside the  $\text{SiO}_x\text{N}_y$  matrix during single-layer embedding remains very low. UV-Vis spectroscopy has shown that the composite films have better transmittance than pure SWCNT films, indicating their innovative potential

as optical antireflection coatings, in addition to other promising applications in optoelectronics, microelectronics, etc.

#### Funding

AGN acknowledges RSF [grant number 22-13-00436] for SWCNT synthesis. This work was supported by the Estonian Ministry of Education and Research [grant number TK210], and by Education and Youth Board of Estonia [in frames of ÖÜF5 project], and NAMUR + core facility funded by the Estonian Research Council [under grant number TT13].

#### CRediT authorship contribution statement

Elizaveta Shmagina: Writing – review & editing, Writing – original draft, Visualization, Methodology, Investigation, Formal analysis, Data curation, Conceptualization. Olga Volobujeva: Visualization, Investigation, Formal analysis. Albert G. Nasibulin: Writing – original draft, Resources. Sergei Bereznev: Writing – review & editing, Writing – original draft, Supervision, Resources, Project administration, Methodology, Funding acquisition, Formal analysis, Data curation, Conceptualization.

#### Declaration of competing interest

The authors declare that they have no known competing financial interests or personal relationships that could have appeared to influence the work reported in this paper.

#### Acknowledgements

The authors thanks Dr. Kaia Tõnsuaadu for her help with the ATR-FTIR measurements.

#### Appendix A. Supplementary data

Supplementary data to this article can be found online at <https://doi.org/10.1016/j.ceramint.2024.06.250>.

#### References

- [1] R.P. Chaudhary, C. Parameswaran, M. Idrees, A.S. Rasaki, C. Liu, Z. Chen, P. Colombo, Additive manufacturing of polymer-derived ceramics: materials, technologies, properties and potential applications, *Prog. Mater. Sci.* 128 (2022) 100969, <https://doi.org/10.1016/J.PMATSCI.2022.100969>.
- [2] R. Sujith, S. Jothi, A. Zimmermann, F. Aldinger, R. Kumar, Mechanical behaviour of polymer derived ceramics – a review, *Int. Mater. Rev.* 66 (2021) 426–449, <https://doi.org/10.1080/09506608.2020.1784616>.
- [3] W.Y. Wang, Y.L. Zhang, X. Guo, L.M. Wang, J.R. Zhang, H. Yang, G.J. Dong, Z. B. Zhang, C.H. Xu, Rapid conversion of perhydropolysilazane into thin silica coating at low temperature, *Chin. J. Polym. Sci.* 41 (2023) 1198–1205, <https://doi.org/10.1007/S10118-023-2959-6/METRICS>.
- [4] F. Riffard, E. Joannet, H. Buscail, R. Rolland, S. Perrier, Beneficial effect of a pre-ceramic polymer coating on the protection at 900 °C of a commercial AISI 304 stainless steel, *Oxid. Metals* 88 (2017) 211–220, <https://doi.org/10.1007/S11085-016-9705-1/FIGURES/7>.
- [5] M. Günthner, M. Pscherer, C. Kaufmann, G. Motz, High emissivity coatings based on polysilazanes for flexible Cu(In,Ga)Se<sub>2</sub> thin-film solar cells, *Sol. Energy Mater. Sol. Cells* 123 (2014) 97–103, <https://doi.org/10.1016/J.SOLMAT.2014.01.027>.
- [6] L. Hu, M. Li, C. Xu, Y. Luo, Perhydropolysilazane derived silica coating protecting Kapton from atomic oxygen attack, *Thin Solid Films* 520 (2011) 1063–1068, <https://doi.org/10.1016/J.TSF.2011.10.011>.
- [7] K. Wang, M. Günthner, G. Motz, B.D. Flinn, R.K. Bordia, Control of surface energy of silicon oxynitride films, *Langmuir* 29 (2013) 2889–2896, [https://doi.org/10.1021/LA304307Y/ASSET/IMAGES/LARGE/LA-2012-04307Y\\_0006.JPG](https://doi.org/10.1021/LA304307Y/ASSET/IMAGES/LARGE/LA-2012-04307Y_0006.JPG).
- [8] K. Wang, X. Zheng, F.S. Ohuchi, R.K. Bordia, The conversion of perhydropolysilazane into SiON films characterized by X-ray photoelectron spectroscopy, *J. Am. Ceram. Soc.* 95 (2012) 3722–3725, <https://doi.org/10.1111/JACE.12045>.
- [9] Y. Zhan, R. Grottenmüller, W. Li, F. Javaid, R. Riedel, Evaluation of mechanical properties and hydrophobicity of room-temperature, moisture-curable polysilazane coatings, *J. Appl. Polym. Sci.* 138 (2021) 50469, <https://doi.org/10.1002/APP.50469>.

- [10] C. Li, J. Wei, M. Chen, X. Guan, X. Yang, Z. Li, C. Ma, X. Ye, Ultralow-temperature fabrication of chromium-free zinc-aluminum coatings based on polysilazane, *Mater. Chem. Phys.* 278 (2022) 125608, <https://doi.org/10.1016/j.materchemphys.2021.125608>.
- [11] T. Niizeki, S. Nagayama, Y. Hasegawa, N. Miyata, M. Sahara, K. Akutsu, Structural study of silica coating thin layers prepared from perhydropolysilazane: substrate dependence and water penetration structure, *Coatings* 6 (2016) 64, <https://doi.org/10.3390/COATINGS6040064>.
- [12] T. Sasaki, L. Sun, Y. Kurosawa, T. Takahashi, Y. Suzuri, Nanometer-thick SiN films as gas barrier coatings densified by vacuum UV irradiation, *ACS Appl. Nano Mater.* 4 (2021) 10344–10353, [https://doi.org/10.1021/ACSANM.1C01862/ASSET/IMAGES/LARGE/AN1C01862\\_0008.JPG](https://doi.org/10.1021/ACSANM.1C01862/ASSET/IMAGES/LARGE/AN1C01862_0008.JPG).
- [13] E. Shmagina, M. Danilson, V. Mikli, S. Bereznev, Comparative study of perhydropolysilazane protective films, *Surf. Eng.* (2022) 1–9, <https://doi.org/10.1080/02670844.2022.2155445>.
- [14] J.J. Baek, S.M. Park, Y.R. Kim, K.C. Chang, Y.J. Heo, G.Y. Bae, K.H. Choi, G. Shin, Intense pulsed UV light treatment to design functional optical films from perhydropolysilazane: an alternative to conventional heat treatment processes, *J. Mater. Sci.* 57 (2022) 254–273, <https://doi.org/10.1007/S10853-021-06598-3/FIGURES/15>.
- [15] D. Kim, G.G. Jeon, J.H. Kim, J. Kim, N. Park, Design of a flexible thin-film encapsulant with sandwich structures of perhydropolysilazane layers, *ACS Appl. Mater. Interfaces* 14 (2022) 34678–34685, <https://doi.org/10.1021/acsmi.2c06699>.
- [16] H.S. Back, M.J. Kim, J.J. Baek, D.H. Kim, G. Shin, K.H. Choi, J.H. Cho, Intense-pulsed-UV-converted perhydropolysilazane gate dielectrics for organic field-effect transistors and logic gates, *RSC Adv.* 9 (2019) 3169–3175, <https://doi.org/10.1039/C8RA09831J>.
- [17] N. Yang, W. Wang, W. Cai, K. Lu, Corrosion and tribocorrosion mitigation of perhydropolysilazane-derived coatings on low carbon steel, *Corrosion Sci.* 177 (2020) 108946, <https://doi.org/10.1016/j.corsci.2020.108946>.
- [18] S. Yue, S. Wang, D. Han, S. Huang, M. Xiao, Y. Meng, Perhydropolysilazane-derived-SiO<sub>2</sub> coated cellulose: a transparent biodegradable material with high gas barrier property, *Cellulose* 29 (2022) 8293–8303, <https://doi.org/10.1007/S10570-022-04746-9/TABLES/3>.
- [19] Z. Zhang, Z. Shao, Y. Luo, P. An, M. Zhang, C. Xu, Hydrophobic, transparent and hard silicon oxynitride coating from perhydropolysilazane, *Polym. Int.* 64 (2015) 971–978, <https://doi.org/10.1002/PL4871>.
- [20] L. Blankenburg, M. Schrödner, Perhydropolysilazane derived silica for flexible transparent barrier foils using a reel-to-reel wet coating technique: single- and multilayer structures, *Surf. Coat. Technol.* 275 (2015) 193–206, <https://doi.org/10.1016/j.surfcoat.2015.05.019>.
- [21] Y. Seo, S. Cho, S. Kim, S. Choi, H. Kim, Synthesis of refractive index tunable silazane networks for transparent glass fiber reinforced composite, *Ceram. Int.* 43 (2017) 7895–7900, <https://doi.org/10.1016/j.ceramint.2017.03.112>.
- [22] Y. Wang, G. Ding, J.Y. Mao, Y. Zhou, S.T. Han, Recent advances in synthesis and application of perovskite quantum dot based composites for photonics, electronics and sensors, *Sci. Technol. Adv. Mater.* 21 (2020) 278–302, <https://doi.org/10.1080/14686996.2020.1752115>.
- [23] L. Duo, Z. Zhang, K. Zheng, D. Wang, C. Xu, Y. Xia, Perhydropolysilazane derived SiON interfacial layer for Cu/epoxy molding compound composite, *Surf. Coat. Technol.* 391 (2020) 125703, <https://doi.org/10.1016/j.surfcoat.2020.125703>.
- [24] D.D.L. Chung, Materials for electromagnetic interference shielding, *Mater. Chem. Phys.* 255 (2020) 123587, <https://doi.org/10.1016/j.materchemphys.2020.123587>.
- [25] E.G. Shmagina, E.A. Konshina, D.P. Shcherbinin, P.D. Khavlyuk, M.S. Stepanova, Photoluminescence enhancement of carbon dots by Ag nanoparticles in thin-film hybrid structures, *Surf. Eng.* 37 (2021) 437–444, <https://doi.org/10.1080/02670844.2020.1747015>.
- [26] I.V. Novikov, D.V. Krasnikov, A.M. Vorobei, Y.I. Zuev, H.A. Butt, F.S. Fedorov, S. A. Gusev, A.A. Safonov, E.V. Shulga, S.D. Konev, I.V. Sergeichev, S.S. Zhukov, T. Kallio, B.P. Gorshunov, O.O. Parenago, A.G. Nasibulin, Multifunctional elastic nanocomposites with extremely low concentrations of single-walled carbon nanotubes, *ACS Appl. Mater. Interfaces* 14 (2022) 18866–18876, [https://doi.org/10.1021/ACSAMI.2C01086/ASSET/IMAGES/LARGE/AM2C01086\\_0007.JPG](https://doi.org/10.1021/ACSAMI.2C01086/ASSET/IMAGES/LARGE/AM2C01086_0007.JPG).
- [27] Z. Fan, C. Xiong, J. Yin, Y. Zhang, Y. Zou, H. Zhou, Ultra low-temperature fabrication of hollow glass microspheres and polysilazane coating for enhanced thermal protection of carbon/epoxy composites, *Surface. Interfac.* 40 (2023) 103064, <https://doi.org/10.1016/j.surfint.2023.103064>.
- [28] S. Abazari, A. Shamsipur, H.R. Baksheshi-Rad, Synergistic effect of hybrid reduced graphene oxide (rGO) and carbon nanotubes (CNTs) reinforcement on microstructure, mechanical and biological properties of magnesium-based composite, *Mater. Chem. Phys.* 301 (2023) 127543, <https://doi.org/10.1016/j.materchemphys.2023.127543>.
- [29] A.G. Nasibulin, A. Kaskela, K. Mustonen, A.S. Anisimov, V. Ruiz, S. Kivistö, S. Rackauskas, M.Y. Timmermans, M. Pudas, B. Aitchison, M. Kauppinen, D. P. Brown, O.G. Okhotnikov, E.I. Kauppinen, Multifunctional free-standing single-walled carbon nanotube films, *ACS Nano* 5 (2011) 3214–3221, [https://doi.org/10.1021/NN200333R/SUPPL\\_FILE/NN200333R\\_SI\\_006.MOV](https://doi.org/10.1021/NN200333R/SUPPL_FILE/NN200333R_SI_006.MOV).
- [30] N. Rouhi, D. Jain, P.J. Burke, High-performance semiconducting nanotube inks: progress and prospects, *ACS Nano* 5 (2011) 8471–8487, <https://doi.org/10.1021/NN201828Y>.
- [31] W. Cheung, M. Patel, Y. Ma, Y. Chen, Q. Xie, J.V. Lockard, Y. Gao, H. He,  $\pi$ -Plasmon absorption of carbon nanotubes for the selective and sensitive detection of Fe<sup>3+</sup> ions, *Chem. Sci.* 7 (2016) 5192–5199, <https://doi.org/10.1039/C6SC00006A>.
- [32] A. Bozeya, Y.F. Makableh, R. Abu-Zurayk, A. Khalaf, A. Al Babaw, Thermal and structural properties of high density polyethylene/carbon nanotube nanocomposites: a comparison study, *Chemosensors* 9 (2021) 136, <https://doi.org/10.3390/CHEMOSENSORS9060136>, 2021.
- [33] B. Arash, Q. Wang, V.K. Varadan, Mechanical properties of carbon nanotube/polymer composites, *Sci. Rep.* 4 (1 4) (2014) 1–8, <https://doi.org/10.1038/srep06479>, 2014.
- [34] C. Ding, Z. Lu, S. Li, Z. Wang, P. Yu, S. Ye, Microstructures, thermal and mechanical properties of Al-Si-CNT composites for thermal management applications, *Mater. Chem. Phys.* 297 (2023) 127368, <https://doi.org/10.1016/j.materchemphys.2023.127368>.
- [35] Q. Cao, J.A. Rogers, Ultrathin films of single-walled carbon nanotubes for electronics and sensors: a review of fundamental and applied aspects, *Adv. Mater.* 21 (2009) 29–53, <https://doi.org/10.1002/ADMA.200801995>.
- [36] M.F.L. De Volder, S.H. Tawfik, R.H. Baughman, A.J. Hart, Carbon nanotubes: present and future commercial applications, *Science* 339 (1979) 535–539, [https://doi.org/10.1126/SCIENCE.1222425/SUPPL\\_FILE/DEVOLDER.SM.PDF](https://doi.org/10.1126/SCIENCE.1222425/SUPPL_FILE/DEVOLDER.SM.PDF), 2013.
- [37] X. Zhang, N. Zhao, C. He, The superior mechanical and physical properties of nanocarbon reinforced bulk composites achieved by architecture design – a review, *Prog. Mater. Sci.* 113 (2020) 100672, <https://doi.org/10.1016/j.pmatsci.2020.100672>.
- [38] D. Shopova-Gospodinova, Z. Burghard, T. Dufaux, M. Burghard, J. Bill, Mechanical and electrical properties of polymer-derived Si-C-N ceramics reinforced by octadecylamine – modified single-wall carbon nanotubes, *Compos. Sci. Technol.* 71 (2011) 931–937, <https://doi.org/10.1016/j.compscitech.2011.02.013>.
- [39] A. Moisa, A.G. Nasibulin, D.P. Brown, H. Jiang, L. Khriachtchev, E.I. Kauppinen, Single-walled carbon nanotube synthesis using ferrocene and iron pentacarbonyl in a laminar flow reactor, *Chem. Eng. Sci.* 61 (2006) 4393–4402, <https://doi.org/10.1016/j.ces.2006.02.020>.
- [40] P.M. Rajanna, H. Meddeb, O. Sergeev, A.P. Tsapenko, S. Bereznev, M. Vehse, O. Volobujeva, M. Danilson, P.D. Lund, A.G. Nasibulin, Rational design of highly efficient flexible and transparent p-type composite electrode based on single-walled carbon nanotubes, *Nano Energy* 67 (2020) 104183, <https://doi.org/10.1016/j.nanoen.2019.104183>.
- [41] A. Jorio, R. Saito, Raman spectroscopy for carbon nanotube applications, *J. Appl. Phys.* 129 (2021) 21102, <https://doi.org/10.1063/5.0030809/1025611>.
- [42] N.S. Komarova, A.G. Krivenko, A.G. Ryabenko, A.V. Naumkin, Active forms of oxygen as agents for electrochemical functionalization of SWCNTs, *Carbon N Y* 53 (2013) 188–196, <https://doi.org/10.1016/j.carbon.2012.10.047>.
- [43] A.A. Alekseeva, D.V. Krasnikov, G.B. Livshits, S.A. Romanov, Z.I. Popov, L. A. Varlamova, E.V. Sukhanova, A.S. Klimovich, P.B. Sorokin, S.V. Savilov, A. G. Nasibulin, Films enriched with semiconducting single-walled carbon nanotubes by aerosol N<sub>2</sub>O etching, *Carbon N Y* 212 (2023) 118094, <https://doi.org/10.1016/j.carbon.2023.118094>.
- [44] L. Minati, G. Speranza, I. Bernagozzi, S. Torrenzo, L. Toniutti, B. Rossi, M. Ferrari, A. Chiasera, Investigation on the electronic and optical properties of short oxidized multiwalled carbon nanotubes, *J. Phys. Chem. C* 114 (2010) 11068–11073, [https://doi.org/10.1021/JP101868S/ASSET/IMAGES/LARGE/JP-2010-01868S\\_0009.JPG](https://doi.org/10.1021/JP101868S/ASSET/IMAGES/LARGE/JP-2010-01868S_0009.JPG).
- [45] S.D. Shandakov, M.V. Lomakin, A.G. Nasibulin, The effect of the environment on the electronic properties of single-walled carbon nanotubes, *Tech. Phys. Lett.* 42 (2016) 1071–1075, <https://doi.org/10.1134/S1063785016110080/METRICS>.
- [46] I.V. Panasenko, M.O. Bulavskiy, A.A. Iurchenkova, Y. Aguilar-Martinez, F. S. Fedorov, E.O. Fedorovskaya, B. Mikladal, T. Kallio, A.G. Nasibulin, Flexible supercapacitors based on free-standing polyaniline/single-walled carbon nanotube films, *J. Power Sources* 541 (2022) 231691, <https://doi.org/10.1016/j.jpowsour.2022.231691>.
- [47] G.A. Ermolaev, A.P. Tsapenko, V.S. Volkov, A.S. Anisimov, Y.G. Gladush, A. G. Nasibulin, Express determination of thickness and dielectric function of single-walled carbon nanotube films, *Appl. Phys. Lett.* 116 (2020) 231103, <https://doi.org/10.1063/5.0012933/38443>.
- [48] Y. Shi, L. He, F. Guang, L. Li, Z. Xin, R. Liu, A review: preparation, performance, and applications of silicon oxynitride film, *Micromachines* 10 (2019) 552, <https://doi.org/10.3390/mi10080552>.
- [49] P.P. Rajanna, S. Luchkin, K.V. Larionov, A. Grebenko, Z.I. Popov, P.B. Sorokin, M. Danilson, S. Bereznev, P.D. Lund, A.G. Nasibulin, Adhesion of single-walled carbon nanotube thin films with different materials, *J. Phys. Chem. Lett.* 11 (2020) 504–509, [https://doi.org/10.1021/ACS.JPCLETT.9B03552/SUPPL\\_FILE/JZ9B03552\\_SI\\_001.PDF](https://doi.org/10.1021/ACS.JPCLETT.9B03552/SUPPL_FILE/JZ9B03552_SI_001.PDF).
- [50] n-Butyl ether, (n.d.), <https://webbook.nist.gov/cgi/book.cgi?ID=C142961&Mask=80> (accessed April 15, 2024).
- [51] M. Kazemi, A.H. Navarchian, F. Ahangaran, Effects of silica surface modification with silane and poly(ethylene glycol) on flexural strength, protein-repellent, and antibacterial properties of acrylic dental nanocomposites, *Dent. Mater.* 39 (2023) 863–871, <https://doi.org/10.1016/j.dental.2023.07.010>.
- [52] S. Rossi, F. Deflorian, M. Fedel, Polysilazane-based coatings: corrosion protection and anti-graffiti properties, *Surf. Eng.* 35 (2018) 343–350, <https://doi.org/10.1080/02670844.2018.1465748>.
- [53] L. Prager, A. Dierdorf, H. Liebe, S. Naumov, S. Stojanović, R. Heller, L. Wennrich, M.R. Buchmeiser, Conversion of perhydropolysilazane into a SiO<sub>x</sub> network triggered by vacuum ultraviolet irradiation: access to flexible, transparent barrier coatings, *Chem. Eur J.* 13 (2007) 8522–8529, <https://doi.org/10.1002/CHEM.200700351>.

- [54] A. Morlier, S. Cros, J.P. Garandet, N. Alberola, Structural properties of ultraviolet cured polysilazane gas barrier layers on polymer substrates, *Thin Solid Films* 550 (2014) 85–89, <https://doi.org/10.1016/j.tsf.2013.10.140>.
- [55] L. Prager, U. Helmstedt, H. Herrnberger, O. Kahle, F. Kita, M. Münch, A. Pender, A. Prager, J.W. Gerlach, M. Stasiak, Photochemical approach to high-barrier films for the encapsulation of flexible laminary electronic devices, *Thin Solid Films* 570 (2014) 87–95, <https://doi.org/10.1016/j.tsf.2014.09.014>.
- [56] N. Chen, B. Reeja-Jayan, A. Liu, J. Lau, B. Dunn, K.K. Gleason, iCVD cyclic polysiloxane and polysilazane as nanoscale thin-film electrolyte: synthesis and properties, *Macromol. Rapid Commun.* 37 (2016) 446–452, <https://doi.org/10.1002/MARC.201500649>.
- [57] J.J. Baek, S.M. Park, Y.R. Kim, K.C. Chang, Y.J. Heo, G.Y. Bae, K.H. Choi, G. Shin, Intense pulsed UV light treatment to design functional optical films from perhydropolysilazane: an alternative to conventional heat treatment processes, *J. Mater. Sci.* 57 (2022) 254–273, <https://doi.org/10.1007/S10853-021-06598-3/FIGURES/15>.
- [58] P.C. Ricci, G. Gulleri, F. Fumagalli, C.M. Carbonaro, R. Corpino, Optical characterization of polysilazane based silica thin films on silicon substrates, *Appl. Surf. Sci.* 265 (2013) 470–474, <https://doi.org/10.1016/j.apsusc.2012.11.030>.
- [59] T.M. Mercier, T. Rahman, C. Krishnan, E. Khorani, P.J. Shaw, M.E. Pollard, S. A. Boden, P.G. Lagoudakis, M.D.B. Charlton, High symmetry nano-photonic quasicrystals providing novel light management in silicon solar cells, *Nano Energy* 84 (2021) 105874, <https://doi.org/10.1016/j.nanoen.2021.105874>.

## Update

### **Ceramics International**

Volume 50, Issue 22PC, 15 November 2024, Page 48887

DOI: <https://doi.org/10.1016/j.ceramint.2024.09.158>



Contents lists available at [ScienceDirect](#)

Ceramics International

journal homepage: [www.elsevier.com/locate/ceramint](http://www.elsevier.com/locate/ceramint)



Corrigendum



## Corrigendum to “Fabrication of novel SiOxNy/SWCNT laminate-type composite protective coating using low-temperature approach” [Ceram. Int. 50 (2024) 34312–34320]

Elizaveta Shmagina<sup>a,\*</sup>, Olga Volobujeva<sup>a</sup>, Albert G. Nasibulin<sup>b</sup>, Sergei Bereznev<sup>a</sup>

<sup>a</sup> Department of Materials and Environmental Technology, School of Engineering, Tallinn University of Technology, Ehitajate tee 5, 19086, Tallinn, Estonia

<sup>b</sup> Skolkovo Institute of Science and Technology, Nobel Str., 3, 121205, Moscow, Russian Federation

The authors regret that some funding information was missing from this original published article. The correct and full information is shown below.

The authors would like to apologise for any inconvenience caused.

Research [grant number TK210], by the project “Increasing the knowledge intensity of Ida-Viru entrepreneurship” co-funded by the European Union [in frames of ÖP5 project], and NAMUR + core facility funded by the Estonian Research Council [under grant number TT13].

### Funding

This work was supported by the Estonian Ministry of Education and

DOI of original article: <https://doi.org/10.1016/j.ceramint.2024.06.250>.

\* Corresponding author.

E-mail addresses: [elshma@taltech.ee](mailto:elshma@taltech.ee), [lizakoritsa@gmail.com](mailto:lizakoritsa@gmail.com) (E. Shmagina), [olga.volobujeva@taltech.ee](mailto:olga.volobujeva@taltech.ee) (O. Volobujeva), [A.Nasibulin@skol.tech](mailto:A.Nasibulin@skol.tech) (A.G. Nasibulin), [sergei.bereznev@taltech.ee](mailto:sergei.bereznev@taltech.ee), [sergei.bereznev@gmail.com](mailto:sergei.bereznev@gmail.com) (S. Bereznev).

<https://doi.org/10.1016/j.ceramint.2024.09.158>

Available online 17 September 2024

0272-8842/© 2024 Elsevier Ltd and Techna Group S.r.l. All rights are reserved, including those for text and data mining, AI training, and similar technologies.





## Appendix 3

### Publication III

E. Shmagina, M. Antonov, A. Kasikov, O. Volobujeva, E.M. Khabushev, T. Kallio, S. Bereznev, Structural, Mechanical, and Optical Properties of Laminate-Type Thin Film SWCNT/SiOxNy Composites, *Nanomaterials* 14 (2024) 1806, <https://doi.org/10.3390/nano14221806>





Article

# Structural, mechanical, and optical properties of laminate-type thin film SWCNT/SiO<sub>x</sub>N<sub>y</sub> composites

Elizaveta Shmagina <sup>a\*</sup>, Maksim Antonov <sup>b</sup>, Aarne Kasikov <sup>c</sup>, Olga Volobujeva <sup>a</sup>, Eldar M. Khabushev <sup>d</sup>, Tanja Kallio <sup>d</sup> and Sergei Bereznev <sup>a</sup>

<sup>a</sup> Department of Materials and Environmental Technology, School of Engineering, Tallinn University of Technology, Ehitajate tee 5, 19086 Tallinn, Estonia

<sup>b</sup> Department of Mechanical & Industrial Engineering, School of Engineering, Tallinn University of Technology, Ehitajate tee 5, 19086 Tallinn, Estonia, maksim.antonov@taltech.ee

<sup>c</sup> University of Tartu, Institute of Physics, W. Ostwaldi 1, Tartu, 50411, Estonia, aarne.kasikov@ut.ee

<sup>d</sup> Aalto University, School of Chemical Engineering, Kemistintie 1, Espoo, 02150, Finland, eldar.khabushev@gmail.com, [tanja.kallio@aalto.fi](mailto:tanja.kallio@aalto.fi)

\* Correspondence: Shmagina, corresponding author, phone +37258308427, email: elizaveta.shmagina@taltech.ee;

**Abstract:** The development of new encapsulating coatings for flexible solar cells (SCs) can help address the complex problem of the short lifespan of these devices, as well as optimize the technological process of their production. In this study, new laminate-type protective composite coatings were prepared using a silicon oxynitride thin-film matrix obtained by curing the pre-ceramic polymer perhydropolysilazane (PHPS) through two low-temperature methods: (i) thermal annealing at 180 °C and (ii) exposure to UV radiation at wavelengths of 185 and 254 nm. Single-walled carbon nanotubes (SWCNTs) were used as a filler via dry transfer, facilitating their horizontal orientation within the matrix. The optical, mechanical, adhesive, and structural properties of the matrix films and SiO<sub>x</sub>N<sub>y</sub>/SWCNT composite coatings, along with their long-term stability, were studied using FTIR and UV-Vis spectroscopy, HR-SEM, spectral ellipsometry, and a progressive-load scratch test. In this work, the optical constants of PHPS-derived films were systematically studied for the first time. An antireflection effect was observed in the composites revealing their two-component nature associated with (i) the refractive index of the SiO<sub>x</sub>N<sub>y</sub> matrix film and (ii) embedding of a SWCNT filler into the SiO<sub>x</sub>N<sub>y</sub> matrix. The curing method of PHPS was shown to significantly affect the resulting properties of the films. In addition to being used as protective multifunctional coatings for SCs, both SiO<sub>x</sub>N<sub>y</sub>/SWCNT composites and SiO<sub>x</sub>N<sub>y</sub> matrix films also function as broadband optical antireflective coatings. Furthermore, due to the very low friction coefficients observed in mechanical tests, they show potential as scratch resistant coatings for mechanical applications.

**Citation:** To be added by editorial staff during production.

Academic Editor: Firstname Last-name

Received: date

Revised: date

Accepted: date

Published: date



**Copyright:** © 2023 by the authors. Submitted for possible open access publication under the terms and conditions of the Creative Commons Attribution (CC BY) license (<https://creativecommons.org/licenses/by/4.0/>).

**Keywords:** Barrier protective coating; Carbon nanotube network; Polysilazane; Transparent optical thin films; Nanocomposite coating

## 1. Introduction

One of the key factors limiting the widespread use of flexible solar cells (SC) is their short lifespan [1]. This is primarily due to the degradation of the materials used inside the SC caused by oxygen, moisture, mechanical stress, temperature changes, and UV radiation [2]. The development of encapsulating barrier coatings, also known as protective coatings, is one possible way to overcome this complex problem [3–5]. By using different approaches to form such a coating, together with focusing on high barrier properties against moisture and gases, it is possible to achieve a positive effect on the optical, mechanical, thermal, and other properties of the protective film [2]. In addition, such a

strategy can reduce the number of functional layers involved, positively affecting the overall thickness and weight of the device, without the necessity of optimizing layer adhesion [3]. The creation of composite films is one of prospective approach, for enabling the integration of additional functional and protective properties into the framework of one single coating [6].

Various materials, such as epoxy resins [3], polymers [6], metallic glasses [7], etc., are being actively studied as protective coatings for flexible solar cells. When forming a composite coating, they can function as a base/matrix or as interlayers, depending on the architecture used [5,8]. Inorganic oxide and nitride films based on silicon are also actively studied barrier materials due to their long list of attractive properties [1], which are similar to those of glass, which is traditionally used for rigid SC protection [8]. These materials offer additional advantages, including the ability to create flexible, thin coatings that exhibit excellent adhesion to a wide range of materials, high resistance to temperature changes, and, in some cases, can be formed using low-temperature, vacuum-free processes [9–11]. These processes can be achieved by using a liquid pre-ceramic polymer from the extensive silazane family as a coating precursor. A prominent representative of this family is perhydropolysilazane (PHPS), which has recently attracted great interest from scientists due to its inorganic nature, allowing the production of high-hardness barrier coatings [12,13]. The backbone of PHPS consists of a  $-\text{Si}-\text{N}-\text{Si}-$  chain with H atoms as substituents. [13]. It is compatible with liquid film formation methods, which are also scalable to industrial roll-to-roll processes, providing a substantial economic advantage [5,14].

Depending on the conditions of transformation or so-called curing (temperature and atmospheric composition), a deposited PHPS layer can be transformed into silicon dioxide, silicon nitride, and silicon oxynitrides ( $\text{SiO}_x\text{N}_y$ ) of different compositions [8]. It should be noted that curing can occur even at room temperature [11]. The range of attractive properties of PHPS is illustrated by the growing variety of applications of this pre-ceramic polymer. PHPS-derived films have already proven their effectiveness as water, oxygen, and anti-UV barrier encapsulation layers for SC and microelectronic devices [15,16]. It has been demonstrated that PHPS-derived films can act very successfully as an anti-corrosion coating for low-carbon steel [17] and show promise as biodegradable materials for packaging applications due to their excellent barrier and optical properties [12]. More recently, PHPS-derived films have been shown to serve as a hydrogen permeation barrier, opening up new possibilities for their applicability in green energy technologies [18].

The creation of composites based on PHPS films can expand the range of functional properties of such coatings. For example, an optimally designed antireflective coating can significantly increase the efficiency of a SC. Due to reduced reflection, more light penetrates inside the device and participates in photoconversion [19]. This strategy has been demonstrated to work successfully for silicon dioxide thin films, increasing the efficiency of a perovskite solar cell by an additional 1% while having a positive effect on the self-cleaning properties of the coating [20]. A similar effect can be achieved for PHPS-derived films by manipulating the optical constants of the coating in various ways, including creating composites.

One of the disadvantages of PHPS-derived films is their high fragility, a consequence of the inorganic nature of the precursor. The creation of laminated composite coatings in which layers of PHPS alternate with organic polymer interlayers is a successful strategy for increasing the flexibility and reducing the brittleness of the protective coating, in addition to improving its barrier properties [5,8,21]. The unique properties of a composite coating are determined by the architecture and materials used. For example, PHPS-derived films have been successfully applied as interface layers in Cu/epoxy molding compound composites used in microelectronics. In these composites, PHPS-derived films increase the adhesion between the functional layers of the coating and improve barrier properties against moisture and ionic components [22].

The introduction of carbon nanotubes (CNTs) can potentially enhance the mechanical and thermal emission properties of the composite. The use of CNTs as a reinforcing

material is widely used in tandem with polymers and other matrices [23]. However, their application in PHPs-derived films has not yet been studied. Alignment of CNTs inside the matrix, or in other words, the creation of a special architecture of the composite, can introduce additional anisotropy of these properties [24].

In our previous study, we reported the successful formation of laminate-type composite thin films based on a PPHPs-derived matrix with embedded single-walled carbon nanotubes (SWCNTs) as a filler [25]. During the initial characterization of the resulting  $\text{SiO}_x\text{N}_y/\text{SWCNT}$  composite structures, an antireflection effect was observed. To explain the effect, it is critically important to know the optical constants of PPHPs-derived films cured by different methods. However, such data were not available in the literature, making it essential to obtain these measurements for the prepared  $\text{SiO}_x\text{N}_y$  matrix films and their  $\text{SiO}_x\text{N}_y/\text{SWCNT}$  composites.

In this work, we characterized the optical, mechanical, and adhesive properties of similar  $\text{SiO}_x\text{N}_y/\text{SWCNT}$  composite coatings. For the first time, we systematically measured the optical constants of PPHPs-derived and cured films using various low-temperature approaches. The mechanical and adhesive properties, as well as the long-term stability of the PPHPs-derived films, were also studied. The relationships between the chemical composition of the films and their properties immediately after curing and during the aging process of all the structures are reported. The antireflection effect observed in the  $\text{SiO}_x\text{N}_y/\text{SWCNT}$  composites was confirmed and associated with composite structure and curing of the coating. It was also determined that the  $\text{SiO}_x\text{N}_y$  matrix films can independently function as antireflective optical protective coatings. The data obtained are particularly important for the practical application of the studied coatings in photovoltaic (PV) technology and other fields.

## 2. Materials and Methods

### 2.1. Samples preparation

As a pre-ceramic precursor for  $\text{SiO}_x\text{N}_y$  matrix layer formation, a commercially available 20% solution of perhydropolysilazane (PHPS) in di-butyl ether (NN-120-20, durX-treme GmbH, Germany) was used. PPHPs thin films were deposited using a Polos SPIN 150i spin-coater at 2000 rpm speed for 60 seconds. Soda-lime glass (SLG) and SLG coated with a 1  $\mu\text{m}$  thick molybdenum layer (SLG/Mo) were used as substrates. PPHPs curing to  $\text{SiO}_x\text{N}_y$  was performed using two low-temperature approaches: (i) thermally induced (annealing at 180  $^\circ\text{C}$  for 60 min) in a Brother HD-14S oven and (ii) under UV-irradiation (185 + 254 nm for 40 min) in a Novascan digital UV ozone system. Detailed information related to the PPHPs films deposition, curing, and characterization can be found elsewhere [26].

Single walled carbon nanotubes (SWCNTs) used as a filler were obtained via the aerosol (floating catalyst) chemical vapor deposition (CVD) method using hydrocarbon feed-stock (ethylene and toluene), ferrocene vapor as a catalyst precursor and hydrogen as a carrier gas. The SWCNTs grown in the gas phase of a high temperature reactor have a mean bundle length of  $\sim 30 \mu\text{m}$ , diameter in range of 1.4 – 2.3 nm and density of approximately 0.12  $\text{g}/\text{cm}^3$ . These nanotubes were collected downstream of the reactor as thin films, oriented randomly in a horizontal plane on filter paper. Detailed information related to the filler material characterization can be found elsewhere [27–29].

$\text{SiO}_x\text{N}_y/\text{SWCNT}$  composite coatings were formed in two configurations: TOP and BOTTOM. In the TOP case, the SWCNT filler film was transferred from paper to a spin-coated and dried PPHPs matrix film using dry transfer method. In the BOTTOM configuration, the SWCNT film was transferred to the substrate (SLG or SLG/Mo), followed by deposition and drying of the PPHPs layer. Both composite configurations were then cured. Treatment of the molybdenum surface with vapors from a 40% aqueous solution of HF acid for 10 minutes facilitated the dry transfer of the SWCNT film onto the Mo surface. More details related to the formation of  $\text{SiO}_x\text{N}_y/\text{SWCNT}$  composites and their primary characterization were reported in our previous study [25].

## 2.2. Characterization

For the SLG-based samples, UV-Vis transmittance and reflectance spectra were recorded by a UV-Vis spectrophotometer (UV-1800, Shimadzu Corp., Japan) in the 280–1100 nm wavelength range.

Spectral ellipsometry (SE) for samples on an SLG substrate was measured on the GES-5E (Semilab Co., Hungary) device, equipped with the microspot option, in immersion mode with other glass sample. Propanol was used as the immersion fluid, and the angle of light incidence was set to 75°. Values of the reflection coefficients-ratio for different light polarizations ( $\tan \Psi$ ) and the phase difference ( $\Delta$ ) of light reflected from the sample were recorded and defined as:

$$\tan \Psi = \frac{|r_p|}{|r_s|} \text{ and } \Delta = \delta_p - \delta_s \quad (1)$$

where  $r_p$  and  $r_s$  are Fresnel reflection coefficients for p- and s- polarization states, and  $\delta_p$  and  $\delta_s$  are phase components in p- and s- polarization states of the reflected light. The measured data were modeled and analyzed using SEA software in the energy range of 1.3–5.5 eV. The dispersion function was modeled using the Cauchy dispersion formulae:

$$n = n_0 + A/\lambda^2 + B/\lambda^4 \quad \text{and} \quad k = C + D/\lambda^2 \quad (2)$$

where  $n$  is the refractive index,  $k$  is the extinction coefficient (absorption index), and  $\lambda$  is the wavelength. A, B, C, and D are material coefficients. For modeling the glass substrates, refractive index was taken as:

$$n = 1.535 + 0.0081/\lambda^2 + 0.00012/\lambda^4 \quad (3)$$

based on former SE measurements.

A Horiba LabRam HR800 micro-Raman spectrometer equipped with a multichannel CCD detection system in the backscattering configuration was used for the Raman studies of SWCNTs. The second harmonic (532 nm) of a solid-state Nd:YAG laser with a spot size of 5  $\mu\text{m}$  was applied for the excitation of the scattering. To achieve more accurate results, the spectra were recorded at a minimum of 4 different areas of the sample surface and then averaged. Measurements were conducted in the range from 55 to 1700  $\text{cm}^{-1}$ .

Fourier transform infrared spectroscopy (FTIR) is the main method used to study the degree of PHPS film transformation after the curing procedure. A Platinum-ATR Alpha (Bruker Optic GmbH, Germany) spectrometer equipped with an attenuated total reflection (ATR) module was used for that purpose. To exclude the influence of the glass signal on the measurement results, glass/Mo substrates were used. The measurements were conducted in the range of 400–4000  $\text{cm}^{-1}$  with a resolution of 4  $\text{cm}^{-1}$ . For each sample, a minimum of 4 measurements were taken at different points to control the uniformity of layers and avoid possible random fluctuations. The nearly identical spectra were then averaged to obtain a representative result.

The thickness, surface, and cross-sectional morphology of the obtained layers were studied using high-resolution scanning electron microscopy (HR-SEM, Zeiss Merlin, Germany) with an accelerating voltage of 4 kV. To eliminate the low-conductivity effect, the samples were covered with a 1 nm Au (80%) and Pd (20%) coating using the magnetron sputtering technique.

To study the mechanical and adhesive properties of the samples on Mo/glass substrates, a scratch test with progressive load was performed using a universal materials tribo-test device, the CETR UMT-2 (Bruker, USA). For the tests, an HRC Rockwell spherical diamond indenter, with a radius of 100  $\mu\text{m}$  and a cone angle of 120°, was used. The surface of the indenter was cleaned with ethanol prior to each scratch. During the tests, the indenter moved along the surface of the films with a linearly increasing load of 200 g/mm (1.96 N/mm), starting from 50 g (0.49 N) and ending at 2050 g (20.10 N). The length of each scratch was 10 mm. The scratching results were examined using HR-SEM. The



critical load (Lc) was determined by the distance from the beginning of the scratch to the first visual appearance of cracks on the surface of the samples. The position of indenter, applied load and coefficient of friction (COF) were In-Situ monitored and recorded during the test to trace the changes in materials performance under the load.

### 3. Results and Discussion

#### 3.1. Long-term stability of $\text{SiO}_x\text{N}_y$ matrix films

As described in the Materials and Methods section, the  $\text{SiO}_x\text{N}_y$  matrix films were obtained by curing the pre-ceramic polymer PPHS using UV irradiation or thermal annealing. In our previous works, we reported that PPHS films cured by both these methods are not completely converted to silicon dioxide. Nitrogen is retained inside the films in different quantities, which was detected using FTIR, SEM energy dispersive X-ray (EDX) spectroscopy, and X-ray photoelectron spectroscopy (XPS). In addition, samples exhibited a tendency to age or ripen in a desiccator at room temperature, gradually replacing residual nitrogen with oxygen [26].

It should be noted that the long-term stability of the composition, structure, and properties of polysilazane-derived films in general has not been sufficiently studied. There is a lack of data on PPHS-derived films. Therefore, in this work, we conducted a detailed study of the dynamics of aging of matrix films using FTIR spectroscopy. The samples were aged in plastic boxes in a desiccator at room temperature without any additional influences. FTIR spectra for each sample were recorded in three marked areas and then averaged. To best track the dynamics of aging, spectra were recorded immediately after curing, after 24 hours, after one week, 3 weeks, and 6 months.

For both curing methods, as the samples age, the shape of the spectra underwent changes (the main changes in peak intensity are marked by red arrows in Fig. 1a and 1b). In both cases, the samples had the same set of characteristic peaks, but their intensities differed, which leading to spectra of different shapes.

The spectra of both freshly cured films reveal a band corresponding to the N–H bond stretching vibrations near  $3365\text{ cm}^{-1}$  [30]. After a week of aging, this peak was no longer visible in either spectrum, and very broad, low intensity vibration bands of the –OH group formed near this position [14], likely due to the penetration of a small amount of water from the atmosphere into the film. Around  $2170\text{ cm}^{-1}$ , bands corresponding to the stretching vibrations of Si–H bonds were observed. The position of this peak shifted towards lower wavenumbers relative to standard values, which may indicate the presence of Si clusters inside the films [30]. During aging, the intensity of this peak noticeably decreased, almost disappearing after six months. Its position shifted slightly towards higher wavenumbers, which may indicate a decrease in silicon clusters and the formation of chemical bonds between silicon, and oxygen or hydroxyl groups as the samples age.

All other bands fall within the fingerprint region ( $1500$  to  $600\text{ cm}^{-1}$ ), where many different vibrational modes of silicon, nitrogen, hydrogen, and oxygen bonds are closely located, making their determination difficult. The band responsible for the stretching vibration of N–H in Si–NH–Si units is distinguishable in both spectra around  $1180\text{ cm}^{-1}$  and is especially pronounced in the spectrum of the annealed sample [31,32]. As the films age, the intensity of this peak decreased; after a week it was no longer clearly detectable for either curing method. Immediately after curing by both methods, the most intense band in the spectra was located around  $954\text{ cm}^{-1}$  and was caused by Si–N stretching vibrations [33]. With aging, the intensity of this band decreased significantly. However, since at the same time vibration bands of the hydroxyl groups appear in the region of large wavenumbers, a low intensity Si–OH stretching vibration may also emerge around  $950\text{ cm}^{-1}$  [14]. In this regard, for aged samples we cannot correctly interpret the peak located in this position.

In the spectrum of a freshly thermally cured sample, a low-intensity peak was detected at about  $1089\text{ cm}^{-1}$ , whose intensity gradually increased with aging, although its



position remained unchanged. That is the transverse optical (TO) mode of asymmetric stretching vibrations of the Si–O–Si bond, and its position, indicates the formation of clusters with a cage-like structure [31]. One week after UV curing, the peak representing this bond began to appear in the spectrum around  $1068\text{ cm}^{-1}$ . In the spectrum of a freshly cured sample, this band overlaps with neighboring bands, but as the sample ages, the relative intensity of this band increases, and its position shifted toward lower wavenumbers. After 6 months, this peak was located at  $1050\text{ cm}^{-1}$ , a peak position indicative of a quartz-like structure within the film [31].

In the spectrum of a six-month aged UV film, a band around  $1123\text{ cm}^{-1}$  appeared, which can also be attributed to vibration modes of the Si–O–Si bonds. The position of these peaks indicates that during the aging process, clusters with a cage-like structure and quartz-like structure are both formed inside the film. Bending vibrations of the Si–O–Si bonds are located around  $830\text{ cm}^{-1}$  [14,34], but due to the change in intensity of the Si–H vibration peak located at  $840\text{ cm}^{-1}$  it is difficult to analyze this region [35]. The rocking vibration of the Si–O–Si bond is localized around  $490\text{ cm}^{-1}$  [8,36]. The intensity of this band increased most significantly during aging, eventually becoming the most prominent in the spectra of samples prepared using both curing methods.

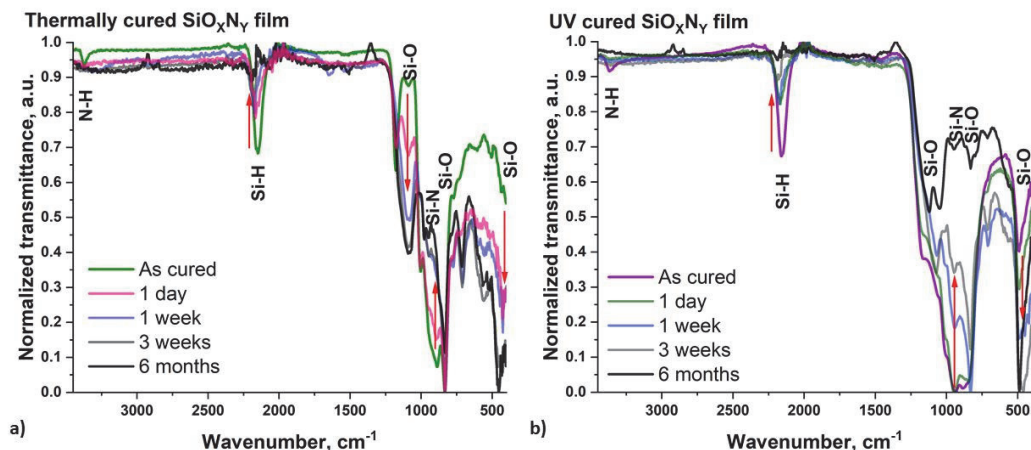


**Figure 1.** ATR-FTIR spectra of  $\text{SiO}_x\text{N}_y$  matrix films measured during aging/ripening process of a) thermally cured sample, b) UV-cured sample.

In the case of a thermally cured sample, the most noticeable changes in the shape of the spectrum occur during the first week after curing, then slowing down significantly. In contrast, for UV-cured samples, this process takes longer. As the films age, significant changes occur in their composition and structure. This process can be called ripening, where the oxygen content increases significantly, but the nitrogen and hydrogen content decreases. As a result, the peaks attributable to bonds between silicon and oxygen dominate in intensity, indicating that the composition of the films is close to silicon dioxide.

After six months of ripening, the spectra of films cured by different methods exhibit different shapes, reflecting differences in their structure, and, therefore, their properties. Notably, immediately after UV curing, the films contain less residual nitrogen and are closer in composition to silicon dioxide than thermally cured films. This is evident from the FTIR spectra and is confirmed by the XPS and SEM-EDX data from our previous studies [25,26]. During the films' aging, this trend continues, as confirmed by the SE results presented below. Therefore, if the goal is to obtain films close in composition to silicon dioxide, UV curing is the preferable method.

### 3.2. SiOxNy composite films with SWCNT

As described in the Materials and Methods section, SWCNTs were collected on filter paper to form thin films, with their thickness controlled by the deposition time. The paper with deposited SWCNT layers were then cut to produce pieces of any smaller size and shape. Fig. 2a and 2b show HR-SEM images of the SWCNT film transferred by dry transfer to the surface of the SLG substrate and carbon adhesive tape, respectively. The thickness of the SWCNT film can be determined using its optical absorption spectrum (Fig. 2d). To calculate the thickness, the absorption value at a wavelength of 550 nm, which is 0.054, must be multiplied by the correlation coefficient value of 239 [37]. Thus, the SWCNT film used in this study had a thickness of approximately 13 nm.

The absorption spectrum contains only one peak at the wavelength of about 290 nm, caused by the absorption of  $\pi$  plasmons [38]. The absence of other absorption bands is due to the doping of SWCNTs by environmental species, such as oxygen, during storage of the films in the lab [39].

Fig. 2c shows the Raman spectrum of a SWCNT film on the SLG substrate. The spectrum contains peaks of the radial breathing mode (RBM), clearly indicating the presence of single-walled carbon nanotubes. The very low intensity of the D peak around  $1350\text{ cm}^{-1}$  indicates a small number of defects in the tubes. The splitting of the G peak at about  $1591\text{ cm}^{-1}$  into two closely spaced components is also a sign of SWCNTs. The shape of this peak corresponds to high-quality nanotubes [40,41].

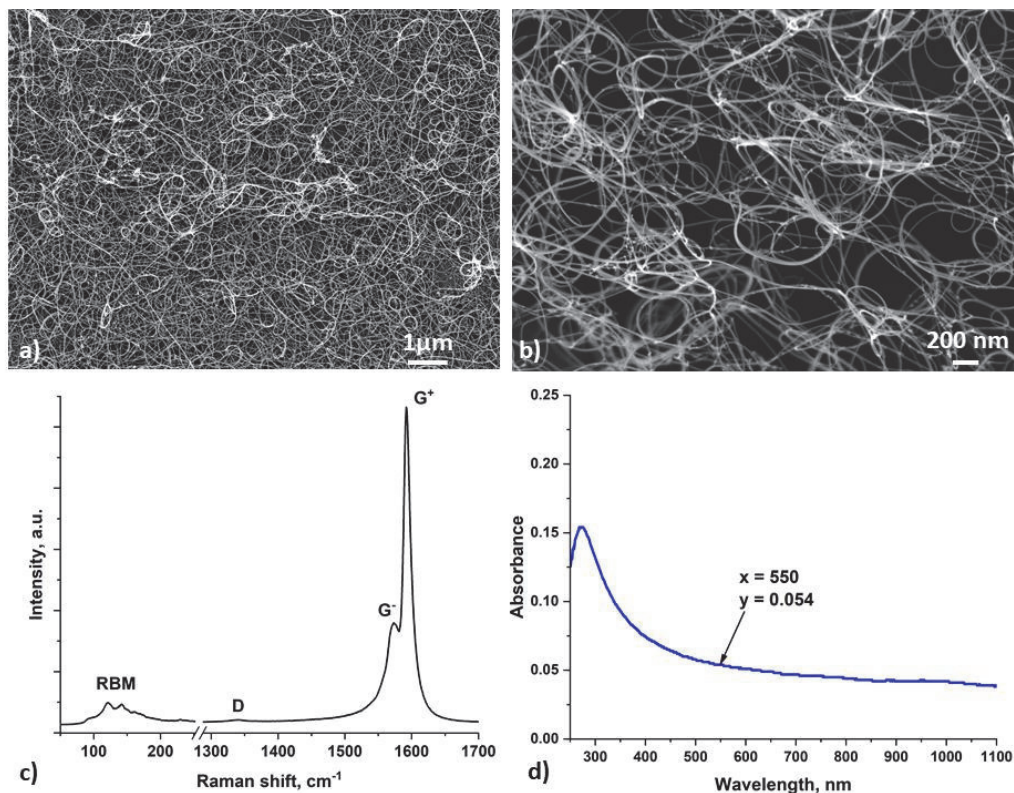


**Figure 2.** HR-SEM images of SWCNT film (a) onto SLG substrate and (b) onto carbon adhesive film, (c) Raman spectrum of a SWCNT film, and (d) optical absorption spectrum of a SWCNT film on a glass substrate with an absorbance of 0.054 at a wavelength of 550 nm (in the middle of visible wavelength range).

In this work, SWCNT films were used as a filler to obtain laminate-type nanocomposites in PHPs-derived thin film matrices. The composites were formed in two configurations: (i) BOTTOM, where the SWCNT film was transferred to the surface of the substrate before spin-coating the PPHP solution; and (ii) TOP, where SWCNTs were transferred to the surface of a formed, but uncured, PPHP film. Investigating these different configurations is important for controlling the distribution of SWCNTs within the matrix film, determining the possible influence of the configuration on the properties of the composite coating. Samples of both configurations were cured using both thermal and UV-assisted methods to thoroughly assess the possible change in their final properties.

Fig. 3 shows cross-sectional images of cured SLG/SiO<sub>x</sub>N<sub>y</sub>/SWCNT composite samples in different configurations. For the BOTTOM configuration, the SWCNT film is located close to the SLG/SiO<sub>x</sub>N<sub>y</sub> interface (Fig. 3c and 3d). In the TOP configuration, SWCNTs are located predominantly in the upper layers of the SiO<sub>x</sub>N<sub>y</sub> matrix film but may shift and spread deeper (Fig. 3a). This behavior could be due to diffusion of the stressed SWCNTs in viscous matrix material. During UV-induced curing, the film is cured gradually, starting from the surface downward, allowing the SWCNTs to remain longer in the viscous uncured matrix film, which can lead to their spreading throughout the volume of the matrix film (Fig. 3b). When the sample is fractured to create a cross-section, the SWCNTs are stretched and torn. These fragments can be seen emerging from the film in the images. This illustrates the additional bonding effect of SWCNT fillers inside the composite film.

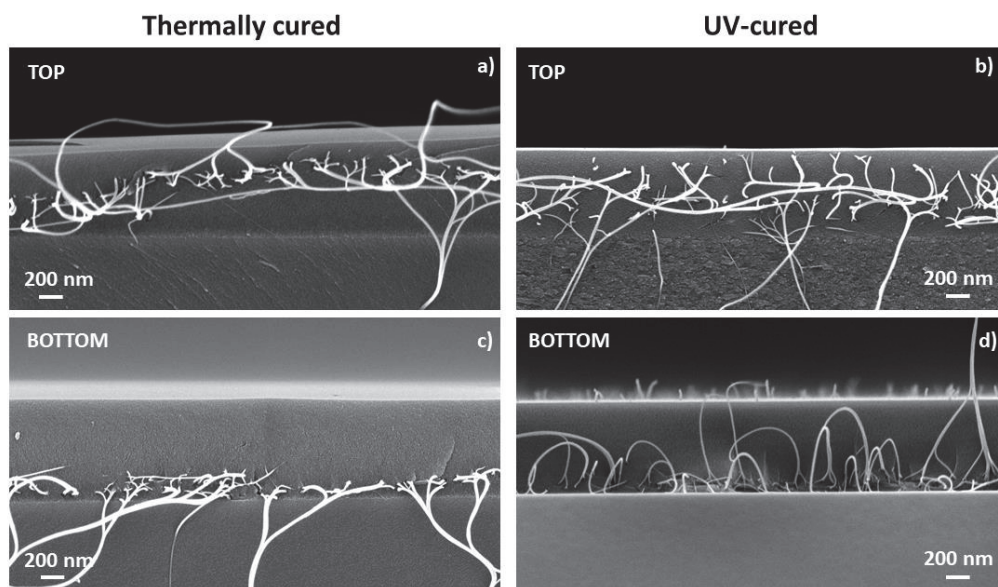


**Figure 3.** Cross-sectional HR-SEM images of SiO<sub>x</sub>N<sub>y</sub>/SWCNT composite films of the studied configurations (TOP and BOTTOM) on an SLG substrate, thermally cured (a, c) or UV-cured (b, d).

The process of formation of SiO<sub>x</sub>N<sub>y</sub>/SWCNT composites, along with their initial characterization, is described in more detail in our previous work [25]. In this study, we focused on studying the optical and mechanical properties of these composites.

### 3.3. Optical constants and properties of prepared SiO<sub>x</sub>N<sub>y</sub> and SiO<sub>x</sub>N<sub>y</sub>/SWCNT coatings

Silicon-containing thin films with varying oxygen and nitrogen contents have been widely used as functional layers and coatings for optical and electronic devices for decades [30]. To successfully integrate such films into these kinds of applications,



determining their optical parameters is critically important. While, these data are well known for the boundary cases of silicon dioxide and silicon nitride obtained under different conditions [42], beyond their high optical transmittance, there are large gaps in information regarding the refractive indices ( $n$ ) of PHPS-derived films cured by different methods, as well as the long-term stability of the optical properties of these films.

As was shown in our previous study, the degree of conversion of PHPS into  $\text{SiO}_x\text{N}_y$  depends on the curing method used, which leads to the formation of films with different chemical compositions and structures [26]. The nitrogen and oxygen content within the film strongly influences its optical properties [43]. Additionally, FTIR results show that during aging/ripening, the  $\text{SiO}_x\text{N}_y$  matrix films change their composition and structure. These changes are expected to affect the optical properties of the films.

There are various ways to determine the optical constants of films deposited on optically transparent substrates. These include spectroscopic ellipsometry (SE), which provides information about the refractive index ( $n$ ), absorption index ( $k$ ), and thickness ( $d$ ) of the film. SE detects the amplitude and phase of the light reflected from the sample for each wavelength of the range used. These quantities allow the optical constants to be calculated mathematically using suitable dispersion models. In our study, we used the Cauchy dispersion formulae to determine the optical constants of the samples (Table 1). The convergence of theoretical data to experimental data was assessed using the  $R^2$  correlation parameter. The closer  $R^2$  is to 1, the closer the calculated data are to the experimental data.

Fig. 4a and 4b show the dependences of the refractive index at wavelengths of 355 and 633 nm, respectively, on the aging/ripening time of the matrix films. To obtain the highest possible  $n$  value, an uncured PHPS film was prepared and measured, with the results shown in the figures as red triangles. This film contained the highest content of nitrogen and the lowest content of oxygen, which led to fairly high  $n$  values of about 1.6.

A thermally cured, 1-day aged  $\text{SiO}_x\text{N}_y$  matrix film also exhibited  $n$  values very close to 1.6, in contrast to the UV-cured film, where  $n$  values are on average were 0.02 lower. In the UV-cured sample, the nitrogen content was lower in comparison with the thermally annealed PHPS film, which led to a decrease in the refractive index value. This is consistent with our previous results illustrating the influence of the curing method on the structure and properties of the resulting  $\text{SiO}_x\text{N}_y$  films.

In the UV-cured, 1-day aged  $\text{SiO}_x\text{N}_y$  film, a fairly thick sub-layer in two-layer model with  $d_2$  of 200 nm and an  $n$  value very close to the values for silicon dioxide, was formed on top of the  $d_1$  sub-layer, which has a higher refractive index (Fig. 4d). The typical refractive index value for amorphous stoichiometric silicon dioxide is 1.465 at a wavelength of 633 nm [44].

The analysis of the transmittance spectra of samples makes it possible to improve the accuracy in calculating optical constants when modeling SE data. To achieve this, we measured the transmittance spectra of  $\text{SiO}_x\text{N}_y$  matrix films cured by both methods and aged for 1.5 months (Fig. 4c). All spectra were measured during a single working session of the spectrophotometer, and the uncoated SLG substrate was placed in the reference channel of the spectrophotometer. The uncured PHPS sample was used as a control, and its transmittance spectrum was measured 2 days after the film was formed. This sample exhibited the lowest transmittance of all measured, indicating the highest refractive index, a value that exceeded the  $n$  value of the substrate.

Both cured samples had refractive indices lower than those of the substrate, which places their transmittance around the 99.7% level (our spectrophotometer channels are unbalanced by approximately 0.3%). The interference minima in the spectra of the cured samples are located below this level, as indicated by the gray line in Fig. 4c. This indicates a negative inhomogeneity of the films, i.e., a gradient in the refractive index across the cross-section of the samples [45]. The beating seen in the spectrum of a UV-cured sample also points on a possible inhomogeneity in the material [46]. Specifically, the  $n$  values at the substrate-film interface were higher than those at the film-air interface. The gradient was higher in the annealed film, as its minima are located lower relative to the gray line.

Meanwhile, the UV-cured film had the lowest absolute value of  $n$  of all measured samples, since its spectrum is located above the others. All the observations described above are also reflected in the SE data (Table 1).

Based on Fig. 4a and b, we claim that the refractive index value shows a tendency to decrease as the films age. This decrease is connected with a gradual reduction in nitrogen content and an increase in oxygen content in films cured by both methods, signaling their gradual ripening towards silicon dioxide. This is in good agreement with the FTIR results presented in Section 3.1. After a month of aging, the  $n$  values of the films approached the refractive index of the SLG substrate (gray dotted line in the Fig. 4a and 4b), or dropped below it, with further aging tending towards the  $n$  values characteristic for silicon dioxide.

As the samples ripen, the structure of sub-layers and the magnitude of the  $n$  gradient also change. According to the SE data, a 1-day-aged UV-cured film had a rather thick upper sub-layer ( $\frac{1}{4}$  of the total thickness) with a smaller  $n$  value and a fairly large gradient value (Fig. 4d). Previous reports have noted the formation of this top sub-layer, which is more converted to silicon dioxide than the buried sub-layer formed during UV curing [47]. In our previous work, we also detected this effect using the XPS and EDX line-scan techniques [26].

When a PHPS film was illuminated from the surface with UV light, the PHPS located closer to the film-air interface transformed more rapidly into a silicon dioxide sub-layer. This sub-layer begins to partially block the diffusion of oxygen deep into the film. As a result, the process of PHPS conversion in the underlying volume slows down. This creates a gradient of cross-sectional chemical composition in the UV-cured  $\text{SiO}_x\text{N}_y$  film. Therefore, we do not see a step-like change in the composition and in the refractive index value, but rather a smooth transition, which is shown by the dash-dotted and solid lines in Fig. 4d, respectively.

With aging, the magnitude of the gradient decreased so much that it was no longer noticeable in SE calculations (Table 1) and was only detected in the 1.5-month-aged sample using the transmittance spectrum (Fig. 4c). In the case of thermal curing, the as-cured film was uniformly converted into silicon oxynitride, with a higher residual nitrogen content than the UV-cured PHPS film. However, after aging, the composition became similar to the UV-cured samples. An upper sub-layer with a lower  $n$  value compared to the rest of the material was detected (Fig. 4e), which then ceased to be determined due to a decrease in the magnitude of the  $n$  gradient in the cross-section of the samples as they continued to ripen (Table 1).

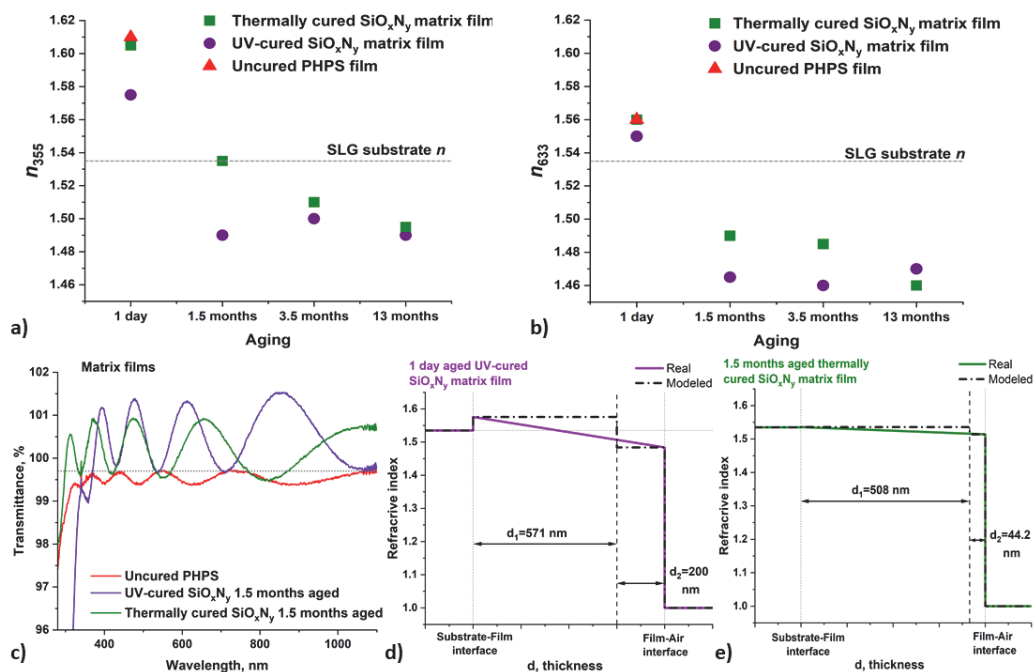


**Figure 4.** Dependence of the refractive index values on the samples aging time for  $n$  at wavelengths (a) 355 nm and (b) 633 nm. Transmittance spectra of uncured PHPS film and 1.5-months-aged UV and thermally cured  $\text{SiO}_x\text{N}_y$  films (c). The refractive index profiles along the thickness of the  $\text{SiO}_x\text{N}_y$  films for 1-day UV-cured (d) and 1.5-months thermally cured (e)  $\text{SiO}_x\text{N}_y$  films.

**Table 1** Optical parameters of PHPS-derived films calculated on the basis of SE measurements.

Sample	Aging	$d_1, \text{nm}$	$n_{355}$	$n_{633}$	$k_{355}$	$d_2, \text{nm}$	$n_{355}$	$n_{633}$	$k_{355}$	$R^2$
Uncured PHPS	1 day	673	1.61	1.56	0.08					0.99
	1 day	625	1.60	1.56	0.09					0.99
	1.5 months	508	1.54	1.49	0	44.2	1.51	1.47	0	0.98
Thermally cured $\text{SiO}_x\text{N}_y$	3.5 months	598	1.51	1.49	0.06					0.99
	13 months	507	1.50	1.46	0					0.99
	1 day	571	1.58	1.55	0.17	200	1.49	1.46	0.15	0.96
UV-cured $\text{SiO}_x\text{N}_y$	1.5 months	752	1.49	1.47	0					0.99
	3.5 months	613	1.50	1.46	0.02					1
	13 months	598	1.49	1.47	0					0.98

We observed a decrease in both refractive and absorption index values for cured films as aging time increased. This change can be explained by the film composition shifting towards  $\text{SiO}_2$ . The film thickness values are not representative due to the relatively non-uniform film thickness. The beam positions for SE measurements were not checked during the measurement. The SE data illustrates the general trends of changes in the optical

values of films during their ripening, since the table represents data measured for different aging periods of the different films.

From the results of these measurements, it is clear that the ripening of UV-cured  $\text{SiO}_x\text{N}_y$  matrix films proceeds noticeably faster compared to thermally cured samples. At the same time, UV-cured films exhibit refractive index values closer to the typical  $n$  values for silicon dioxide, due to a lower residual nitrogen content compared to annealed samples. This finding complements and expands the data obtained in this and our previous studies. The observed patterns were the same for the composite samples.

The results suggest that  $\text{SiO}_x\text{N}_y$  matrix films can function as antireflective coatings for materials with refractive indices higher than theirs. As the  $\text{SiO}_x\text{N}_y$  film ripens, the magnitude of the antireflection effect will increase due to an increase in  $\Delta n$  between the film and the underlying material.

#### 3.4. Antireflection effect in $\text{SiO}_x\text{N}_y$ and $\text{SiO}_x\text{N}_y/\text{SWCNT}$ structures

In our previous work, we discovered an antireflection effect in a UV-cured  $\text{SiO}_x\text{N}_y/\text{SWCNT}$  composite sample in a BOTTOM configuration, which was confirmed by measuring the reflectance spectra [25]. In this work, we extended our measurements to a similar composite and the remaining samples studied in this work.

In order to estimate the value of antireflection, the transmittance spectra of the SWCNT films transferred to the SLG substrate were first measured (Fig. 5a). Then, in accordance with the BOTTOM configuration, PHPS/SWCNT composite films were prepared, which were cured by both thermal and UV assisted methods. As shown in Fig. 5a, the transmittance of different areas of SWCNT film varied slightly, making it difficult to adequately assess the magnitude of the effect in TOP configuration composites. This was due to the inability to measure the transmittance of the specific piece of SWCNT film used in the formation of the TOP composite.

After curing, the transmittance spectra of the BOTTOM  $\text{SiO}_x\text{N}_y/\text{SWCNT}$  samples were measured again within the same operating session of the device, which eliminated the influence of additional factors associated with the operation of the spectrophotometer. For all spectra in this figure measurements were taken vs. the uncoated SLG substrate in the reference channel. It can be seen that for both curing methods, the transmittance of the composite samples increased in comparison with the transmittance of a pure SWCNT film on the SLG substrate. In the case of UV curing, the increase in transmittance was higher (approximately 2.5%) than the thermally cured composite (approximately 1.4%).

For better evaluation of the observed effect, we studied the change in transmittance depending on the stage of formation of the composite film during UV curing (Fig. 5b). First, the spectrum of the SWCNT film transferred to the SLG substrate was measured (black curve). A PHPS film was then spin-coated on top of the SWCNTs, and the spectrum of this uncured composite sample showed a 1.6% increase in transmittance in the mid-visible range (blue curve). After curing, the transmittance increased by another 1.4% (purple solid curve). All spectra were recorded within a single spectrophotometer run with the same baseline and without bare SLG substrate in reference channel.

Thus, in the case of UV curing, we have two factors that influence the magnitude of the antireflection effect. The first is associated with the formation of the composite sub-layer in PHPS matrix (see Fig. 3c, d) by the introduction of SWCNTs into the PHPS. The second factor, which increases the magnitude of the effect is related to the curing of the PHPS-derived matrix film accompanied by a decrease in the refractive index in the formed  $\text{SiO}_x\text{N}_y$ .

The increase in transmittance after curing of PHPS is associated with a change in the refractive index of the coating during the curing process. The SE results showed that immediately after UV curing, the film had a fairly thick top  $d_2$  layer with a low  $n$  value, which led to the appearance of an antireflection effect. The broadband nature of the antireflection effect was caused by the presence of a gradient in the  $n$  across the film, which was identified in Section 3.3. Broadband antireflection is in great demand in many areas of

photonics, as it replaces the construction of a traditional package of thin antireflection films with one coating, thereby simplifying and accelerating the manufacturing process [48,49]. This makes PHPS-derived matrix films very promising as antireflective coatings.

A week after curing, a new transmittance spectrum of the composite film was measured (dash-dotted curve). The transmittance value remained virtually unchanged after a week of aging, indicating that despite noticeable changes in the FTIR spectra, these changes are not sufficient to significantly affect the antireflective properties of the UV-cured coating.

An increase of 1.6% for the UV-cured sample as well as an increase of 1.4% for the thermally annealed sample are associated with the formation of the PHPS/SWCNT composite coating. The effect occurs when a SWCNT film is introduced into a matrix whose refractive index is higher than that of the SLG substrate. This phenomenon may be related to the creation of a nanostructured interface from the walls of SWCNTs within the PHPS matrix, which affects the propagation of light through the composite. Nanostructuring is one of the promising strategies for creating antireflection coatings [49].

Previous reports have highlighted significant increase in transmittance (about 4.5%) and a decrease in reflection in nanostructured composite polymer electrodes with SWCNTs, especially when nanotubes arranged as vertical arrays [50]. Additionally, the antireflection effect has been observed for SWCNT films randomly oriented in the horizontal plane deposited on the surface of a silicon wafer. With a small thickness (about 32 nm), the films were semi-transparent while acting as an antireflection coating for the substrate [48].

In the reflection spectra (Fig. 5c and 5d), it is clear that both matrix films had less reflection compared to the SLG substrate. However, when SWCNTs were introduced into the matrix, the reflection of the composite film decreased even more, which confirms the presence of a synergistic antireflection effect.



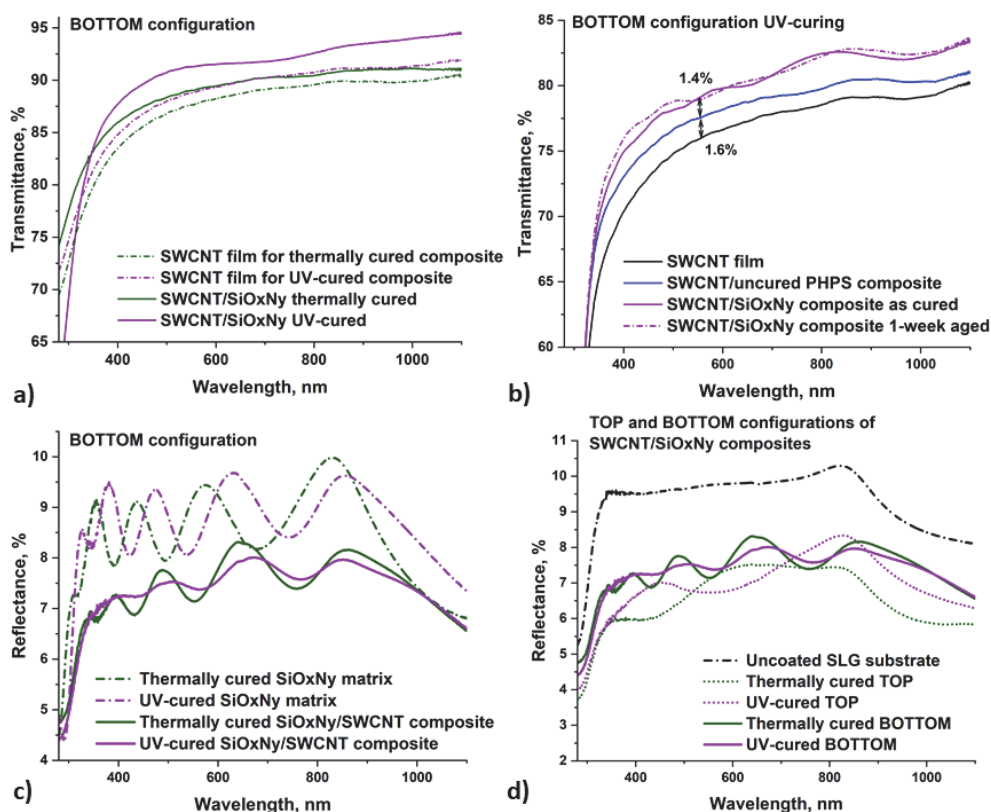


**Figure 5.** (a) and (b) transmittance spectra showing the antireflection effect in the SiO<sub>x</sub>N<sub>y</sub>/SWCNT composite samples; (c) and (d) reflection spectra confirming the presence of an antireflection effect in the SiO<sub>x</sub>N<sub>y</sub>/SWCNT composite samples.

It should be noted that the matrix films allowed an increase of around a 1.4% in transmittance immediately after UV curing, which is a relatively small value compared to other developed coatings. On the basis of the results of SE, an increase in the transmittance value should occur as the value of  $n$  decreases with ripening for films cured by both methods. It is reported that by creating a microporous structure inside a silica film deposited on a glass slide substrate, it is possible to increase transmittance by just over 3%. This is caused by a decrease in the refractive index of the film due to the possible creation of a large number of pores [20]. Thus, one of the possible ways to increase the antireflection effect in PHPS-derived films can be connected with controlled creation of inhomogeneous porosity in the deposited layer to decrease the  $n$  value closer to the film-air interface.

### 3.5. Mechanical and adhesive properties of SiO<sub>x</sub>N<sub>y</sub> and SiO<sub>x</sub>N<sub>y</sub>/SWCNT coatings

The scratch test is a standard method for assessing the mechanical resistance and adhesion of a coating to the underlying substrate. It helps to identify and study many different types of failures, such as coating peeling, plastic deformation, and film or substrate cracking. This test is conducted by pressing a special indenter onto the surface of the coating being evaluated and moving it with a constant or increasing load at a constant speed [51,52]. In our studies, we used a single pass of the indenter along the film surface under increasing load. This approach allowed us to determine the point of failure of the coating, which is called the critical load ( $L_c$ ) point.  $L_c$  values were determined using HR-SEM by measuring the distance from the beginning of the scratch to the first visible

damage to the coating. The initial load at the point of contact was 50 g, the rate of load increase was 200 g/mm, and the length of each scratch was 10 mm. In this study, we determine the  $L_c$  when the first visible damage occurred since the remaining modes of destruction were difficult to accurately determine.

During the tests, the change in the coefficient of friction (COF) of the films was also measured as the load increased. The coefficient of friction became unstable and began to increase sharply when the adhesion of the coating to the substrate changed (failure is initiated). Thus, the critical load can also be confirmed by measuring the change in the COF during the test.

The  $\text{SiO}_x\text{N}_y$  matrix films and  $\text{SiO}_x\text{N}_y/\text{SWCNT}$  composites were scratched 1 day, and 1 and 3 weeks after curing. It was found that mechanical and adhesive properties were also critically dependent on the curing method.

UV-cured  $\text{SiO}_x\text{N}_y/\text{SWCNT}$  composites exhibited high hardness and excellent adhesion to the Mo/SLG substrate, maintaining these properties during the aging process (Fig. 6b). The critical load value did not change noticeably with film aging/ripening. At low loads, no traces of the indenter remained on the samples (Fig. 6a). The point of the indenter contact with the film surface can sometimes be determined only by the presence of a subtle contrast in SEM images or by measuring the length from the end of the scratch. After reaching the  $L_c$ , semicircular cracks began to appear on the surface of the sample. As the load increased, they turned into ring-shaped cracks. At high magnification, it becomes clear that fractures occurred in the substrate, while the film remained tightly attached to the substrate fragments, thus illustrating very good adhesion to the molybdenum layer (Fig. 6d and 7c). This type of damage occurred due to the fact that brittle glass was located under the Mo layer. The compressive stress from the indenter passed deep into the film-substrate system and led to brittle fracturing of the glass [52]. Notably, the film did not peel off from the substrate beyond the scratch, although with very heavy loads, damage can spread beyond the scratch area.

The results for the UV-cured  $\text{SiO}_x\text{N}_y$  matrix films are identical (Fig. 7a and 7c). The introduction of SWCNTs into the matrix caused a visible reinforcing effect against rupture of the composite coating (Fig. 6f, 7b, and 7d), however, the presence of one filler layer was not enough to influence the values of the critical load withstood by the coating.

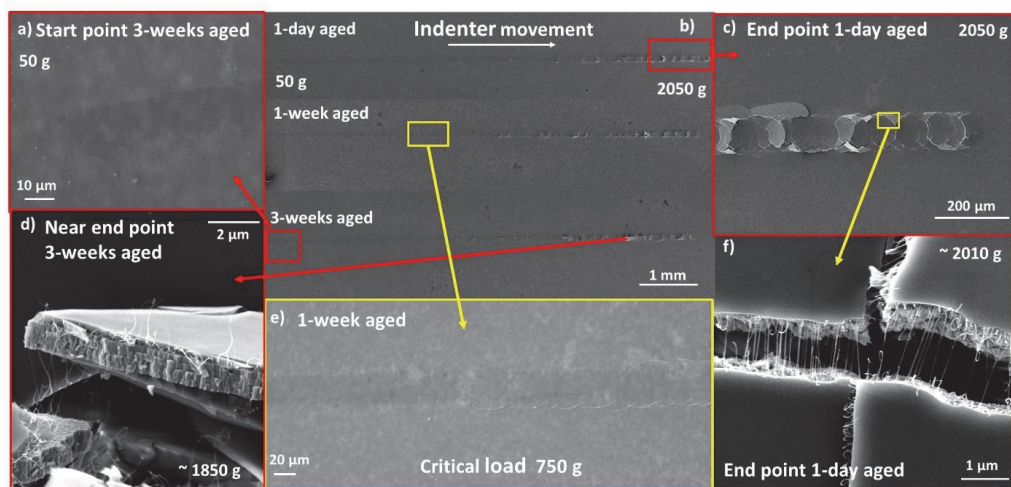


**Figure 6.** HR-SEM images of scratches from progressive load tests taken after 1-day and 1- and 3-weeks of aging of a UV-cured  $\text{SiO}_x\text{N}_y/\text{SWCNT}$  composite sample on a Mo/SLG substrate: a) area of the indenter contact with the film, 50 g; b) general appearance of all scratches; c) the end of a scratch, 2050 g; d) a fragment of the Mo/SLG substrate with a composite film on top of it; e) the appearance

of the first visible damage to the film, making it possible to determine Lc; f) fragments of the substrate with a composite film on top of them, held together by stretched SWCNTs.

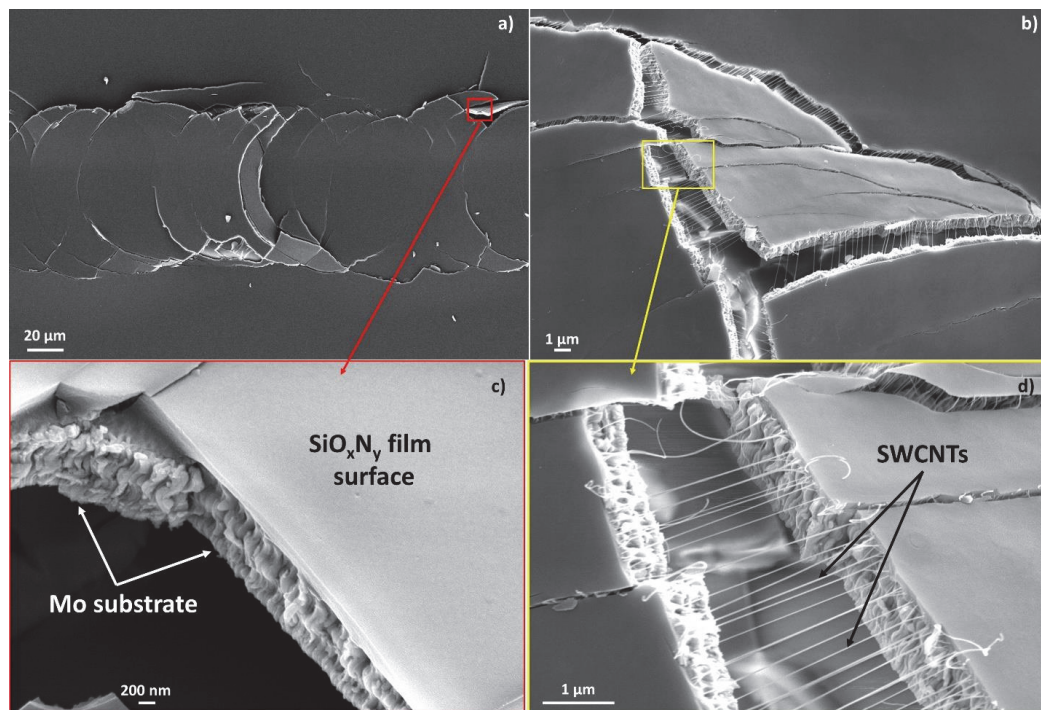


**Figure 7.** HR-SEM images of UV-cured samples: (a) a fracture of a scratch on a  $\text{SiO}_x\text{N}_y$  matrix film under high load (near the end of the scratch) and (c) a magnified image of one of the fragments; (b) a scratch fragment on a  $\text{SiO}_x\text{N}_y/\text{SWCNT}$  composite sample and (d) its enlarged area.

In contrast, all thermally cured samples showed relatively lower adhesion to the Mo/SLG substrate, as well as lower hardness and high ductility (Fig. 8a, 8c, 8d, 8e, and Fig. 9). Immediately after contact with the surface of the sample (at the lowest load of 50g), the indenter began to damage the coating (Fig. 8a and 8d), with the scratch visually identified along its entire length (Fig. 8e). The freshly cured film had very high ductility and was subject to a thinning effect. Under heavy loads leaving behind only a very thin and uneven layer on top of Mo (Fig. 9). Notably, the SWCNT film remained inside this very thin layer (Fig. 9c and 9d). However, one week after curing, the behavior of the annealed films became similar to UV-cured samples, with adhesion to the substrate becoming strong, and hardness increasing noticeably (Fig. 8f). The Lc value increased several times, from 250 g for 1-day aged to 970 g for 1-week aged film. The results for the thermally cured  $\text{SiO}_x\text{N}_y/\text{SWCNT}$  composite film were similar.

This difference in the behavior of 1-day aged films is also associated with their cross-sectional structure after curing, which was studied in our previous works [25,26]. The plasticity and lack of hardness of fresh thermally cured films is associated with the absence of a top layer of silicon dioxide and the presence of a very high nitrogen content throughout the film thickness. As the films age and ripen, the nitrogen content in the film decreases and a layer similar in composition to silicon dioxide appears on the surface. These changes make the aged film more comparable to the UV-cured samples.

The value of Lc depends on many factors, including the thickness of the coating. The SE results indicate that the samples have different thicknesses, and the HR-SEM cross-sectional images showed some variation in thickness within the sample. Since we cannot



always determine the thickness of the film over the entire scratch area precisely, it would be incorrect to compare the values of  $L_c$  without considering the thickness of the coating. Therefore, we do not present the  $L_c$  values of samples for all studied samples and scratches.

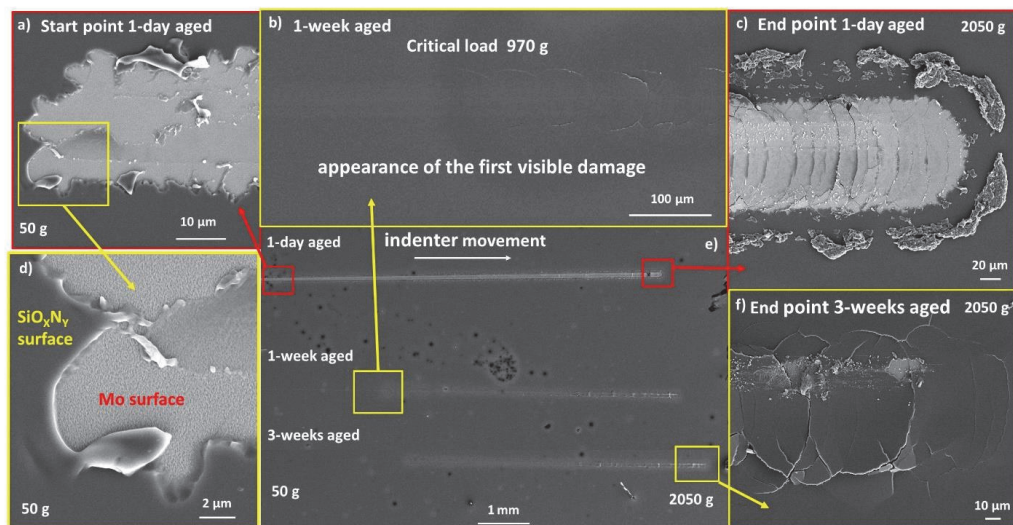


**Figure 8.** HR-SEM images of scratches obtained from the progressive load tests taken after 1-day and 1- and 3-weeks of aging of a thermally cured  $\text{SiO}_x\text{N}_y$  matrix film on a Mo/SLG substrate: a) the contact point of the indenter with the surface, 50 g; b) the appearance of the first visible damage to the film used to determine  $L_c$ ; c) the end of a scratch, 2050 g; d) magnified image of the contact point, 50 g; e) general appearance of all scratches; f) end point, 2050 g. Aging time and load are indicated in the images.

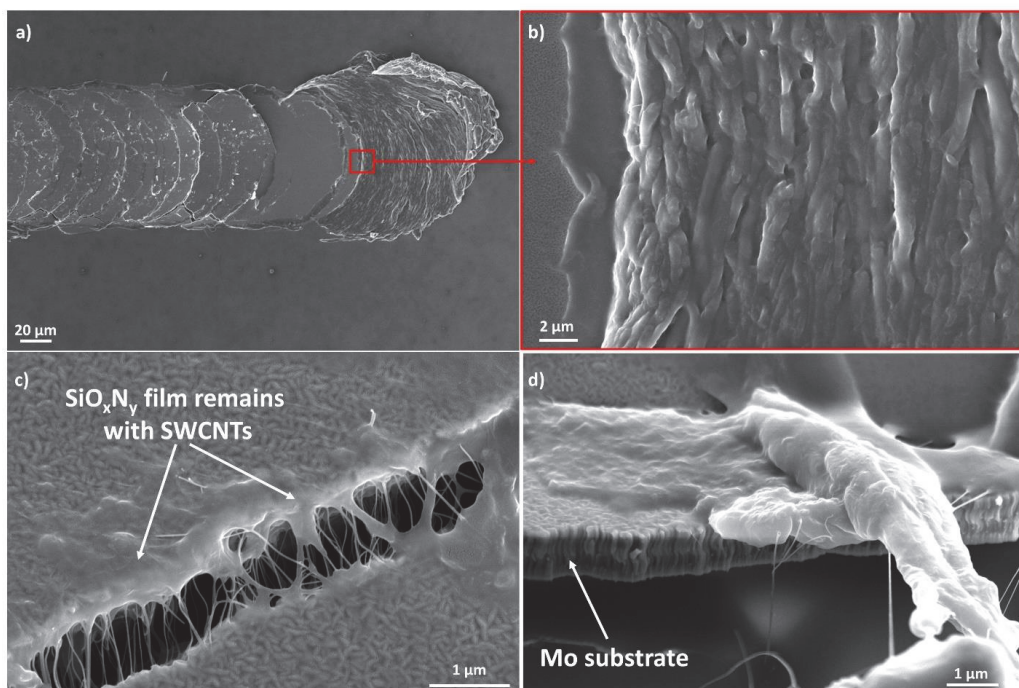


**Figure 9.** HR-SEM images of as-annealed SiO<sub>x</sub>N<sub>y</sub>/SWCNT composite sample: (a) destruction of the end of a scratch at 2050 g load and (b) magnified image of the plastically deformed and extruded film beyond the end point of the scratch; (c) and (d) fragments of the substrate with the remains of the composite film inside the scratch track.

For all samples, COF values did not exceed an average of 0.05. These values are an order of magnitude lower than those obtained by another scientific group during similar progressive load scratch tests for PPHS-derived films, but under completely different experimental conditions [17].

Such low COF values indicate the high smoothness of the film surface. Fig. 10 shows coefficients of friction curves for some samples. For all samples, the same behavior was observed for the COF value depending on the scratching time. Several areas can be distinguished on the graphs. Initially, when the indenter made contact with the film surface (load close to 50 g), the COF had the highest values. This was followed by a significant decrease, with COF values sometimes approaching zero during the first 30 seconds. Then there was a slight increase in COF, which then stabilizes (with a very steady increase) as the indenter moves along the surface of the film.

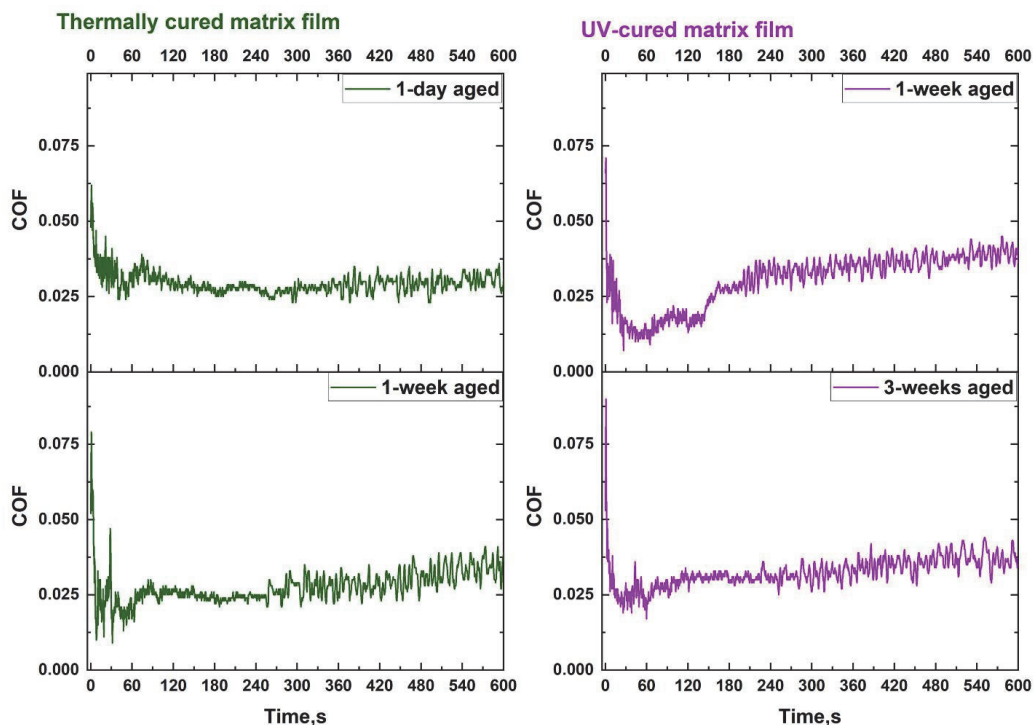


**Figure 10.** Typical friction coefficient curves recorded during progressive load scratch tests of  $\text{SiO}_x\text{N}_y$  matrix films. Curing method and aging time are indicated in the pictures.

Thus, the scratch test with progressive load showed that the composition of the films greatly influences the mechanical and adhesive properties. The introduction of SWCNTs into the  $\text{SiO}_x\text{N}_y$  matrix did not affect the adhesive properties of the resulting composites. However, there was a visible reinforcing effect of the SWCNT network against the tearing of the  $\text{SiO}_x\text{N}_y$ /SWCNT coatings. Thermal curing has proven to be a less fortunate method for the formation of protective coatings from PHPS, while UV curing produces harder, more stable films with excellent adhesion to the Mo/SLG substrate. The low COF values make PHPS-derived matrix films and composites based on them promising coatings for improved lubricious and scratch-resistant properties, which is an especially important factor in many industrial processes [17,53].

#### 4. Conclusions

In this work, the optical and mechanical properties of PHPS-derived  $\text{SiO}_x\text{N}_y$  films cured by two low-temperature methods, as well as their long-term stability, were studied. Similar studies were conducted for laminate-type composite coatings prepared by introducing a SWCNT filler film into a  $\text{SiO}_x\text{N}_y$  matrix film via dry transfer in different configurations. It was found that the PHPS-derived oxynitride films obtained by UV and thermal curing methods continue to ripen to silicon dioxide during the aging process. Active ripening during the first week after thermal curing leads to a change in the mechanical and adhesive properties of the films. The initial ductility and low adhesion are replaced by high strength and adhesion similar to UV-cured films.

The incorporation of SWCNT fillers leads to an improvement in the mechanical properties of the composite  $\text{SiO}_x\text{N}_y$ /SWCNT coatings. It has been confirmed that UV-cured films have a gradient in composition and refractive index in the cross-section, and thermally cured films also acquire this feature during the ripening process. In this work, the

optical constants of SiO<sub>x</sub>N<sub>y</sub> PHPs-derived films, as well as their changes over time, were systematically studied for the first time. An antireflection effect was detected in the SiO<sub>x</sub>N<sub>y</sub>/SWCNT composite films, caused by the optical properties of the cured matrix film and the interaction of the matrix with the SWCNT filler. It was found that in addition to the presence of a refractive index gradient, when films age, its value tends to approach the values for silicon dioxide, which, coupled with excellent barrier properties, make these coatings a promising material for broadband antireflection and encapsulation of optics. The low friction coefficients of the studied films can be useful to improve the sliding of mechanical parts and increase resistance to scratching.

**Funding:** This work was supported by the Estonian Ministry of Education and Research [grant number TK210], by the project "Increasing the knowledge intensity of Ida-Viru entrepreneurship" co-funded by the European Union and Education and Youth Board of Estonia [in frames of ÖÜF5 project] and NAMUR + core facility funded by the Estonian Research Council [under grant number TT13]. The mechanical measurement part of the work was supported in frames of MNHA22040 M-ERA.NET DuplexCER project.

**Acknowledgments:** The authors thanks Dr. Kaia Tõnsuaadu for her help with the ATR-FTIR measurements.

**Author Contributions:** Conceptualization, Elizaveta Shmagina and Sergei Bereznev; Data curation, Elizaveta Shmagina, Maksim Antonov, Aarne Kasikov and Sergei Bereznev; Formal analysis, Elizaveta Shmagina, Maksim Antonov, Aarne Kasikov and Sergei Bereznev; Funding acquisition, Sergei Bereznev; Investigation, Elizaveta Shmagina and Aarne Kasikov; Methodology, Maksim Antonov, Aarne Kasikov and Sergei Bereznev; Project administration, Elizaveta Shmagina and Sergei Bereznev; Resources, Maksim Antonov, Aarne Kasikov, Olga Volobujeva, Eldar Khabushev, Tanja Kallio and Sergei Bereznev; Supervision, Sergei Bereznev; Validation, Elizaveta Shmagina, Maksim Antonov, Aarne Kasikov and Sergei Bereznev; Visualization, Elizaveta Shmagina and Olga Volobujeva; Writing – original draft, Elizaveta Shmagina; Writing – review & editing, Elizaveta Shmagina, Maksim Antonov, Aarne Kasikov, Olga Volobujeva, Eldar Khabushev, Tanja Kallio and Sergei Bereznev.

## References:

1. R.K. Raman, S.A.G. Thangavelu, S. Venkataraj, A. Krishnamoorthy, Materials, methods and strategies for encapsulation of perovskite solar cells: From past to present, *Renew. Sustain. Energy Rev.* 151 (2021) 111608, <https://doi.org/10.1016/j.rser.2021.111608>.
2. K. Aitola, G.G. Sonai, M. Markkanen, J.J. Kaschuk, X. Hou, K. Miettunen, P.D. Lund, Encapsulation of commercial and emerging solar cells with focus on perovskite solar cells, *Sol. Energy* 237 (2022) 264–283, <https://doi.org/10.1016/j.solener.2022.03.060>.
3. M. Wu, B. Ma, S. Li, J. Han, W. Zhao, Powering the future: A critical review of research progress in enhancing stability of high-efficiency organic solar cells, *Adv. Funct. Mater.* 33 (2023) 2305445, <https://doi.org/10.1002/adfm.202305445>.
4. R.A. Afre, D. Pugliese, Perovskite solar cells: A review of the latest advances in materials, fabrication techniques, and stability enhancement strategies, *Micromachines* 15 (2024) 192, <https://doi.org/10.3390/mi15020192>.
5. I.A. Channa, A. Distler, M. Zaiser, C.J. Brabec, H.-J. Egelhaaf, Thin film encapsulation of organic solar cells by direct deposition of polysilazanes from solution, *Adv. Energy Mater.* 9 (2019) 1900598, <https://doi.org/10.1002/aenm.201900598>.
6. J. Peng, P. Ye, F. Xu, X. Bu, R. Wang, D. Lin, S. Yuan, Y. Zhu, H. Wang, Highly transparent, self-cleaning, and UV-shielding composite coating: When eco-friendly waterborne omniphobic surface cooperates with quantum dots, *Compos. B: Eng.* 284 (2024) 111731, <https://doi.org/10.1016/j.compositesb.2024.111731>.
7. J.-H. Woo, S.-Y. Park, D. Koo, M.H. Song, H. Park, J.-Y. Kim, Highly elastic and corrosion-resistive metallic glass thin films for flexible encapsulation, *ACS Appl. Mater. Interfaces* 14 (2022) 5578–5585, <https://doi.org/10.1021/acsami.1c20551>.
8. L. Prager, U. Helmstedt, H. Herrnberger, O. Kahle, F. Kita, M. Münch, A. Pender, A. Prager, J.W. Gerlach, M. Stasiak, Photochemical approach to high-barrier films for the encapsulation of flexible laminary electronic devices, *Thin Solid Films* 570 (2014) 87–95, <https://doi.org/10.1016/j.tsf.2014.09.014>.



9. D. Amouzou, L. Fourdrinier, R. Sporcken, Investigation of adhesion between molybdenum and polysilazane by XPS, *Appl. Surf. Sci.* 343 (2015) 202–206, <https://doi.org/10.1016/J.APSUSC.2015.03.110>.
10. C. Sun, D. Wang, C. Xu, W. Chen, Z. Zhang, Comparative study on polysilazane and silicone resins as high-temperature-resistant coatings, *High Perform. Polym.* 34 (2022) 474–486, <https://doi.org/10.1177/09540083211069041>.
11. Y. Zhan, R. Grottenmüller, W. Li, F. Javaid, R. Riedel, Evaluation of mechanical properties and hydrophobicity of room-temperature, moisture-curable polysilazane coatings, *J. Appl. Polym. Sci.* 138 (2021) 50469, <https://doi.org/10.1002/APP.50469>.
12. S. Yue, S. Wang, D. Han, S. Huang, M. Xiao, Y. Meng, Perhydropolysilazane-derived-SiO<sub>x</sub> coated cellulose: A transparent biodegradable material with high gas barrier property, *Cellulose* 29 (2022) 8293–8303, <https://doi.org/10.1007/S10570-022-04746-9>.
13. D. Burak, M.A. Rahman, D.-C. Seo, J.Y. Byun, J. Han, S.E. Lee, S.-H. Cho, *In situ* metal deposition on perhydropolysilazane-derived silica for structural color surfaces with antiviral activity, *ACS Appl. Mater. Interfaces* 15 (2023) 54143–54156, <https://doi.org/10.1021/ACSAMI.3C12622>.
14. J.J. Baek, S.M. Park, Y.R. Kim, K.C. Chang, Y.-J. Heo, G.Y. Bae, K.H. Choi, G. Shin, Intense pulsed UV light treatment to design functional optical films from perhydropolysilazane: an alternative to conventional heat treatment processes, *J. Mater. Sci.* 57 (2022) 254–273, <https://doi.org/10.1007/S10853-021-06598-3>.
15. J. Kim, J.H. Jang, J.-H. Kim, K. Park, J.S. Jang, J. Park, N. Park, Inorganic encapsulation method using solution-processible polysilazane for flexible solar cells, *ACS Appl. Energy Mater.* 3 (2020) 9257–9263, <https://doi.org/10.1021/ACSAEM.0C01593>.
16. H.S. Back, M.J. Kim, J.J. Baek, D.H. Kim, G. Shin, K.H. Choi, J.H. Cho, Intense-pulsed-UV-converted perhydropolysilazane gate dielectrics for organic field-effect transistors and logic gates, *RSC Adv.* 9 (2019) 3169–3175, <https://doi.org/10.1039/C8RA09831J>.
17. N. Yang, W. Wang, W. Cai, K. Lu, Corrosion and tribocorrosion mitigation of perhydropolysilazane-derived coatings on low carbon steel, *Corros. Sci.* 177 (2020) 108946, <https://doi.org/10.1016/J.CORSCI.2020.108946>.
18. P.C. With, T. Pröhl, J.W. Gerlach, A. Prager, A. Konrad, F. Arena, U. Helmstedt, Hydrogen permeation through uniaxially strained SiO<sub>x</sub> barrier thin films photochemically prepared on PET foil substrates, *Int. J. Hydrogen Energy* 81 (2024) 405–410, <https://doi.org/10.1016/J.IJHYDENE.2024.07.249>.
19. E. Shi, H. Li, L. Yang, L. Zhang, Z. Li, P. Li, Y. Shang, S. Wu, X. Li, J. Wei, K. Wang, H. Zhu, D. Wu, Y. Fang, A. Cao, Colloidal antireflection coating improves graphene-silicon solar cells, *Nano Lett.* 13 (2013) 1776–1781, <https://doi.org/10.1021/NL400353F>.
20. M. Lu, Q. Liu, Z. Wang, X. Zhang, G. Luo, J. Lu, D. Zeng, X. Zhao, S. Tian, Facile preparation of porous SiO<sub>2</sub> antireflection film with high transmittance and hardness via self-templating method for perovskite solar cells, *Mater. Today Chem.* 29 (2023) 101473, <https://doi.org/10.1016/J.MTCHEM.2023.101473>.
21. D. Kim, G.G. Jeon, J.H. Kim, J. Kim, N. Park, Design of a flexible thin-film encapsulant with sandwich structures of perhydropolysilazane layers, *ACS Appl. Mater. Interfaces* 14 (2022) 34678–34685, <https://doi.org/10.1021/acsami.2c06699>.
22. L. Duo, Z. Zhang, K. Zheng, D. Wang, C. Xu, Y. Xia, Perhydropolysilazane derived SiON interfacial layer for Cu/epoxy molding compound composite, *Surf. Coat. Technol.* 391 (2020) 125703, <https://doi.org/10.1016/J.SURFCOAT.2020.125703>.
23. B. Arash, Q. Wang, V.K. Varadan, Mechanical properties of carbon nanotube/polymer composites, *Sci. Rep.* 4 (2014) 6479, <https://doi.org/10.1038/srep06479>.
24. X. Zhang, N. Zhao, C. He, The superior mechanical and physical properties of nanocarbon reinforced bulk composites achieved by architecture design – A review, *Prog. Mater. Sci.* 113 (2020) 100672, <https://doi.org/10.1016/J.PMATSCI.2020.100672>.
25. E. Shmagina, O. Volobujeva, A.G. Nasibulin, S. Bereznev, Fabrication of novel SiO<sub>x</sub>N<sub>y</sub>/SWCNT laminate-type composite protective coating using low-temperature approach, *Ceram. Int.* 50 (2024) 34312–34320, <https://doi.org/10.1016/j.ceramint.2024.06.250>.
26. E. Shmagina, M. Danilson, V. Mikli, S. Bereznev, Comparative study of perhydropolysilazane protective films, *Surf. Eng.* 38 (2022) 769–777, <https://doi.org/10.1080/02670844.2022.2155445>.



27. E. M. Khabushev, D. V. Krasnikov, A. E. Goldt, E. O. Fedorovskaya, A. P. Tsapenko, Q. Zhang, E. I. Kauppinen, T. Kallio, A. G. Nasibulin, Joint effect of ethylene and toluene on carbon nanotube growth, *Carbon* 189 (2022) 474–483, <https://doi.org/10.1016/j.carbon.2021.12.052>.
28. P.M. Rajanna, H. Meddeb, O. Sergeev, A.P. Tsapenko, S. Bereznev, M. Vehse, O. Volobujeva, M. Danilson, P.D. Lund, A.G. Nasibulin, Rational design of highly efficient flexible and transparent p-type composite electrode based on single-walled carbon nanotubes, *Nano Energy* 67 (2020) 104183, <https://doi.org/10.1016/J.NANOEN.2019.104183>.
29. G. Drozdov, I. Ostanin, H. Xu, Y. Wang, T. Dumitrică, A. Grebenko, A.P. Tsapenko, Y. Gladush, G. Ermolaev, V.S. Volkov, S. Eibl, U. Rűde, A.G. Nasibulin, Densification of single-walled carbon nanotube films: Mesoscopic distinct element method simulations and experimental validation, *J. Appl. Phys.* 128 (2020) 184701, <https://doi.org/10.1063/5.0025505>.
30. M.I. Alayo, I. Pereyra, W.L. Scopel, M.C.A. Fantini, On the nitrogen and oxygen incorporation in plasma-enhanced chemical vapor deposition (PECVD) SiO<sub>x</sub>N<sub>y</sub> films, *Thin Solid Films* 402 (2002) 154–161, [https://doi.org/10.1016/S0040-6090\(01\)01685-6](https://doi.org/10.1016/S0040-6090(01)01685-6).
31. L. Prager, A. Dierdorf, H. Liebe, S. Naumov, S. Stojanović, R. Heller, L. Wennrich, M.R. Buchmeiser, Conversion of perhydropolysilazane into a SiO<sub>x</sub> network triggered by vacuum ultraviolet irradiation: Access to flexible, transparent barrier coatings, *Chem. Eur. J.* 13 (2007) 8522–8529, <https://doi.org/10.1002/CHEM.200700351>.
32. T. Sasaki, L. Sun, Y. Kurosawa, T. Takahashi, Y. Suzuri, Nanometer-thick SiN films as gas barrier coatings densified by vacuum UV irradiation, *ACS Appl. Nano Mater.* 4 (2021) 10344–10353, <https://doi.org/10.1021/ACSANM.1C01862>.
33. Z. Zhang, Z. Shao, Y. Luo, P. An, M. Zhang, C. Xu, Hydrophobic, transparent and hard silicon oxynitride coating from perhydropolysilazane, *Polym. Int.* 64 (2015) 971–978, <https://doi.org/10.1002/PI.4871>.
34. M. Günthner, K. Wang, R.K. Bordia, G. Motz, Conversion behaviour and resulting mechanical properties of polysilazane-based coatings, *J. Eur. Ceram. Soc.* 32 (2012) 1883–1892, <https://doi.org/10.1016/J.JEURCERAMSOC.2011.09.005>.
35. X. Jin, X. Guo, L. Zhai, F. Vogelbacher, Y. Xia, M. Li, C. Xu, Z. Zhang, Robust and flexible free-standing polyimide/SiO<sub>x</sub> nanocomposite one-dimensional photonic crystals with high reflectance, *J. Mater. Sci.* 58 (2023) 1656–1669, <https://doi.org/10.1007/S10853-022-08136-1>.
36. K. Nakajima, H. Uchiyama, T. Kitano, H. Kozuka, Conversion of solution-derived perhydropolysilazane thin films into silica in basic humid atmosphere at room temperature, *J. Am. Ceram. Soc.* 96 (2013) 2806–2816, <https://doi.org/10.1111/JACE.12513>.
37. G.A. Ermolaev, A.P. Tsapenko, V.S. Volkov, A.S. Anisimov, Y.G. Gladush, A.G. Nasibulin, Express determination of thickness and dielectric function of single-walled carbon nanotube films, *Appl. Phys. Lett.* 116 (2020) 231103, <https://doi.org/10.1063/5.0012933>.
38. W. Cheung, M. Patel, Y. Ma, Y. Chen, Q. Xie, J.V. Lockard, Y. Gao, H. He,  $\pi$ -Plasmon absorption of carbon nanotubes for the selective and sensitive detection of Fe<sup>3+</sup> ions, *Chem. Sci.* 7 (2016) 5192–5199, <https://doi.org/10.1039/C6SC00006A>.
39. S.D. Shandakov, M.V. Lomakin, A.G. Nasibulin, The effect of the environment on the electronic properties of single-walled carbon nanotubes, *Tech. Phys. Lett.* 42 (2016) 1071–1075, <https://doi.org/10.1134/S1063785016110080>.
40. A. Jorio, R. Saito, Raman spectroscopy for carbon nanotube applications, *J. Appl. Phys.* 129 (2021) 021102, <https://doi.org/10.1063/5.0030809>.
41. A.A. Alekseeva, D.V. Krasnikov, G.B. Livshits, S.A. Romanov, Z.I. Popov, L.A. Varlamova, E.V. Sukhanova, A.S. Klimovich, P.B. Sorokin, S.V. Savilov, A.G. Nasibulin, Films enriched with semiconducting single-walled carbon nanotubes by aerosol N<sub>2</sub>O etching, *Carbon* 212 (2023) 118094, <https://doi.org/10.1016/j.carbon.2023.118094>.
42. V. Kanclíř, J. Václavík, K. Židek, Precision of silicon oxynitride refractive-index profile retrieval using optical characterization, *Acta Phys. Pol. A* 140 (2021) 215–221, <https://doi.org/10.12693/APhysPolA.140.215>.
43. Y. Shi, L. He, F. Guang, L. Li, Z. Xin, R. Liu, A review: Preparation, performance, and applications of silicon oxynitride film, *Micromachines* 10 (2019) 552, <https://doi.org/10.3390/mi10080552>.

44. A. Kalnitsky, S.P. Tay, J.P. Ellul, S. Chongsawangvirod, J.W. Andrews, E.A. Irene, Measurements and modeling of thin silicon dioxide films on silicon, *J. Electrochem. Soc.* 137 (1990) 234–238, <https://doi.org/10.1149/1.2086373>.
45. M. Montecchi, R.M. Montereali, E. Nichelatti, Reflectance and transmittance of a slightly inhomogeneous thin film bounded by rough, unparallel interfaces, *Thin Solid Films* 396 (2001) 264–275, [https://doi.org/10.1016/S0040-6090\(01\)01253-6](https://doi.org/10.1016/S0040-6090(01)01253-6).
46. B. Akaoglu, I. Atilgan, B. Katircioglu, Correlation between optical path modulations and transmittance spectra of a-Si:H thin films, *Appl Opt.* 39 (2000) 1611–1616, <https://doi.org/10.1364/AO.39.001611>.
47. A. Morlier, S. Cros, J.-P. Garandet, N. Alberola, Structural properties of ultraviolet cured polysilazane gas barrier layers on polymer substrates, *Thin Solid Films* 550 (2014) 85–89, <https://doi.org/10.1016/j.TSF.2013.10.140>.
48. F. De Nicola, P. Hines, M. De Crescenzi, N. Motta, Moth-eye effect in hierarchical carbon nanotube anti-reflective coatings, *Carbon* 108 (2016) 262–267, <https://doi.org/10.1016/j.carbon.2016.07.011>.
49. K.-T. Chiang, S.-H. Lin, Y.-Z. Ye, B.-H. Zeng, Y.-L. Cheng, R.-H. Lee, K.-Y.A. Lin, H. Yang, Leafhopper-inspired reversibly switchable antireflection coating with sugar apple-like structure arrays, *J. Colloid Interface Sci.* 650 (2023) 81–93, <https://doi.org/10.1016/j.jcis.2023.06.179>.
50. N. Boulanger, D.R. Barbero, Nanostructured networks of single wall carbon nanotubes for highly transparent, conductive, and anti-reflective flexible electrodes, *Appl. Phys. Lett.* 103 (2013) 021116, <https://doi.org/10.1063/1.4813498>.
51. M. Barletta, V. Tagliaferri, A. Gisario, S. Venettacci, Progressive and constant load scratch testing of single- and multi-layered composite coatings, *Tribol. Int.* 64 (2013) 39–52, <https://doi.org/10.1016/j.triboint.2013.03.002>.
52. M.F. Othman, A.R. Bushroa, W.N.R. Abdullah, Evaluation techniques and improvements of adhesion strength for TiN coating in tool applications: A review, *J. Adhes. Sci. Technol.* 29 (2015) 569–591, <https://doi.org/10.1080/01694243.2014.997379>.
53. Z. Zhang, H. Dong, A state-of-the-art overview - Recent development in low friction and wear-resistant coatings and surfaces for high-temperature forming tools, *Manuf. Rev.* 1 (2014) 24, <https://doi.org/10.1051/mfreview/2015001>.

# Curriculum vitae

## Personal data

Name: Elizaveta Shmagina  
Date of birth: 17.05.1996  
Place of birth: Saint-Petersburg, Russian Federation  
Citizenship: Russian

## Contact data

E-mail: [elizaveta.shmagina@taltech.ee](mailto:elizaveta.shmagina@taltech.ee)

## Education

2020–2025 Tallinn University of Technology, Chemical and Materials Technology, PhD  
2018–2020 ITMO University, Saint-Petersburg, MSc in Physics and Technology of Nanostructures (cum laude)  
2014–2018 ITMO University, Saint-Petersburg, BSc in Laser Technology  
2012–2014 Kuzmolovskaya Secondary Comprehensive School No. 1, Kuzmolovsky, Leningrad region, Advanced study of technical subjects

## Language competence

Russian Native  
English Fluent  
Estonian Basic

## Professional employment

2014–2017 Restaurant team member, Burger King, Saint-Petersburg  
2018–2020 Engineer, ITMO University, Saint-Petersburg  
2022–2025 Junior Research Fellow, Department of Materials and Environmental Technology, School of Engineering, Tallinn University of Technology, Tallinn

## Defended dissertations

Master's Degree, 2020, Supervisor: Prof. Elena Konshina, Luminescence enhancement of carbon dots by silver nanoparticles in their hybrid thin-film structures, ITMO University, Saint-Petersburg, Russia

## Participation in conferences

2024 European Materials Research Society (E-MRS) Spring Meeting & Exhibit Conference, Strasbourg, France, Oral presentation  
2024 Surfaces, Interfaces and Coatings Technologies International conference, Vienna, Austria, Poster presentation  
2023 European Materials Research Society (E-MRS) Spring Meeting & Exhibit Conference, Strasbourg, France, Oral presentation  
2022 Surfaces, Interfaces and Coatings Technologies International conference, Barcelona, Spain, Poster presentation  
2021–2023 Graduate School of Functional Materials and Technologies (GSFMT) Scientific Conferences, Tartu and Tallinn, Estonia, Poster and Oral presentations  
2020 IX international conference on photonics and information optics, Moscow, Russia, Poster presentation

- 2019 Smart Nanosystems for Life Conference, Saint-Petersburg, Russia, Poster presentation
- 2019 XI International Conference “Fundamental Problems of Optics”, Saint-Petersburg, Russia, Poster presentation
- 2019 Congress of Young Scientists, Saint-Petersburg, Russia. Poster presentation

#### **Participation in internships and summer schools**

- 2022 Graduate School of Functional Materials and Technologies (GSFMT) Summer School “Modern Technologies for Green Future”, Pärnu, Estonia
- 2020 Erasmus+ Grant internship at Institut Jean Lamour, Mines Nancy, University de Lorraine, France
- 2019 Jyväskylä Summer School, Finland, University of Jyväskylä, Course: “Biom mineralization and biological materials in nanotechnology”
- 2019 Internship “Summer Bridge Scholarship”, ITMO University, Project: “Femtosecond Laser Ablation of Metal-Nitrides thin films”

#### **Research projects**

- “Development of new materials for photonics”, ITMO university, Russia
- “Nanoscale white light sources based on metal-dielectric particles”, ITMO University, Russia
- “Optical and electrical properties of hybrid nanomaterials based on carbon, semiconductor and metal nanostructures”, ITMO University, Russia
- ÕÜF5 “Nanocomposite materials for renewable energetics and energy storage technology”, TalTech, Estonia
- PRG1023 “Sustainable, cost-efficient, flexible, lightweight and semitransparent multinary chalcogenide based solar cells for building integrated photovoltaics”, TalTech, Estonia
- TK210U7 “GREENTECH”, TalTech, Estonia

#### **Articles in indexed scientific journals**

1. E.G. Shmagina, E.A. Konshina, D.P. Shcherbinin, P.D. Khavlyuk & M.S. Stepanova, “Photoluminescence enhancement of carbon dots by Ag nanoparticles in thin-film hybrid structures”, Surface Engineering (2020), DOI: 10.1080/02670844.2020.1747015
2. E. Shmagina, M. Danilson, V. Mikli, S. Bereznev, Comparative study of perhydropolysilazane protective films, Surf. Eng. 38 (2022) 769–777, <https://doi.org/10.1080/02670844.2022.2155445>.
3. E. Shmagina, O. Volobujeva, A.G. Nasibulin, S. Bereznev, Fabrication of novel SiOxNy/SWCNT laminate-type composite protective coating using low-temperature approach, Ceram. Int. 50 (2024) 34312–34320, <https://doi.org/10.1016/j.ceramint.2024.06.250>.
4. E. Shmagina, M. Antonov, A. Kasikov, O. Volobujeva, E.M. Khabushev, T. Kallio, S. Bereznev, Structural, Mechanical, and Optical Properties of Laminate-Type Thin Film SWCNT/SiOxNy Composites, Nanomaterials 14 (2024) 1806, <https://doi.org/10.3390/nano14221806>

## Elulookirjeldus

### Isikuandmed

Nimi: Elizaveta Shmagina  
Sünniaeg: 17.05.1996  
Sünnikoht: Sankt-Peterburg, Venemaa  
Kodakondsus: Venemaa

### Kontaktandmed

E-post: [elizaveta.shmagina@taltech.ee](mailto:elizaveta.shmagina@taltech.ee)

### Hariduskäik

2020–2025 Tallinna Tehnikaülikool, Keemia- ja materjalitehnoloogia, PhD  
2018–2020 Sankt-Peterburi ITMO ülikool, Nanostruktuuride eksperimentaalne füüsika, MSc (cum laude)  
2014–2018 Sankt-Peterburi ITMO ülikool, laseritehnikad ja -tehnoloogiad, BSc  
2012–2014 Kuzmolovskaya keskkool No. 1, Kuzmolovsky alevik, Leningradi oblast

### Keelteoskus

Vene keel Emakeel  
Inglise keel Kõrgtase  
Eesti keel Algtase

### Teenistuskäik

2014–2017 Restorani töötaja, Burger King, Sankt-Peterburg  
2018–2020 Insener, ITMO ülikool, Sankt-Peterburg  
2022–2025 Doktorant-nooremteadur, Materjali- ja keskkonnatehnoloogia instituut, Inseneriteaduskond, Tallinna Tehnikaülikool, Tallinn

### Kaitstud lõputööd:

Magistrikraad, 2020, Juhendaja: Prof. Elena Konshina, Süsiniku punktide luminesentsi suurendamine hõbeda nanoosakeste abil nende hübriidsetes õhukese kile struktuurides, ITMO ülikool, Sankt-Peterburg, Venemaa

### Konverentsidel osalemine

2024 Euroopa Materjaliuuringute Selts (E-MRS) 2024 kevadkonverents, Strasbourg, Prantsusmaa, Suuline ettekanne  
2024 Pinnad, liidesed ja kattetehnoloogiad, rahvusvaheline konverents 2024, Viin, Austria, Posterettekanne  
2023 Euroopa Materjaliuuringute Selts (E-MRS) 2023 kevadkonverents, Strasbourg, Prantsusmaa, Suuline ettekanne  
2022 Pinnad, liidesed ja kattetehnoloogiad, rahvusvaheline konverents 2022, Barcelona, Hispaania, Posterettekanne  
2021–2023 Funktsionaalsete materjalide ja tehnoloogiate doktorikool (FMTDK) teaduskonverentsid, Tartu ja Tallinn, Eesti, Poster- ja suuline ettekanne  
2020 IX Rahvusvaheline fotoonika ja infooptika konverents 2020, Moskva, Venemaa, Posterettekanne

- 2019 Nutikate nanosüsteemide eluks konverents 2019, Sankt-Peterburg, Venemaa, Posterettekann
- 2019 XI Rahvusvaheline konverents "Optika põhiprobleemid" 2019, Sankt-Peterburg, Venemaa, Posterettekann
- 2019 Noorte teadlaste kongress, Sankt-Peterburg, Venemaa, Posterettekann

#### **Osalemine suvekoolides**

- 2022 Funktsionaalsete Materjalide ja Tehnoloogiate Kõrgkool (GSFMT) suvekool, Pärnu, Eesti
- 2020 Erasmus+ grandipraktika, Jean Lamour instituut, Mines Nancy, de Lorraine ülikool, Prantsusmaa
- 2019 Jyväskylä suvekool, Soome, Jyväskylä ülikool, Kursus: "Biomineeraliseerimine ja bioloogilised materjalid nanotehnoloogias"
- 2019 Praktika "Suvesilla stipendium", ITMO ülikool, Projekt: "Metall-nitriidide õhukeste kilede femtosekundiline laserablatsioon"

#### **Teadusprojektid**

- "Fotoonika uute materjalide väljatöötamine", ITMO ülikool
- "Metallidielektrilistel osakestel põhinevad nanoskaala valgud valgusallikad", ITMO ülikool
- "Süsiniku, pooljuhtide ja metallide nanostruktuuridel põhinevate hübriidnanomaterjalide optilised ja elektrilised omadused", ITMO ülikool
- ÕÜF5 "Nanokomposiitmaterjalid taastuveneergetika ja salvestustehnoloogia jaoks", TalTech
- PRG1023 "Mitmik-kalkogeniididel põhinevad jätkusuutlikud, kuluefektiivsed, kerged, painduvad ja poolläbipaistvad ehitisingreeritavad päikesepatareid", TalTech
- TK210U7 "Jätkusuutliku rohevesiniku ja energiatehnoloogia tippkeskus", TalTech

#### **Publikatsioonide loend**

1. E.G. Shmagina, E.A. Konshina, D.P. Shcherbinin, P.D. Khavlyuk & M.S. Stepanova, "Photoluminescence enhancement of carbon dots by Ag nanoparticles in thin-film hybrid structures", *Surface Engineering* (2020), DOI: 10.1080/02670844.2020.1747015
2. E. Shmagina, M. Danilson, V. Mikli, S. Bereznev, Comparative study of perhydropolysilazane protective films, *Surf. Eng.* 38 (2022) 769–777, <https://doi.org/10.1080/02670844.2022.2155445>.
3. E. Shmagina, O. Volobujeva, A.G. Nasibulin, S. Bereznev, Fabrication of novel SiOxNy/SWCNT laminate-type composite protective coating using low-temperature approach, *Ceram. Int.* 50 (2024) 34312–34320, <https://doi.org/10.1016/j.ceramint.2024.06.250>.
4. E. Shmagina, M. Antonov, A. Kasikov, O. Volobujeva, E.M. Khabushev, T. Kallio, S. Bereznev, Structural, Mechanical, and Optical Properties of Laminate-Type Thin Film SWCNT/SiOxNy Composites, *Nanomaterials* 14 (2024) 1806, <https://doi.org/10.3390/nano14221806>

ISSN 2585-6901 (PDF)  
ISBN 978-9916-80-278-6 (PDF)